

AWARD NUMBER: W81XWH-19-1-0045

TITLE: A Targeted Alpha-Particle Radiopharmaceutical for Bone Metastatic Breast Cancer

PRINCIPAL INVESTIGATOR: Yusuke Shiozawa, M.D., Ph.D.

CONTRACTING ORGANIZATIONS: Wake Forest University Health Sciences  
Winston-Salem, NC

REPORT DATE: May 2021

TYPE OF REPORT: Annual report

PREPARED FOR: U.S. Army Medical Research and Materiel Command  
Fort Detrick, Maryland 21702-5012

DISTRIBUTION STATEMENT: Approved for Public Release;  
Distribution Unlimited

The views, opinions and/or findings contained in this report are those of the author(s) and should not be construed as an official Department of the Army position, policy or decision unless so designated by other documentation.

REPORT DOCUMENTATION PAGE				Form Approved OMB No. 0704-0188	
Public reporting burden for this collection of information is estimated to average 1 hour per response, including the time for reviewing instructions, searching existing data sources, gathering and maintaining the data needed, and completing and reviewing this collection of information. Send comments regarding this burden estimate or any other aspect of this collection of information, including suggestions for reducing this burden to Department of Defense, Washington Headquarters Services, Directorate for Information Operations and Reports (0704-0188), 1215 Jefferson Davis Highway, Suite 1204, Arlington, VA 22202-4302. Respondents should be aware that notwithstanding any other provision of law, no person shall be subject to any penalty for failing to comply with a collection of information if it does not display a currently valid OMB control number. <b>PLEASE DO NOT RETURN YOUR FORM TO THE ABOVE ADDRESS.</b>					
1. REPORT DATE May 2021		2. REPORT TYPE Annual		3. DATES COVERED 01Apr2020-31Mar2021	
4. TITLE AND SUBTITLE  A Targeted Alpha-Particle Radiopharmaceutical for Bone Metastatic Breast Cancer				5a. CONTRACT NUMBER	
				5b. GRANT NUMBER W81XWH-19-1-0045	
				5c. PROGRAM ELEMENT NUMBER	
6. AUTHOR(S)  Yusuke Shiozawa, MD, PhD; Thaddeus Wadas, PhD  E-Mail: yshiozaw@wakehealth.edu, thaddeus-wadas@uiowa.edu				5d. PROJECT NUMBER	
				5e. TASK NUMBER	
				5f. WORK UNIT NUMBER	
7. PERFORMING ORGANIZATION NAME(S) AND ADDRESS(ES)  Wake Forest University Health Sciences    University of Iowa Medical Center Blvd.,                      Iowa City, IA 52242 Winston-Salem NC 27157				8. PERFORMING ORGANIZATION REPORT NUMBER	
9. SPONSORING / MONITORING AGENCY NAME(S) AND ADDRESS(ES)  U.S. Army Medical Research and Materiel Command Fort Detrick, Maryland 21702-5012				10. SPONSOR/MONITOR'S ACRONYM(S)	
				11. SPONSOR/MONITOR'S REPORT NUMBER(S)	
12. DISTRIBUTION / AVAILABILITY STATEMENT  Approved for Public Release; Distribution Unlimited					
13. SUPPLEMENTARY NOTES					
14. ABSTRACT The proposed studies will develop and evaluate a new therapeutic strategy for treating breast cancer bone metastasis by disrupting the interactions between breast cancer cells and sensory neurons within bone using alpha particle-emitting radiopharmaceuticals that target the CGRP-CRLR axis. The successful completion of this project will establish a new therapeutic target for cancer-induced bone pain and bone metastatic breast cancer; while providing the foundation required to develop new therapies that will decrease suffering and improve survival of breast cancer patients with bone metastases.  During this period, we encountered some personnel changes and COVID-19-related issues which have negatively impacted our productivity. However, Drs. Shiozawa and Wadas are planning on conducting training so that Dr. Shiozawa is able to perform radioactive work at Wake Forest School of Medicine. Despite these setbacks, Drs. Shiozawa and Wadas published a review article relevant to this area in the journal <i>Molecules</i> . This article was featured on the front cover of the issue ( <a href="https://www.mdpi.com/1420-3049/26/8">https://www.mdpi.com/1420-3049/26/8</a> ). Additionally, we have prepared the PTCA-CGRP <sub>27-37</sub> peptides and are developing a CRLR over-expressing viral vector to create the CRLC-over-expressing breast cancer cells which will be used to evaluate the <sup>225</sup> Ac-PTCA-CGRP <sub>27-37</sub> peptides <i>in vitro</i> and <i>in vivo</i> during the next year.					
15. SUBJECT TERMS Breast Cancer; Bone metastasis; Cancer-induced bone pain; Radiopharmaceuticals; Calcitonin receptor-like receptor; Actinium-225					
16. SECURITY CLASSIFICATION OF:			17. LIMITATION OF ABSTRACT	18. NUMBER OF PAGES	19a. NAME OF RESPONSIBLE PERSON
a. REPORT	b. ABSTRACT	c. THIS PAGE			USAMRMC
Unclassified	Unclassified	Unclassified	Unclassified	89	19b. TELEPHONE NUMBER (include area code)

## Table of Contents

	<u>Page</u>
<b>1. Introduction.....</b>	<b>4-5</b>
<b>2. Keywords.....</b>	<b>5</b>
<b>3. Accomplishments.....</b>	<b>6-10</b>
<b>4. Impact.....</b>	<b>11</b>
<b>5. Changes/Problems.....</b>	<b>12</b>
<b>6. Products.....</b>	<b>13-16</b>
<b>7. Participants &amp; Other Collaborating Organizations.....</b>	<b>17-18</b>
<b>8. Special Reporting Requirements.....</b>	<b>19</b>
<b>9. Appendices.....</b>	<b>20-89</b>

---

## 1. INTRODUCTION:

When breast cancer (BCa) patients develop bone metastases, their 5-year survival rate declines by more than 70%. External beam radiation is used primarily for palliative treatment for patients with bone metastases. Bisphosphonate and anti-receptor activator of nuclear factor  $\kappa$ B ligand (RANKL) antibody to decrease bone resorption can reduce the onset of pain, but they ultimately fail to improve overall survival. Radium-223 ( $^{223}\text{RaCl}_2$ ) can extend overall survival of prostate cancer patients with bone metastases, but only to a limited extent. Since these treatments mainly target bone remodeling, **new approaches that target factors other than bone remodeling are needed.**

Cancer-induced bone pain is the most common and intractable symptom of bone metastases, and it substantially impairs quality of life. Eighty percent of patients with bone metastasis have cancer-induced bone pain, and its management is a tremendous challenge for patients and caregivers. It has also been suggested that cancer-induced bone pain may be a negative indicator of survival. The ALSYMPCA trial, which investigated the role of  $^{223}\text{RaCl}_2$  in prostate cancer patients with bone metastases, revealed that decreased pain levels correlated with increased overall survival. Thus, treating bone metastases by targeting pain signals are a promising approach to improve mortality.

Calcitonin gene-related peptide (CGRP), a 37-amino acid neuropeptide widely distributed in the peripheral and central nervous systems, is closely associated with pain behavior. Sensory nerves that express CGRP were enriched in the periosteum and bone marrow of a murine model of BCa bone metastasis. Patients with bone metastatic prostate cancer have elevated serum levels of CGRP. Sensory nerve-derived CGRP stimulated lung cancer growth. We have also found that: (i) bone metastatic prostate cancer directly affects sensory nerves to induce bone pain; (ii) sensory nerves that express CGRP are enriched in the marrow of those with bone metastatic prostate cancer; (iii) prostate cancer patients with bone metastatic disease have elevated serum levels of CGRP; (iv) samples from patients with bone metastatic BCa expressed higher levels of a CGRP receptor, calcitonin receptor-like receptor (CRLR); and (v) CGRP induces proliferation of BCa cells through CRLR. These data suggest that the CGRP/CRLR axis influences bone metastatic progression and could be a valuable therapeutic target.

The recent therapeutic efficacy of  $^{223}\text{RaCl}_2$  ( $t_{1/2} = 11.4$  d;  $E_{\alpha_{\max}} = 6-7$  MeV) for treatment of prostate cancer patients with bone metastases has renewed interest in the development of alpha particle-based therapies. The effectiveness of  $^{223}\text{RaCl}_2$  results from its ability to form complexes with hydroxylapatite in remodeling bone.  $^{223}\text{RaCl}_2$  emits alpha particles and deposits substantial ionizing energy via high linear energy transfer (LET) over  $< 100$   $\mu\text{m}$  within bone tissue. When DNA is exposed to high LET, irreparable double-stranded breaks occur, resulting in cell death.  $^{223}\text{RaCl}_2$  is more potent than low LET  $\beta$ -emitting bone-seeking agents, and its cytotoxicity is not affected by hypoxia or mechanisms of radio- or chemoresistance. However, its chemical properties make it difficult to conjugate to molecular delivery systems, such as antibodies that target solid tumors.

There is growing consensus that actinium-225 ( $^{225}\text{Ac}$ ) ( $t_{1/2} = 10$  d;  $E_{\alpha_{\max}} = 6-8$  MeV) could be a superior alternative for targeted alpha particle therapy of bone metastases. Unlike other alpha particles,  $^{225}\text{Ac}$  of high specific activity and radionuclide purity is available. It has a long half-life, which synergizes well with the biological half-life of a circulating antibody. At the target site, it releases a large amount of kinetic energy per nuclear decay, making it highly cytotoxic when properly targeted. **Unlike  $^{223}\text{RaCl}_2$ ,  $^{225}\text{Ac}$ 's chemistry is amenable to chelation and conjugation to targeting molecules such as antibodies and peptides.** Recent *in vivo* preclinical evaluation of  $^{225}\text{Ac}$  radiotherapeutics demonstrates that  $^{225}\text{Ac}$  may provide new strategies for targeted alpha particle therapy development. Although the recent clinical success of  $^{225}\text{Ac}$  radiotherapeutics that target prostate-specific membrane antigen (PSMA) demonstrate that targeted alpha particle therapy approaches

AWARD: BC180720, BC180720P1

TITLE: A targeted alpha particle radiopharmaceutical for bone metastatic breast cancer

PI: Yusuke Shiozawa, M.D., Ph.D., Partnering PI: Thaddeus Wadas, Ph.D.

---

could have a significant and positive impact on the management of prostate cancer, targeting PSMA is not applicable for other cancer types including breast cancer.

### **Hypothesis:**

The delivery of alpha particle radiation to bone metastatic foci using CRLR-targeting ligands will reduce BCa tumor burden and cancer-induced bone pain.

### **Specific Aims:**

#### **Aim 1: Determine the best alpha particle radiopharmaceuticals targeted to the CRLR.**

We will develop CRLR-targeted peptide (CGRP<sub>27-37</sub>) conjugated with actinium-225 (<sup>225</sup>Ac, <sup>225</sup>Ac-CGRP<sub>27-37</sub>). Then, the binding affinity of <sup>225</sup>Ac-CGRP<sub>27-37</sub> to CRLR will be determined *in vitro*. The biodistribution of <sup>225</sup>Ac-CGRP<sub>27-37</sub> and organ dosimetry will be determined *in vivo*.

#### **Aim 2: Determine the impact of CRLR-targeted alpha particle therapy on BCa bone metastases and cancer-induced bone pain.**

Using an *in vivo* bone metastatic model that allows us to measure tumor growth, bone remodeling, skeletal innervation, and pain behaviors within each mouse, we will determine the safety and efficacy of <sup>225</sup>Ac-CGRP<sub>27-37</sub> in the treatment of bone metastatic progression and its resultant pain.

Our proposal would be the first to rigorously investigate the use of <sup>225</sup>Ac-based targeted alpha particle therapy to target the CRLR, a receptor for the pain-related neuropeptide CGRP, in breast cancer bone metastases. If successful, the proposed studies will yield a paradigm-shifting treatment strategy for BCa patients with bone metastases.

The **immediate benefits** of this research will provide essential preliminary data for the design of subsequent clinical translational studies. Our results could be quickly translated into novel treatment strategies to reduce breast cancer-associated morbidity and mortality.

The potential for **long-term and positive impact** of our work is substantial. This work will inform new treatment strategies to address both bone metastatic progression and cancer-induced bone pain of BCa.

## **2. KEYWORDS:**

Breast Cancer; Bone metastasis; Cancer-induced bone pain; Radiopharmaceuticals; Calcitonin receptor-like receptor; Actinium-225

### **3. ACCOMPLISHMENTS:**

#### **What were the major goals and objectives of the project?**

This application will test a new and innovative approach for  $^{225}\text{Ac}$ -based targeted alpha particle therapy of breast cancer bone metastases by exploiting CRLR as a potential therapeutic target for breast cancer bone metastases, with the goal of improving both patients' quality of life and overall survival.

#### **Task 1: *In vitro* selection of CRLR-targeted alpha particle radiopharmaceuticals.**

##### **Months 1-12.**

- Synthesize the CGRP<sub>27-37</sub> (**Months 1-2; Dr. Shiozawa**).
- Conjugate CGRP<sub>27-37</sub> to  $^{225}\text{Ac}$ -PCTA (**Months 3-5; Dr. Wadas**).
- Test the serum stability of  $^{225}\text{Ac}$ -CGRP<sub>27-37</sub> (**Months 6-8; Dr. Wadas**).
- Establish CRLR-down-regulated, CRLR-overexpressed breast cancer cells (**Months 6-8; Dr. Shiozawa**).
- Perform receptor binding assays and internalization assays (**Months 9-12; Dr. Wadas**).

#### **Task 2: *In vivo* selection of CRLR-targeted alpha particle radiopharmaceuticals.**

##### **Months 1-18.**

- Submit documents for local IACUC review. (**Months 1-2; Dr. Shiozawa**).
- Submit IACUC approval and necessary documents for review by the Animal Care and Use Review Office (ACURO). (**Months 3-4; Dr. Shiozawa**).
- Perform biodistribution and dosimetry assays (**Months 13-18; Drs. Shiozawa and Wadas**).

#### **Task 3: Determine the maximum tolerated dose of CRLR-based targeted alpha particle therapy.**

##### **Months 18-24.**

- Perform maximum tolerated dose studies (**Months 18-24; Drs. Shiozawa and Wadas**).

- 
- Co-author comprehensive review of radiopharmaceutical treatment and bone metastasis. (**Months 20-14; Drs. Shiozawa and Wadas**).

**Task 4: Determine treatment efficacy of CRLR-based targeted alpha particle therapy.**

**Months 25-34.**

- Test the effects of  $^{225}\text{Ac}$ -CGRP<sub>27-37</sub> on tumor growth in the marrow, bone remodeling, and pain-related behavior within the same animal (**Months 25-34; Drs. Shiozawa and Wadas**).
- Co-authored manuscript summarizing all the results. (**Months 33-36; Drs. Shiozawa and Wadas**).

**What was accomplished under these goals?**

(2019-2020)

**The Award Transfer (Drs. Wadas and Shiozawa).**

$^{225}\text{Ac}$ -PCTA-CGRP<sub>27-37</sub> was stable in human serum (**Dr. Wadas**): Task 1.

The CALCRL in breast cancer cells were down-regulated using shRNA (**Dr. Shiozawa**): Task 1.

(2020-2021)

**The plan for training Dr. Shiozawa in the safe use of radioactive materials (Drs. Wadas and Shiozawa).**

To accomplish the remaining goals of the award at Wake Forest, Dr. Shiozawa was required to obtain approval for his own radioactive materials protocol due to Dr. Wadas' institution change. Currently, he has received the necessary didactic training provided by WFUHS Radiation Safety Committee. However, before his protocol is approved, the WFUHS Radiation Safety Committee has required him to gain "hands-on" training at the University of Iowa from Dr. Wadas, who is an internationally recognized expert in the safe use of alpha-particle-emitting radionuclides. Unfortunately, the University of Iowa shut-down and non-essential air travel restrictions put in place due to the COVID-19 outbreak have delayed this training. Therefore, Drs. Shiozawa and Wadas are currently trying to conduct the online training (we are currently setting this up and we may require 2-3 times) between Wake Forest and University of Iowa. This will be followed by in-person training at the University of Iowa so that Dr. Shiozawa may gain experience with the safe handling of alpha particle emitting radionuclides.

**The joint publication (Drs. Shiozawa and Wadas): Task 3.**

Drs. Shiozawa and Wadas published together a review manuscript relevant to this study. This paper is selected by the editors as the cover of the 2021; Volume 26 (Issue 8) (<https://www.mdpi.com/1420-3049/26/8>).

Patel CM, **Wadas TJ**, **Shiozawa Y**. Progress in Targeted Alpha-Particle-Emitting Radiopharmaceuticals as Treatments for Prostate Cancer Patients with Bone Metastases. *Molecules*. 2021; In Press. PMID: In Progress. PMCID: In Progress.

### The synthesis of CGRP<sub>27-37</sub> analogs (Dr. Wadas): Task 1.

During the current funding period, we focused on the largescale synthesis of the CGRP peptides described in the application. This was completed to ensure that sufficient material would be available once the resumption of research is allowed at the University of Iowa and at Wake Forest University Health Sciences. Briefly, the CGRP peptides were prepared on an AAPTEC APEX-396 automated peptides synthesizer using standard Fmoc chemistry, HBTU and 9-hydroxybenzotriazole. Deprotection using a standard trifluoroacetic acid, water and triisopropylsilane solution afforded all of the peptides in good yields. To conjugate the PCTA chelator to each peptide, standard NCS coupling chemistry was utilized. In these reactions, 1.2 mole equivalents of the PCTA-NCS bifunctional chelator (Macrocyclics, Inc.) was reacted with 1 mole equivalent of the unconjugated peptide in HEPES buffer (pH 9). The crude conjugates were then purified by semi-preparative reverse phase HPLC. The purity and identity of each product was assessed using an Agilent 1200 series HPLC interfaced with

an AB Sciex 4000QT LC-MS system. After the confirmation of purity and identity, each conjugate underwent lyophilization to yield a white fluffy powder. The structures of each complex to be studied are shown in **Fig. 1**. The conjugates are highly lipophilic and insoluble on the macro-scale in aqueous media. Considering this observation, we have expended additional efforts to test different organic-aqueous solvent systems that will 1) keep the peptides in solution once the lyophilized powder is rehydrated, 2) not cause conjugate degradation after solubilization, and 3) be robust enough to withstand the degradative effects of ionizing radiation. These studies are ongoing.

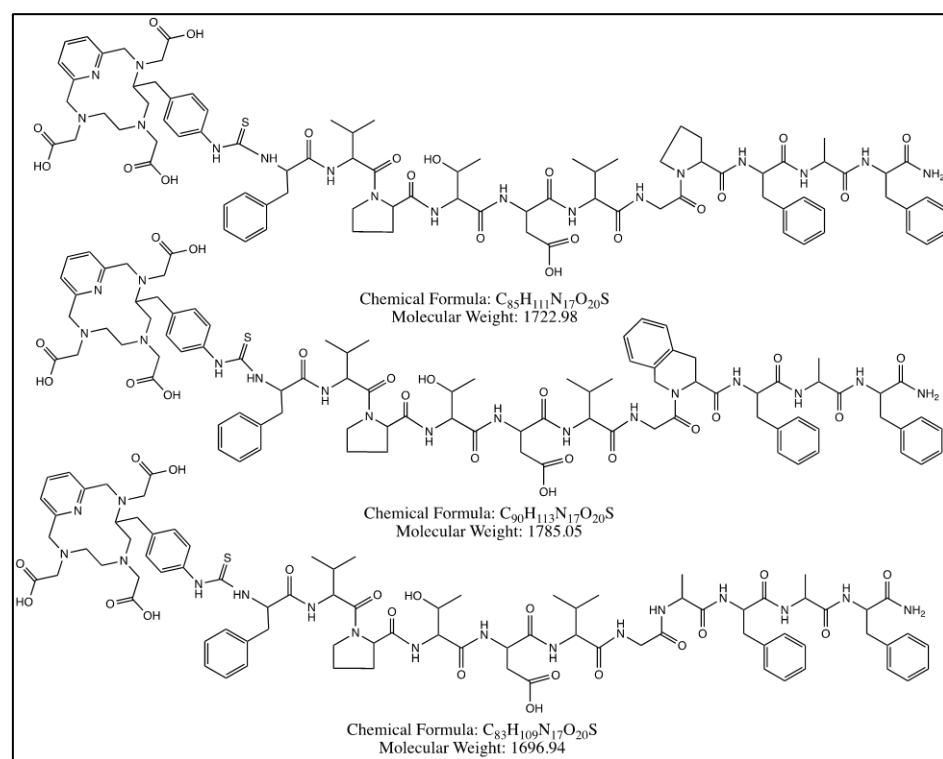


**Fig. 1. The chemical structure of the PCTA-CGRP peptides.**

### The development of the over-expression virus vector for CRLR (Dr. Shiozawa): Task 1.

To first create CRLR-over-expressing breast cancer cells, MDA-MB-231 and ZR-75-1 cells were transfected with pCMV3-CALCRL (gene name of CRLR) expression vector [pCMV3-CALCRL vector (SinoBiological, cat: #HG11518-UT)] using lipofectamine reagents (Lipofectamine 2000) following a company's recommended protocol. However, the survival rate of resulting cells after antibiotic selection was extremely low, suggesting that the transfection efficiency was low. Since MDA-MB-231 cells are known to be a hard-to-transfect cell line, we upgraded lipofectamine reagents to Lipofectamine 3000, which is a more optimized reagent for hard-to-



transfect cells and then repeated transfection using pCMV3-CALCRL expression vector. However, the survival rate of resulting cells after antibiotic selection was still extremely low. After this attempt, we also modified the ratio between the number of cells and the amount of transfection reagents several times. However, these protocol modifications also failed to improve the transfection efficiency. To overcome this problem, we decided to generate a lentiviral vector containing a full length human CALCRL ORF. We are currently subcloning CALCRL ORF into a lentiviral vector (Bioscience company). This subcloning includes (i) the synthesis of the full length CALCRL ORF sequences with addition of the 5' cloning site (SpeI) and the 3' cloning site (EcoRI), (ii) the deletion of Oct4 ORF in the receiving plasmid [pSin-EF2-Oct4-pur (Addgene, cat: #16579) (**Fig. 2**)] between 5' SpeI and 3' EcoRI cloning sites, (iii) the ligation of the synthesized CALCRL ORF into the receiving plasmid between 5' SpeI and 3' EcoRI cloning sites, and (iv) the verification of the successful ligation by sequencing the final plasmid, pSin-EF2-CALCRL-puro plasmid. Thereafter, the lentiviral particles will be generated using these final plasmids. CALCRL ORF be transduced into the MDA-MD-231 and ZR-75-1 cells using the resulting lentiviral vector.

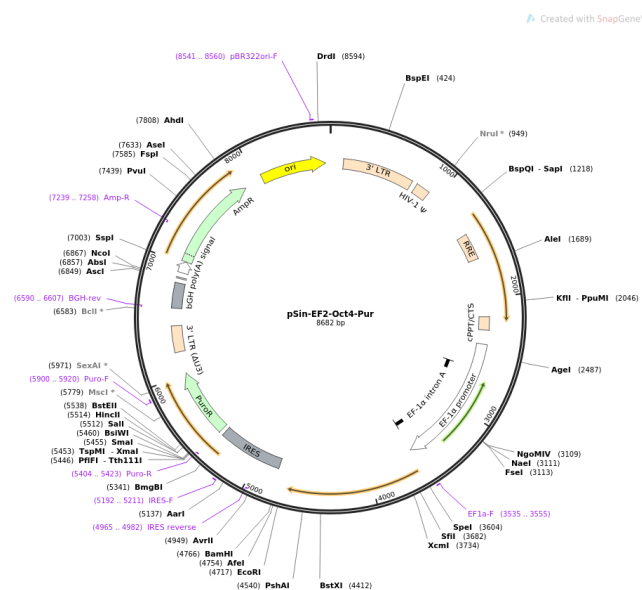


**Fig. 2. The map of pSin-EF2-Oct4-pur plasmid.**

### **What opportunities for training and professional development did the project provide?**

(2019-2020)

Dr. Shiozawa was invited to give a talk at The U.S. Bone and Joint Initiative (USBJI) and Bone and Joint Canada (BJC) Young Investigator Initiative Workshop Spring 2019 (Rosemont, IL) on April 27, 2019.

Dr. Shiozawa was invited to give a seminar at University of North Carolina at Chapel hill, Adams School of Dentistry (Chapel hill, NC) on December 03, 2019.

Dr. Wadas gave a lecture at the University of Iowa's Free Radical and Radiation Biology Program. This lecture dealt with the use of alpha particle therapy in cancer care. University of Iowa, Iowa City, IA (February 25, 2020).

AWARD: BC180720, BC180720P1

TITLE: A targeted alpha particle radiopharmaceutical for bone metastatic breast cancer

PI: Yusuke Shiozawa, M.D., Ph.D., Partnering PI: Thaddeus Wadas, Ph.D.

---

Dr. Wadas accepted the role as Guest Editor of a Special Issue of *Molecules* that focuses on the use of radiotherapy of disease. The Issue description and call for papers can be found at [https://www.mdpi.com/journal/molecules/special\\_issues/radiopharmaceutical\\_chemistry\\_radiotherapy](https://www.mdpi.com/journal/molecules/special_issues/radiopharmaceutical_chemistry_radiotherapy).

(2020-2021)

Dr. Wadas gave a lecture at the University of Iowa's Cancer Biology Program. This lecture dealt with the development of targeted alpha particle-based radiotherapy and its use in oncology. University of Iowa, Iowa City, IA (November 26, 2020).

Dr. Wadas gave a lecture at the University of Iowa's Human Toxicology Program. This lecture dealt with the use of PET imaging in the precision medicine era. University of Iowa, Iowa City, IA (December 20, 2020).

### **How were the results disseminated to communities of interest?**

There is nothing to report.

### **What do you plan to do during the next reporting period to accomplish the goals and objectives?**

Currently, research at both institutions has ceased due to the COVID-19 pandemic. Once normal research operations resume the following tasks will be initiated. These include:

- 1) Determine the binding affinity of radiopharmaceuticals to breast cancer cells *in vitro* (Aim 1).
- 2) Determine the biodistribution and dosimetry of radiopharmaceuticals *in vivo* (Aim 1).
- 3) Dr. Shiozawa will complete his radioactive material handling training with Dr. Wadas.

#### **4. IMPACT:**

##### **What was the impact on the development of the principal discipline(s) of the project?**

(2019-2020)

1. We found that  $^{225}\text{Ac}$ -PTCA-CGRP<sub>27-37</sub> were stable in human serum.
2. We were able to down-regulate CRLC expression levels in BCa using shRNA.

(2020-2021)

1. Drs. Shiozawa and Wadas published together a review manuscript relevant to this study.
2. We were able to synthesize several different analogs of CGRP<sub>27-37</sub>.
3. We are currently developing the over-expression virus vector for CRLR.

##### **What was the impact on other disciplines?**

We were able to develop new methods of radiopharmaceutical production. While specific to this project, they may have broad applicability to radiopharmaceutical development in general.

##### **What was the impact on technology transfer?**

There is nothing to report at this time.

##### **What was the impact on society beyond science and technology?**

There is nothing to report at this time.

## **5. CHANGES/PROBLEMS:**

### **Changes in approach and reasons for change**

Nothing to report.

### **Actual or anticipated problems or delays and actions or plans to resolve them**

Nothing to report.

### **Changes that have a significant impact on expenditures**

There has been some non-key personnel turnover (Technician) and maternity leave (Postdoc) in Dr. Shiozawa's lab as well as the recent COVID-19 pandemic which have impacted the timeliness of conducting the proposed studies. Due to COVID-19, Wake Forest University Health Sciences (WFUHS) issued an institutional stop work order from the middle of March to the end of May 2020. The personnel have been replaced and the lab has resumed normal operations.

In the original application, all of the experimental work involving radioactivity was to be conducted by Dr. Wadas' laboratory and under his radiation safety protocol. Shortly after this application was funded however, Dr. Wadas accepted a position in the Department of Radiology at the University of Iowa and moved his laboratory there. Unfortunately, his move to the University of Iowa coincided with the COVID-19 pandemic. At that time the University of Iowa enacted an institutional stop work order from the middle of March to the end of July 2020. This stop work order hindered Dr. Wadas' productivity on two levels. Foremost, he was unable to work on the aims as currently outlined in the SOW after the award was successfully transferred to the University of Iowa. Secondly, this stop work order prevented the renovation of Dr. Wadas' laboratories to accommodate radioactive materials. The expected completion date of renovations is July 1, 2021. The renovation schedule also affected the timeline of the hands-on radiation safety training, which we are planning to conduct so that Dr. Shiozawa may receive approval to use radioactive materials at WFUHS. Although Dr. Shiozawa has completed the appropriate radiation safety training required by WFUHS and additional didactic training with Dr. Wadas via videoconference, the WFUHS Radiation Committee is still requiring that Dr. Shiozawa receive hands-on training in the proper handling, use, storage and disposal of alpha particle-emitting radioisotopes from Dr. Wadas at the University of Iowa. Once the WFUHS' COVID-19 travel restriction order, which prevents work-related travel, is rescinded on June 30, 2021 Drs. Wadas and Shiozawa will schedule a week-long radiation safety training session at the University of Iowa.

In the next year term, we will try to catch up the speed of project productivity and continue to (i) determine the binding affinity of radiopharmaceuticals to breast cancer cells *in vitro* (Aim 1) and (ii) determine the biodistribution and dosimetry of radiopharmaceuticals *in vivo* (Aim 1).

### **Significant changes in use or care of human subjects, vertebrate animals, biohazards, and/or select agents**

Nothing to report.

## 6. PRODUCTS:

### Publications, conference papers, and presentations

#### Journal Publications

Peer reviewed journal

(2019-2020)

1. Lycan TW, Hsu F, Ahn CS, Thomas A, Walker FO, Sanguenza OP, **Shiozawa Y**, Park SH, Peters CM, Romero-Sandoval EA, Melin SA, Sorscher S, Ansley K, Lesser GJ, Cartwright MS, Strowd RE. Neuromuscular ultrasound for taxane peripheral neuropathy in breast cancer. **Muscle and Nerve**. 2020; 61(5):587-594. PMID: 32052458. PMCID: In Progress.  
Status of Publication: Published  
Acknowledgement of federal support: Yes
2. Tafreshi NK, Tichacek CJ, Pandya DN, Doligalski ML, Budzevich M, Kil H-J, Bhatt NB, Kock ND, Messina J, Ruiz EE, Delva NC, Weaver A, Gibbons WR, Boulware DC, Khushalani NL, El-Haddad G, Triozzi PL, Moros EG, McLaughlin ML, **Wadas TJ**, Morse DL. Melanocortin 1 Receptor–Targeted  $\alpha$ -Particle Therapy for Metastatic Uveal Melanoma. **J. Nucl. Med.** 2019; 60(8): 1124-1133. PMID: 30733316. PMCID: PMC6681690.  
Status of Publication: Published  
Acknowledgement of federal support: No
3. Tichacek CJ, Budzevich MM, **Wadas TJ**, Morse DL, Moros EG. A Monte Carlo Method for Determining the Response Relationship between Two Commonly Used Detectors to Indirectly Measure Alpha Particle Radiation Activity. **Molecules**. 2019; 24(18): 3397-3402. PMID: 31546752. PMCID: PMC6767018.  
Status of Publication: Published  
Acknowledgement of federal support: No
4. Tafreshi NK, Doligalski ML, Tichacek CJ, Pandya DN, Budzevich MM, El-Haddad G, Khushalani NI, Moros EG, McLaughlin ML, **Wadas TJ**, Morse DL. Development of Targeted Alpha Particle Therapy for Solid Tumors. **Molecules**. 2019; 24(23): 4314-4362. PMID: 31779154. PMCID: PMC6930656.  
Status of Publication: Published  
Acknowledgement of federal support: No

(2020-2021)

1. Wu S-Y, Xing F, Sharma S, Wu K, Tyagi A, Liu Y, Zhao D, Deshpande RP, **Shiozawa Y**, Ahmed T, Zhang W, Chan M, Ruiz J, Lycan TW, Dothard A, Watabe K. Nicotine promotes brain metastasis by polarizing microglia and suppressing innate immune function. **JEM**. 2020;217:e20191131. PMID: 32496556. PMCID: PMC7398164.  
Status of Publication: Published

Acknowledgement of federal support: No

2. Eber MR, Park SH, Contino KF, Patel CM, Hsu F-C, **Shiozawa Y**. Osteoblasts derived from mouse mandible enhance tumor growth of prostate cancer more than osteoblasts derived from long bone. ***J Bone Oncology***. 2021;26:100346. PMID: 33425674. PMCID: PMC7779864.  
Status of Publication: Published  
Acknowledgement of federal support: Yes
3. Park SH, Eber MR, M. Fonseca M, Patel CM, Cunnane KA, Ding H, Hsu F-C, Peters CM, Ko M-C, Strowd RE, Wilson JA, Hsu W, Romero-Sandoval EA, **Shiozawa Y**. Usefulness of the measurement of neurite outgrowth of primary sensory neurons to study cancer-related painful complications. ***Biochem Pharmacol***. 2021;188:114520. PMID: **33741328**. PMCID: In Progress.  
Status of Publication: Published  
Acknowledgement of federal support: Yes
4. Widner DB, Liu C, Qingxia Z, Sharp S, Eber MR, Park SH, Files DC, **Shiozawa Y**. Activated Mast Cells in Skeletal Muscle Can be a Potential Mediator for Cancer-Associated Cachexia. ***J. Cachexia Sarcopenia Muscle***. 2021; In Press. PMID: In Progress. PMCID: In Progress.  
Status of Publication: In Press  
Acknowledgement of federal support: Yes

#### Invited reviews

(2019-2020)

Nothing to report.

(2020-2021)

1. Patel CM, **Wadas TJ**, **Shiozawa Y**. Progress in Targeted Alpha-Particle-Emitting Radiopharmaceuticals as Treatments for Prostate Cancer Patients with Bone Metastases. ***Molecules***. 2021; In Press. PMID: In Progress. PMCID: In Progress.  
Status of Publication: In Press  
Acknowledgement of federal support: Yes

#### **Book**

(2019-2020)

1. Park SH, **Shiozawa Y**. (2019) Genomic mutation as a potential driver of the development of bone-related cancers. In Zaidi M (Ed.), *Encyclopedia of Bone Biology*. In Press. Elsevier.  
Status of Publication: In Press  
Acknowledgement of federal support: Yes

2. **Shiozawa Y.** (2019) The roles of bone marrow-resident cells as a microenvironment for bone metastasis. In Birbrair A (Ed.), *Tumor Microenvironments in Different Organs – Part A*. In Press. Switzerland: Springer Nature.

Status of Publication: Published

Acknowledgement of federal support: Yes

(2020-2021)

1. Eber MR, Jimenez-Andrade JM, Peters CM, **Shiozawa Y.** (2020) A method of bone-metastatic tumor progression assessment in mice using longitudinal radiography. In Deep G (Ed.), *Cancer Biomarkers: Methods and Protocols*, Methods in Molecular Biology, In Press. New York: Humana Press. Methods Mol Biol. In Press. PMID: In Progress. PMCID: N/A.

Status of Publication: In Press

Acknowledgement of federal support: Yes

## **Presentation**

(2019-2020)

1. Stowd RE, Lycan T, Thomas A, Hsu FC, Ahn C, Sanguenza O, **Shiozawa Y**, Park SH, **Peters CM**, EA Romero-Sandoval, Melin SA, Sorscher S, Lesser GJ, Walker FO, Cartwright MS. Neuromuscular ultrasound for the non-invasive assessment of breast cancer patients with peripheral neuropathy from taxanes. The American Academy of Neurology 71st Annual Meeting, Philadelphia, PA, USA, May 4-10, 2019. Poster.
2. Tsuzuki S, Park S, Eber M, Widner B, Kamata Y, Kimura T, Bianchi-Frias D, Coleman I, Nelson P, Hsu F-C, **Peters C**, **Shiozawa Y.** A pain-related neuropeptide calcitonin gene-related peptide promotes bone metastatic progression of prostate cancer through p38. American Society for Bone and Mineral Research (ASBMR) 2019 Annual Meeting, Orland, FL, USA, September 20-23, 2019. Poster.
3. Park S, Eber M, Tsuzuki S, Cain R, Widner B, Kamata Y, Kimura T, Bianchi-Frias D, Coleman I, Nelson P, Hsu F-C, **Peters C**, **Shiozawa Y.** The role of the SCF/c-kit pathway in cancer-induced bone pain. American Society for Bone and Mineral Research (ASBMR) 2019 Annual Meeting, Orland, FL, USA, September 20-23, 2019. Poster.
  - **Selected as a Plenary Poster**
4. Cain R, Park SH, Eber M, Martin TJ, Parker R, Jimenez-Andrade JM, **Shiozawa Y**, **Peters C.** Characterization of a syngeneic mouse model of prostate cancer induced bone pain. Neuroscience 2019, Chicago, IL, USA, October 19-23, 2019. Poster.

(2020-2021)

1. Ding H, Kiguchi N, Park SH, Kishioka S, **Shiozawa Y**, Peters C, Ko M-C. Functional roles of neuromedin B and gastrin-releasing peptide in regulating itch and pain in the spinal cord of primates.

**FASEB J.** 2030;34 (S1):03569. Experimental Biology 2020 (Cancelled, but abstract was published).

2. Eber M, Park S, Hsu F-C, **Shiozawa Y.** Osteoblasts Derived from Mouse Mandible Enhance Tumor Growth of Prostate Cancer More Than Osteoblasts Derived from Long Bone. The Cancer and Bone Society (CABS) / American Society for Bone and Mineral Research (ASBMR) Pre- Meeting, The Seed and Soil: Therapeutic Targets for Cancer in Bone, Virtual, September 9-10, 2020. e-Poster.
3. Eber M, Park S, Hsu F-C, **Shiozawa Y.** Osteoblasts Derived from Mouse Mandible Enhance Tumor Growth of Prostate Cancer More Than Osteoblasts Derived from Long Bone. American Society for Bone and Mineral Research (ASBMR) 2020 Annual Meeting, Virtual, September 11-14, 2020. e-Poster.
4. Widner DB, Eber M, Park S, **Shiozawa Y.** Skeletal Muscle Resident Mast Cells as a Potential Novel Biomarker for Cancer-Associated Cachexia. Cancer Cachexia 2020, Virtual, September 10-11, 2020. e-Poster.

**Website(s) or other Internet site(s)**

Nothing to report.

**Technologies or techniques**

Nothing to report.

**Inventions, patent applications, and/or licenses**

Nothing to report.

**Other products**

Nothing to report.



## 7. PARTICIPANTS & OTHER COLLABORATING ORGANIZATIONS

### What individuals have worked on the project?

Name: Yusuke Shiozawa

Project Role: PI, W81XWH-19-1-0045

Researcher Identifier (e.g. ORCID ID): [orcid.org/0000-0001-9814-9230](https://orcid.org/0000-0001-9814-9230)

Nearest person month worked: 1.2

Contribution to Project: Dr. Shiozawa is an Assistant Professor in the Department of Cancer Biology. He has extensive experience in the study of prostate cancer bone metastasis, and will provide oversight of the entire program including development and implementation of all policies, procedures, and processes. In this role, Dr. Shiozawa will be responsible for the completion of the project and for ensuring that systems are in place to guarantee institutional compliance with US laws, including biosafety and animal research guidelines, data collection and analyses, and facilities. Dr. Shiozawa will supervise other personnel on the project to ensure timely and effective studies.

Funding Support: Department of Defense, National Cancer Institute, Matavivor, TEVA Pharmaceuticals

Name: Thaddeus Wadas

Project Role: Partnering PI, W81XWH-19-1-0046

Researcher Identifier (e.g. ORCID ID):

Nearest person month worked: 1.2

Contribution to Project: Dr. Wadas is an Associate Professor in the Department of Radiology at University of Iowa. Dr. Wadas will share oversight of the entire program with Dr. Shiozawa, including development and implementation of all policies, procedures, and processes. Dr. Wadas has a Ph.D. in Chemistry and has extensive experience in peptide chemistry, radiochemistry and developing *in vivo* studies in various tumor models as well as microPET imaging to evaluate radiopharmaceuticals. Dr. Wadas will assist Dr. Shiozawa's laboratory in radiochemistry, radiopharmaceutical-related *in vitro* experiments and all imaging data analysis. Dr. Wadas has access to all the resources and facilities needed to execute this research successfully, and his lab has successfully collaborated with the Dr. Shiozawa. Dr. Wadas will meet with Dr. Shiozawa remotely on a monthly basis to discuss progress on projects related to this Award.

Funding Support: Department of Defense, National Cancer Institute, Matavivor

Name: Christopher Peters

Project Role: Co-Investigator, W81XWH-19-1-0045

Researcher Identifier (e.g. ORCID ID):

Nearest person month worked: 0.6

Contribution to Project: Dr. Peters is an Assistant Professor in the Department of Anesthesiology. Dr. Peters' research interests are in central and peripheral mechanisms of pain chronicity including postsurgical, bone cancer and chemotherapy induced pain and neuropathy. Dr. Peters will be responsible for supervising and training personnel in evoked and non-evoked bone cancer pain behavioral assays. Dr. Peters will also assist with histological and immunohistochemical analysis of skeletal tissue as part of Aims 2. He has extensive experience with the behavioral analysis, immunohistochemistry, biochemical analysis and fluorescent, brightfield, and confocal microscopic imaging required for this project.

Funding Support: National Institutes of Health, Department of Defense

AWARD: BC180720, BC180720P1

TITLE: A targeted alpha particle radiopharmaceutical for bone metastatic breast cancer

PI: Yusuke Shiozawa, M.D., Ph.D., Partnering PI: Thaddeus Wadas, Ph.D.

---

Name: Fang-Chi Hsu

Project Role: Co-Investigator, W81XWH-19-1-0045

Researcher Identifier (e.g. ORCID ID):

Nearest person month worked: 0.36

Contribution to Project: Dr. Hsu is a Professor in the Department of Biostatistical Sciences. She will work closely with Dr. Shiozawa and the team to analyze the results of the project.

Funding Support: National Institutes of Health, Department of Defense

**Has there been a change in the other active support of the PD/PI(s) or senior/key personnel since the last reporting period?**

Nothing to report.

**What other organizations have been involved as partners?**

Nothing to report.

**8. SPECIAL REPORTING REQUIREMENTS:**

QUAD CHARTS.

**9. APPENDICES:**

The original copies of manuscript are attached.

# A targeted alpha particle radiopharmaceutical for bone metastatic breast cancer

BC180720, BC180720P1

W81XWH-19-1-0045, W81XWH-19-1-0046

PI: Yusuke Shiozawa  
Thaddeus Wadas

Org: Wake Forest University Health Sciences  
University of Iowa

Award Amount: \$299,999 (Shiozawa)  
\$299,999 (Wadas)



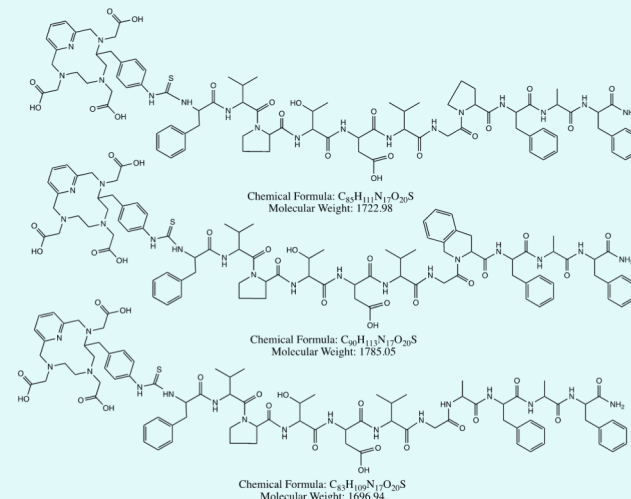
## Study/Product Aim(s)

- Aim 1: Determine the best alpha particle radiopharmaceuticals targeted to the CRLR.**
- Aim 2: Determine the impact of CRLR-targeted alpha particle therapy on breast cancer bone metastases and cancer-induced bone pain.**

## Approach

The proposed studies will develop a new therapeutic strategy for treating bone metastatic breast cancer using an alpha-particle radiopharmaceutical. This work will lay the needed foundation to develop new therapeutic targets for both cancer-induced bone pain and bone metastatic breast cancer, to decrease suffering and improve survival of breast cancer patients with bone metastases.

Figure 1. The PCTA-CGRP peptides to be evaluated in this proposal.



- We synthesized the PCTA-CGRP<sub>27-37</sub> analogs .**

## Timeline and Cost

Activities	CY	19	20	21	22
Aim 1 (In vitro studies)					
Aim 1 (Animal studies)					
Aim 2 (Animal studies)					
Estimated Budget (\$K)		\$100	\$100	\$200	\$200

Updated: 03/31/2021

## Goals/Milestones (Example)

**CY19 Goal** – Team development

- ✓ Set up and organize the monthly meeting

**CY20 Goals** – In vitro studies

- ☐ In vitro selection of <sup>225</sup>Ac-CGRP<sub>27-37</sub>
- ☐ In vivo selection of <sup>225</sup>Ac-CGRP<sub>27-37</sub>

**CY21 Goal** – Animal studies

- ☐ In vivo selection of <sup>225</sup>Ac-CGRP<sub>27-37</sub>
- ☐ Determine the maximum tolerated dose of <sup>225</sup>Ac-CGRP<sub>27-37</sub>

**CY22 Goal** – Animal studies

- ☐ Determine the maximum tolerated dose of <sup>225</sup>Ac-CGRP<sub>27-37</sub>
- ☐ Determine treatment efficacy of <sup>225</sup>Ac-CGRP<sub>27-37</sub>

## Comments/Challenges/Issues/Concerns

- Personnel changes and COVID-19-related issues have negatively affected our productivity.

## Budget Expenditure to Date

Projected Expenditure: \$200K

Actual Expenditure: \$62K (Shiozawa) + \$94K (Wadas)

## Review

# Progress in Targeted Alpha-Particle-Emitting Radiopharmaceuticals as Treatments for Prostate Cancer Patients with Bone Metastases

Chirayu M. Patel <sup>1</sup>, Thaddeus J. Wadas <sup>2</sup>  and Yusuke Shiozawa <sup>1,\*</sup> 
<sup>1</sup> Department of Cancer Biology and Comprehensive Cancer Center, Wake Forest University Health Sciences, Winston-Salem, NC 27157, USA; cpatel@wakehealth.edu

<sup>2</sup> Department of Radiology, University of Iowa, Iowa City, IA 52242, USA; thaddeus-wadas@uiowa.edu

\* Correspondence: yshiozaw@wakehealth.edu; Tel.: +1-336-716-8743; Fax: +1-336-716-0255

**Abstract:** Bone metastasis remains a major cause of death in cancer patients, and current therapies for bone metastatic disease are mainly palliative. Bone metastases arise after cancer cells have colonized the bone and co-opted the normal bone remodeling process. In addition to bone-targeted therapies (e.g., bisphosphonate and denosumab), hormone therapy, chemotherapy, external beam radiation therapy, and surgical intervention, attempts have been made to use systemic radiotherapy as a means of delivering cytotoxic radiation to every bone metastatic lesion. Initially, several bone-seeking beta-minus-particle-emitting radiopharmaceuticals were incorporated into the treatment for bone metastases, but they failed to extend the overall survival in patients. However, recent clinical trials indicate that radium-223 dichloride (<sup>223</sup>RaCl<sub>2</sub>), an alpha-particle-emitting radiopharmaceutical, improves the overall survival of prostate cancer patients with bone metastases. This success has renewed interest in targeted alpha-particle therapy development for visceral and bone metastasis. This review will discuss (i) the biology of bone metastasis, especially focusing on the vicious cycle of bone metastasis, (ii) how bone remodeling has been exploited to administer systemic radiotherapies, and (iii) targeted radiotherapy development and progress in the development of targeted alpha-particle therapy for the treatment of prostate cancer bone metastasis.

**Keywords:** bone metastases; radiopharmaceuticals; radium-223; actinium-225; targeted alpha-particle-emitting radiopharmaceuticals



**Citation:** Patel, C.M.; Wadas, T.J.; Shiozawa, Y. Progress in Targeted Alpha-Particle-Emitting Radiopharmaceuticals as Treatments for Prostate Cancer Patients with Bone Metastases. *Molecules* **2021**, *26*, 2162. <https://doi.org/10.3390/molecules26082162>

Academic Editor: João D. G. Correia

Received: 18 March 2021

Accepted: 6 April 2021

Published: 9 April 2021

**Publisher's Note:** MDPI stays neutral with regard to jurisdictional claims in published maps and institutional affiliations.



**Copyright:** © 2021 by the authors. Licensee MDPI, Basel, Switzerland. This article is an open access article distributed under the terms and conditions of the Creative Commons Attribution (CC BY) license (<https://creativecommons.org/licenses/by/4.0/>).

## 1. Introduction

As a result of improvements in cancer research, prevention, early diagnosis, and treatment, the survival time of cancer patients with localized disease has increased. However, the prognosis for cancer patients with disseminated disease has decreased dramatically; distant metastases are responsible for 90% of all cancer-related deaths [1]. Although cancer cells may spread to any part of the body, different cancers have been observed to colonize different organs of the body at different rates and bone is a major metastatic site for several cancers. The relative incidence of bone metastasis is 65–75% in breast cancer, 65–75% in prostate cancer, 60% in thyroid cancer, 30–40% in lung cancer, 40% in bladder cancer, 20–25% in renal cell carcinoma, and 14–45% in melanoma [2]. Furthermore, the median survival time of patients with bone metastases is 19–25 months for breast cancer, 12–53 months for prostate cancer, 28 months for thyroid cancer, 6 months for lung cancer, 6 months for bladder cancer, 12 months for renal carcinoma, and 6 months for melanoma [3]. Importantly, the presence of metastatic bone disease alters the course of clinical care of patients, increases the immense physical and emotional burdens faced by patients, and augments the economic burden faced by patients and society [4–13]. For example, prostate cancer patients experiencing bone metastases incurred health care costs that were approximately \$8000 more than those incurred by men without bone metastasis [14]. Interestingly, it has

been demonstrated that the total medical care costs for breast cancer patients with bone metastases who experienced skeletal-related events (SREs) are nearly \$50,000 greater than for those without SREs [4,7].

Since bone metastasis is one of the major causes of death of cancer patients, eradicating cancer-induced bone diseases represents one of the greatest challenges of modern health care. Thus, there is a critical need to integrate our current understanding of cancer metastasis with emerging concepts in bone biology to advance our understanding of cancer-induced bone diseases, with the goal of improving treatment strategies and clinical outcomes, while reducing the financial difficulties experienced by patients. The treatment strategies for bone metastases are somewhat unique when compared to those for other metastases. Normally, the treatment strategies for both primary and metastatic tumors are similar—targeting the tumors themselves or inducing the immune system surrounding the tumors. However, for bone metastases, the treatments target the function of the metastatic organ, which is bone (an organ that continuously remodels throughout life by coupling osteoclast and osteoblast activity, which is called bone remodeling [15]). It has been suggested that the cells involved in bone remodeling (e.g., osteoclasts, osteoblasts, and osteocytes) and bone metastatic cancer cells interact with each other, and this crosstalk between bone-related cells and bone metastatic cancer cells stimulates further bone metastatic progression, known as “the vicious cycle of bone metastases” [16]. It is therefore natural to target bone remodeling to interfere with this cycle. Indeed, bisphosphonate and denosumab, a human monoclonal anti-receptor activator of nuclear factor  $\kappa$ B ligand (RANKL) antibody, which decreases osteoclastic activity, have been used as treatments for bone metastases [17,18]. These treatments have been effective in reducing the painful complications of bone metastases but ultimately fail to improve the overall survival of cancer patients with bone metastases [17,18]. However, recent clinical trials indicate that an alpha-particle-emitting radiopharmaceutical radium-223 dichloride ( $^{223}\text{RaCl}_2$ ), which targets hydroxyapatite or osteoblastic bone metastatic lesions, improves the overall survival of prostate cancer patients with bone metastases. Importantly, to date, this is the only bone-targeted treatment modality that can prolong the survival time of cancer patients with bone metastases, although several combinations of systemic treatments (e.g., hormone therapies and chemotherapies) are known to enhance the overall survival of metastatic castration-resistant prostate cancer patients, including patients with bone metastases [19]. Although  $^{223}\text{RaCl}_2$ 's success holds promise for alpha-particle-emitting radiopharmaceuticals for bone metastatic disease and has renewed interest in the development of these therapies [20–32], little is known as to the targeted treatment strategies for bone metastatic disease using alpha-particle-emitting radiopharmaceuticals.

While many excellent reviews relating to targeted radiotherapy have been published [22,33–35], this review will highlight (i) the biology of bone metastases by emphasizing the vicious cycle of bone metastasis, (ii) the treatment strategies for bone metastasis by mainly focusing on radiopharmaceuticals, and (iii) the future directions for targeted alpha-particle-emitting radiopharmaceutical treatment strategies in bone metastasis.

## 2. The Biology of the Vicious Cycle of Bone Metastases

Although personalized medicine strategies continue to be adopted in the clinic, the tumor phenotype at the primary site typically dictates the treatment regimen. However, these conventional treatment strategies usually fail to eradicate metastases. This leads to a more aggressive combination treatment, including chemotherapies, radiotherapies, immunotherapies, and/or targeted therapies, for cancer patients with metastases. Importantly, when considering the treatment of bone metastasis, the dynamics of bone turnover also needs to be considered during treatment planning.

Unlike other organs, bone is continuously renewed throughout life to maintain its structural integrity. Bone is composed of three parts: compact bone, trabecular bone, and bone marrow. Compact bone is a hard, solid bone tissue and forms the outside layer of bone. Trabecular bone (or spongy bone) and bone marrow are found in the inside of

bones. A part of trabecular bone eventually converts into compact bone. The bone marrow is composed of two distinct stem cell lineages, cells of hematopoietic origin and those of mesenchymal origin. Hematopoietic stem cells (HSCs) give rise to all blood cell types, including macrophages that differentiate into osteoclasts, while mesenchymal stem cells (MSCs) are responsible for the generation of stromal cells, osteoblasts, and osteocytes [36]. Additionally, these cells of mesenchymal origin are crucial for trabecular bone development. Interestingly, these two cell lineages interact with each other to maintain each other's functions. For example, osteoblasts serve as the microenvironment for HSCs, or the HSC niche [37–42], while HSCs support osteoblastic differentiation to establish the HSC niche [43]. Another example is that osteoblasts are responsible for the activation of osteoclasts [44], while these activated osteoclasts resorb the bone matrix to create the space for osteoblasts to form new bone [45]. As a result, compact bone, trabecular bone, and bone marrow crosstalk to maintain healthy bone development. This process, called bone remodeling, is a delicate balance that is often exploited by cancer cells that successfully colonize the bone [46].

Since Paget's seed and soil theory was proposed over a century ago [47], efforts have been made to understand why particular cancers prefer specific organs over others. Although blood flow and anatomical structure are considered as among the major contributing factors to the development of bone metastasis [48,49], proper physiological mechanisms of why particular types of cancers disseminate to the bone have not been fully uncovered. Additionally, recent evidence suggests that the establishment of organ-specific metastases is the result of not only the passive reception of circulating tumor cells through blood flow and anatomical structure but also the fact that the bone microenvironment selectively and actively recruits these circulating tumor cells [50]. This indicates that the interactions between the microenvironment of the bone marrow and bone metastatic cancer cells are crucial for the bone metastatic progression process.

Once these tumor cells have effectively seeded on the bone marrow, they begin to proliferate and interact with the cells involved in bone remodeling (e.g., osteoclasts, osteoblasts, and osteocytes) through paracrine and juxtacrine signaling events. This interaction creates an imbalance in the normal bone remodeling process in what has been termed the vicious cycle of bone metastases (Figure 1) [51]. Recent studies have revealed that bone metastatic prostate cancer cells hijack the interaction between the cells of hematopoietic and mesenchymal lineages, which is important for maintaining healthy bone remodeling, to establish metastatic growth within the marrow. For example, bone metastatic prostate cancer cells target the osteoblastic HSC niche during their dissemination to the bone and compete for occupancy of the HSC niche [52,53]. These observations are consistent with previous research that has demonstrated that metastatic colonization is frequently observed in bones that contain red marrow, where blood cell formation and bone formation are active (e.g., the axial skeleton, vertebrae, ribs, and the pelvis) [54].



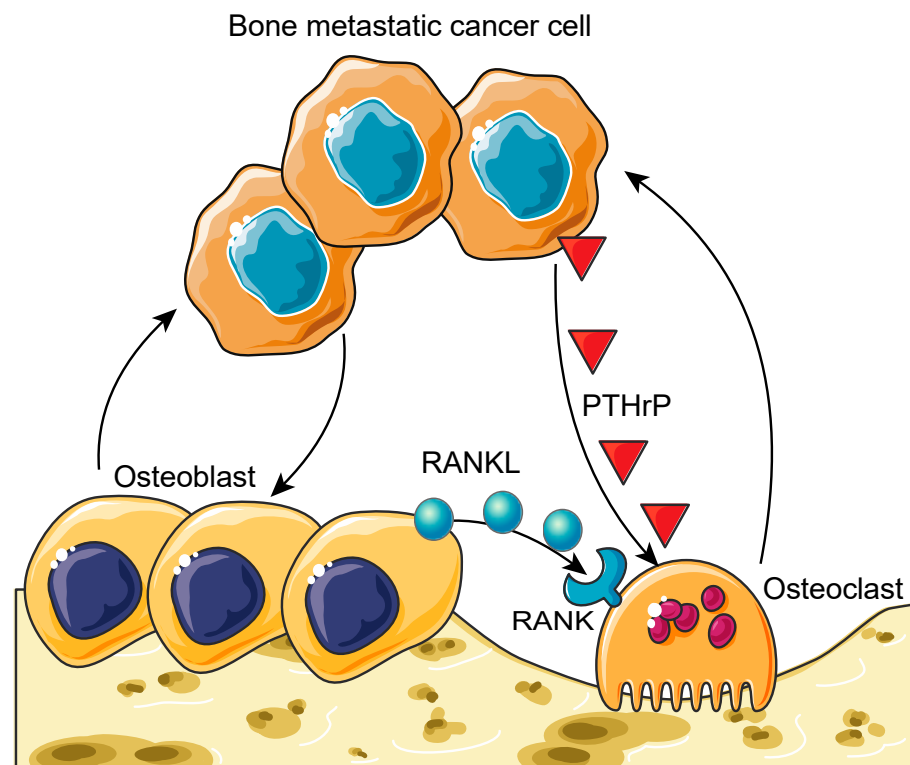


**Figure 1.** The vicious cycle of bone metastases. Bone metastatic cancer cells break the healthy bone remodeling processes to create a suitable microenvironment for the growing cancer cells and induce hyperosteoclastogenesis by activating osteoclasts through the secretion of parathyroid hormone-related peptide (PTHrP). This process leads to osteolytic bone lesions and provides bone metastatic cancer cells more space to grow. On the other hand, cancer cells can over-activate osteoblasts, resulting in osteoblastic bone lesions. These hyper-activated osteoblasts also stimulate osteoclastogenesis through the receptor activator of the nuclear factor  $\kappa$ B ligand (RANKL) (secreted from osteoblasts)/RANK (expressed on osteoclasts) axis. Furthermore, these hyper-activated osteoblasts and osteoclasts enhance the growth and survival of bone metastatic cancer cells. This process is called the vicious cycle of bone metastases. Graphics adapted from Smart Servier Medical Art (<https://smart.servier.com/bone-metastasis-March2021>) adapted from Smart Servier Medical Art (<https://smart.servier.com/>, accessed on 18 March 2021).

Additionally, once the vicious cycle has been initiated, bone metastases may present as osteolytic (bone destructive), osteoblastic (bone forming), or mixed metastases, depending on how the infiltrating cancer cells have exploited the normal bone remodeling mechanisms. Although there are osteolytic and osteoblastic-only bone metastases, most metastases arising from solid tumors have a heterogeneous phenotype [55]. Osteolytic bone metastatic lesions are characterized by the destruction of normal bone formation, primarily mediated by the hyper-activation of osteoclasts (multinucleated cells that resorb the bone matrix and develop from a monocyte-macrophage lineage) [56]. In this destructive mechanism, bone metastatic cells induce the release of parathyroid-hormone-related peptide (PTHrP), which is known to activate osteoclasts and induce bone resorption [57,58]. Conversely, osteoblastic bone metastatic lesions are characterized by the deposition of new bone. Although the mechanisms of osteoblastic bone metastases are still poorly understood, they are believed to occur through the hyper-activation of osteoblasts [59]. However, the newly formed bone matrix is poorly organized, weak, and fragile [60,61]. This leads to a lack of mechanical strength and frequent fracture [60,61]. Moreover, as osteoblasts continue to proliferate, they can inadvertently cause increased bone resorption, since they release cytokines, such as RANKL, which stimulates osteoclast differentiation and activation [59,60,62].

Taken together, the bone marrow microenvironment, especially where active hematopoiesis and bone remodeling take place, may play a crucial role in the establishment

Taken together, the bone marrow microenvironment, especially where active hematopoiesis and bone remodeling take place, may play a crucial role in the establishment and development of bone metastases, and therefore bone-marrow-microenvironment-targeting strategies have been used to treat bone metastatic disease.

### 3. Treatment of Bone Metastases

Current treatment options for bone metastasis include agents targeting bone remodeling (e.g., bisphosphonate and denosumab), hormone therapy, chemotherapy, external beam radiation therapy (EBRT), systemic radiotherapy, and surgical intervention [3,63,64]. Often, more than one intervention is used to suppress bone metastatic growth and maintain a patient's quality of life [65]. Although EBRT, bisphosphonate, and denosumab can reduce the onset of the painful complications of bone metastasis [17,18,66–71], delivering EBRT to every bone metastatic lesion is not practical and bisphosphonate and denosumab fail to improve the overall survival of bone metastatic patients (since these therapies mainly target bone remodeling but not cancer cells within the bone). Because of these limitations, bone metastasis is currently considered a hard-to-treat disease. Therefore, significant effort has been expended to develop ways to use the systemic delivery of therapeutic radionuclides to every bone metastatic lesion so that bone metastatic cancer cells can be exposed to the cytotoxic effects of radiation.

#### 3.1. Radiopharmaceuticals for Bone Metastases

Radionuclides derive their cytotoxicity from the particles they release during radioactive decay, which has been considered a systemic radiotherapy for bone metastasis. These particles include auger electrons ( $e^-$ ), beta minus ( $\beta^-$ ) particles, and alpha ( $\alpha^{++}$ ) particles (Table 1) [72].

**Table 1.** General characteristics of therapeutic radionuclides.

Decay	Particle	Maximum Particle Range (mm)	Maximum Particle Energy (MeV)	Linear Energy Transfer (keV/ $\mu$ m)
Electron capture internal conversion	Non-energetic electrons	0.0005	0.001	26
Beta minus particle	Energetic electrons	12	2.3	0.2
Alpha particle	Helium nuclei	0.1	9	80

Auger electrons are released from an atom that undergoes electron capture or internal conversion. These particles have low energy, travel a maximum distance of a micron in tissue and have moderately high linear energy transfer (LET), which allows for many destructive ionization events along the path traveled by the particles [73]. These properties require that the emitting atom be localized in close proximity to the cancer cell's DNA to have a therapeutic effect [74,75].

Beta-minus-particle-emitting radionuclides decay by  $\beta^-$  emission. These negatively charged electrons have widely varying energies and path lengths, which may range from 0.05 keV to 2.3 MeV and from 0.05 mm to 12 mm, respectively. As these particles travel, they exhibit a lower LET than auger electrons. This results in few ionization events along the particles' path. Their cytotoxic effect is believed to occur through the particles' ability to generate reactive oxygen species (ROS). In turn, these ROS generate single-stranded DNA breaks within the cancer cell. High concentrations of these  $\beta^-$ -particles are required to create enough single-stranded DNA breaks to overwhelm DNA damage repair mechanisms and yield a therapeutic benefit.

Alpha-particle-emitting radionuclides are, by far, the most cytotoxic radionuclides that have been used as systemic radiotherapy [76,77]. These particles have mass and charge equivalent to those of a helium nucleus. Alpha-particles are emitted with an energy range of 5–9 MeV, travel short distances (equivalent to no more than 10 cell diameters), and have an



LET that surpasses the LET of auger electrons to ensure a significant number of ionization events along the alpha-particle's path through tissue. These properties make the therapeutic efficacy of these radionuclides less dependent on chemo- and radio-resistance mechanisms or hypoxia. Although their cytotoxic properties have been recognized for decades, they are only now achieving clinical translation due to successful research initiatives that have explored how to efficiently attach these  $\alpha$ -emitting radionuclides to targeting ligands such as antibodies and peptides for effective delivery to cancer cells.

Historically, the Food and Drug Administration (FDA) has approved beta-minus-particle-emitting radiopharmaceuticals as adjunct treatments for bone metastases because of their chemical properties that give them an affinity for the bone matrix [78–81]. These radiotherapies are either administered as an ionic salt solution or chelated to bone-seeking ligands, such as hydroxyethylidene diphosphonic acid (HEDP) or tetramethylene phosphonic acid (EDTMP) (Figure 2A); a brief review of each radionuclide is outlined below.

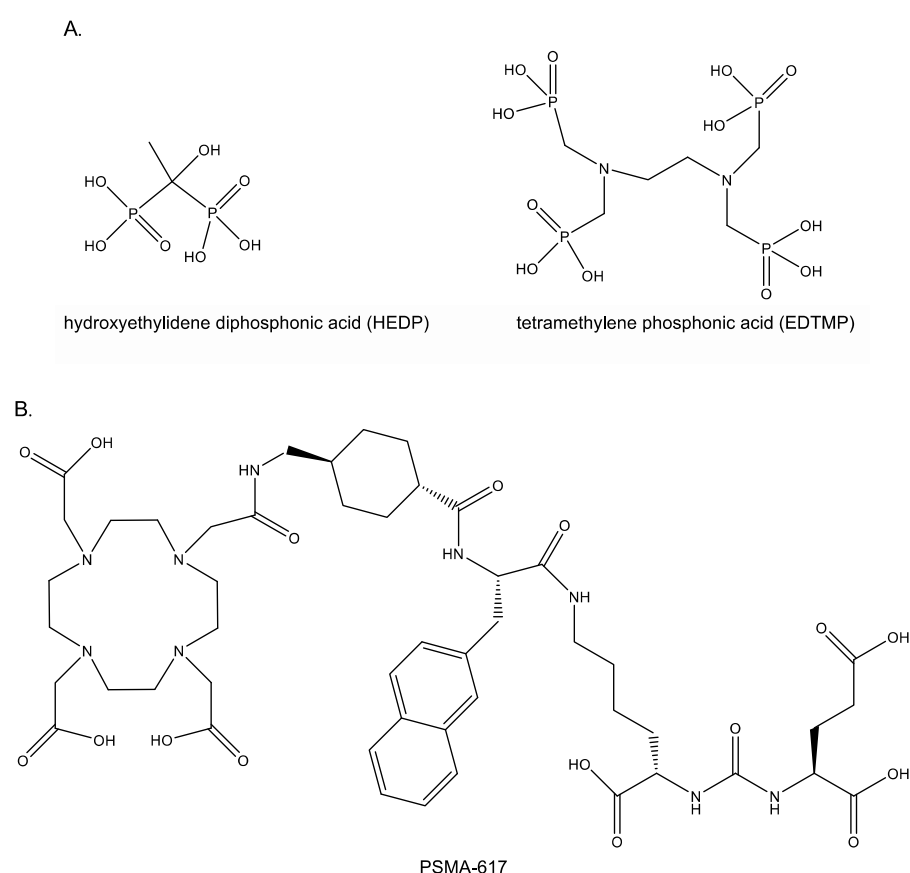


**Figure 2.** Several ligands used to deliver alpha-particle-emitting and beta-minus-particle-emitting radionuclides to bone metastasis. While ligands such as (A) hydroxyethylidene diphosphonic acid (HEDP) and tetramethylene phosphonic acid (EDTMP) target bone remodeling to deliver therapeutic radiation to bone metastases, ligands like (B) prostate-specific membrane antigen (PSMA)-617 target prostate cancer cell biomarkers.

**Phosphorus-32 and strontium-89:** Phosphorus-32 ( $^{32}\text{P}$ ;  $t_{1/2} = 14.3$  d;  $E_{\beta\text{max}} = 1.71$  MeV; maximum penetration in tissue (average) = 8 mm (3 mm)) is produced by the irradiation of sulfur-32 ( $^{32}\text{S}$ ) through neutron capture and is distributed as  $^{32}\text{P}$  orthophosphate. It has been investigated as a bone pain palliating radiopharmaceutical for more than 50 years [82]. After intravenous injection, approximately 90% of the injected dose is known to be incorporated into sites of bone remodeling due to the radiopharmaceutical's affinity for the hydroxyapatite within the bone matrix. In dose-palliative regimens, response rates approach 80% of treated bone [83–85] and were observed to last more than a year in patients with multiple sites of the disease. Unfortunately, due to the long particle range and relatively high relatively high energy of the  $\beta$ -particle, pancytopenia was observed in most patients, resulting in disfavor of its clinical use [86,87]. Strontium-89 ( $^{89}\text{Sr}$ ;  $t_{1/2} = 50.5$  d;  $E_{\beta\text{max}} = 1.46$

energy of the  $\beta^-$ -particle, pancytopenia was observed in most patients, resulting in disfavor of its clinical use [86,87]. Strontium-89 ( $^{89}\text{Sr}$ :  $t_{1/2} = 50.5$  d;  $E_{\beta\text{max}} = 1.46$  MeV; maximum penetration in tissue (average) = 6 mm (2.4 mm)) is produced by nuclear fission or through neutron capture and is distributed as  $^{89}\text{SrCl}_2$ . Since  $^{89}\text{Sr}^{2+}$  ions exhibit similar chemical properties to  $\text{Ca}^{2+}$  ions, they are readily incorporated into the hydroxyapatite where active bone remodeling is occurring due to metastatic disease [78]. Typically, overall response rates, as defined by a reduction in bone pain, for patients receiving  $^{89}\text{Sr}$  therapy approached 80%, with the palliative effects lasting approximately 15 months [87,88]. Although significant changes in red blood cell counts are not observed with this therapy, a decrease in white blood cell counts and platelets has been observed in 80% of patients [89–92], but these toxicities are resolved within 4 months of treatment cessation.

**Rhenium-186 and Rhenium-188:** Rhenium-186 ( $^{186}\text{Re}$ :  $t_{1/2} = 3.8$  d;  $E_{\beta\text{max}} = 1.07$  MeV; maximum penetration in tissue (average) = 4.5 mm (1.1 mm)) is routinely produced in nuclear reactors by direct neutron activation of metallic-enriched  $^{185}\text{Re}$ . Rhenium-186 decays with a maximum beta energy of 1.07 MeV and a low abundance 137 keV gamma emission. It has a physical half-life of 89.3 h. Because of its maximum beta energy and particle path length, efforts have been made to determine its ability to treat bone metastasis, but since its chemical properties are not similar to those of calcium, it must be chelated to a bone-seeking ligand before injection. In the comparative study between the skeletal and soft-tissue uptake of  $^{186}\text{Re}$ -HEDP (0.13 GBq) and  $^{153}\text{Sm}$ -EDTMP (37 MBq/kg-body weight) in patients with confirmed bone metastasis, significantly less bone uptake was observed in patients receiving  $^{186}\text{Re}$ -HEDP therapy, while soft-tissue retention was comparable for both radiopharmaceuticals [78]. Despite this fact, several studies have demonstrated that more than 80% of patients receiving  $^{186}\text{Re}$  therapy reported an improvement in their bone pain [93–97]. Similar to other agents, thrombocytopenia was observed to be a major but reversible side effect of treatment [98,99]. Rhenium-188 ( $^{188}\text{Re}$ :  $t_{1/2} = 0.7$  d;  $E_{\beta\text{max}} = 2.12$  MeV; maximum penetration in tissue (average) = 10.4 mm (3.1 mm)), although not approved for clinical use, has also been investigated as an agent for bone pain management, since it can be produced and shipped to clinical sites as a  $^{188}\text{W}/^{188}\text{Re}$  generator [100]. When chelated to HEDP, it demonstrated therapeutic efficacy, and repeated administrations improved progression-free and overall survival [101]. Additionally, it was observed that only 63% of the patients receiving  $^{188}\text{Re}$ -HEDP therapy reported grade I thrombocytopenia, 3% reported Grade II thrombocytopenia, and 3% of the patients reported grade I leukopenia, which were comparable for patients treated with  $^{186}\text{Re}$ -HEDP or  $^{153}\text{Sm}$ -EDTMP [101]. Furthermore, platelet and leukocyte counts returned to pretreatment levels within 3 months, suggesting that these toxicities are clinically manageable.

**Samarium-153:** Samarium-153 ( $^{153}\text{Sm}$ :  $t_{1/2} = 1.9$  d;  $E_{\beta\text{max}} = 0.81$  MeV; maximum penetration in tissue (average) = 2.5 mm (0.6 mm)), which is produced by the neutron irradiation of a samarium-152 target, has a half-life of 46.3 h and a range in bone of 1.7 mm [102]. To be effective, however,  $^{153}\text{Sm}$  needs to be chelated to a ligand such as EDTMP, which like other phosphonic acid complexes has a high affinity for skeletal tissue while being rapidly cleared from the blood and local soft tissue. This radiopharmaceutical has shown clinical benefit in several clinical trials, with the majority of patients experiencing pain relief [103]. In one study involving 100 patients with confirmed metastatic disease, subjects received 18–37 MBq/kg of  $^{153}\text{Sm}$ -EDTMP and were followed for several weeks after treatment [102]. Nearly 70% of the patients experienced symptomatic relief of their bone pain. Myelotoxicity was the main side effect of treatment, with nearly 90% of the subjects experiencing grade II thrombocytopenia or leukopenia, which resolved approximately 2 months after therapy. While several patients experienced grade III/IV myelotoxicity, these patients were observed to have a depleted hematopoietic reserve because of previous therapeutic interventions.

**Lutetium-177:** Lutetium-177 ( $^{177}\text{Lu}$ :  $t_{1/2} = 6.7$  d;  $E_{\beta\text{max}} = 0.50$  MeV; maximum penetration in tissue (average) = 2.2 mm (0.67 mm)) is produced by neutron irradiation of  $^{176}\text{Lu}$  or  $^{176}\text{Yb}$  targets. Although several cancer-targeting agents, such as Lutathera® and  $^{117}\text{Lu}$ -PSMA-617, have been used to deliver targeted radiation therapy to cancer cells expressing

specific cancer cell antigens [104], additional studies have sought to use the radioactive decay properties of  $^{177}\text{Lu}$  for treating bone metastasis. Several groups have investigated the utility of  $^{177}\text{Lu}$ -EDTMP as a bone-seeking radiopharmaceutical since the energy of the emitted  $\beta^-$  is low enough to reduce bone marrow suppression, which has consistently been a major disadvantage of other  $\beta^-$ -emitting bone-seeking agents [105,106]. Recently, the use of low- and high-dose  $^{177}\text{Lu}$ -EDTMP was examined in a phase II study in patients with metastatic breast or prostate cancer [107]. In this study, subjects received either a low (0.13 GBq) or a high (0.26 GBq) dose of  $^{177}\text{Lu}$ -EDTMP and were followed for 16 weeks post-treatment. Based upon pain assessment scores, the overall response rate was 86%. Additionally, treatment-related toxicity was evaluated in all patients. Grade I/II hematological toxicities were observed in 34% of the subjects, while grade III/IV toxicities were observed in 23% of the study participants. However, the observed toxicities were not significantly different in either the low- or the high-dose cohort, and this finding prompted the authors to conclude that  $^{177}\text{Lu}$ -EDTMP is safe and effective as a treatment for bone pain palliation. More recently, several groups investigated whether using a bisphosphonate to deliver the cytotoxic radiation released by  $^{177}\text{Lu}$  to the metastatic deposit in bone would provide greater relief. While many bisphosphonates were studied, zoledronic acid was chosen for further study since it had significantly higher incorporation into hydroxyapatite [108,109]. Consequently, several groups studied  $^{177}\text{Lu}$ -DOTA-zoledronic acid ( $^{177}\text{Lu}$ -DOTA-ZOL) and demonstrated that it has pharmacokinetics comparable to those of  $^{177}\text{Lu}$ -EDTMP [110,111]. These studies also revealed higher absorption of the dose by the trabecular bone in patients who received  $^{177}\text{Lu}$ -DOTA-ZOL vs.  $^{177}\text{Lu}$ -EDTMP, but the dose absorbed by critical organs was much lower for the former radiopharmaceutical. Recently, the safety and efficacy of  $^{177}\text{Lu}$ -DOTA-ZOL in 40 patients with metastatic bone disease was evaluated [112]. Eligible subjects received 0.13 GBq of  $^{177}\text{Lu}$ -DOTA-ZOL at monthly intervals and then were monitored for a 12-week period after therapy. Based upon criteria such as pain palliation, an overall response rate of 90% was observed. However, unlike patients receiving  $^{177}\text{Lu}$ -EDTMP, grade III/IV hematological toxicities were not observed, although several patients did experience grade II anemia. Moreover, renal toxicity and hypercalcemia, which can be complications of bisphosphonate administration, were not observed in study participants. Interestingly, pain palliation was observed within 7 days of treatment, with relief lasting 10 months, which is more than twice that experienced by patients receiving  $^{177}\text{Lu}$ -EDTMP.

Not only beta-minus-particle-emitting radiopharmaceuticals but also alpha-particle-emitting radiopharmaceuticals have been used as a treatment modality for bone metastatic disease. Radium-223 dichloride ( $^{223}\text{RaCl}_2$ ;  $T_{1/2} = 11.4$  d;  $E_{\alpha_{\text{max}}} = 6\text{--}7$  MeV) is a water-soluble salt that was approved nearly a decade ago by the FDA for the treatment of bone metastasis associated with metastatic prostate cancer. Similar to calcium ions, this alkaline earth ion accumulates in bone, where it decays through seven daughter radionuclides, while releasing four  $\alpha^{++}$ -particles and two  $\beta^-$ -particles, generating approximately 30 MeV of total kinetic energy, which is deposited in the surrounding bone cancer microenvironment [67–69,78,113]. This large energy deposition is believed to generate irreparable double-stranded DNA breaks within the DNA of tumor cells that have localized in the bone, causing cancer cell death [114–117]. This strategy has yielded clinical success. For example, in the ALSYMPCA trial (NCT00699751), which was a randomized, double-blind, placebo-controlled phase III trial that investigated the role of  $^{223}\text{RaCl}_2$  in metastatic castration-resistant prostate cancer patients ( $n = 921$ ), the median overall survival of patients treated with  $^{223}\text{RaCl}_2$  ( $n = 614$ , 14.9 months) significantly improved compared with those treated with a placebo ( $n = 307$ , 11.3 months) (hazard ratio, 0.70; 95% confidence interval, 0.58 to 0.83;  $p < 0.001$ ) [66]. Moreover, patients treated with  $^{223}\text{RaCl}_2$  experienced decreased pain levels that correlated with increased overall survival [118]. Diarrhea, nausea, and vomiting were the most common side effects reported by patients. Additionally, pancytopenia was observed in many patients with grade III/IV thrombocytopenia, and neutropenia was observed in patients with compromised bone marrow function [119]. Since those initial trials, the use of  $^{223}\text{RaCl}_2$  therapy in combination with other agents using a strategy that has

proven successful with non-radioactive therapeutics has been sought [120]. For example, a post hoc exploratory analysis of an international, early access, open-label, single-arm phase IIIb trial of the testing efficacy of  $^{223}\text{RaCl}_2$  in metastatic castration-resistant prostate cancer patients following the ALSYMPCA trial revealed that a combination of  $^{223}\text{RaCl}_2$  and androgen deprivation therapies (ADTs; abiraterone or enzalutamide) extended the patients' overall survival compared to therapy with  $^{223}\text{RaCl}_2$  alone [118]. However, a recent multinational, multicenter, randomized, double-blind, placebo-controlled phase III trial of the combination of abiraterone and  $^{223}\text{RaCl}_2$  in patients with metastatic castration-resistant prostate cancer (NCT02043678) not only failed to improve skeletal event-free survival but also increased the frequency of bone fractures compared to the placebo [121]. These contradictory results suggest that additional prospective studies are needed and caution is warranted when choosing an effective combination strategy that involves the use of ADTs and  $^{223}\text{RaCl}_2$  therapy for treating prostate cancer patients with bone metastasis.

### 3.2. Targeted Radiopharmaceuticals for Bone Metastases

To date, the strategy for integrating systemic radiotherapies into the treatment plans of cancer patients with bone metastases has relied on bone metabolism to target bone metastatic disease. While successful, the results of this strategy have been primarily palliative, since the bone metastatic cancer cells are not specifically targeted by the radiopharmaceutical. As a result, efforts are being made to expand this strategy by developing agents that can selectively target biomarkers that are over-expressed on the cancer cells within the bone metastatic microenvironment, with the goal of improving therapeutic efficacy and patient outcomes. For example, one such strategy that has been successful in the treatment of metastatic prostate cancer has been the development of radiotherapies that specifically target prostate-specific membrane antigen (PSMA) [122]. PSMA is known to be highly expressed on prostate cancer cells at the primary tumor and within visceral and bone metastases [123]. PSMA-617, a small molecule that binds to PSMA with high affinity, was designed to target PSMA-expressing prostate cancer cells (Figure 2B) [124]. In a recent single-arm, single-center, phase II trial,  $^{177}\text{Lu}$ -PSMA-617 was administered to men with metastatic castration-resistant prostate cancer ( $n = 30$ ) [125]. After four cycles of radiotherapy, 57% of these patients experienced minimal toxicity and achieved a greater-than-50% reduction in prostate-specific antigen (PSA) levels, which is one of the clinical surrogate markers for prostate cancer treatment response [125]. Based on these promising results, an international prospective open-label randomized phase III trial comparing the treatment efficacy between  $^{177}\text{Lu}$ -PSMA-617 and the best standard of care in men with metastatic castration-resistant prostate cancer (VISION trial, NCT03511664) is currently underway [126], and as of 23 March 2021, the initial result that  $^{177}\text{Lu}$ -PSMA-617 significantly improves the overall survival and radiographic progression-free survival of PSMA-positive metastatic castration-resistant prostate cancer patients was announced (<https://www.novartis.com/news/media-releases/novartis-announces-positive-result-phase-iii-study-radioligand-therapy-177lu-psma-617-patients-advanced-prostate-cancer>, (accessed on 1 April 2021)).

Despite the promise of  $^{177}\text{Lu}$ -PSMA-617 therapy, approximately 30% of patients do not respond to this treatment [127]. These observations have led to the investigation of the use of  $^{225}\text{Ac}$ -PSMA-617 as an alternative alpha-particle-emitting radiotherapy for refractory patients [127–129]. Actinium-225 ( $^{225}\text{Ac}$ ;  $t_{1/2} = 10$  d;  $E_{\alpha_{\text{max}}} = 6\text{--}8$  MeV) is a radioactive metal of the actinide series. Similar to  $^{223}\text{RaCl}_2$ ,  $^{225}\text{Ac}$  has a relatively long half-life and emits four  $\alpha^{++}$ - and two  $\beta^{-}$ -particles per nuclear decay. However, unlike  $^{223}\text{RaCl}_2$ ,  $^{225}\text{Ac}$  can be linked to a variety of targeting ligands [130–137]. In the early stage of the development of  $^{225}\text{Ac}$ -PSMA-617, two patients received this therapy [127]. The first patient exhausted conventional chemotherapies, bone remodeling therapy, ADTs, and six cycles of  $^{223}\text{RaCl}_2$  therapy. The patient received three cycles of approximately 10 MBq (100 kBq/kg body weight) of  $^{225}\text{Ac}$ -PSMA-617. After 8 weeks, all visible visceral and bone metastases had decreased to a size that was below the limit of detection of clinical imaging scanners, while PSA levels had decreased from 3000 to 0.26 ng/mL. Similar to the first



patient, the second patient was refractory to conventional chemotherapies and ADTs and failed to respond to several cycles of  $^{177}\text{Lu}$ -PSMA-617 therapy. This patient received three cycles of  $^{225}\text{Ac}$ -PSMA-617 therapy (100 kBq/kg body weight) at bimonthly intervals. After completing the three cycles, the patient experienced complete remission, as indicated by the results of the restaging PSMA-PET/CT scans (Figure 3). Similar to the first patient, no relevant hematological toxicities were observed, although both subjects did experience moderate xerostomia.

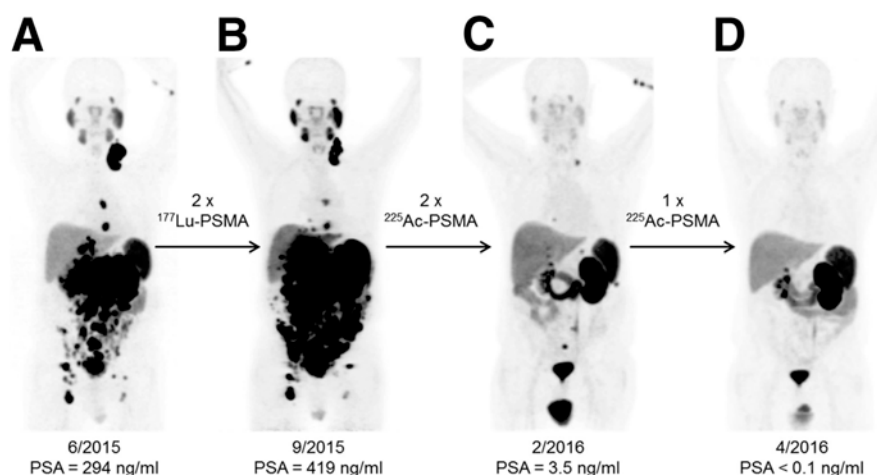


**Figure 3.** An example of the effective response of a prostate cancer patient to  $^{225}\text{Ac}$ -PSMA-617 treatment. This research was originally published in the *Journal of Nuclear Medicine* [127].  $^{68}\text{Ga}$ -PSMA-11 PET/CT scans of patient B were progressive under  $^{177}\text{Lu}$ -PSMA-617 therapy. In comparison to the initial tumor spread (A), restaging after 2 cycles of  $\beta$ -emitting  $^{177}\text{Lu}$ -PSMA-617 presented progression (B). In contrast, restaging after second (C) and third (D) cycles of  $\alpha$ -emitting  $^{225}\text{Ac}$ -PSMA-617 presented an impressive response. Adapted from ref. [127].

In additional studies by this same group, chemotherapy-naïve prostate cancer patients with extensive bone and lymph node metastases were selected to receive  $^{225}\text{Ac}$ -PSMA-617 therapy [138]. All patients ( $n = 17$ ) had failed prior treatments, which included radical prostatectomy, EBRT, ADT, brachytherapy, and  $^{177}\text{Lu}$ -PSMA-617 therapy. Patients received between two and six cycles of  $^{225}\text{Ac}$ -PSMA-617, with an average administered activity range of between 1 and 13 MBq. Following treatment, 82% of the patients experienced a  $\geq 90\%$  reduction in PSA levels. Moreover, PSMA-PET/CT revealed that 65% of the treated patients had no metastatic lesions. Similar to the initial two patients, though all patients did experience moderate xerostomia, which prompts additional investigations into the most efficient ways to salvage salivary gland function [139,140].

While a recent report of a patient achieving complete remission lasting longer than 5 years was published in the literature [141], this result could be tempered by recent observations that while patients report a partial reduction in metastatic disease, longer  $^{225}\text{Ac}$ -PSMA-617 therapy does not appear to improve overall survival [142]. In addition, a recent study by the same group, which investigated the effect of  $^{225}\text{Ac}$ -PSMA-617 on PSA levels, found that while PSA levels decreased, the reduction was not statistically significant [143]. These findings suggest that while  $^{225}\text{Ac}$ -PSMA-617 may be effective in reducing PSA levels, it may not be sufficient to improve overall survival. This is likely due to the fact that  $^{225}\text{Ac}$ -PSMA-617 is a targeted therapy that only targets the PSMA receptor, which is expressed on the surface of prostate cancer cells. While this strategy is not specific for bone metastases, a majority of the patients with metastatic castration-resistant prostate cancer experience bone metastases during the course of disease progression. Therefore, the development of PSMA-

in both preclinical and clinical settings (Table 2). Since PSMA is expressed by not only bone metastatic prostate cancer cells but also those at the primary site and soft-tissue metastatic sites, this strategy is not specific for bone metastases. However, a majority of the patients with metastatic castration-resistant prostate cancer experience bone metastases during the course of disease progression. Therefore, the development of PSMA-targeted alpha-particle-emitting radiopharmaceuticals is crucial if eradicating bone metastatic prostate cancer is to be an achievable clinical goal. Further studies, including the assessments of their clinical efficacy and safety, are clearly warranted.

**Table 2.** The recent status of PSMA-targeted alpha-particle-emitting radiopharmaceuticals.

Agent	Conjugator	Development Phase	Refs.
$^{213}\text{Bi}$ -J591	PSMA-targeting murine monoclonal antibody, J591	Preclinical study	[143–145]
$^{213}\text{Bi}$ -PSMA I&T	PSMA-targeting (3S,7S)-29,32-dibenzyl-5,13,20,28,31,34-hexaoxo-37-(4,7,10-tris(carboxymethyl)-1,4,7,10-tetraazacyclododecan-1-yl)-4,6,12,21,27,30,33-heptaazaheptatriacontane-1,3,7,26,37-pentacarboxylic acid (DOTAGA-FFK(Sub-KuE)), PSMA I&T	Preclinical study	[146]
$^{213}\text{Bi}$ -JVZ-008	PSMA-targeting nanobody, JVZ-008	Preclinical study	[146]
$^{211}\text{At}$ -6	PSMA-targeting (2S)-2-(3-(1-carboxy-5-(4- $^{211}\text{At}$ -astatobenzamido)pentyl)ureido)-pentanedioic acid, compound 6	Preclinical study	[147]
$^{225}\text{Ac}$ -PSMA-617	PSMA-targeting small molecule, PSMA-617	Clinical study	[127,138,141,148]
$^{227}\text{Th}$ -PSMA-TTC	PSMA-targeting fully human antibody, BAY 2315158	Clinical trial (phase I: NCT03724747)	[149]
$^{225}\text{Ac}$ -J591	PSMA-targeting murine monoclonal antibody, J591	Clinical trial (phase I: NCT03276572)	

#### 4. Conclusions

Bone metastasis creates enormous physical, emotional, and financial burdens for cancer patients and society; it is a significant contributor to cancer mortality rates. Systemically delivered radionuclides have been explored as potential therapies for bone metastasis. Initially,  $\beta^-$ -emitting radionuclides were used because they could be delivered easily to sites of active bone remodeling. However, their efficacy has been limited to pain mitigation. Recently, systemically delivered  $^{223}\text{RaCl}_2$ , which decays through  $\alpha^{++}$ -particle emission, has been observed to extend the overall survival of men with metastatic prostate cancer. These results have renewed interest in alpha-particle-emitting radiotherapies, and new molecularly targeted strategies to deliver this highly cytotoxic radiation directly to bone metastatic cancer cells within the bone marrow microenvironment are being investigated. Using this strategy,  $^{225}\text{Ac}$ -PSMA-617, which has been an effective treatment for men with metastatic prostate cancer, which was previously believed to be refractory to conventional chemotherapies and standard of care radiotherapy, has been developed. While further clinical evaluation is warranted, current data suggest that targeted alpha-particle-emitting radiopharmaceuticals used alone or in concert with current standard treatments may lead to much-needed improvements in the clinical management of cancer bone metastasis.

**Author Contributions:** Conceptualization, T.J.W. and Y.S.; writing—original draft preparation, C.M.P., T.J.W., and Y.S.; writing—review and editing, T.J.W. and Y.S.; supervision, T.J.W. and Y.S.; and funding acquisition, T.J.W. and Y.S. All authors have read and agreed to the published version of the manuscript.

**Funding:** This research was funded by the National Cancer Institute, R01-CA238888; R44-CA203184; R21-CA227709; and P30-CA012197; the U.S. Department of Defense, W81XWH-17-1-0541; W81XWH-19-1-0045; and W81XWH-19-1-0046; and METAvivor, METAvivor Research Award. The APC was funded by W81XWH-19-1-0045.

**Institutional Review Board Statement:** Not applicable.

**Informed Consent Statement:** Not applicable.

**Data Availability Statement:** Not applicable.

**Acknowledgments:** This work is directly supported by the National Cancer Institute (R01-CA238888, Y.S.; R44-CA203184, Y.S.; and R21-CA227709, T.J.W.), the U.S. Department of Defense (W81XWH-17-1-0541, Y.S.; W81XWH-19-1-0045, Y.S.; and W81XWH-19-1-0046, T.J.W.), METAvivor (METAvivor Research Award, Y.S.), and the Wake Forest Baptist Comprehensive Cancer Center Internal Pilot Funding (Y.S.). This work is also supported by the National Cancer Institute's Cancer Center Support Grant award number P30-CA012197, issued to the Wake Forest Baptist Comprehensive Cancer Center. The content is solely the responsibility of the authors and does not necessarily represent the official views of the National Cancer Institute and Department of Defense.

**Conflicts of Interest:** Y.S. has received research funding from TEVA Pharmaceuticals, but not relevant to this study. No conflict of interest exists for the remaining authors.

## References

1. Seyfried, T.N.; Huysentruyt, L.C. On the origin of cancer metastasis. *Crit. Rev. Oncog.* **2013**, *18*, 43–73. [\[CrossRef\]](#) [\[PubMed\]](#)
2. Macedo, F.; Ladeira, K.; Pinho, F.; Saraiva, N.; Bonito, N.; Pinto, L.; Goncalves, F. Bone Metastases: An Overview. *Oncol. Rev.* **2017**, *11*, 321. [\[PubMed\]](#)
3. Selvaggi, G.; Scagliotti, G.V. Management of bone metastases in cancer: A review. *Crit. Rev. Oncol. Hematol.* **2005**, *56*, 365–378. [\[CrossRef\]](#) [\[PubMed\]](#)
4. Hagiwara, M.; Delea, T.E.; Chung, K. Healthcare costs associated with skeletal-related events in breast cancer patients with bone metastases. *J. Med. Econ.* **2014**, *17*, 223–230. [\[CrossRef\]](#)
5. Barlev, A.; Song, X.; Ivanov, B.; Setty, V.; Chung, K. Payer costs for inpatient treatment of pathologic fracture, surgery to bone, and spinal cord compression among patients with multiple myeloma or bone metastasis secondary to prostate or breast cancer. *J. Manag. Care Pharm.* **2010**, *16*, 693–702. [\[CrossRef\]](#) [\[PubMed\]](#)
6. Delea, T.; Langer, C.; McKiernan, J.; Liss, M.; Edelsberg, J.; Brandman, J.; Sung, J.; Raut, M.; Oster, G. The cost of treatment of skeletal-related events in patients with bone metastases from lung cancer. *Oncology* **2004**, *67*, 390–396. [\[CrossRef\]](#)
7. Delea, T.; McKiernan, J.; Brandman, J.; Edelsberg, J.; Sung, J.; Raut, M.; Oster, G. Retrospective study of the effect of skeletal complications on total medical care costs in patients with bone metastases of breast cancer seen in typical clinical practice. *J. Support. Oncol.* **2006**, *4*, 341–347.
8. Delea, T.E.; McKiernan, J.; Brandman, J.; Edelsberg, J.; Sung, J.; Raut, M.; Oster, G. Impact of skeletal complications on total medical care costs among patients with bone metastases of lung cancer. *J. Thorac. Oncol.* **2006**, *1*, 571–576. [\[CrossRef\]](#)
9. Lage, M.J.; Barber, B.L.; Harrison, D.J.; Jun, S. The cost of treating skeletal-related events in patients with prostate cancer. *Am. J. Manag. Care* **2008**, *14*, 317–322.
10. Krupski, T.L.; Foley, K.A.; Baser, O.; Long, S.; Macarios, D.; Litwin, M.S. Health care cost associated with prostate cancer, androgen deprivation therapy and bone complications. *J. Urol.* **2007**, *178*, 1423–1428. [\[CrossRef\]](#)
11. Groot, M.T.; Boeken Kruger, C.G.; Pelger, R.C.; Uyl-de Groot, C.A. Costs of prostate cancer, metastatic to the bone, in the Netherlands. *Eur. Urol.* **2003**, *43*, 226–232. [\[CrossRef\]](#)
12. Duran, I.; Garzon, C.; Sanchez, A.; Garcia-Carbonero, I.; Perez-Gracia, J.L.; Segui-Palmer, M.A.; Wei, R.; Restovic, G.; Gasquet, J.A.; Gutierrez, L. Cost analysis of skeletal-related events in Spanish patients with bone metastases from solid tumours. *Clin. Transl. Oncol.* **2014**, *16*, 322–329. [\[CrossRef\]](#)
13. Hechmati, G.; Cure, S.; Gouepo, A.; Hoefeler, H.; Lorusso, V.; Luftner, D.; Duran, I.; Garzon-Rodriguez, C.; Ashcroft, J.; Wei, R.; et al. Cost of skeletal-related events in European patients with solid tumours and bone metastases: Data from a prospective multinational observational study. *J. Med. Econ.* **2013**, *16*, 691–700. [\[CrossRef\]](#) [\[PubMed\]](#)
14. Tangirala, K.; Appukkuttan, S.; Simmons, S. Costs and Healthcare Resource Utilization Associated with Hospital Admissions of Patients with Metastatic or Nonmetastatic Prostate Cancer. *Am. Health Drug Benef.* **2019**, *12*, 306–312.
15. Hadjidakis, D.J.; Androulakis, I.I. Bone remodeling. *Ann. N. Y. Acad. Sci.* **2006**, *1092*, 385–396. [\[CrossRef\]](#) [\[PubMed\]](#)
16. Guise, T.A. The vicious cycle of bone metastases. *J. Musculoskelet. Neuronal. Interact.* **2002**, *2*, 570–572. [\[PubMed\]](#)
17. Stopeck, A.T.; Lipton, A.; Body, J.J.; Steger, G.G.; Tonkin, K.; de Boer, R.H.; Lichinitser, M.; Fujiwara, Y.; Yardley, D.A.; Viniegra, M.; et al. Denosumab compared with zoledronic acid for the treatment of bone metastases in patients with advanced breast cancer: A randomized, double-blind study. *J. Clin. Oncol.* **2010**, *28*, 5132–5139. [\[CrossRef\]](#)

18. Fizazi, K.; Carducci, M.; Smith, M.; Damiao, R.; Brown, J.; Karsh, L.; Milecki, P.; Shore, N.; Rader, M.; Wang, H.; et al. Denosumab versus zoledronic acid for treatment of bone metastases in men with castration-resistant prostate cancer: A randomised, double-blind study. *Lancet* **2011**, *377*, 813–822. [\[CrossRef\]](#)
19. McCain, J. Drugs that offer a survival advantage for men with bone metastases resulting from castration-resistant prostate cancer: New and emerging treatment options. *Pharm. Ther.* **2014**, *39*, 130–143.
20. Nguyen, N.C.; Shah, M.; Appleman, L.J.; Parikh, R.; Mountz, J.M. Radium-223 Therapy for Patients with Metastatic Castrate-Resistant Prostate Cancer: An Update on Literature with Case Presentation. *Int. J. Mol. Imaging* **2016**, *2016*, 2568031. [\[CrossRef\]](#) [\[PubMed\]](#)
21. Vogelzang, N.J.; Coleman, R.E.; Michalski, J.M.; Nilsson, S.; O'Sullivan, J.M.; Parker, C.; Widmark, A.; Thuresson, M.; Xu, L.; Germino, J.; et al. Hematologic Safety of Radium-223 Dichloride: Baseline Prognostic Factors Associated with Myelosuppression in the ALSYMPCA Trial. *Clin. Genitourin Cancer* **2017**, *15*, 42–52. [\[CrossRef\]](#)
22. Wadas, T.J.; Pandya, D.N.; Solingapuram Sai, K.K.; Mintz, A. Molecular targeted alpha-particle therapy for oncologic applications. *AJR Am. J. Roentgenol.* **2014**, *203*, 253–260. [\[CrossRef\]](#) [\[PubMed\]](#)
23. Scheinberg, D.A.; McDevitt, M.R. Actinium-225 in targeted alpha-particle therapeutic applications. *Curr. RadioPharm.* **2011**, *4*, 306–320. [\[CrossRef\]](#) [\[PubMed\]](#)
24. Yamazaki, H.; Nakamura, S.; Suzuki, G.; Yoshida, K.; Yoshioka, Y.; Koizumi, M.; Ogawa, K. Hypofractionated Radiotherapy for Localized Prostate Cancer: A Challenging Accelerated Hypofractionated Radiotherapy. *Anticancer Res.* **2015**, *35*, 5167–5177. [\[PubMed\]](#)
25. Lewis, B.; Chalhoub, E.; Chalouhy, C.; Sartor, O. Radium-223 in Bone-Metastatic Prostate Cancer: Current Data and Future Prospects. *Oncology (Williston Park)* **2015**, *29*, 483–488. [\[PubMed\]](#)
26. de Kruijff, R.M.; Wolterbeek, H.T.; Denkova, A.G. A Critical Review of Alpha Radionuclide Therapy-How to Deal with Recoiling Daughters? *Pharmaceuticals (Basel)* **2015**, *8*, 321–336. [\[CrossRef\]](#)
27. Guerard, F.; Barbet, J.; Chatal, J.F.; Kraeber-Bodere, F.; Cherel, M.; Haddad, F. Which radionuclide, carrier molecule and clinical indication for alpha-immunotherapy? *Q. J. Nucl. Med. Mol. Imaging* **2015**, *59*, 161–167.
28. McGann, S.; Horton, E.R. Radium-223 dichloride: A novel treatment option for castration-resistant prostate cancer patients with symptomatic bone metastases. *Ann. Pharmacother.* **2015**, *49*, 469–476. [\[CrossRef\]](#)
29. Qi, W.X.; Fu, S.; Zhang, Q.; Guo, X.M. Charged particle therapy versus photon therapy for patients with hepatocellular carcinoma: A systematic review and meta-analysis. *Radiother. Oncol.* **2015**, *114*, 289–295. [\[CrossRef\]](#) [\[PubMed\]](#)
30. Buroni, F.E.; Persico, M.G.; Pasi, F.; Lodola, L.; Nano, R.; Aprile, C. Radium-223: Insight and Perspectives in Bone-metastatic Castration-resistant Prostate Cancer. *Anticancer Res.* **2016**, *36*, 5719–5730. [\[CrossRef\]](#)
31. Cordier, D.; Krolicki, L.; Morgenstern, A.; Merlo, A. Targeted Radiolabeled Compounds in Glioma Therapy. *Semin. Nucl. Med.* **2016**, *46*, 243–249. [\[CrossRef\]](#)
32. Ettari, R.; Previti, S.; Bitto, A.; Grasso, S.; Zappala, M. Immunoproteasome-Selective Inhibitors: A Promising Strategy to Treat Hematologic Malignancies, Autoimmune and Inflammatory Diseases. *Curr. Med. Chem.* **2016**, *23*, 1217–1238. [\[CrossRef\]](#)
33. Sgouros, G.; Bodei, L.; McDevitt, M.R.; Nedrow, J.R. Radiopharmaceutical therapy in cancer: Clinical advances and challenges. *Nat. Rev. Drug Discov.* **2020**, *19*, 589–608. [\[CrossRef\]](#)
34. Tafreshi, N.K.; Doligalski, M.L.; Tichacek, C.J.; Pandya, D.N.; Budzevich, M.M.; El-Haddad, G.; Khushalani, N.I.; Moros, E.G.; McLaughlin, M.L.; Wadas, T.J.; et al. Development of Targeted Alpha Particle Therapy for Solid Tumors. *Molecules* **2019**, *24*, 4314. [\[CrossRef\]](#)
35. Schae, D.; McBride, W.H. Opportunities and challenges of radiotherapy for treating cancer. *Nat. Rev. Clin. Oncol.* **2015**, *12*, 527–540. [\[CrossRef\]](#)
36. Laurenti, E.; Gottgens, B. From haematopoietic stem cells to complex differentiation landscapes. *Nature* **2018**, *553*, 418–426. [\[CrossRef\]](#)
37. Shiozawa, Y.; Taichman, R.S. Getting blood from bone: An emerging understanding of the role that osteoblasts play in regulating hematopoietic stem cells within their niche. *Exp. Hematol.* **2012**, *40*, 685–694. [\[CrossRef\]](#)
38. Galan-Diez, M.; Kousteni, S. The osteoblastic niche in hematopoiesis and hematological myeloid malignancies. *Curr. Mol. Biol. Rep.* **2017**, *3*, 53–62. [\[CrossRef\]](#) [\[PubMed\]](#)
39. Yin, T.; Li, L. The stem cell niches in bone. *J. Clin. Invest.* **2006**, *116*, 1195–1201. [\[CrossRef\]](#)
40. Askmyr, M.; Sims, N.A.; Martin, T.J.; Purton, L.E. What is the true nature of the osteoblastic hematopoietic stem cell niche? *Trends Endocrinol. Metab.* **2009**, *20*, 303–309. [\[CrossRef\]](#)
41. Szade, K.; Gulati, G.S.; Chan, C.K.F.; Kao, K.S.; Miyamishi, M.; Marjon, K.D.; Sinha, R.; George, B.M.; Chen, J.Y.; Weissman, I.L. Where Hematopoietic Stem Cells Live: The Bone Marrow Niche. *Antioxid. Redox Signal.* **2018**, *29*, 191–204. [\[CrossRef\]](#)
42. Pinho, S.; Frenette, P.S. Haematopoietic stem cell activity and interactions with the niche. *Nat. Rev. Mol. Cell Biol.* **2019**, *20*, 303–320. [\[CrossRef\]](#)
43. Jung, Y.; Song, J.; Shiozawa, Y.; Wang, J.; Wang, Z.; Williams, B.; Havens, A.; Schneider, A.; Ge, C.; Franceschi, R.T.; et al. Hematopoietic stem cells regulate mesenchymal stromal cell induction into osteoblasts thereby participating in the formation of the stem cell niche. *Stem Cells* **2008**, *26*, 2042–2051. [\[CrossRef\]](#) [\[PubMed\]](#)
44. Chen, X.; Wang, Z.; Duan, N.; Zhu, G.; Schwarz, E.M.; Xie, C. Osteoblast-osteoclast interactions. *Connect. Tissue Res.* **2018**, *59*, 99–107. [\[CrossRef\]](#)



45. Sims, N.A.; Martin, T.J. Coupling the activities of bone formation and resorption: A multitude of signals within the basic multicellular unit. *Bonekey Rep.* **2014**, *3*, 481. [\[CrossRef\]](#) [\[PubMed\]](#)
46. Vessella, R.L.; Corey, E. Targeting factors involved in bone remodeling as treatment strategies in prostate cancer bone metastasis. *Clin. Cancer Res.* **2006**, *12*, 6285s–6290s. [\[CrossRef\]](#)
47. Paget, S. The distribution of secondary growths in cancer of the breast. 1889. *Cancer Metastasis Rev.* **1989**, *8*, 98–101.
48. Raubenheimer, E.J.; Noffke, C.E. Pathogenesis of bone metastasis: A review. *J. Oral. Pathol. Med.* **2006**, *35*, 129–135. [\[CrossRef\]](#)
49. Guise, T.A.; Mundy, G.R. Cancer and bone. *Endocr. Rev.* **1998**, *19*, 18–54.
50. Chantry, C.F.; Feron, O.; Marbaix, E.; DeClerck, Y.A. Bone marrow microenvironment and tumor progression. *Cancer Microenviron.* **2008**, *1*, 23–35. [\[CrossRef\]](#)
51. Cook, L.M.; Shay, G.; Araujo, A.; Lynch, C.C. Integrating new discoveries into the “vicious cycle” paradigm of prostate to bone metastases. *Cancer Metastasis Rev.* **2014**, *33*, 511–525. [\[CrossRef\]](#) [\[PubMed\]](#)
52. Shiozawa, Y.; Pedersen, E.A.; Havens, A.M.; Jung, Y.; Mishra, A.; Joseph, J.; Kim, J.K.; Patel, L.R.; Ying, C.; Ziegler, A.M.; et al. Human prostate cancer metastases target the hematopoietic stem cell niche to establish footholds in mouse bone marrow. *J. Clin. Investig.* **2011**, *121*, 1298–1312. [\[CrossRef\]](#)
53. Shiozawa, Y.; Berry, J.E.; Eber, M.R.; Jung, Y.; Yumoto, K.; Cackowski, F.C.; Yoon, H.J.; Parsana, P.; Mehra, R.; Wang, J.; et al. The marrow niche controls the cancer stem cell phenotype of disseminated prostate cancer. *Oncotarget* **2016**, *7*, 41217–41232. [\[CrossRef\]](#)
54. Hage, W.D.; Aboulafia, A.J.; Aboulafia, D.M. Incidence, location, and diagnostic evaluation of metastatic bone disease. *Orthop. Clin. N. Am.* **2000**, *31*, 515–528. [\[CrossRef\]](#)
55. Mundy, G.R. Metastasis to bone: Causes, consequences and therapeutic opportunities. *Nat. Rev. Cancer* **2002**, *2*, 584–593. [\[CrossRef\]](#)
56. Taube, T.; Elomaa, I.; Blomqvist, C.; Beneton, M.N.; Kanis, J.A. Histomorphometric evidence for osteoclast-mediated bone resorption in metastatic breast cancer. *Bone* **1994**, *15*, 161–166. [\[CrossRef\]](#)
57. Martin, T.J. Osteoblast-derived PTHrP is a physiological regulator of bone formation. *J. Clin. Investig.* **2005**, *115*, 2322–2324. [\[CrossRef\]](#)
58. Iwamura, M.; di Sant’Agnese, P.A.; Wu, G.; Benning, C.M.; Cockett, A.T.; Deftos, L.J.; Abrahamsson, P.A. Immunohistochemical localization of parathyroid hormone-related protein in human prostate cancer. *Cancer Res.* **1993**, *53*, 1724–1726. [\[PubMed\]](#)
59. Weilbaecher, K.N.; Guise, T.A.; McCauley, L.K. Cancer to bone: A fatal attraction. *Nat. Rev. Cancer* **2011**, *11*, 411–425. [\[CrossRef\]](#)
60. Keller, E.T.; Brown, J. Prostate cancer bone metastases promote both osteolytic and osteoblastic activity. *J. Cell Biochem.* **2004**, *91*, 718–729. [\[CrossRef\]](#)
61. Ganguly, S.S.; Li, X.; Miranti, C.K. The host microenvironment influences prostate cancer invasion, systemic spread, bone colonization, and osteoblastic metastasis. *Front. Oncol.* **2014**, *4*, 364. [\[CrossRef\]](#) [\[PubMed\]](#)
62. Kohli, S.S.; Kohli, V.S. Role of RANKL-RANK/osteoprotegerin molecular complex in bone remodeling and its immunopathologic implications. *Indian J. Endocrinol. Metab.* **2011**, *15*, 175–181. [\[CrossRef\]](#)
63. Pinski, J.; Dorff, T.B. Prostate cancer metastases to bone: Pathophysiology, pain management, and the promise of targeted therapy. *Eur. J. Cancer* **2005**, *41*, 932–940. [\[CrossRef\]](#)
64. Lipton, A. Management of bone metastases in breast cancer. *Curr. Treat. Options Oncol.* **2005**, *6*, 161–171. [\[CrossRef\]](#)
65. Woolf, D.K.; Padhani, A.R.; Makris, A. Assessing response to treatment of bone metastases from breast cancer: What should be the standard of care? *Ann. Oncol.* **2015**, *26*, 1048–1057. [\[CrossRef\]](#)
66. Parker, C.; Nilsson, S.; Heinrich, D.; Helle, S.I.; O’Sullivan, J.M.; Fossa, S.D.; Chodacki, A.; Wiechno, P.; Logue, J.; Seke, M.; et al. Alpha emitter radium-223 and survival in metastatic prostate cancer. *N. Engl. J. Med.* **2013**, *369*, 213–223. [\[CrossRef\]](#)
67. Badrising, S.K.; van der Noort, V.; Hamberg, P.; Coenen, J.L.; Aarts, M.J.; van Oort, I.M.; van den Eertwegh, A.J.; Los, M.; van den Berg, H.P.; Gelderblom, H.; et al. Enzalutamide as a Fourth- or Fifth-Line Treatment Option for Metastatic Castration-Resistant Prostate Cancer. *Oncology* **2016**, *91*, 267–273. [\[CrossRef\]](#)
68. Vignani, F.; Bertaglia, V.; Buttiglieri, C.; Tucci, M.; Scagliotti, G.V.; Di Maio, M. Skeletal metastases and impact of anticancer and bone-targeted agents in patients with castration-resistant prostate cancer. *Cancer Treat. Rev.* **2016**, *44*, 61–73. [\[CrossRef\]](#)
69. Abou, D.S.; Ulmert, D.; Doucet, M.; Hobbs, R.F.; Riddle, R.C.; Thorek, D.L. Whole-Body and Microenvironmental Localization of Radium-223 in Naive and Mouse Models of Prostate Cancer Metastasis. *J. Natl Cancer Inst.* **2016**, *108*, djv380. [\[CrossRef\]](#)
70. Laird, B.J.; Walley, J.; Murray, G.D.; Clausen, E.; Colvin, L.A.; Fallon, M.T. Characterization of cancer-induced bone pain: An exploratory study. *Support. Care Cancer* **2011**, *19*, 1393–1401. [\[CrossRef\]](#)
71. De Felice, F.; Piccioli, A.; Musio, D.; Tombolini, V. The role of radiation therapy in bone metastases management. *Oncotarget* **2017**, *8*, 25691–25699. [\[CrossRef\]](#)
72. Kassis, A.I.; Adelstein, S.J. Radiobiologic principles in radionuclide therapy. *J. Nucl. Med.* **2005**, *46* (Suppl. 1), 4S–12S. [\[PubMed\]](#)
73. Cole, A. Absorption of 20-eV to 50,000-eV electron beams in air and plastic. *Radiat. Res.* **1969**, *38*, 7–33. [\[CrossRef\]](#) [\[PubMed\]](#)
74. Kassis, A.I.; Adelstein, S.J.; Haydock, C.; Sastry, K.S.; McElvany, K.D.; Welch, M.J. Lethality of Auger electrons from the decay of bromine-77 in the DNA of mammalian cells. *Radiat. Res.* **1982**, *90*, 362–373. [\[CrossRef\]](#)
75. Kassis, A.I.; Sastry, K.S.; Adelstein, S.J. Kinetics of uptake, retention, and radiotoxicity of <sup>125</sup>IUdR in mammalian cells: Implications of localized energy deposition by Auger processes. *Radiat. Res.* **1987**, *109*, 78–89. [\[CrossRef\]](#)

76. Walicka, M.A.; Vaidyanathan, G.; Zalutsky, M.R.; Adelstein, S.J.; Kassis, A.I. Survival and DNA damage in Chinese hamster V79 cells exposed to alpha particles emitted by DNA-incorporated astatine-211. *Radiat. Res.* **1998**, *150*, 263–268. [\[CrossRef\]](#)
77. Goddu, S.M.; Howell, R.W.; Rao, D.V. Cellular dosimetry: Absorbed fractions for monoenergetic electron and alpha particle sources and S-values for radionuclides uniformly distributed in different cell compartments. *J. Nucl. Med.* **1994**, *35*, 303–316. [\[PubMed\]](#)
78. Choi, J.Y. Treatment of Bone Metastasis with Bone-Targeting Radiopharmaceuticals. *Nucl. Med. Mol. Imaging* **2018**, *52*, 200–207. [\[CrossRef\]](#)
79. Paes, F.M.; Serafini, A.N. Systemic metabolic radiopharmaceutical therapy in the treatment of metastatic bone pain. *Semin Nucl. Med.* **2010**, *40*, 89–104. [\[CrossRef\]](#)
80. Lepareur, N.; Lacoeyille, F.; Bouvry, C.; Hindre, F.; Garcion, E.; Cherel, M.; Noiret, N.; Garin, E.; Knapp, F.F.R., Jr. Rhenium-188 Labeled Radiopharmaceuticals: Current Clinical Applications in Oncology and Promising Perspectives. *Front. Med. (Lausanne)* **2019**, *6*, 132. [\[CrossRef\]](#)
81. Alavi, M.; Omidvari, S.; Mehdizadeh, A.; Jalilian, A.R.; Bahrami-Samani, A. Metastatic Bone Pain Palliation using (177)Lu-Ethylenediaminetetramethylene Phosphonic Acid. *World J. Nucl. Med.* **2015**, *14*, 109–115. [\[CrossRef\]](#) [\[PubMed\]](#)
82. Friedell, H.L.; Storaasli, J.P. The use of radioactive phosphorus in the treatment of carcinoma of the breast with widespread metastases to bone. *Am. J. Roentgenol. Radium Ther.* **1950**, *64*, 559–575. [\[PubMed\]](#)
83. Maxfield, J.R., Jr.; Maxfield, J.G.; Maxfield, W.S. The use of radioactive phosphorus and testosterone in metastatic bone lesions from breast and prostate. *South. Med. J.* **1958**, *51*, 320–327. [\[CrossRef\]](#)
84. Miller, A.D. Radiophosphorus (P32) treatment in carcinoma of the breast and prostate: Report of 39 cases. *J. Am. Osteopath Assoc.* **1974**, *74*, 217–222. [\[PubMed\]](#)
85. Cheung, A.; Driedger, A.A. Evaluation of radioactive phosphorus in the palliation of metastatic bone lesions from carcinoma of the breast and prostate. *Radiology* **1980**, *134*, 209–212. [\[CrossRef\]](#)
86. Silberstein, E.B. The treatment of painful osseous metastases with phosphorus-32-labeled phosphates. *Semin. Oncol.* **1993**, *20* (Suppl. 2), 10–21.
87. Nair, N. Relative efficacy of 32P and 89Sr in palliation in skeletal metastases. *J. Nucl. Med.* **1999**, *40*, 256–261.
88. Blake, G.M.; Zivanovic, M.A.; McEwan, A.J.; Ackery, D.M. Sr-89 therapy: Strontium kinetics in disseminated carcinoma of the prostate. *Eur. J. Nucl. Med.* **1986**, *12*, 447–454. [\[CrossRef\]](#)
89. Finlay, I.G.; Mason, M.D.; Shelley, M. Radioisotopes for the palliation of metastatic bone cancer: A systematic review. *Lancet Oncol.* **2005**, *6*, 392–400. [\[CrossRef\]](#)
90. Silberstein, E.B.; Williams, C. Strontium-89 therapy for the pain of osseous metastases. *J. Nucl. Med.* **1985**, *26*, 345–348. [\[PubMed\]](#)
91. Robinson, R.G.; Preston, D.F.; Spicer, J.A.; Baxter, K.G. Radionuclide therapy of intractable bone pain: Emphasis on strontium-89. *Semin. Nucl. Med.* **1992**, *22*, 28–32. [\[CrossRef\]](#)
92. Mertens, W.C.; Stitt, L.; Porter, A.T. Strontium 89 therapy and relief of pain in patients with prostatic carcinoma metastatic to bone: A dose response relationship? *Am. J. Clin. Oncol.* **1993**, *16*, 238–242. [\[CrossRef\]](#)
93. Maxon, H.R., 3rd; Schroder, L.E.; Thomas, S.R.; Hertzberg, V.S.; Deutsch, E.A.; Scher, H.I.; Samaratunga, R.C.; Libson, K.F.; Williams, C.C.; Moulton, J.S.; et al. Re-186(Sn) HEDP for treatment of painful osseous metastases: Initial clinical experience in 20 patients with hormone-resistant prostate cancer. *Radiology* **1990**, *176*, 155–159. [\[CrossRef\]](#)
94. Giannakenas, C.; Kalofonos, H.P.; Apostolopoulos, D.J.; Zarakovitis, J.; Kosmas, C.; Vassilakos, P.J. Preliminary results of the use of Re-186-HEDP for palliation of pain in patients with metastatic bone disease. *Am. J. Clin. Oncol.* **2000**, *23*, 83–88. [\[CrossRef\]](#)
95. Kolesnikov-Gauthier, H.; Carpentier, P.; Depreux, P.; Vennin, P.; Caty, A.; Sulman, C. Evaluation of toxicity and efficacy of 186Re-hydroxyethylidene diphosphonate in patients with painful bone metastases of prostate or breast cancer. *J. Nucl. Med.* **2000**, *41*, 1689–1694.
96. Sciuto, R.; Tofani, A.; Festa, A.; Giannarelli, D.; Pasqualoni, R.; Maini, C.L. Short- and long-term effects of 186Re-1,1-hydroxyethylidene diphosphonate in the treatment of painful bone metastases. *J. Nucl. Med.* **2000**, *41*, 647–654.
97. Quirijnen, J.M.; Han, S.H.; Zonnenberg, B.A.; de Klerk, J.M.; van het Schip, A.D.; van Dijk, A.; ten Kroode, H.F.; Blijham, G.H.; van Rijk, P.P. Efficacy of rhenium-186-etidronate in prostate cancer patients with metastatic bone pain. *J. Nucl. Med.* **1996**, *37*, 1511–1515.
98. Maxon, H.R., 3rd; Schroder, L.E.; Hertzberg, V.S.; Thomas, S.R.; Englaro, E.E.; Samaratunga, R.; Smith, H.; Moulton, J.S.; Williams, C.C.; Ehrhardt, G.J.; et al. Rhenium-186(Sn)HEDP for treatment of painful osseous metastases: Results of a double-blind crossover comparison with placebo. *J. Nucl. Med.* **1991**, *32*, 1877–1881.
99. Han, S.H.; de Klerk, J.M.; Tan, S.; van het Schip, A.D.; Derksen, B.H.; van Dijk, A.; Kruitwagen, C.L.; Blijham, G.H.; van Rijk, P.P.; Zonnenberg, B.A. The PLACORHEN study: A double-blind, placebo-controlled, randomized radionuclide study with (186)Re-etidronate in hormone-resistant prostate cancer patients with painful bone metastases. Placebo Controlled Rhenium Study. *J. Nucl. Med.* **2002**, *43*, 1150–1156.
100. Liepe, K. (188)Re-HEDP therapy in the therapy of painful bone metastases. *World J. Nucl. Med.* **2018**, *17*, 133–138. [\[CrossRef\]](#)
101. Liepe, K.; Kotzerke, J. A comparative study of 188Re-HEDP, 186Re-HEDP, 153Sm-EDTMP and 89Sr in the treatment of painful skeletal metastases. *Nucl. Med. Commun.* **2007**, *28*, 623–630. [\[CrossRef\]](#)

102. Resche, I.; Chatal, J.F.; Pecking, A.; Ell, P.; Duchesne, G.; Rubens, R.; Fogelman, I.; Houston, S.; Fauser, A.; Fischer, M.; et al. A dose-controlled study of <sup>153</sup>Sm-ethylenediaminetetramethylenephosphonate (EDTMP) in the treatment of patients with painful bone metastases. *Eur. J. Cancer* **1997**, *33*, 1583–1591. [[CrossRef](#)]
103. Tian, J.H.; Zhang, J.M.; Hou, Q.T.; Oyang, Q.H.; Wang, J.M.; Luan, Z.S.; Chuan, L.; He, Y.J. Multicentre trial on the efficacy and toxicity of single-dose samarium-153-ethylene diamine tetramethylene phosphonate as a palliative treatment for painful skeletal metastases in China. *Eur. J. Nucl. Med.* **1999**, *26*, 2–7. [[CrossRef](#)] [[PubMed](#)]
104. Yadav, M.P.; Ballal, S.; Sahoo, R.K.; Dwivedi, S.N.; Bal, C. Radioligand Therapy With (177)Lu-PSMA for Metastatic Castration-Resistant Prostate Cancer: A Systematic Review and Meta-Analysis. *AJR Am. J. Roentgenol.* **2019**, *213*, 275–285. [[CrossRef](#)] [[PubMed](#)]
105. Chakraborty, S.; Das, T.; Banerjee, S.; Balogh, L.; Chaudhari, P.R.; Sarma, H.D.; Polyak, A.; Mathe, D.; Venkatesh, M.; Janoki, G.; et al. <sup>177</sup>Lu-EDTMP: A viable bone pain palliative in skeletal metastasis. *Cancer Biother. Radio Pharm.* **2008**, *23*, 202–213. [[CrossRef](#)] [[PubMed](#)]
106. Mathe, D.; Balogh, L.; Polyak, A.; Kiraly, R.; Marian, T.; Pawlak, D.; Zaknun, J.J.; Pillai, M.R.; Janoki, G.A. Multispecies animal investigation on biodistribution, pharmacokinetics and toxicity of <sup>177</sup>Lu-EDTMP, a potential bone pain palliation agent. *Nucl. Med. Biol.* **2010**, *37*, 215–226. [[CrossRef](#)]
107. Agarwal, K.K.; Singla, S.; Arora, G.; Bal, C. (177)Lu-EDTMP for palliation of pain from bone metastases in patients with prostate and breast cancer: A phase II study. *Eur. J. Nucl. Med. Mol. Imaging* **2015**, *42*, 79–88. [[CrossRef](#)] [[PubMed](#)]
108. Chakraborty, S.; Das, T.; Sarma, H.D.; Venkatesh, M.; Banerjee, S. Comparative studies of <sup>177</sup>Lu-EDTMP and <sup>177</sup>Lu-DOTMP as potential agents for palliative radiotherapy of bone metastasis. *Appl. Radiat. Isot.* **2008**, *66*, 1196–1205. [[CrossRef](#)]
109. Das, T.; Shinto, A.; Karuppuswamy Kamaleshwaran, K.; Banerjee, S. Theranostic Treatment of Metastatic Bone Pain with <sup>177</sup>Lu-DOTMP. *Clin. Nucl. Med.* **2016**, *41*, 966–967. [[CrossRef](#)]
110. Bahrami-Samani, A.; Anvari, A.; Jalilian, A.R.; Shirvani-Arani, S.; Yousefnia, H.; Aghamiri, M.R.; Ghannadi-Maragheh, M. Production, Quality Control and Pharmacokinetic Studies of (177)Lu-EDTMP for Human Bone Pain Palliation Therapy Trials. *Iran. J. Pharm. Res.* **2012**, *11*, 137–144.
111. Yousefnia, H.; Zolghadri, S.; Jalilian, A.R. Absorbed dose assessment of (177)Lu-zoledronate and (177)Lu-EDTMP for human based on biodistribution data in rats. *J. Med. Phys.* **2015**, *40*, 102–108. [[PubMed](#)]
112. Yadav, M.P.; Ballal, S.; Meckel, M.; Roesch, F.; Bal, C. [(177)Lu]Lu-DOTA-ZOL bone pain palliation in patients with skeletal metastases from various cancers: Efficacy and safety results. *EJNMMI Res.* **2020**, *10*, 130. [[CrossRef](#)] [[PubMed](#)]
113. Wissing, M.D.; van Leeuwen, F.W.; van der Pluijm, G.; Gelderblom, H. Radium-223 chloride: Extending life in prostate cancer patients by treating bone metastases. *Clin. Cancer Res.* **2013**, *19*, 5822–5827. [[CrossRef](#)] [[PubMed](#)]
114. Kassis, A.I. Therapeutic radionuclides: Biophysical and radiobiologic principles. *Semin Nucl. Med.* **2008**, *38*, 358–366. [[CrossRef](#)] [[PubMed](#)]
115. Baidoo, K.E.; Yong, K.; Brechbiel, M.W. Molecular pathways: Targeted alpha-particle radiation therapy. *Clin. Cancer Res.* **2013**, *19*, 530–537. [[CrossRef](#)] [[PubMed](#)]
116. Sgouros, G.; Hobbs, R.F.; Song, H. Modelling and dosimetry for alpha-particle therapy. *Curr. Radio Pharm.* **2011**, *4*, 261–265. [[CrossRef](#)] [[PubMed](#)]
117. Song, H.; Hobbs, R.F.; Vajravelu, R.; Huso, D.L.; Esaias, C.; Apostolidis, C.; Morgenstern, A.; Sgouros, G. Radioimmunotherapy of breast cancer metastases with alpha-particle emitter <sup>225</sup>Ac: Comparing efficacy with <sup>213</sup>Bi and <sup>90</sup>Y. *Cancer Res.* **2009**, *69*, 8941–8948. [[CrossRef](#)]
118. Saad, F.; Carles, J.; Gillesen, S.; Heidenreich, A.; Heinrich, D.; Gratt, J.; Levy, J.; Miller, K.; Nilsson, S.; Petrenciuc, O.; et al. Radium-223 and concomitant therapies in patients with metastatic castration-resistant prostate cancer: An international, early access, open-label, single-arm phase 3b trial. *Lancet Oncol.* **2016**, *17*, 1306–1316. [[CrossRef](#)]
119. Delgado Bolton, R.C.; Giammarile, F. Bone radionuclide therapy and increased survival with radium-223 is the way to go for nuclear medicine: The offer that oncologists cannot refuse. *Eur. J. Nucl. Med. Mol. Imaging* **2018**, *45*, 822–823. [[CrossRef](#)] [[PubMed](#)]
120. Gravis, G. Systemic treatment for metastatic prostate cancer. *Asian J. Urol.* **2019**, *6*, 162–168. [[CrossRef](#)]
121. Smith, M.; Parker, C.; Saad, F.; Miller, K.; Tombal, B.; Ng, Q.S.; Boegemann, M.; Matveev, V.; Piulats, J.M.; Zucca, L.E.; et al. Addition of radium-223 to abiraterone acetate and prednisone or prednisolone in patients with castration-resistant prostate cancer and bone metastases (ERA 223): A randomised, double-blind, placebo-controlled, phase 3 trial. *Lancet Oncol.* **2019**, *20*, 408–419. [[CrossRef](#)]
122. Chang, S.S. Overview of prostate-specific membrane antigen. *Rev. Urol.* **2004**, *6* (Suppl. 10), S13–S18. [[PubMed](#)]
123. Hupe, M.C.; Philippi, C.; Roth, D.; Kumpers, C.; Ribbat-Idel, J.; Becker, F.; Joerg, V.; Duensing, S.; Lubczyk, V.H.; Kirfel, J.; et al. Expression of Prostate-Specific Membrane Antigen (PSMA) on Biopsies Is an Independent Risk Stratifier of Prostate Cancer Patients at Time of Initial Diagnosis. *Front. Oncol.* **2018**, *8*, 623. [[CrossRef](#)]
124. Sun, M.; Niaz, M.O.; Nelson, A.; Skafida, M.; Niaz, M.J. Review of <sup>177</sup>Lu-PSMA-617 in Patients with Metastatic Castration-Resistant Prostate Cancer. *Cureus* **2020**, *12*, e8921. [[CrossRef](#)]
125. Hofman, M.S.; Violet, J.; Hicks, R.J.; Ferdinandus, J.; Thang, S.P.; Akhurst, T.; Iravani, A.; Kong, G.; Ravi Kumar, A.; Murphy, D.G.; et al. [(177)Lu]-PSMA-617 radionuclide treatment in patients with metastatic castration-resistant prostate cancer (LuPSMA trial): A single-centre, single-arm, phase 2 study. *Lancet Oncol.* **2018**, *19*, 825–833. [[CrossRef](#)]



126. Rahbar, K.; Bodei, L.; Morris, M.J. Is the Vision of Radioligand Therapy for Prostate Cancer Becoming a Reality? An Overview of the Phase III VISION Trial and Its Importance for the Future of Theranostics. *J. Nucl. Med.* **2019**, *60*, 1504–1506. [\[CrossRef\]](#)
127. Kratochwil, C.; Bruchertseifer, F.; Giesel, F.L.; Weis, M.; Verburg, F.A.; Mottaghy, F.; Kopka, K.; Apostolidis, C.; Haberkorn, U.; Morgenstern, A. 225Ac-PSMA-617 for PSMA-Targeted alpha-Radiation Therapy of Metastatic Castration-Resistant Prostate Cancer. *J. Nucl. Med.* **2016**, *57*, 1941–1944. [\[CrossRef\]](#) [\[PubMed\]](#)
128. Yadav, M.P.; Ballal, S.; Sahoo, R.K.; Tripathi, M.; Seth, A.; Bal, C. Efficacy and safety of (225)Ac-PSMA-617 targeted alpha therapy in metastatic castration-resistant Prostate Cancer patients. *Theranostics* **2020**, *10*, 9364–9377. [\[CrossRef\]](#) [\[PubMed\]](#)
129. Kratochwil, C.; Haberkorn, U.; Giesel, F.L. (225)Ac-PSMA-617 for Therapy of Prostate Cancer. *Semin. Nucl. Med.* **2020**, *50*, 133–140. [\[CrossRef\]](#)
130. Deblonde, G.J.; Abergel, R.J. Active actinium. *Nat. Chem.* **2016**, *8*, 1084. [\[CrossRef\]](#) [\[PubMed\]](#)
131. Vasiliev, A.; Severin, A.; Lapshina, E.; Chernykh, E.; Ermolaev, S.; Kalmykov, S. Hydroxylapatite particles as carriers for <sup>223</sup>Ra. *J. Radioanal. Nuclear Chem.* **2016**, *311*, 1503–1509. [\[CrossRef\]](#)
132. McDevitt, M.R.; Ma, D.; Simon, J.; Frank, R.K.; Scheinberg, D.A. Design and synthesis of 225Ac radioimmunopharmaceuticals. *Appl. Radiat. Isot.* **2002**, *57*, 841–847. [\[CrossRef\]](#)
133. Sofou, S.; Kappel, B.J.; Jaggi, J.S.; McDevitt, M.R.; Scheinberg, D.A.; Sgouros, G. Enhanced retention of the alpha-particle-emitting daughters of Actinium-225 by liposome carriers. *Bioconjug. Chem.* **2007**, *18*, 2061–2067. [\[CrossRef\]](#) [\[PubMed\]](#)
134. Antczak, C.; Jaggi, J.S.; LeFave, C.V.; Curcio, M.J.; McDevitt, M.R.; Scheinberg, D.A. Influence of the linker on the biodistribution and catabolism of actinium-225 self-immolative tumor-targeted isotope generators. *Bioconjug. Chem.* **2006**, *17*, 1551–1560. [\[CrossRef\]](#) [\[PubMed\]](#)
135. Borchardt, P.E.; Yuan, R.R.; Miederer, M.; McDevitt, M.R.; Scheinberg, D.A. Targeted actinium-225 in vivo generators for therapy of ovarian cancer. *Cancer Res.* **2003**, *63*, 5084–5090.
136. Davis, I.A.; Glowienka, K.A.; Boll, R.A.; Deal, K.A.; Brechbiel, M.W.; Stabin, M.; Bochsler, P.N.; Mirzadeh, S.; Kennel, S.J. Comparison of 225actinium chelates: Tissue distribution and radiotoxicity. *Nucl. Med. Biol.* **1999**, *26*, 581–589. [\[CrossRef\]](#)
137. Deal, K.A.; Davis, I.A.; Mirzadeh, S.; Kennel, S.J.; Brechbiel, M.W. Improved in vivo stability of actinium-225 macrocyclic complexes. *J. Med. Chem.* **1999**, *42*, 2988–2992. [\[CrossRef\]](#) [\[PubMed\]](#)
138. Sathekge, M.; Bruchertseifer, F.; Knoesen, O.; Reyneke, F.; Lawal, I.; Lengana, T.; Davis, C.; Mahapane, J.; Corbett, C.; Vorster, M.; et al. (225)Ac-PSMA-617 in chemotherapy-naïve patients with advanced prostate cancer: A pilot study. *Eur. J. Nucl. Med. Mol. Imaging* **2019**, *46*, 129–138. [\[CrossRef\]](#)
139. Paganelli, G.; Sarnelli, A.; Severi, S.; Sansovini, M.; Belli, M.L.; Monti, M.; Foca, F.; Celli, M.; Nicolini, S.; Tardelli, E.; et al. Dosimetry and safety of (177)Lu PSMA-617 along with polyglutamate parotid gland protector: Preliminary results in metastatic castration-resistant prostate cancer patients. *Eur. J. Nucl. Med. Mol. Imaging* **2020**, *47*, 3008–3017. [\[CrossRef\]](#)
140. Langbein, T.; Chausse, G.; Baum, R.P. Salivary Gland Toxicity of PSMA Radioligand Therapy: Relevance and Preventive Strategies. *J. Nucl. Med.* **2018**, *59*, 1172–1173. [\[CrossRef\]](#) [\[PubMed\]](#)
141. Rathke, H.; Bruchertseifer, F.; Kratochwil, C.; Keller, H.; Giesel, F.L.; Apostolidis, C.; Haberkorn, U.; Morgenstern, A. First patient exceeding 5-year complete remission after (225)Ac-PSMA-TAT. *Eur. J. Nucl. Med. Mol. Imaging* **2021**, *48*, 311–312. [\[CrossRef\]](#) [\[PubMed\]](#)
142. Kratochwil, C.; Giesel, F.L.; Heussel, C.P.; Kazdal, D.; Endris, V.; Nientiedt, C.; Bruchertseifer, F.; Kippenberger, M.; Rathke, H.; Leichsenring, J.; et al. Patients Resistant Against PSMA-Targeting alpha-Radiation Therapy Often Harbor Mutations in DNA Damage-Repair-Associated Genes. *J. Nucl. Med.* **2020**, *61*, 683–688. [\[CrossRef\]](#)
143. McDevitt, M.R.; Barendswaard, E.; Ma, D.; Lai, L.; Curcio, M.J.; Sgouros, G.; Ballangrud, A.M.; Yang, W.H.; Finn, R.D.; Pellegrini, V.; et al. An alpha-particle emitting antibody ([213Bi]591) for radioimmunotherapy of prostate cancer. *Cancer Res.* **2000**, *60*, 6095–6100.
144. Ballangrud, A.M.; Yang, W.H.; Charlton, D.E.; McDevitt, M.R.; Hamacher, K.A.; Panageas, K.S.; Ma, D.; Bander, N.H.; Scheinberg, D.A.; Sgouros, G. Response of LNCaP spheroids after treatment with an alpha-particle emitter (213Bi)-labeled anti-prostate-specific membrane antigen antibody (J591). *Cancer Res.* **2001**, *61*, 2008–2014. [\[PubMed\]](#)
145. Li, Y.; Tian, Z.; Rizvi, S.M.; Bander, N.H.; Allen, B.J. In vitro and preclinical targeted alpha therapy of human prostate cancer with Bi-213 labeled J591 antibody against the prostate specific membrane antigen. *Prostate Cancer Prostatic Dis.* **2002**, *5*, 36–46. [\[CrossRef\]](#) [\[PubMed\]](#)
146. Nonnekens, J.; Chatalic, K.L.; Molkenboer-Kuennen, J.D.; Beerens, C.E.; Bruchertseifer, F.; Morgenstern, A.; Veldhoven-Zweistra, J.; Schottelius, M.; Wester, H.J.; van Gent, D.C.; et al. (213)Bi-Labeled Prostate-Specific Membrane Antigen-Targeting Agents Induce DNA Double-Strand Breaks in Prostate Cancer Xenografts. *Cancer Biother. Radio Pharm.* **2017**, *32*, 67–73.
147. Kiess, A.P.; Minn, I.; Vaidyanathan, G.; Hobbs, R.F.; Josefsson, A.; Shen, C.; Brummet, M.; Chen, Y.; Choi, J.; Koumariannou, E.; et al. (2S)-2-(3-(1-Carboxy-5-(4-211At-Astatobenzamido)Pentyl)Ureido)-Pentanedioic Acid for PSMA-Targeted alpha-Particle Radio-pharmaceutical Therapy. *J. Nucl. Med.* **2016**, *57*, 1569–1575. [\[CrossRef\]](#) [\[PubMed\]](#)
148. Khreish, F.; Ebert, N.; Ries, M.; Maus, S.; Rosar, F.; Bohnenberger, H.; Stemler, T.; Saar, M.; Bartholoma, M.; Ezziddin, S. (225)Ac-PSMA-617/(177)Lu-PSMA-617 tandem therapy of metastatic castration-resistant prostate cancer: Pilot experience. *Eur. J. Nucl. Med. Mol. Imaging* **2020**, *47*, 721–728. [\[CrossRef\]](#) [\[PubMed\]](#)

- 
149. Hammer, S.; Hagemann, U.B.; Zitzmann-Kolbe, S.; Larsen, A.; Ellingsen, C.; Geraudie, S.; Grant, D.; Indrevoll, B.; Smeets, R.; von Ahsen, O.; et al. Preclinical Efficacy of a PSMA-Targeted Thorium-227 Conjugate (PSMA-TTC), a Targeted Alpha Therapy for Prostate Cancer. *Clin. Cancer Res.* **2020**, *26*, 1985–1996. [[CrossRef](#)]



## Research Paper

## Osteoblasts derived from mouse mandible enhance tumor growth of prostate cancer more than osteoblasts derived from long bone

Matthew R. Eber<sup>a</sup>, Sun H. Park<sup>a</sup>, Kelly F. Contino<sup>a</sup>, Chirayu M. Patel<sup>a</sup>, Fang-Chi Hsu<sup>b</sup>, Yusuke Shiozawa<sup>a,\*</sup><sup>a</sup> Department of Cancer Biology and Wake Forest Baptist Comprehensive Cancer Center, Wake Forest University Health Sciences, Winston-Salem, NC 27157, USA<sup>b</sup> Department of Biostatistics and Data Science and Wake Forest Baptist Comprehensive Cancer Center, Wake Forest University Health Sciences, Winston-Salem, NC 27157, USA

## ARTICLE INFO

## Article history:

Received 6 May 2020

Revised 12 December 2020

Accepted 14 December 2020

Available online 30 December 2020

## Keywords:

Prostate cancer

Osteoblasts

Mandible osteoblasts

Hind limb osteoblasts

Bone metastasis

Tumor cell proliferation

## ABSTRACT

Prostate cancer (PCa) metastasizes to bone, where the bone marrow microenvironment controls disease progression. However, the cellular interactions that result in active bone marrow metastases are poorly understood. A better understanding of these interactions is critical to success in the pursuit of effective treatments for this life ending disease. Anecdotally, we observe that after intracardiac injection of PCa cells, one of the greatest tools to investigate the mechanisms of bone-metastatic disease, animals frequently present with mandible metastasis before hind limb metastasis. Therefore, in this study, we investigated whether the bone cells derived from the mouse mandible influence PCa progression differently than those from the hind limb. Interestingly, we found that osteoblasts harvested from mouse mandibles grew faster, expressed more vascular endothelial growth factor (VEGF), increased vascularity and formed more bone, and stimulated faster growth of PCa cells when cultured together than osteoblasts harvested from mouse hind limbs. Additionally, these findings were confirmed *in vivo* when mouse mandible osteoblasts were co-implanted into mice with PCa cells. Importantly, the enhancement of PCa growth mediated by mandible osteoblasts was not shown to be due to their differentiation or proliferation activities, but may be partly due to increased vascularization and expression of VEGF.

© 2020 The Author(s). Published by Elsevier GmbH. This is an open access article under the CC BY-NC-ND license (<http://creativecommons.org/licenses/by-nc-nd/4.0/>).

## 1. Introduction

Prostate cancer (PCa) is deadly when it metastasizes to bone, often years after a patient is cured of the primary disease. These metastases are believed to originate from disseminated tumor cells (DTCs) shed from the primary tumor that made their way to the bone marrow and became dormant. Once in the bone marrow, progression of dormant DTCs in the bone is directed by influences from the bone marrow microenvironment. Still, a full understanding of the more complex interactions that result in active bone marrow metastases remains elusive. Our group recently discovered that early in the metastatic process, PCa cells target and commandeer the hematopoietic stem cell (HSC) specific marrow microenvironment, or HSC niche, using mechanisms similar to those involved in HSC homing to bone [1]. Osteoblasts are a major component of the HSC niche and have been shown to participate in the regulation of HSC homing and quiescence (or dormancy) [2–5]. Interestingly, DTCs also utilize osteoblasts to establish early colonization within the marrow [1,6]. Thereafter, the DTCs lie dormant

within the osteoblastic niche until they begin to proliferate again, controlled by mechanisms still poorly understood, and eventually develop into full-blown metastases [7].

A tool frequently used to investigate the mechanisms of metastasis is the intracardiac injection mouse model. After a small volume of cancer cells is inoculated into the left ventricle of the mouse heart, the circulatory system becomes flooded with cancer cells that eventually colonize organs of preference, such as bone. As expected, this model consistently results in long bone metastases, including lesions in the femur and tibia. However, mandible metastases are also frequently observed in this model [8]. This appears to be a phenomenon unique to this model, as metastasis to the human mandible is uncommon for solid tumors known to metastasize to the bone, such as PCa [9]. Anecdotally, using this model we have found that sometimes the only site of metastasis is the mandible, and that in animals with multiple bone metastatic lesions, many demonstrate faster growth in the mandible than those in the hind limbs of the same animal (unpublished observations). These findings raise the question whether the bone marrow microenvironment of the mandible stimulates the growth of DTCs more than that of the hind limbs. One difference between bone cells derived from mandible and long bones that has been documented is their proliferative and differentiation potential. Indeed,

\* Corresponding author at: Department of Cancer Biology, Wake Forest University Health Sciences, Medical Center Blvd., Winston-Salem, NC 27157-1082, USA.

E-mail address: [yshiozaw@wakehealth.edu](mailto:yshiozaw@wakehealth.edu) (Y. Shiozawa).

osteoblasts derived from rat mandible bone marrow grew faster and formed more bone *in vivo* than those differentiated from long bone marrow [10]. The same effects were seen in human tissue cultures of mandible and iliac marrow derived osteoblasts [11]. Interestingly, it has recently been revealed that different subpopulations of osteoblasts contribute differently to bone metastatic progression [12]. Therefore, we hypothesized that osteoblasts harvested from mouse mandible bones would enhance the growth of PCa cells when they interact with each other, more than those harvested from hind limb bones.

In this study, we found that osteoblasts harvested from mouse mandible bones grew faster than those harvested from hind limb bones, similar to the reports of osteoblasts derived from rat and human tissues. Additionally, osteoblasts harvested from mouse mandibles expressed higher levels of vascular endothelial growth factor (VEGF). Moreover, when these osteoblasts were co-cultured with PCa cells, osteoblasts harvested from mouse mandibles significantly increased the growth of PCa cells compared to osteoblasts harvested from hind limbs. Most importantly, these findings were confirmed *in vivo*, and immunofluorescent staining of pathological specimens revealed that vascularity of mandible osteoblast implants was greater than hind limb osteoblast implants.

## 2. Materials and methods

### 2.1. Cell culture

Human PCa cell line PC-3 [American Type Culture Collection (ATCC), Manassas, VA, Cat #: CRL-1435] and DU145 cells (ATCC, Cat #: HTB-81) were transformed to stably express green fluorescent protein (GFP) and firefly luciferase (PC3-GFP-luc, and DU145-GFP-luc) by transduction with a lentivirus (Lenti-GF1-CMV-VSVG) generated by the University of Michigan Vector Core. The transduced cells were sorted for GFP positive cells at the Wake Forest Baptist Comprehensive Cancer Center Flow Cytometry Shared Resource using an Astrios EQ (Beckman Coulter, Pasadena, CA), expanded and frozen at low passage (<10). The growth media for PC-3 and DU145 was RPMI 1640 (Gibco, Gaithersburg, MD, Cat #: 11875093) supplemented with 10% FBS (Sigma-Aldrich, St. Louis, MO, Cat #: F2442), 1% Penicillin-Streptomycin (Gibco, Cat #: 15140122), and 1% L-Glutamine (Gibco, Cat #: 25030081). Murine calvarial pre-osteoblast cell line MC3T3-E1 Subclone 4 (ATCC, Cat #: CRL-2593) were cultured with MEM $\alpha$  without nucleosides (Gibco, Cat #: 12561056) supplemented with 10% FBS, 1% Penicillin-Streptomycin, and 1% L-Glutamine. Before supplementation, this formulation of MEM $\alpha$  already contains 50 mg/L Ascorbic Acid, and therefore no additional Ascorbic Acid was required. Cells were incubated at 37°C, 5% CO<sub>2</sub>, and 100% humidity and were routinely passaged when no more than 80% confluent.

### 2.2. Animal care and use certification

All animal studies were approved by the Institutional Animal Care and Use Committee (Protocol A18-036) at Wake Forest University Health Sciences.

### 2.3. Intracardiac PCa inoculation and imaging of tumor growth

DU145-GFP-Luc ( $1 \times 10^6$  cells/100  $\mu$ L of PBS) cells were injected into immunocompromised Athymic Nude mice (Charles River Laboratories, Wilmington, MA, Cat #: 490) by left ventricular intracardiac injection, as previously described [13]. To monitor cancer growth, luciferase signal was followed at least once a week for

10 weeks using the IVIS Lumina Series III system and Living Image software (Xenogen, Alameda, CA).

### 2.4. Primary murine osteoblast culture

Hind limbs and mandibles were dissected from 5-week old male C57BL6/J mice (The Jackson Laboratory, Bar Harbor, ME, Cat #: 000664). Epiphyses from the femurs and tibias were cut and the marrow was removed by centrifugation, as previously described [14]. Briefly, an 18g hole was bored into the bottom of a 0.6 mL microcentrifuge tube with a needle, and then the tube was placed in a 1.7 mL microcentrifuge tube. The diaphyses of the bones were placed in the smaller tube, and the apparatus was then centrifuged at max speed for 30 sec. Afterward, the bone fragments remained in the upper 0.6 mL tube, and the marrow was pelleted in the bottom 1.7 mL tube. The empty diaphyses were placed into a 10 cm dish in HBSS, no calcium, no magnesium, no phenol red (Gibco, Cat #: 14175095) supplemented with 1% Penicillin-Streptomycin and minced into smaller pieces using a scalpel. The molars, incisors and dental pulp of the mandibles were removed and the remaining pieces (ascending ramus containing the coronoid, condylar and angular processes) were placed into a 10 cm dish in HBSS supplemented with 1% Penicillin-Streptomycin and minced into smaller pieces using a scalpel. After forceful washing to remove all marrow, a 10 min Trypsin-EDTA digestion was performed on the bone and mandible pieces at 37°C. Complete MEM $\alpha$  [MEM $\alpha$  without nucleosides supplemented with 10% FBS, 1% Penicillin-Streptomycin, 1% L-Glutamine, and 10nM dexamethasone (Sigma-Aldrich, Cat #: D4902) [15]] was then added to the explant cultures and the mature bone cells were allowed to migrate out of the bone and mandible pieces and expand for two weeks. In some cases, the cells were grown in bone mineralization medium (BMM) to induce further osteoblastic differentiation and mineral deposition: this media is complete MEM $\alpha$  supplemented with 0.5mM L-Ascorbic acid (Sigma, Cat #: A5960), 2mM  $\beta$ -Glycerophosphate disodium salt hydrate (Sigma-Aldrich, Cat #: G9422), and 10mM HEPES (Thermo Fisher Scientific, Hampton, NH, Cat #: BP299). The control media for BMM is complete MEM $\alpha$  supplemented with 10mM HEPES (vehicle).

### 2.5. MTT assay

Cells were seeded at a density of  $4 \times 10^3$  cells/100  $\mu$ L complete MEM $\alpha$  into each well of a 96-well plate and incubated for 1, 3, and 5 days. To measure relative cell numbers, 500  $\mu$ g/mL MTT (Tocris Bioscience, Minneapolis, MN, Cat #: 5224) was added to each well and incubated for 4 h. The reaction was halted, and the formazan precipitate was dissolved by the addition of an equal volume of 10% SDS in 0.01 M HCl (10 g/100 mL). The plate was incubated at 37°C, 5% CO<sub>2</sub>, and 100% humidity overnight and read on a plate reader at 560 nm with a background measurement at 650 nm.

### 2.6. In vitro mineralization assay

Cells were seeded at a density of  $1 \times 10^5$  cells/250  $\mu$ L complete MEM $\alpha$  into each well of a 24-well plate and incubated for 24 h. The complete MEM $\alpha$  was then replaced with 500  $\mu$ L fresh complete MEM $\alpha$  and the plate was incubated for 48 h. The media was replaced with vehicle or BMM and incubated for 72 h. This process was continued every other day for a total of 14 days from first treatment. Half of the wells were harvested for mRNA. The remaining wells were stained with Alizarin Red S (ARS) to quantify total mineralization. Briefly, cells were fixed with 10% neutral buffered formalin for 5 min at room temperature and then stained with 2% ARS (Sigma-Aldrich, Cat #: A5533-25G) at pH 4.1 in water (2 g/100 mL) for 30 min at room temperature. Excess stain was

washed out in running tap water until the water ran clear. Representative images were captured on an EVOS inverted microscope (Thermo Fisher Scientific). Stain from each wells was quantified after lysing entire contents as described elsewhere using an acetic acid extraction method and plate reader absorbance at 405 nm [16].

## 2.7. Real Time qPCR

Confluent and multilayered osteoblastic cells were lysed, and RNA was harvested using the RNeasy Plus Mini Kit (Qiagen, Germantown, MD, Cat#: 74134). The RNA concentrations were determined and subsequently normalized between samples prior to cDNA generation using Invitrogen SuperScript II Reverse Transcriptase (Invitrogen, Carlsbad, CA, Cat#: 18064022). Real time qPCR was performed using TaqMan Gene Expression Master Mix (Applied Biosystems, Foster City, CA Cat#: 4369016) and Taqman Gene Expression Assays [Applied Biosystems, Cat#: 4331182, Assay IDs: Mm03413826\_mH (*Bglap*: Osteocalcin, OCN), Mm00436767\_m1 (*Spp1*: Osteopontin, OPN), Mm00437306\_m1 (*Vegfa*: vascular endothelial growth factor, VEGF), Mm00441906\_m1 (*Tnfrsf11*: RANKL), Mm00435454\_m1 (*Tnfrsf11b*: Osteoprotegerin, OPG), Hs00921372\_m1 (*TNFRSF1*: RANK), Hs02786624\_g1 (*GAPDH*), and Mm99999915\_g1 (*Gapdh*)] on the Bio-Rad CFX Connect instrument (Hercules, CA). Data is presented as relative gene expression using the delta-delta Ct method, with *Gapdh* used as the reference gene.

## 2.8. Co-culture assay

Primary cells, or MC3T3-E1 cells, were seeded at a density of  $2 \times 10^4$  cells/100  $\mu$ L complete MEM $\alpha$  into each well of a 96-well plate and incubated for 24 h. In some cases, cells were growth arrested for 2.5 h with 10  $\mu$ g/mL mitomycin-C (Sigma-Aldrich, Cat #: 10107409001). Thereafter, cancer cells were seeded on top of the bone cells or by themselves in new 96-well plates, at a density of  $2 \times 10^3$  cells/100  $\mu$ L complete MEM $\alpha$ . Plates were incubated for 48 h and the media replaced with vehicle or BMM, and incubated for 1, 3, and 5 days, with media replacement at each time point. To monitor cancer growth in real time, luciferase signal was checked before each media replacement using the IVIS system, after addition of 200 $\mu$ g/mL D-Luciferin (PerkinElmer, Waltham, MA, Cat #:122799) and 10 min incubation at 37°C.

## 2.9. Ossicle implantation

$1 \times 10^5$  DU145-GFP-luc and/or  $1 \times 10^6$  primary cells [mandible osteoblasts (MaOBs) or hind limb osteoblasts (HLOBs)] were suspended in 10  $\mu$ L BMM in individual microcentrifuge tubes (inoculum tube) and stored on ice until implantation. Under sterile conditions, absorbable gelatin sponges (Ethicon, Somerville, NJ, Cat #: 1973) were cut into small cubes ( $\sim 5$  mm<sup>3</sup>) and placed in a petri dish containing BMM on ice until implantation. Mice were anesthetized, backs shaved if necessary, and the surgical site was prepared using betadine. Blunt tipped scissors were used to create a small incision ( $\sim 1$ cm) in the dorsal skin parallel to the spine, and the scissors were used to create subcutaneous pouches on both sides of the incision. Using fine tipped forceps, a sponge piece was removed from the petri dish, excess liquid was blotted using sterile gauze, and then seeded by placing it in the bottom of an inoculum tube and allowing it to absorb the entire inoculum. The seeded sponge was then implanted into one of the subcutaneous pouches. Each animal received an implant seeded with HLOBs in one pouch and an implant with MaOBs in the opposite pouch. The incision was closed with surgical staples, which were removed after 7 days. Animals implanted with tumor seeded cells were

athymic nude mice and animals implanted with only primary cells were C57BL6/J (male, 5 weeks old). In order to monitor cancer growth in co-culture seeded ossicles *in vivo*, luciferase signal was followed at least once a week for 20 weeks using the IVIS system, whereas primary cell only seeded ossicles were grown for 7 weeks *in vivo*.

## 2.10. Tissue processing

After euthanasia, the implants were dissected and placed in 10% neutral buffered formalin for 24 h at 4°C under agitation. They were then radiographed using the MultiFocus 10x15 Digital Radiography System (Faxitron Bioptics, Tucson, AZ). Radiographs were analyzed using ImageJ software (NIH, Bethesda, MD) for densitometry. Briefly, tissue was outlined using the freehand tool and Max Gray values were determined for each implant. Next, the implants were placed in cassettes and decalcified for 14 days in 10% ethylenediaminetetraacetic acid (EDTA), with fresh solutions replaced on day 7. The tissues were then cryopreserved in 30% sucrose for 48 h. They were halved with a razor blade and one half of each tissue was arranged in plastic molds containing optimal cutting temperature (OCT) media and frozen on dry ice. Using a cryostat, 10 and 20  $\mu$ m sections were made and stored at -80°C. The other tissue halves were processed for paraffin embedding and sectioned on a microtome at 5  $\mu$ m sections. Hematoxylin and Eosin (H&E) staining was performed on sections, as well as immunohistochemistry (IHC) for Ki67 (Abcam, Cambridge, MA, Cat#: ab16667), and immunofluorescence (IF) for Osteocalcin (Takara Bio USA, Mountain View, CA, Cat#: M173), Pancytokeratin (Novus Biologicals, Centennial, CO, Cat #: NB600-579SS), Endomucin (Santa Cruz Biotechnology, Dallas, TX, Cat#: sc-65496), VEGF (Santa Cruz Biotechnology, Cat#: sc-7269), and CD31 (R&D Systems, Minneapolis, MN, Cat #: AF3628) as previously described [17]. Antigen retrieval was performed using Biogenex DeCal Retrieval Solution (Biogenex, San Ramon, CA, Cat#: HK089-5K) before incubating with the primary antibody at a concentration of 1:500 overnight at 4°C. Sections were then labeled with secondary rabbit antibody (Biogenex, Cat#: HK336-5R), Vectastain Elite ABC HRP kit (Vector, Burlingame, CA, Cat#: PK-6100) and DAB Peroxidase (HRP) Substrate Kit (Vector, Cat#: SK-4100). Slides were mounted in permanent mounting media and scanned on a NanoZoomer slide scanner (Hamamatsu, Japan) at 40x magnification. Quantitative analysis was performed using Visiopharm software (Westminster, CO) and an APP designed to automatically count DAB and hematoxylin alone positive nuclei, as well as determine tissue section area on the entire slide.

## 2.11. Statistical analysis

Metastatic tumor growth was measured by bioluminescent imaging (BLI), and radiance values were log transformed in order to satisfy the conditional normality assumption. The mean and standard error of the mean (SEM) of log transformed radiance values were calculated by time and location of metastatic lesions (mandible vs. hind limb). For exploratory purposes, comparisons of log transformed radiance values between locations at each time point were performed using the paired Student's t-tests. Mean differences in log transformed radiance between locations were also estimated using the mixed effects model with time, location, and interaction between time and location included in the model. The advantage of using this model was that all data were analyzed simultaneously, resulting in more efficient estimates. The hypothesis test for location effect at each time point was performed using a contrast. The nested (location within each mouse) random intercepts were used to take into account the correlated structure (e.g., repeated measures over time; measures at different locations in



the same mouse). Sub-analysis of the same data was performed to compare metastasis-free survivals, as measured with a 75% signal cut off. Event time was defined as the time from the beginning of the study to the initial endpoint ( $\geq$  the 75<sup>th</sup> percentile of log transformed radiance) and censoring time as the time from the beginning of the study to the last assessment or death. The Kaplan-Meier survival curves for the initial endpoint by location were plotted. The comparison between the two survival curves were performed using the Cox proportional hazards model with robust sandwich estimates to take into account the correlated structure (e.g., different locations in the same mouse). The same statistical approaches were applied to analyses of tumors co-cultured with primary cells (MaOBs or HLOBs).

The distributions for the other outcome measures such as gene expression and OD were confirmed to be normal. The means and SEM of the outcome measures were calculated by tissue origin (mandible vs. hind limb) and by treatment (vehicle vs. BMM), and comparisons of the outcome measures were performed using the unpaired Student's t-test. The means and standard errors of the tissue section areas and of MaOB or HLOB ossicles were calculated and compared using the paired Student's t-test.

The comparison of log transformed average radiance between the combination of primary cells (MaOBs vs. HLOBs) and treatment (vehicle vs. BMM) at each time point was performed using the analysis of variance (ANOVA) for exploratory purpose. Mean differences in log transformed radiance between primary cells and treatments at each time point were also estimated using the mixed effects model with time, location, treatment, and two-way and three-way interactions included in the model. If higher order interactions were not statistically significant, they were removed from the model. For PC3 co-culture analyses, the interaction between primary cells and time as well as the interaction between treatment and time were included in the model. For DU145 co-culture analyses, only the interaction between primary cells and time was included in the model. The random intercept was used to handle repeated measurements over time. The hypothesis tests for primary cell effect and BMM effect at each time point were performed using contrasts. All the analyses were performed using the GraphPad Prism statistical program (GraphPad Software, San Diego, CA) and the SAS software (SAS Inc, Cary, NC) with significance at  $P \leq 0.05$ .

### 3. Results

#### 3.1. Intracardiac injection results in lesions in the mandibles before the hind limbs.

Since we have anecdotally found that mandible metastases occur faster than hind limb metastases in mice following intracardiac injection of PCa cells, we sought to examine more detailed metastatic patterns and tumor growth capacities of PCa cells in the intracardiac model. To do so, human PCa cell line DU145-GFP-luc cells were inoculated intracardially into immunocompromised athymic nude mice. When the bioluminescent imaging (BLI) signals of nude mice inoculated with DU145-GFP-luc were followed, detectable tumors in the mandibles were significantly brighter, and therefore larger in size than those in the hindlimbs at day 29, but over time signals at both sites became similar (Fig. 1A&B). Curiously, the BLI signals of the mandibles actually begin to decrease after day 29, which might be explained by tumor necrosis or hypoxic environments associated with fast-growing tumors [18]. Sub-analysis of the same data was performed to compare metastasis-free survivals, as measured with a 75% signal cut off, and the onset of metastasis in the mandible appeared to occur

sooner than the hindlimb, although not statistically significant (Fig. 1C).

#### 3.2. Cells derived from mandible and hind limb bone explants have osteoblastic characteristics.

To dissect out the differences between cells in the mandibles and hind limbs, we decided to compare the functions of osteoblasts from these two areas, since proliferation of PCa is known to be regulated in part by osteoblasts [19–21]. After cleared of soft tissue and bone marrow, bone pieces obtained from the mandibles and hind limbs (femurs and tibias) of adult C57BL6/J mice were minced (Fig. 2A) and cultured in media containing dexamethasone (10nM) to differentiate any remaining cells into osteoblasts [15]. After two weeks of culture, cells derived from the bone explants were assessed of their osteoblastic characteristics. Both cultures expressed relatively high levels of the osteoblastic markers Osteocalcin and Osteopontin (Fig. 2B&C). Basal expression of Osteocalcin and Osteopontin were both lower in the mandible cell cultures than the hind limb cultures, but the presence of both markers in vehicle-treated cells revealed that the cultured bone explant cells are mostly differentiated even without the use of differentiation supplements, unlike traditional bone marrow stromal cell culture preps (Fig. 2B&C). After treatment with known osteoblastic differentiation supplements L-Ascorbic acid and  $\beta$ -Glycerophosphate, the levels of these markers were significantly increased in both explant cultures, however cultures of mandible cells responded to L-Ascorbic acid and  $\beta$ -Glycerophosphate to a greater degree than cultures of hind limb cells (Fig. 2B&C). As vascular endothelial growth factor (VEGF) derived from osteoblasts, encoded by the mouse gene *Vegfa*, has been shown to be involved in osteoblast differentiation and mineralization [22], and VEGF is implicated in PCa migration to bone and growth through induction of angiogenesis [23], we tested whether *Vegfa* expression was increased in mandible cultures. Basal expression of *Vegfa* was higher in cultures of mandible cells than those of hind limb cells and was not significantly changed in response to L-Ascorbic acid and  $\beta$ -Glycerophosphate supplementation in either mandible or hind limb cultures (Fig. 2D). To further test osteoblastic functional capabilities, the mineralization potentials of these cells were evaluated using Alizarin Red S (ARS) staining. Both cells derived from mandible and hind limb explants were able to mineralize, as evidenced by ARS staining (Fig. 3A&B). Interestingly, cells from mandible explants showed more mineralization than cells from hind limb explants, regardless of L-Ascorbic acid and  $\beta$ -Glycerophosphate supplementation (Fig. 3B). We attribute this observation to the previous finding that differentiation supplements were not required for osteoblast marker expression in our bone explant cultures (Fig. 2B&C), and therefore, not required for mineralization either. Altogether, this suggests that the cells derived from mandible and hind limb bone explants have osteoblastic characteristics. Therefore, from here on, the cells derived from mandible and hind limb bone explants will be referred to as mandible osteoblasts (MaOBs) and hind limb osteoblasts (HLOBs), respectively.

#### 3.3. Mandible osteoblasts form more bone than hind limb osteoblasts *in vivo*

To further confirm the osteoblastic characteristics of MaOBs and HLOBs, these cells were implanted together with gelatin scaffolds (ossicles) subcutaneously into C57BL6/J mice, and the ossicles were allowed to grow *in vivo* for 7 weeks. Radiographs of the resulting ossicles revealed that the MaOB seeded ossicles had more mineralization than HLOB seeded ossicles (Fig. 4A&B). The ossicles were decalcified and cryosectioned in order to perform immunofluores-

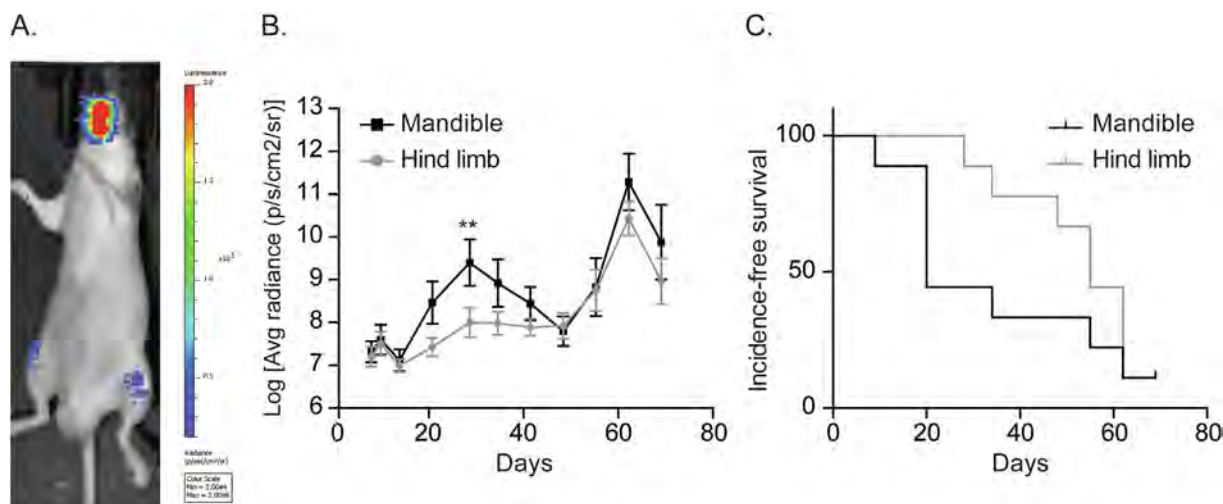


**Fig. 1.** Metastasis to mandible occurs first after intracardiac injection of PCa cells. Five-week old male nude mice were injected intracardially with  $1 \times 10^6$  DU145-GFP-luc cells ( $n=8$ ) and observed with bioluminescent imaging (BLI) for 10 weeks. (A) Representative image of a mouse at day 29 demonstrating brighter signal in the mandible than the hindlimbs. (B) All collected longitudinal BLI data after log transformation. Results displayed as Mean  $\pm$  SEM. Mixed effects model.  $p \leq 0.01$ . (C) A 75% cut-off was employed to examine metastasis-free survival (mandible vs. hind limb). Cox proportional hazards model with robust sandwich estimates.

cence for Osteocalcin, hematoxylin and eosin (H&E) staining, and immunohistochemistry for Ki67 (Fig. 4C-E). In order to test whether the cells contained in the ossicles were still osteoblasts, immunofluorescence was performed on the cryosections for Osteocalcin. It is clear that the cells located near and on bone nodules in the ossicles remained Osteocalcin positive, and substantial Osteocalcin appeared to be deposited within the bone itself (Fig. 4C). H&E staining confirmed what was seen by radiograph, as evidenced by increased frequency of woven bone nodules in the MaOB seeded ossicles (Fig. 4D). Visiopharm software was used to automatically quantify tissue section area, and Ki67 positive and negative nuclei. MaOB seeded ossicles were no larger in area than HLOB ossicles (Fig. 4F), but contained a significantly greater number of total and proliferating cells, as evidenced by Ki67 nuclear positivity (Fig. 4G&H).

A possible explanation for the increased proliferation of MaOB cells *in vivo* could be increased vascularity of the MaOB ossicles due to higher levels of VEGF. Interestingly, we did observe greater immunostaining for the endothelial cell markers Endomucin and CD31 in the tissue surrounding and within the implants seeded with MaOBs, when compared to those seeded with HLOBs (Fig. 5A). Still, vascularity of all the implants appeared somewhat scarce and could explain why relative levels of bone formation in the implants appeared lower than other models which use bone marrow stromal cells as the inoculum for ossicle models of bone formation [15]. We also performed immunofluorescence for VEGF using ossicle cryosections as we found differential expression of *Vegfa* in our cell cultures *in vitro* (Fig. 2D). Strangely, we did not see VEGF staining in Osteocalcin positive MaOBs within the implants. However, we did detect VEGF near Osteocalcin positive MaOBs (Fig. 5B), but not HLOBs (data not shown). These results suggest that MaOBs seeded in ossicles may secrete VEGF to the tissues surrounding the implant.

#### 3.4. Mandible osteoblasts support prostate cancer growth more than hind limb osteoblasts *in vitro* and *in vivo*

Our next attempt was then to determine whether there are differential effects between MaOBs and HLOBs on PCa growth. To address this question, human PCa cell lines PC3-GFP-luc and DU145-GFP-luc cells were seeded on top of MaOB or HLOB cells. After 3–5 days of co-culture, more PCa cells were observed on

MaOBs than HLOBs using BLI (Fig. 6A&B). However, L-Ascorbic acid and  $\beta$ -Glycerophosphate supplement failed to induce further tumor proliferation (Fig. 6A&B), suggesting that osteoblastic mineralization was not the major cause of greater PCa proliferation mediated by MaOBs. Then, the changes in the relative amounts of viable cells during *in vitro* culture between MaOBs and HLOBs were compared. As previously reported in rat and human bones [10,11], the cultures containing MaOBs had more viable cells compared to those containing HLOBs (Fig. 6C), suggesting that MaOBs grew significantly faster than HLOBs. However, when mitomycin-C growth arrested MC3T3-E1 cells were cocultured using the same methods, PCa cells actually grew faster on top of growth arrested osteoblasts (Fig. 6D&E). These data suggest that the differences between PCa growth in culture with MaOBs vs. HLOBs are not likely due to baseline differences in mineralization or proliferation.

Next, DU145-GFP-luc cells were co-implanted with either MaOB or HLOB ossicles subcutaneously into athymic nude mice. Similar to what was seen *in vitro*, the growth of DU145-GFP-luc cells co-implanted with MaOB ossicles, as evidenced by significantly brighter BLI signals on the last five measurements, appeared to be greater than those co-implanted with HLOB ossicles (Fig. 7A&B). These results were significantly different despite the fact that one mouse had a much smaller MaOB co-implant tumor than the other four mice (Fig. 8A). With such a limited group size, this tumor cannot be considered an outlier, but it is the reason why the differences observed in the longitudinal data also seem limited (Fig. 7A&B). Sub-analysis of the same data was performed to compare incidence-free survivals, as measured with a 75% signal cut off, and tumors in the MaOB ossicles occurred significantly sooner than in the HLOB ossicles (Fig. 7C). These differences were consistent with *ex vivo* BLI analyses performed on the dissected tumors which again showed significantly brighter signal in the MaOB ossicles (Fig. 7D). As before, radiographs revealed that the MaOB seeded ossicles had more calcification than HLOB seeded ossicles (Fig. 8A&B). In order to test the composition of the cells contained in the co-implanted ossicles, immunofluorescence for pancytokeratin was performed on the cryosections of decalcified ossicles. Clearly, the implants with both MaOBs and HLOBs at 20 weeks contained PCa tumor cells (Fig. 8C). H&E staining and immunohistochemistry for Ki67 were also performed on the co-implanted ossicles to further determine their morphology and cell proliferation status (Fig. 8D&E). Visiopharm software was used to auto-

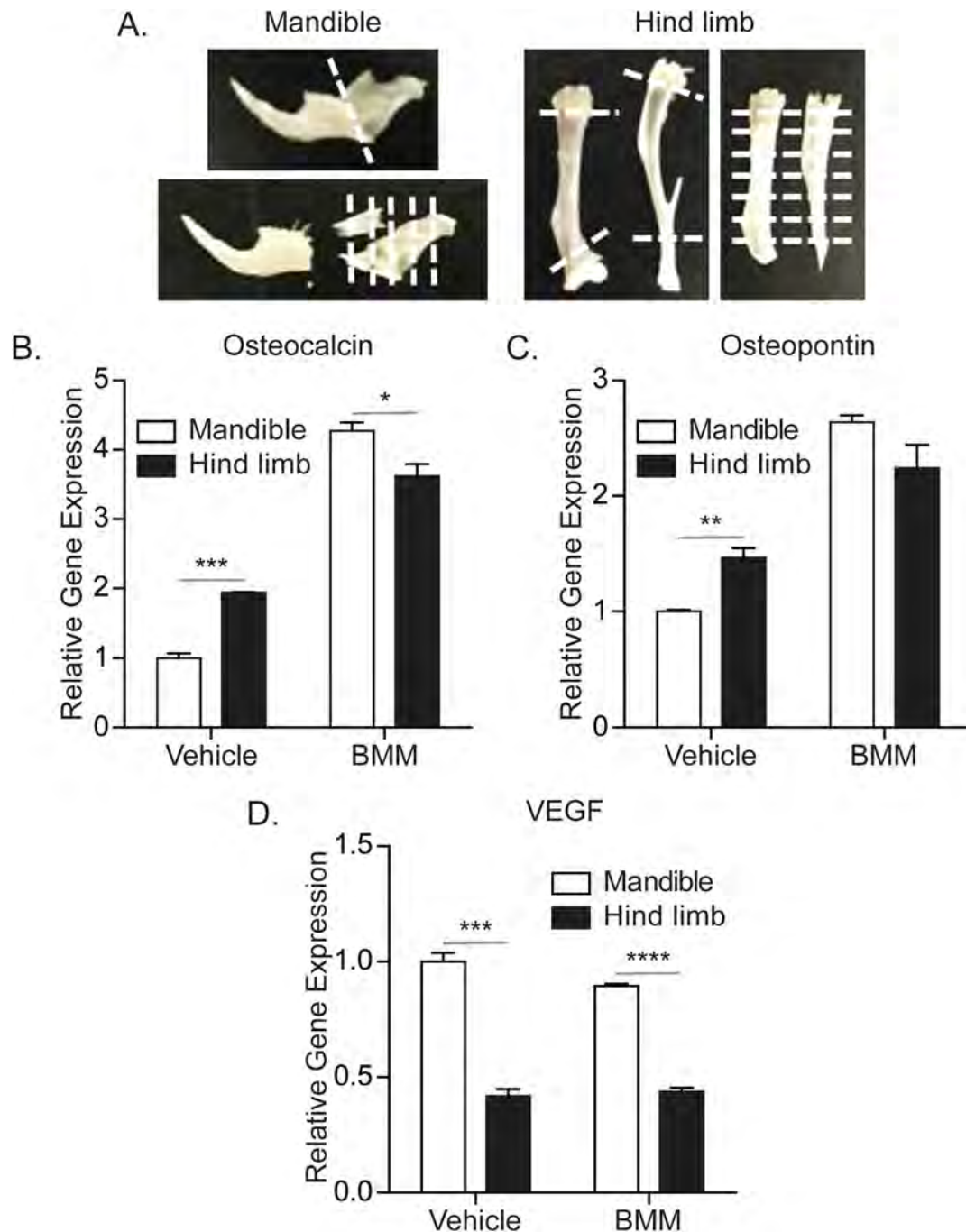


**Fig. 2.** Cells harvested from mandible and hind limb bones express osteoblast markers. Five-week old male C57BL/6J mice were euthanized, and mandibles and hind limbs were harvested. Mandible and hind limb cells were cultured with bone mineralization medium (BMM) (0.5mM L-Ascorbic acid, 2mM  $\beta$ -Glycerophosphate disodium salt hydrate, and 10mM HEPES) or vehicle (10mM HEPES) for 10 days. (A) Schematic of bone culture preparation: molars, incisors and dental pulp of the mandibles were removed and discarded; epiphyses from the femurs and tibias were cut and the marrow was removed by centrifugation; remaining pieces of the mandibles and femurs/tibias were minced into smaller pieces, digested with trypsin, and cultured and expanded for two weeks before experiments. (B) Relative gene expression of Osteocalcin (Bglap), normalized to vehicle treated mandible cell cultures. (C) Relative gene expression of Osteopontin (Spp1), normalized to vehicle treated mandible cell cultures. (D) Relative gene expression of vascular endothelial growth factor (VEGF), normalized to vehicle treated mandible cell cultures. Gapdh was used as reference gene. Delta-delta Ct method. Results displayed as Mean  $\pm$  SEM. Unpaired Student's *t*-test. \* $p \leq 0.05$ , \*\* $p \leq 0.01$ , \*\*\* $p \leq 0.001$ , \*\*\*\* $p \leq 0.0001$ .

matically quantify tissue section area, and Ki67 positive and negative nuclei. MaOB seeded ossicles appeared larger in area than HLOB ossicles, although not quite significant (Fig. 8F), but contained a significantly greater number of total and proliferating cells, as evidenced by Ki67 nuclear positivity (Fig. 8G&H).

#### 4. Discussion

In this study, we first demonstrated that in the intracardiac model of metastatic PCa, mandible bone lesions often occur before hind limb bone lesions, which is anecdotally well-recognized. We



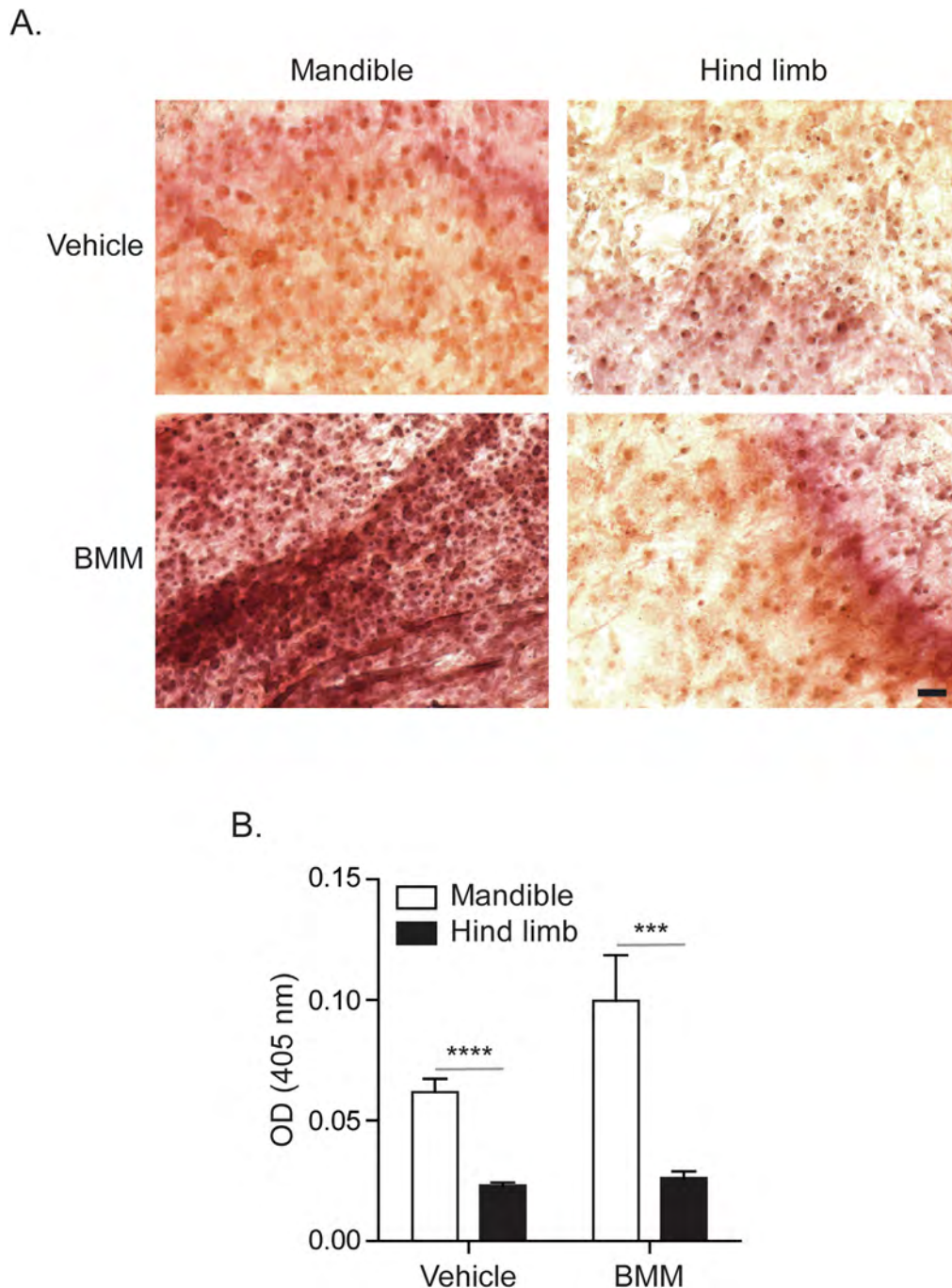


**Fig. 3.** Cells harvested from mandibles mineralize more than those from hind limbs. Mandible and hind limb cells were cultured with bone mineralization medium (BMM) (0.5mM L-Ascorbic acid, 2mM  $\beta$ -Glycerophosphate disodium salt hydrate, and 10mM HEPES) or vehicle (10mM HEPES) for 14 days. Cells were stained with 2% Alizarin Red S. (A) Representative Alizarin Red S image. Magnification 10x. Bar = 50  $\mu$ m. (B) Residual stain from whole plates were extracted with acetic acid and read at 405 nm on a plate reader. Results displayed as Mean  $\pm$  SEM. Unpaired Student's *t*-test. \*\*\**p*  $\leq$  0.001, \*\*\*\**p*  $\leq$  0.0001.

showed that cells derived from both the mandible and hind limb bones of mice have osteoblastic properties, and that MaOBs have a higher potential for osteoblastic differentiation than HLOBs both *in vitro* and *in vivo*. Interestingly, when PCa cells were co-cultured with these osteoblasts, PCa cells grew significantly faster in co-culture with MaOBs compared to HLOBs. Consistently, PCa cells co-implanted with MaOBs into animals grew faster and larger tumors than those co-implanted with HLOBs. Altogether, the data suggest that these differences may not be due to differences in mineralization status, as L-Ascorbic acid and  $\beta$ -Glycerophosphate supplementation failed to increase PCa growth *in vitro*, nor differ-

ences in osteoblast proliferation, as mitomycin-C growth arrest of osteoblasts actually increased PCa growth *in vitro*. However, the observations that MaOBs vascularize more *in vivo* and express significantly higher levels of *Vegfa* *in vitro* may be clues to a possible mechanism, although careful mechanistic studies must be performed in order to investigate this further.

The idea that there are different subpopulations of osteoblasts that exhibit different functions in the bone microenvironment has been discussed. For example, while mature osteoblasts form mineral deposits by differentiating osteocytes in healthy bone during homeostasis [24], immature osteoblasts are involved in the

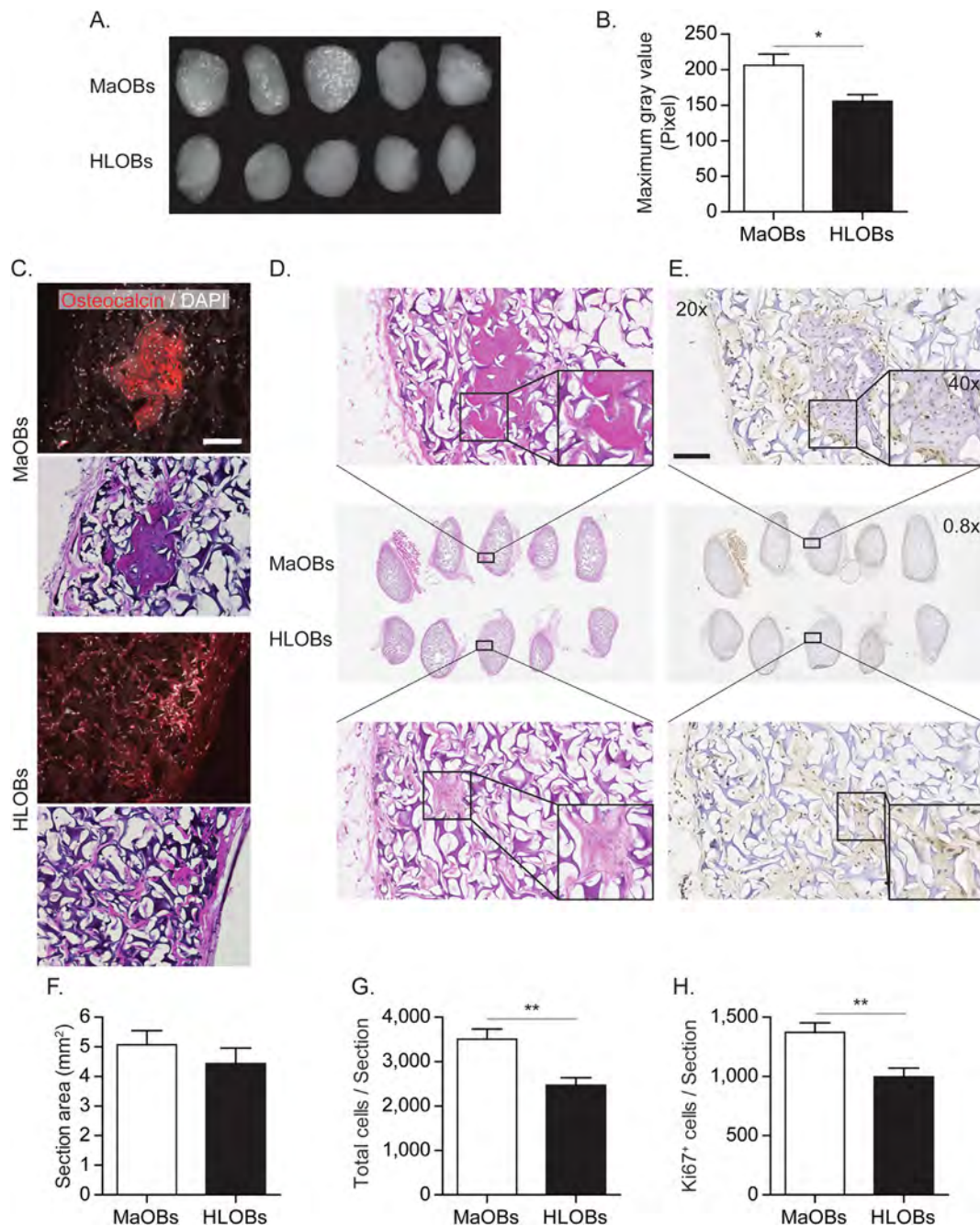


**Fig. 4.** Cells harvested from mandibles are more proliferative and form more bone than from hind limbs.  $1 \times 10^6$  primary cells (MaOBs or HLOBs) were seeded onto absorbable gelatin sponges and implanted into subcutaneous pouches of 5-week old male C57BL/6J mice ( $n=5$ ) and grown for 7 weeks *in vivo*. (A) After euthanasia, implants were dissected, fixed, and radiographed. (B) Densitometry quantification using ImageJ of (A). (C) Representative osteocalcin immunofluorescence and H&E image of (A). DAPI was used for nuclear staining. Magnification 20x. Bar = 100  $\mu$ m. (D) Representative H&E image of (A). Bar = 100  $\mu$ m. (E) Representative Ki67 immunohistochemical image of (A). Bar = 100  $\mu$ m. (F-H) Automated quantification using Visiopharm software of (F) tissue section area, (G) total cells per tissue section, and (H) Ki67 nuclear positive cells per tissue section. Results displayed as Mean  $\pm$  SEM. Paired Student's *t*-test. \* $p \leq 0.05$ , \*\* $p \leq 0.01$ .

process of bone resorption by activating osteoclasts through the production of receptor activator of NF- $\kappa$ B ligand (RANKL) [25,26]. In fact, when we tested relative gene expression of RANKL, we found that MaOBs express higher levels than HLOBs ( $1.00 \pm 0.023$  vs  $0.097 \pm 0.021$ ), although they also expressed higher levels of osteoprotegerin ( $1.00 \pm 0.12$  vs  $0.29 \pm 0.014$ ). Osteoprotegerin is a molecule that binds RANKL, inhibiting its ability to activate its receptor RANK on osteoclasts [27]. Similarly, intercellular adhesion molecule (ICAM)-1 positive osteoblasts, which are in G0/G1 phase of the cell cycle arrest, contributed more to osteoclastogenesis than

bone formation, by interacting with monocytes [28]. This phenomenon is also known in the process of hematopoiesis. It has been demonstrated that the activated leukocyte cell adhesion molecule (ALCAM) positive/Sca-1 negative immature osteoblasts are responsible for maintenance of long-term reconstitution activity of HSCs [29]. On the other hand, it has been suggested that the major function of mature osteoblasts is to control the maintenance of lymphoid progenitors, but not hematopoietic stem cells or myeloid progenitors [30]. Moreover, it has been recently revealed that specific subpopulations of osteoblasts influence bone



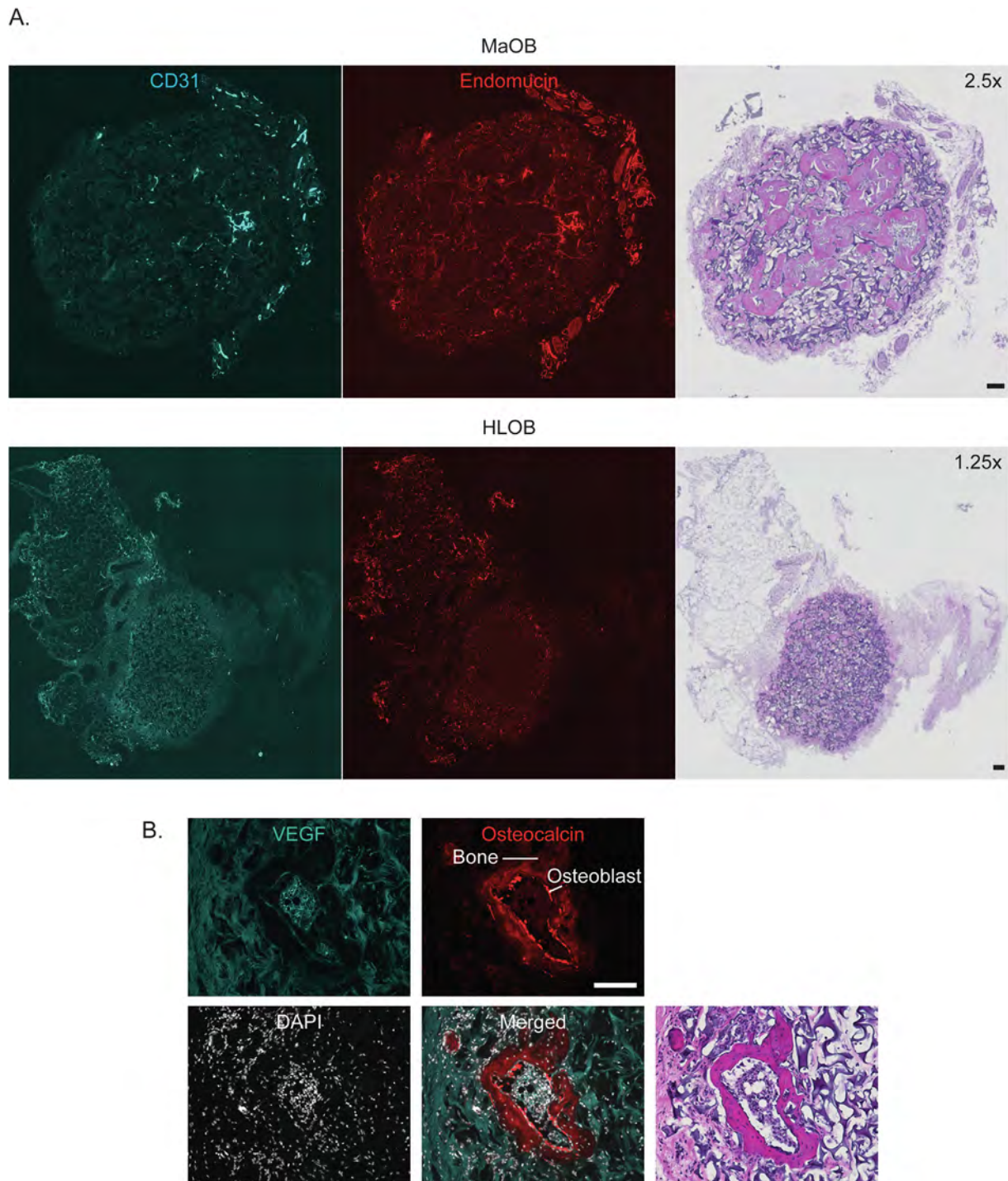


**Fig. 5.** Ossicle vascularity is mainly localized to tissue surrounding implant. Immunofluorescence was performed on cryosections from Fig. 4 to assess ossicle vascularity. (A) Representative CD31 and Endomucin staining, and H&E image. DAPI was used for nuclear staining. Magnification 10 $\times$ . Bar = 100  $\mu$ m. (B) Representative vascular endothelial growth factor (VEGF) and Osteocalcin immunofluorescence, and H&E image. DAPI was used for nuclear staining. Magnification 20 $\times$ . Bar = 100  $\mu$ m.

metastatic progression in the tumor microenvironment. Osteoblast progenitors, but not differentiated or mature osteoblasts, were shown to promote breast cancer cell migration through the release of hepatocyte growth factor (HGF), suggesting that the immature osteoblasts are involved in the early steps of the bone seeding process [31]. When osteoblasts interact with breast cancer cells, they are transformed into OPN positive/interleukin (IL)-6 negative/ $\alpha$ -smooth muscle actin (SMA) negative osteoblasts [12]. When these cancer-associated osteoblasts were co-cultured with breast cancer

cells, the growth of breast cancer cells was significantly suppressed and the expression of the cell cycle arrest marker p21 was activated [12].

To investigate the specific effect of osteoblasts on bone metastatic growth of PCa, we took a simplified approach, by focusing solely on the osteoblast component of the bone-metastatic tumor microenvironment. This is an obvious limitation of this study, as there are many cell types other than osteoblasts that exist in the marrow, and these cells are also known to contribute to tumor

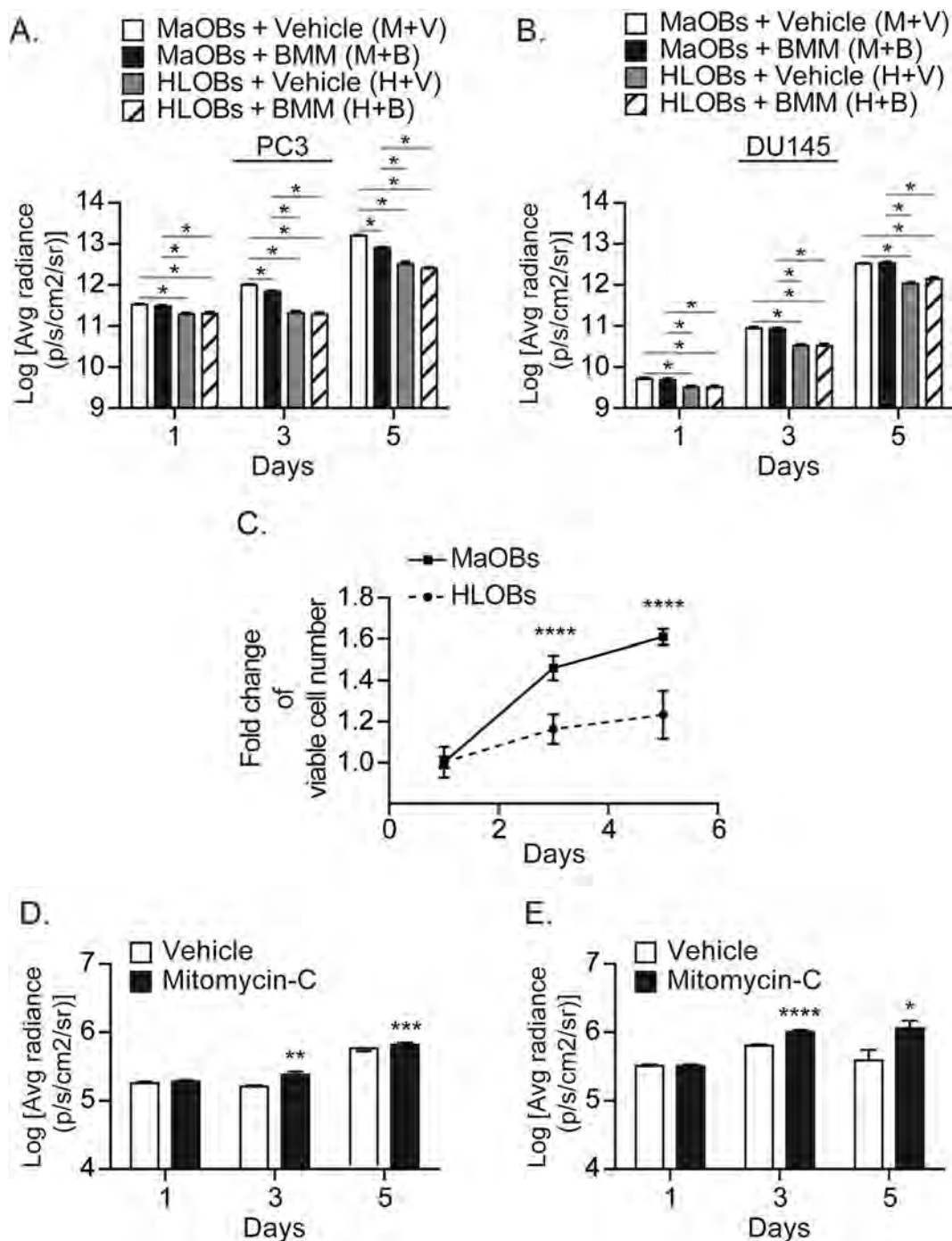


**Fig. 6.** PCa cells grow faster on osteoblasts harvested from mandibles than osteoblasts from hind limbs. (A) PC3-GFP-luc and (B) DU145-GFP-luc human prostate cancer cells were seeded on top of the primary cells (MaOBs or HLOBs) at a 1:10 ratio. Co-cultures were treated with bone mineralization medium (BMM) (0.5mM L-Ascorbic acid, 2mM  $\beta$ -Glycerophosphate disodium salt hydrate, and 10mM HEPES) or vehicle (10mM HEPES) for 5 days. Bioluminescent imaging (BLI) was measured at day 1, 3, and 5. Two-way ANOVA with Tukey's Studentized Range (HSD) Test for multiple comparisons. (C) MaOBs and HLOBs were seeded in multi-well plates and analyzed for cell proliferation after 1, 3, and 5 days of culture by MTT assay. Proliferation displayed as fold change normalized to day 1. Mixed effects models. (D) PC3-GFP-luc and (E) DU145-GFP-luc human prostate cancer cells were seeded on top of the MC3T3-E1 cells at a 1:10 ratio. To induce cell growth arrest, the MC3T3-E1 cells were pre-treated with vehicle or 10  $\mu$ g/mL mitomycin-C for 2.5 h prior to co-culture. BLI was measured at day 1, 3, and 5. Paired Student's *t*-test. Results displayed as Mean  $\pm$  SEM. \**p*  $\leq$  0.05, \*\**p*  $\leq$  0.01, \*\*\**p*  $\leq$  0.001, \*\*\*\**p*  $\leq$  0.0001.

growth, homeostasis, or dormancy [32]. Although further study is clearly needed, this may be part of the reason why osteoblasts failed to express VEGF during differentiation within the ossicles. Additionally, osteoblasts are not the only cells responsible for general bone health. We believe this is a major reason that we did not observe as robust bone formation as others have reported in their ossicle models of bone marrow stromal cell or mesenchymal stem

cell implantation [10,11]. We believe that in the absence of other stromal cells, the VEGF and other growth factors such as RANKL released by osteoblasts are less effective at promoting angiogenesis and general bone health in an implant model. For instance, osteoblast-derived VEGF has been shown to promote bone formation in a paracrine fashion (which might explain why MaOB ossicles formed more bone than HLOB ossicles in this study), but was

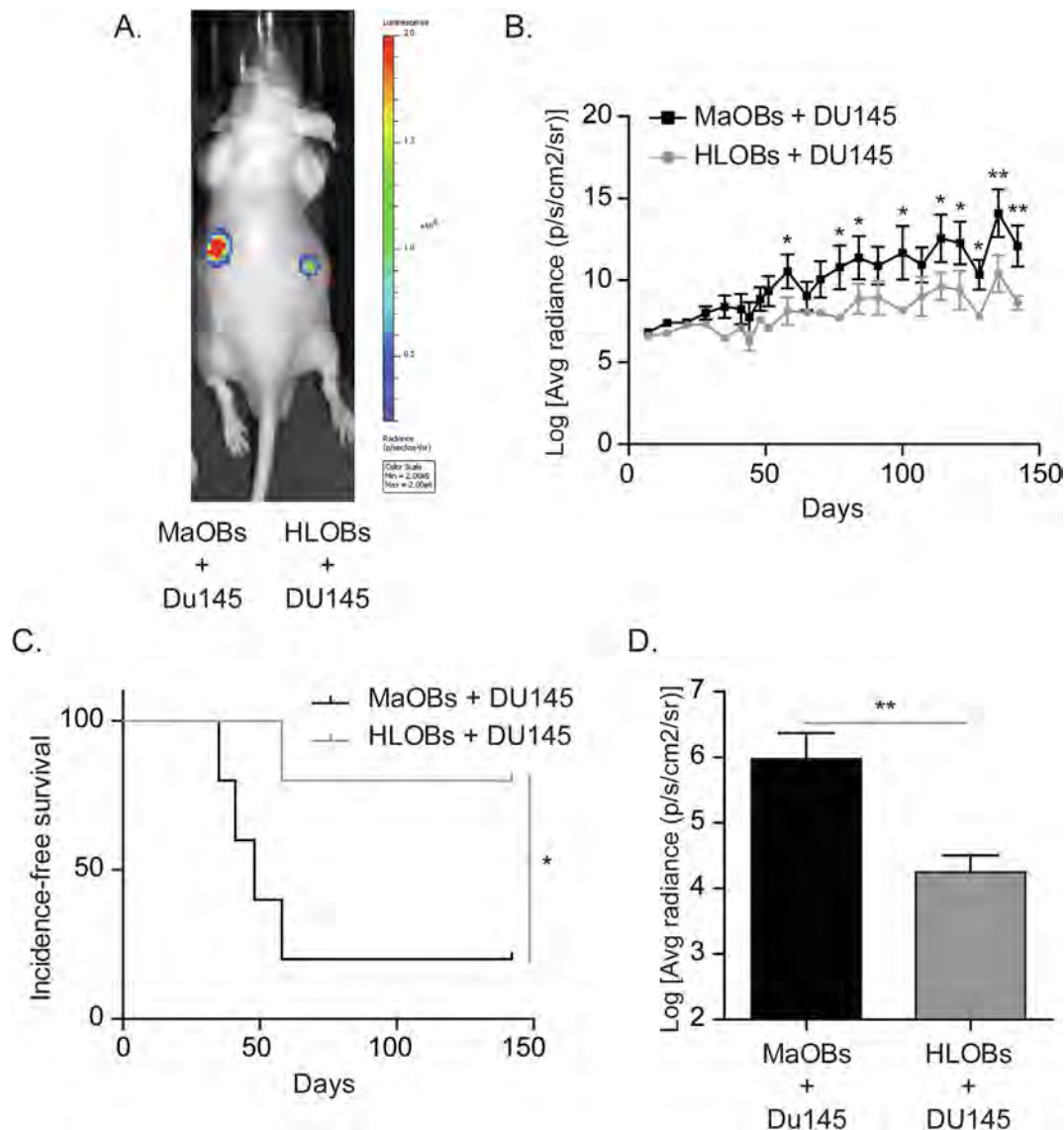


**Fig. 7.** PCA cells grow faster *in vivo* co-implanted with mandible bone cells.  $1 \times 10^6$  primary cells (MaOBs or HLOBs) were seeded onto absorbable gelatin sponges and co-implanted into subcutaneous pouches of 5-week old male athymic nude mice ( $n=5$ ) with  $1 \times 10^5$  DU145-GFP-luc cells and grown for 20 weeks *in vivo*. (A) Representative bioluminescent imaging (BLI) at 20 weeks. (B) All collected longitudinal BLI data after log transformation. Results displayed as Mean  $\pm$  SEM. Mixed effects model. (C) 75% cut-off was employed to examine incidence-free survival (MaOBs vs. HLOBs). Cox proportional hazards model with robust sandwich estimates. (D) After euthanasia, tumors were dissected and *ex vivo* BLI performed. Results displayed as Mean  $\pm$  SEM. Paired Student's *t*-test. \* $p \leq 0.05$ , \*\* $p \leq 0.01$ .

also shown to recruit endothelial cells, macrophages, and promote osteoclastogenesis [22]. Further studies to reveal the effects of not only osteoblasts, but also the stroma, endothelium, nerves, osteocytes, osteoclasts, immune cells, and hematopoietic and mesenchymal stem cells on bone and tumor physiology are clearly warranted. The strength of our study is in the *in vivo* co-implant model, which demonstrated that MaOBs contributed to faster tumor cell proliferation than HLOBs. Although the mechanisms behind these differences remain uncertain, the observation that MaOBs promoted greater vascularization *in vivo* could serve as a foundation for further studies. Another finding deserving of future studies was the increased gene expression of RANKL and OPG in MaOBs, as we were also able to detect RANK gene expression in DU145 cells ( $32.2 \pm 1.2$  mean cycle threshold; and GAPDH:  $26.3 \pm 1.1$  mean cycle threshold). This finding may help to inform future investigations into mouse mandible tumor frequency, as the question regarding possible differences in tissue seeding and tumor cell anchorage following intracardiac injection remains, and RANKL has

previously been implicated in the bone-metastatic process [33]. Altogether, we believe that these culture methods will be valuable tools in further investigating the mechanisms of tumor cell proliferation in the bone and discovering new interventions to manipulate osteoblast proliferation, activity, or growth factor signaling, which may improve the susceptibility of PCa cells to existing cytotoxic treatments, including chemotherapies.

The findings of this study can be interpreted through the lens of existing treatments used to treat bone metastatic PCa. Current established treatments for bone metastases mainly target bone remodeling, specifically resorption, but these have only had modest success so far, namely denosumab (a human monoclonal antibody against RANKL) and bisphosphonates, which suppress osteoclast activity. Osteoclasts promote bone resorption, creating sufficient space for osteolytic bone tumors to expand and grow [34]. Denosumab and bisphosphonates antagonize bone resorption and as such were hypothesized to slow tumor growth. However, both treatments ultimately fail to improve overall survival



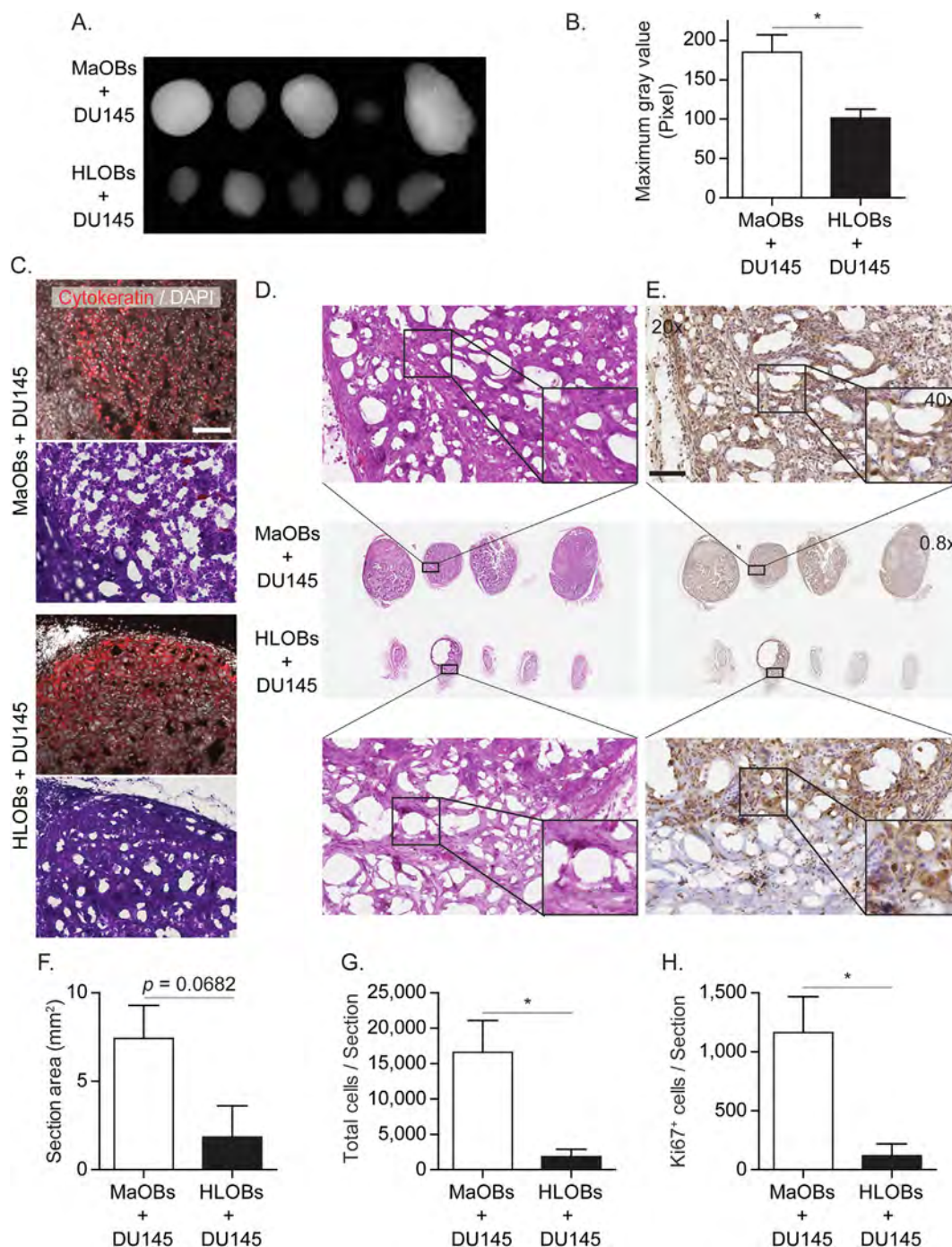


**Fig. 8.** Tumors from PCa/mandible bone cell co-cultures are more proliferative. (A) After euthanasia, tumors from Fig. 6 were dissected, fixed, and radiographed. (B) Densitometry quantification using ImageJ of (A). (C) Representative Pan-cytokeratin immunofluorescence and H&E image of (A). Magnification 20x. Bar = 100  $\mu$ m. (D) Representative H&E image of (A). Bar = 100  $\mu$ m. (E) Representative Ki67 immunohistochemical image of (A). Bar = 100  $\mu$ m. (F–H) Automated quantification using Visiopharm software of (F) tissue section area, (G) total cells per tissue section, and (H) Ki67 nuclear positive cells per tissue section. Results displayed as Mean  $\pm$  SE. Paired Student's *t*-test. \* $p \leq 0.05$ .

[35,36]. On the other hand, radium-223 ( $\text{Ra}^{223}$ ), which forms complexes with hydroxyapatite in bone [37–39], can extend overall survival in PCa patients with bone metastases [40], but only by a few months (mean = 3 months). A variety of combinations of therapies [e.g. docetaxel, second generation androgen deprivation therapies (ADTs) such as abiraterone, enzalutamide, or others] have been shown to extend overall survival of metastatic PCa patients [41]. However, when choosing an effective combination strategy for PCa bone metastases, it may be best to avoid ADTs

since they are known to negatively affect bone health [42,43]. Indeed, a recent trial of the combination of abiraterone and  $\text{Ra}^{223}$  in patients with bone-metastatic PCa not only failed to improve skeletal event-free survival, but it also increased the frequency of bone fractures compared with placebo [44]. Alternatively, the idea of inducing bone formation by enhancing osteoblastic activity as a treatment for bone metastatic disease has recently been appreciated [45,46], as inactive/immature osteoblasts can reduce PCa susceptibility to chemotherapy [47,48]. However, the results of this

study suggest that inducing osteoblastic differentiation may not be the best strategy for treating progressive bone metastatic tumors, as BMM treatments failed to increase PCa growth in co-culture models. A popular strategy to treat many cancers has been to use drugs that inhibit angiogenesis, but this strategy has been somewhat unsuccessful in the treatment of bone-metastatic PCa [49,50]. This may be in part because these inhibitors mainly target the receptor for VEGF, but not VEGF itself. Here, we see that high *Vegfa* expressing, fast growing, and bone forming MaOBs induced more tumor growth *in vivo* than HLOBs, which expressed less *Vegfa* *in vitro*, are slower growing, and form less bone *in vivo*. More studies are clearly necessary to elucidate whether osteoblast-derived VEGF, or other angiogenic factors, is required for the faster tumor growth observed in the mandibles of intracardially-injected mice, whether osteoblast-derived VEGF can be targeted to treat bone metastatic disease, and ultimately whether these findings correspond with bone metastatic PCa in humans. We believe that the models described here are valuable tools to aid in this research.

### Author contributions

Matthew R. Eber and Yusuke Shiozawa wrote the manuscript with input from all authors. Matthew R. Eber and Yusuke Shiozawa designed study and contributed to data interpretation. Matthew R. Eber, Sun H. Park, Kelly F. Contino, and Chirayu M. Patel performed *in vitro* and *in vivo* experiments. Fang-Chi Hsu performed statistical analyses. Yusuke Shiozawa supervised the study. All authors reviewed and approved the final manuscript.

### CRedit authorship contribution statement

**Matthew R. Eber:** Conceptualization, Data curation, Investigation, Methodology, Writing - original draft, Writing - review & editing. **Sun H. Park:** Data curation, Investigation, Methodology, Writing - review & editing. **Kelly F. Contino:** Data curation, Investigation, Writing - review & editing. **Chirayu M. Patel:** Data curation, Investigation, Writing - review & editing. **Fang-Chi Hsu:** Formal analysis, Methodology, Software, Writing - review & editing. **Yusuke Shiozawa:** Conceptualization, Funding acquisition, Methodology, Project administration, Resources, Supervision, Writing - original draft, Writing - review & editing.

### Declaration of Competing Interest

Yusuke Shiozawa has received research funding from TEVA Pharmaceuticals, but not relevant to this study. The remaining authors declare that they have no known competing financial interests or personal relationships that could have appeared to influence the work reported in this paper.

### Acknowledgements

This work is directly supported by the National Cancer Institute (R01-CA238888, Y.S.; R44-CA203184, Y.S.), the Department of Defense (W81XWH-14-1-0403, Y.S.; W81XWH-17-1-0541, Y.S.; W81XWH-19-1-0045, Y.S.), METAvivor (METAvivor Research Award, Y.S.), and the Wake Forest Baptist Comprehensive Cancer Center Internal Pilot Funding (Y.S.). This work is also supported by the National Cancer Institute's Cancer Center Support Grant award number P30-CA012197 issued to the Wake Forest Baptist Comprehensive Cancer Center. The authors wish to acknowledge the support of the Wake Forest Baptist Comprehensive Cancer Center Cell Engineering Shared Resource and Flow Cytometry Shared Resource, supported by the National Cancer Institute's Cancer Center Support Grant award number P30-CA012197. The content is

solely the responsibility of the authors and does not necessarily represent the official views of the National Cancer Institute.

### References

- [1] Y. Shiozawa, E.A. Pedersen, A.M. Havens, Y. Jung, A. Mishra, J. Joseph, J.K. Kim, L. R. Patel, C. Ying, A.M. Ziegler, M.J. Pienta, J. Song, J. Wang, R.D. Loberg, P.H. Krebsbach, K.J. Pienta, R.S. Taichman, Human prostate cancer metastases target the hematopoietic stem cell niche to establish footholds in mouse bone marrow, *J. Clin. Invest.* 121 (4) (2011) 1298–1312.
- [2] Y. Shiozawa, R.S. Taichman, Getting blood from bone: an emerging understanding of the role that osteoblasts play in regulating hematopoietic stem cells within their niche, *Exp. Hematol.* 40 (9) (2012) 685–694.
- [3] L.M. Calvi, G.B. Adams, K.W. Weibrecht, J.M. Weber, D.P. Olson, M.C. Knight, R. P. Martin, E. Schipani, P. Divieti, F.R. Bringhurst, L.A. Milner, H.M. Kronenberg, D.T. Scadden, Osteoblastic cells regulate the haematopoietic stem cell niche, *Nature* 425 (6960) (2003) 841–846.
- [4] F. Arai, A. Hirao, M. Ohmura, H. Sato, S. Matsuoka, K. Takubo, K. Ito, G.Y. Koh, T. Suda, Tie2/angiopoietin-1 signaling regulates hematopoietic stem cell quiescence in the bone marrow niche, *Cell* 118 (2) (2004) 149–161.
- [5] J. Zhang, C. Niu, L. Ye, H. Huang, X. He, W.G. Tong, J. Ross, J. Haug, T. Johnson, J. Q. Feng, S. Harris, L.M. Wiedemann, Y. Mishina, L. Li, Identification of the haematopoietic stem cell niche and control of the niche size, *Nature* 425 (6960) (2003) 836–841.
- [6] H. Wang, C. Yu, X. Gao, T. Welte, A.M. Muscarella, L. Tian, H. Zhao, Z. Zhao, S. Du, J. Tao, B. Lee, T.F. Westbrook, S.T. Wong, X. Jin, J.M. Rosen, C.K. Osborne, X. H. Zhang, The osteogenic niche promotes early-stage bone colonization of disseminated breast cancer cells, *Cancer Cell* 27 (2) (2015) 193–210.
- [7] Y. Shiozawa, J.E. Berry, M.R. Eber, Y. Jung, K. Yumoto, F.C. Cackowski, H.J. Yoon, P. Parsana, R. Mehra, J. Wang, S. McGee, E. Lee, S. Nagrath, K.J. Pienta, R.S. Taichman, The marrow niche controls the cancer stem cell phenotype of disseminated prostate cancer, *Oncotarget* 7 (27) (2016) 41217–41232.
- [8] F. Arguello, R.B. Baggs, C.N. Frantz, A murine model of experimental metastasis to bone and bone marrow, *Cancer Res.* 48 (23) (1988) 6876–6881.
- [9] Y.T. Qiu, C. Yang, M.J. Chen, W.L. Qiu, Metastatic spread to the mandibular condyle as initial clinical presentation: radiographic diagnosis and surgical experience, *J. Oral Maxillofac. Surg.* 71 (4) (2013) 809–820.
- [10] T.L. Aghaloo, T. Chaichanasakul, O. Bezouglaia, B. Kang, R. Franco, S.M. Dry, E. Atti, S. Tetradis, Osteogenic potential of mandibular vs. long-bone marrow stromal cells, *J. Dent. Res.* 89 (11) (2010) 1293–1298.
- [11] S.O. Akintoye, T. Lam, S. Shi, J. Brahim, M.T. Collins, P.G. Robey, Skeletal site-specific characterization of orofacial and iliac crest human bone marrow stromal cells in same individuals, *Bone* 38 (6) (2006) 758–768.
- [12] A.D. Kolb, A.B. Shupp, D. Mukhopadhyay, F.C. Marini, K.M. Bussard, Osteoblasts are “educated” by crosstalk with metastatic breast cancer cells in the bone tumor microenvironment, *Breast Cancer Res.* 21 (1) (2019) 31.
- [13] S.H. Park, M.R. Eber, Y. Shiozawa, Models of Prostate Cancer Bone Metastasis, *Methods Mol. Biol.* 2019 (2019) 295–308.
- [14] S.R. Amend K.C. Valkenburg K.J. Pienta Murine Hind Limb Long Bone Dissection and Bone Marrow Isolation *J. Vis. Exp.* (110) (2016).
- [15] G.J. Pettway, L.K. McCauley, Ossicle and vossicle implant model systems, *Methods Mol. Biol.* 455 (2008) 101–110.
- [16] C.A. Gregory, W.G. Gunn, A. Peister, D.J. Prockop, An Alizarin red-based assay of mineralization by adherent cells in culture: comparison with cetylpyridinium chloride extraction, *Anal. Biochem.* 329 (1) (2004) 77–84.
- [17] S.H. Park, M.R. Eber, S. Tsuzuki, M.E. Booker, A.G. Sunil, D.B. Widner, R.A. Parker, C.M. Peters, Y. Shiozawa, Adeno-associated virus serotype rh10 is a useful gene transfer vector for sensory nerves that innervate bone in immunodeficient mice, *Sci. Rep.* 7 (1) (2017) 17428.
- [18] A.A. Khalil, M.J. Jameson, W.C. Broadus, P.S. Lin, S.M. Dever, S.E. Golding, E. Rosenberg, K. Valerie, T.D. Chung, The Influence of Hypoxia and pH on Bioluminescence Imaging of Luciferase-Transfected Tumor Cells and Xenografts, *Int. J. Mol. Imaging* 2013 (2013) 287697.
- [19] L.Y. Yu-Lee, Y.C. Lee, J. Pan, S.C. Lin, T. Pan, G. Yu, D.H. Hawke, B.F. Pan, S.H. Lin, Bone secreted factors induce cellular quiescence in prostate cancer cells, *Sci. Rep.* 9 (1) (2019) 18635.
- [20] L.Y. Yu-Lee, G. Yu, Y.C. Lee, S.C. Lin, J. Pan, T. Pan, K.J. Yu, B. Liu, C.J. Creighton, J. Rodriguez-Canales, P.A. Villalobos, E. Wistuba II, F. de Nadal, G.E. Posas, S.H.L. Gallick, Osteoblast-Secreted Factors Mediate Dormancy of Metastatic Prostate Cancer in the Bone via Activation of the TGFβRIII-p38MAPK-pS249/T252RB Pathway, *Cancer Res.* 78 (11) (2018) 2911–2924.
- [21] Y. Shiozawa, E.A. Pedersen, L.R. Patel, A.M. Ziegler, A.M. Havens, Y. Jung, J. Wang, S. Zalucha, R.D. Loberg, K.J. Pienta, R.S. Taichman, GAS6/AXL axis regulates prostate cancer invasion, proliferation, and survival in the bone marrow niche, *Neoplasia* 12 (2) (2010) 116–127.
- [22] K. Hu, B.R. Olsen, Osteoblast-derived VEGF regulates osteoblast differentiation and bone formation during bone repair, *J. Clin. Invest.* 126 (2) (2016) 509–526.
- [23] E. Roberts, D.A. Cossigny, G.M. Quan, The role of vascular endothelial growth factor in metastatic prostate cancer to the skeleton, *Prostate Cancer* 2013 (2013) 418340.
- [24] N. Sawa, H. Fujimoto, Y. Sawa, J. Yamashita, Alternating Differentiation and Dedifferentiation between Mature Osteoblasts and Osteocytes, *Sci. Rep.* 9 (1) (2019) 13842.
- [25] H. Li, X. Jiang, J. Delaney, T. Franceschetti, I. Bilic-Curcic, J. Kalinovsky, J.A. Lorenzo, D. Grcevic, D.W. Rowe, I. Kalajzic, Immature osteoblast lineage cells

- increase osteoclastogenesis in osteogenesis imperfecta murine, *Am. J. Pathol.* 176 (5) (2010) 2405–2413.
- [26] G.P. Thomas, S.U. Baker, J.A. Eisman, E.M. Gardiner, Changing RANKL/OPG mRNA expression in differentiating murine primary osteoblasts, *J. Endocrinol.* 170 (2) (2001) 451–460.
- [27] B.F. Boyce, L. Xing, Biology of RANK, RANKL, and osteoprotegerin, *Arthritis Res Ther* 9 (Suppl 1) (2007) S1.
- [28] Y. Tanaka, A. Maruo, K. Fujii, M. Nomi, T. Nakamura, S. Eto, Y. Minami, Intercellular adhesion molecule 1 discriminates functionally different populations of human osteoblasts: characteristic involvement of cell cycle regulators, *J. Bone Miner. Res.* 15 (10) (2000) 1912–1923.
- [29] Y. Nakamura, F. Arai, H. Iwasaki, K. Hosokawa, I. Kobayashi, Y. Gomei, Y. Matsumoto, H. Yoshihara, T. Suda, Isolation and characterization of endosteal niche cell populations that regulate hematopoietic stem cells, *Blood* 116 (9) (2010) 1422–1432.
- [30] L. Ding, S.J. Morrison, Haematopoietic stem cells and early lymphoid progenitors occupy distinct bone marrow niches, *Nature* 495 (7440) (2013) 231–235.
- [31] S. Vallet, M.H. Bashari, F.J. Fan, S. Malvestiti, A. Schneeweiss, P. Wuchter, D. Jager, K. Podar, Pre-Osteoblasts Stimulate Migration of Breast Cancer Cells via the HGF/MET Pathway, *PLoS ONE* 11 (3) (2016) e0150507.
- [32] Y. Shiozawa, M.R. Eber, J.E. Berry, R.S. Taichman, Bone marrow as a metastatic niche for disseminated tumor cells from solid tumors, *Bonekey Rep.* 4 (2015) 689.
- [33] T. Asano, K. Okamoto, Y. Nakai, M. Tsutsumi, R. Muro, A. Suematsu, K. Hashimoto, T. Okamura, S. Ehata, T. Nitta, H. Takayanagi, Soluble RANKL is physiologically dispensable but accelerates tumour metastasis to bone, *Nat. Metab.* 1 (9) (2019) 868–875.
- [34] A. Maurizi, N. Rucci, The Osteoclast in Bone Metastasis: Player and Target, *Cancers (Basel)* 10 (7) (2018).
- [35] A.T. Stopeck, A. Lipton, J.J. Body, G.G. Steger, K. Tonkin, R.H. de Boer, M. Lichinitser, Y. Fujiwara, D.A. Yardley, M. Viniegra, M. Fan, Q. Jiang, R. Dansey, S. Jun, A. Braun, Denosumab compared with zoledronic acid for the treatment of bone metastases in patients with advanced breast cancer: a randomized, double-blind study, *J. Clin. Oncol.* 28 (35) (2010) 5132–5139.
- [36] K. Fizazi, M. Carducci, M. Smith, R. Damiao, J. Brown, L. Karsh, P. Milecki, N. Shore, M. Rader, H. Wang, Q. Jiang, S. Tadros, R. Dansey, C. Goessl, Denosumab versus zoledronic acid for treatment of bone metastases in men with castration-resistant prostate cancer: a randomised, double-blind study, *Lancet* 377 (9768) (2011) 813–822.
- [37] S.K. Badrising, V. van der Noort, P. Hamberg, J.L. Coenen, M.J. Aarts, I.M. van Oort, A.J. van den Eertwegh, M. Los, H.P. van den Berg, H. Gelderblom, S. Vrijaldenhoven, E.D. Kerver, T. van Voorthuizen, I.J. de Jong, J.B. Haanen, A.M. Bergman, Enzalutamide as a Fourth- or Fifth-Line Treatment Option for Metastatic Castration-Resistant Prostate Cancer, *Oncology* 91 (5) (2016) 267–273.
- [38] F. Vignani, V. Bertaglia, C. Buttigliero, M. Tucci, G.V. Scagliotti, M. Di Maio, Skeletal metastases and impact of anticancer and bone-targeted agents in patients with castration-resistant prostate cancer, *Cancer Treat. Rev.* 44 (2016) 61–73.
- [39] D.S. Abou, D. Ulmert, M. Doucet, R.F. Hobbs, R.C. Riddle, D.L. Thorek, Whole-Body and Microenvironmental Localization of Radium-223 in Naive and Mouse Models of Prostate Cancer Metastasis, *J. Natl Cancer Inst.* 108 (5) (2016).
- [40] C. Parker, S. Nilsson, D. Heinrich, S.I. Helle, J.M. O'Sullivan, S.D. Fossa, A. Chodacki, P. Wiechno, J. Logue, M. Seke, A. Widmark, D.C. Johannessen, P. Hoskin, D. Bottomley, N.D. James, A. Solberg, I. Syndikus, J. Kliment, S. Wedel, S. Boehmer, M. Dall'Oglio, L. Franzen, R. Coleman, N.J. Vogelzang, C.G. O'Bryan-Tear, K. Staudacher, J. Garcia-Vargas, M. Shan, O.S. Bruland, O. Sartor, A. Investigators, Alpha emitter radium-223 and survival in metastatic prostate cancer, *N. Engl. J. Med.* 369 (3) (2013) 213–223.
- [41] G. Gravis, Systemic treatment for metastatic prostate cancer, *Asian J. Urol.* 6 (2) (2019) 162–168.
- [42] C.E. Lee, W.D. Leslie, P. Czaykowski, J. Gingerich, M. Geirnaert, Y.K. Lau, A comprehensive bone-health management approach for men with prostate cancer receiving androgen deprivation therapy, *Curr. Oncol.* 18 (4) (2011) e163–e172.
- [43] D.K. Kim, J.Y. Lee, K.J. Kim, N. Hong, J.W. Kim, Y.S. Hah, K.C. Koo, J.H. Kim, K.S. Cho, Effect of Androgen-Deprivation Therapy on Bone Mineral Density in Patients with Prostate Cancer: A Systematic Review and Meta-Analysis, *J. Clin. Med.* 8 (1) (2019).
- [44] M. Smith, C. Parker, F. Saad, K. Miller, B. Tombal, Q.S. Ng, M. Boegemann, V. Matveev, J.M. Piulats, L.E. Zucca, O. Karyakin, G. Kimura, N. Matsubara, W.C. Nahas, F. Nole, E. Rosenbaum, A. Heidenreich, Y. Kakehi, A. Zhang, H. Krissel, M. Teufel, J. Shen, V. Wagner, C. Higano, Addition of radium-223 to abiraterone acetate and prednisone or prednisolone in patients with castration-resistant prostate cancer and bone metastases (ERA 223): a randomised, double-blind, placebo-controlled, phase 3 trial, *Lancet Oncol.* 20 (3) (2019) 408–419.
- [45] E. Hesse, S. Schroder, D. Brandt, J. Pamperin, H. Saito, H. Taipaleenmaki, Sclerostin inhibition alleviates breast cancer-induced bone metastases and muscle weakness, *JCI Insight* 5 (2019).
- [46] D. Toscani, M. Bolzoni, M. Ferretti, C. Palumbo, N. Giuliani, Role of Osteocytes in Myeloma Bone Disease: Anti-sclerostin Antibody as New Therapeutic Strategy, *Front. Immunol.* 9 (2018) 2467.
- [47] H. Zheng, Y. Bae, S. Kasimir-Bauer, R. Tang, J. Chen, G. Ren, M. Yuan, M. Esposito, W. Li, Y. Wei, M. Shen, L. Zhang, N. Tupitsyn, K. Pantel, C. King, J. Sun, J. Moriguchi, H.T. Jun, A. Coxon, B. Lee, Y. Kang, Therapeutic Antibody Targeting Tumor- and Osteoblastic Niche-Derived Jagged1 Sensitizes Bone Metastasis to Chemotherapy, *Cancer Cell* 32(6) (2017) 731–747 e6.
- [48] N. Sethi, X. Dai, C.G. Winter, Y. Kang, Tumor-derived JAGGED1 promotes osteolytic bone metastasis of breast cancer by engaging notch signaling in bone cells, *Cancer Cell* 19 (2) (2011) 192–205.
- [49] A. Spreafico, K.N. Chi, S.S. Sridhar, D.C. Smith, M.A. Carducci, P. Kavsak, T.S. Wong, L. Wang, S.P. Ivy, S.D. Mukherjee, C.K. Kollmannsberger, M.A. Sukhai, N. Takebe, S. Kamel-Reid, L.L. Siu, S.J. Hotte, A randomized phase II study of cediranib alone versus cediranib in combination with dasatinib in docetaxel resistant, castration resistant prostate cancer patients, *Invest. New Drugs* 32 (5) (2014) 1005–1016.
- [50] E. Heath, L. Heilbrun, H. Mannuel, G. Liu, P. Lara, J.P. Monk, T. Flaig, A. Zurita, P. Mack, U. Vaishampayan, P. Stella, D. Smith, S. Bolton, A. Hussain, A. Al-Janadi, D. Silbiger, M. Usman, S.P. Ivy, Phase II, Multicenter, Randomized Trial of Docetaxel plus Prednisone with or Without Cediranib in Men with Chemotherapy-Naive Metastatic Castrate-Resistant Prostate Cancer, *Oncologist* 24 (9) (2019) 1149–e807.





# Usefulness of the measurement of neurite outgrowth of primary sensory neurons to study cancer-related painful complications

Sun H. Park<sup>a</sup>, Matthew R. Eber<sup>a</sup>, Miriam M. Fonseca<sup>b</sup>, Chirayu M. Patel<sup>a</sup>, Katharine A. Cunnane<sup>b</sup>, Huiping Ding<sup>c</sup>, Fang-Chi Hsu<sup>d</sup>, Christopher M. Peters<sup>b</sup>, Mei-Chuan Ko<sup>c</sup>, Roy E. Strowd<sup>e</sup>, John A. Wilson<sup>f</sup>, Wesley Hsu<sup>f</sup>, E. Alfonso Romero-Sandoval<sup>b</sup>, Yusuke Shiozawa<sup>a,\*</sup>

<sup>a</sup> Department of Cancer Biology and Wake Forest Baptist Comprehensive Cancer Center, Wake Forest University Health Sciences, Winston-Salem, NC 27157, USA

<sup>b</sup> Department of Anesthesiology, Wake Forest University Health Sciences, Winston-Salem, NC 27157, USA

<sup>c</sup> Department of Physiology and Pharmacology, Wake Forest University Health Sciences, Winston-Salem, NC 27157, USA

<sup>d</sup> Department of Biostatistics and Data Science and Wake Forest Baptist Comprehensive Cancer Center, Wake Forest University Health Sciences, Winston-Salem, NC 27157, USA

<sup>e</sup> Department of Neurology and Wake Forest Baptist Comprehensive Cancer Center, Wake Forest University Health Sciences, Winston-Salem, NC 27157, USA

<sup>f</sup> Department of Neurosurgery, Wake Forest University Health Sciences, Winston-Salem, NC 27157, USA

## ARTICLE INFO

### Keywords:

Dorsal root ganglia  
Nerve sprouting  
Cancer-derived condition medium  
Chemotherapeutic agent  
Semi-automated quantification of neurite outgrowth

## ABSTRACT

Abnormal outgrowth of sensory nerves is one of the important contributors to pain associated with cancer and its treatments. Primary neuronal cultures derived from dorsal root ganglia (DRG) have been widely used to study pain-associated signal transduction and electrical activity of sensory nerves. However, there are only a few studies using primary DRG neuronal culture to investigate neurite outgrowth alterations due to underlying cancer-related factors and chemotherapeutic agents. In this study, primary DRG sensory neurons derived from mouse, non-human primate, and human were established in serum and growth factor-free conditions. A bovine serum albumin gradient centrifugation method improved the separation of sensory neurons from satellite cells. The purified DRG neurons were able to maintain their heterogeneous subpopulations, and displayed an increase in neurite growth when exposed to cancer-derived conditioned medium, while they showed a reduction in neurite length when treated with a neurotoxic chemotherapeutic agent. Additionally, a semi-automated quantification method was developed to measure neurite length in an accurate and time-efficient manner. Finally, these exogenous factors altered the gene expression patterns of murine primary sensory neurons, which are related to nerve growth, and neuro-inflammatory pain and nociceptor development. Together, the primary DRG neuronal culture in combination with a semi-automated quantification method can be a useful tool for further understanding the impact of exogenous factors on the growth of sensory nerve fibers and gene expression changes in sensory neurons.

## 1. Introduction

Recent evidence suggests that crosstalk between the peripheral nervous system and cancer plays an important role in both cancer development and cancer-associated pain [1–3]. In head and neck cancer, tumors innervated by peripheral nerves are known to be more aggressive than those with less innervation [4]. Recent studies using mouse models have revealed that the sympathetic nervous system regulates prostate cancer tumorigenesis and bone metastasis [5], and that

denervation can even attenuate tumorigenesis and metastasis in several types of cancer [5–8]. Moreover, it has been indicated that cancer-associated pain may be a negative indicator of survival in cancer patients [9], suggesting that sensory nerves influence disease progression in patients with poor prognoses. This accumulating evidence indicates that the peripheral nervous system within the tumor microenvironment may enhance disease progression.

Conversely, cancer cells are also known to affect neuronal activities. Cancer often causes pain by interacting with sensory nerves. Especially,

\* Corresponding author.

E-mail address: [yshiozaw@wakehealth.edu](mailto:yshiozaw@wakehealth.edu) (Y. Shiozawa).

<https://doi.org/10.1016/j.bcp.2021.114520>

Received 14 December 2020; Received in revised form 8 March 2021; Accepted 10 March 2021

Available online 17 March 2021

0006-2952/© 2021 Elsevier Inc. All rights reserved.

when cancer cells metastasize to the bone, patients experience bone pain, referred to as cancer-induced bone pain (CIBP). Bone is richly innervated by sensory nerves [10], and it has been suggested that the acidic environment surrounding cancer, or factors, such as growth factors, cytokines, or chemokines, secreted by cancer cells can all stimulate receptors on sensory nerves to induce CIBP [11–14]. Additionally, recent studies have also demonstrated that sensory nerve outgrowth (or sprouting) is one of the potential mechanisms of CIBP [15–19]. A neurotrophic factor nerve growth factor (NGF) is known to be involved in the regulation of survival and growth of neurons [20]. NGF derived from osteosarcoma cells stimulated neuroma-like formation in the periosteum of cancer-inoculated mouse bones, resulting in CIBP [19]. When an NGF antagonist was administered to cancer-bearing mice, CIBP as well as the accompanying nerve sprouting were attenuated [19]. Consistently, abnormal sensory nerve sprouting also causes pain behaviors in other chronic pain conditions [10,21–23].

Not only nerve growth, but also nerve damage is associated with the induction of chronic pain conditions. Chemotherapy-induced peripheral neuropathy (CIPN) is a consequence of the neurotoxic effects of chemotherapy agents [24–26]. Indeed, paclitaxel reduced the density of intraepidermal nerve fibers in hind paw skin and produced pain-related behaviors in rodents [26,27].

These findings suggest (i) that nerves and cancer interact very closely with one another and (ii) abnormal plasticity or remodeling of sensory neurons may contribute to cancer-induced pain. Therefore, it is crucial to understand how nerve growth is regulated in the context of cancer and its treatments. In pursuit of this goal, animal studies are often used to investigate the systemic effects of disease states and therapies on peripheral nerves, but they are not always suitable to study local interactions. For that reason, various *in vitro* neuronal culture systems have been developed to understand the mechanisms of neurite outgrowth. The mouse pheochromocytoma cell line PC12, which is known to form neurite-like structures in response to NGF [28], has been previously used to assess the effects of cancer-derived factors on neurite outgrowth. Conditioned medium (CM) derived from pancreatic cancer cells [29] or head and neck cancer-derived exosomes [30] were shown to enhance neurite sprouting of PC12 cells. Cell lines are easy to maintain and handle but may not fully recapitulate the phenotype of sensory neurons. Moreover, only few neuronal cell lines which extend neurites are currently available. The use of primary culture of dorsal root ganglia (DRG) neurons may overcome this hurdle. To date primary DRG culture has mainly been used to investigate physiological alterations in neuronal activity [31] and to a lesser degree neurite outgrowth.

In the current study, we established methods for reliable *in vitro* primary cultures of sensory neurons derived from mouse, non-human primate, and human DRGs. Additionally, we found that these primary DRG neuronal cultures were suitable to study the neurite length alterations and changes in gene expression associated with nerve growth, and neuro-inflammatory pain and nociceptor development, mediated by CM obtained from cancer cells or paclitaxel-induced neurotoxicity. We also developed a semi-automated method for the measurement of neurite outgrowth, resulting in the reduction of overall analysis time.

## 2. Materials and methods

All methods were carried out in accordance with relevant guidelines and regulations. All human studies and all animal studies followed the Declaration of Helsinki and the Institutional Animal Care and Use Committee Guidelines, respectively.

### 2.1. Human subjects research certification

All human studies are approved by the Institutional Review Board (IRB #00056846) at Wake Forest University Health Sciences. Informed consent was obtained from all subjects involved in the current study.

### 2.2. Animal care and use certification

All animal studies are approved by the Institutional Animal Care and Use Committee (Protocol A18-026 for mouse and Protocol A18-161 for non-human primate) at Wake Forest University Health Sciences.

### 2.3. Murine DRG isolation and primary neuronal culture establishment

Primary DRG neuronal culture was prepared, according to previously published protocols [32,33] with modifications. Nine-twelve lumbar DRGs (L2–L4) of male C57BL/6 mice (8–12 weeks of age, Jackson Laboratory, Bar Harbor, ME) were dissected and directly placed into a 15 mL conical tube, containing 14 mL of ice-cold  $1 \times$  Hanks' balanced salt solution (HBSS) without  $Mg^{++}/Ca^{++}$  (Thermo Fisher Scientific, Gibco, Waltham, MA). Isolated DRGs were enzymatically digested in 3 mL of papain solution [30 U/mL papain (Worthington Biochemical Corp., Lakewood, NJ), 0.1% saturated  $NaHCO_3$  solution (Sigma-Aldrich, St. Louis, MO), 0.3 mg/mL L-Cys (Sigma-Aldrich) in HBSS without  $Mg^{++}/Ca^{++}$ ] for 30 min at 37°C with 5%  $CO_2$ , and then incubated in 3 mL of collagenase type II (CLS2)/dispase type II (Dispase II) solution [4 mg/mL CLS2 (Worthington Biochemical Corp.) and 4.7 mg/mL dispase (Sigma-Aldrich) in HBSS without  $Mg^{++}/Ca^{++}$ ] for 30 min at 37°C with 5%  $CO_2$ . The DRGs were mixed gently every 10 mins. The resulting DRGs were centrifuged at  $200 \times g$  for 2 min and washed with HBSS without  $Mg^{++}/Ca^{++}$ . The pellet was transferred to a 15 mL conical tube, containing 500  $\mu$ L of neuronal growth (NG) medium [Neurobasal-A (Thermo Fisher Scientific, Gibco), 1% N2 (Thermo Fisher Scientific), 2% B-27 (Thermo Fisher Scientific), 2 mM L-glutamine (Thermo Fisher Scientific), 1% penicillin–streptomycin (Thermo Fisher Scientific), and 0.4% glucose (Sigma-Aldrich)]. The DRGs were triturated 15–20 times using p1000 and then p200 pipette tips and filtered through a stainless mesh sieve (40  $\mu$ m, Thermo Fisher Scientific) to obtain single-cell suspensions and remove undigested tissue debris. After bovine serum albumin (BSA) purification [3.5% (W/V) BSA solution] (see below), 500–1,000 cells of DRGs in 30  $\mu$ L of warm NG medium were seeded onto the center of 12 mm round coverslips (MatTek Corp., Ashland, MA), pre-coated with Poly-D-lysine (50  $\mu$ g/mL, overnight at 4°C, Thermo Fisher Scientific, Corning) and laminin (20  $\mu$ g/mL, 1 h at 37°C, Thermo Fisher Scientific, Corning), in 24-well plate. After 1–2 h, 1 mL of warm NG medium was gently added to the sides of wells and the cells were maintained at 37°C with 5%  $CO_2$ .

### 2.4. BSA purification

After trituration and filtration, single-cell suspensions from DRGs were centrifuged through 3.5% (W/V) BSA solution (Thermo Fisher Scientific) (5 mL of BSA solution: 1 mL of HBSS without  $Mg^{++}/Ca^{++}$ ; 1 mL of cell suspension in a 15 mL conical tube) at  $14 \times g$  for 20 min at room temperature (RT) to separate sensory neurons (in pellet) from satellite cells and debris (in BSA layer).

### 2.5. Non-human primate DRG isolation and primary neuronal culture establishment

Non-human primate primary neuronal culture was prepared similarly as described in the murine primary neuronal culture with minor modifications. DRGs (T12 and L1) of a healthy 8-year old female Rhesus macaque (Worldwide Primates, Inc., Miami, FL) were dissected and directly placed in a 15 mL conical tube containing 14 mL of ice-cold HBSS without  $Mg^{++}/Ca^{++}$  and transferred to the laboratory for further procedures. Isolated DRGs were cleaned up by removing non-nervous tissues and nerve root under the laminar flow hood using sterile blade, scissors, and forceps, and cut into small pieces achieved at approximately 1–3 mm side length of a cubical volume in ice-cold HBSS without  $Mg^{++}/Ca^{++}$  and transferred to a 15 mL conical tube containing papain solution. DRGs were enzymatically digested in 6 mL of papain

solution for 1 h at 37°C with 5% CO<sub>2</sub> and then incubated in 6 mL of CLS2/Dispase II solution for 1 h at 37°C with 5% CO<sub>2</sub>. During the digestion, DRGs were triturated 10–15 times using p1000 tips every 20 min and filtered through a stainless mesh sieve (100 µm, Thermo Fisher Scientific) to obtain single-cell suspensions and remove undigested tissue debris. After BSA purification [3.5% (W/V) BSA solution], 600 cells of DRGs in 30 µL of warm NG medium were seeded onto the center of 12 mm round coverslips, pre-coated with Poly-D-lysine and laminin, in 24-well plate. After 1–2 h, 1 mL of warm NG medium was gently added to the sides of wells and the cells were maintained at 37°C with 5% CO<sub>2</sub>.

## 2.6. Human DRG isolation and primary neuronal culture establishment

Human primary neuronal culture was prepared similarly as the non-human primate neuronal culture with minor modifications, according to previously published studies [34–38]. DRG (T10) of a male patient (41 years old age) were dissected during a T10 corpectomy for correction of kyphotic deformity secondary to discitis/osteomyelitis and directly placed in a 15 mL conical tube containing 14 mL of ice-cold HBSS without Mg<sup>++</sup>/Ca<sup>++</sup> and transferred to the laboratory for the further procedures. Isolated DRGs were cleaned up by removing non-nervous tissues and nerve root under the laminar flow hood using sterile blade, scissors, and forceps, and at approximately 1–3 mm side length of a cubical volume in ice-cold HBSS without Mg<sup>++</sup>/Ca<sup>++</sup> and transferred to a 15 mL conical tube containing papain solution. DRGs were enzymatically digested in 9 mL of papain solution for 1 h at 37°C with 5% CO<sub>2</sub> and then incubated in 9 mL of CLS2/Dispase II solution for 1.5 h at 37°C with 5% CO<sub>2</sub>. During the digestion, DRGs were triturated 10–15 times using p1000 tips every 20 min and filtered through a stainless mesh sieve (100 µm) to obtain single-cell suspensions and remove undigested tissue debris. After BSA purification [3.5% (W/V) BSA solution], DRGs in 30 µL of warm NG medium were seeded onto the center of 12 mm round coverslips, pre-coated with Poly-D-lysine and laminin, in 24-well plate. After 1–2 h, 1 mL of warm NG medium was gently added to the sides of wells and the cells were maintained at 37°C with 5% CO<sub>2</sub>.

## 2.7. Cancer cell or normal prostate epithelial cell derived conditioned medium generation

To collect the conditioned medium (CM) from cancer cells,  $5 \times 10^5$  cells of a human breast cancer cell line established from a pleural effusion, MDA-MB-231 [American Type Culture Collection (ATCC), Manassas, VA], a human prostate cancer cell line established from bone metastasis, PC-3 (ATCC), a human lung adenocarcinoma cell line established from lung carcinomatous tissue, A549 (ATCC), or a murine lung carcinoma cell line established from a primary tumor nodule from the Lewis lung carcinoma model, LL/2 (ATCC) were seeded onto a 10 cm dish with 10 mL of growth medium. These cancer cell lines were chosen since they have been shown to grow in the bone and/or can induce CIBP [39–42]. The passage number for all cell lines used was less than 25 passages. MDA-MB-231 and LL/2 cells were cultured in Dulbecco's modified eagle medium (DMEM) (Thermo Fisher Scientific, Gibco) containing 10% fetal bovine serum (FBS, Thermo Fisher Scientific, Gibco), 1% penicillin–streptomycin and glutamine (PSG) (Thermo Fisher Scientific, Gibco), while PC-3 and A549 cells were cultured in Roswell park memorial institute (RPMI) 1640 medium (Thermo Fisher Scientific, Gibco) containing 10% FBS and 1% PSG. At 24 h, the growth medium was removed and replaced with 10 mL of serum free DMEM or RPMI 1640 medium (Thermo Fisher Scientific, Gibco) containing 1% PSG. For the control medium, 10 mL of serum free DMEM or RPMI medium were added to a 10 cm dish without adding any cancer cells. To collect the CM from non-cancer cells,  $5 \times 10^5$  cells of a human normal epithelial prostate cell line, PWR-1E (ATCC) were seeded onto a 10 cm dish with 10 mL of Keratinocyte-serum free medium (K-SFM) containing human recombinant EGF (5 ng/mL) and bovine pituitary extract (0.05 mg/mL) provided with the K-SFM kit (Thermo Fisher Scientific, Gibco).

The passage number for all cell lines used was less than 25 passages. At 24 h, the growth medium was removed and replaced with 10 mL of K-SFM without any supplements. For the control medium, 10 mL of K-SFM were added to a 10 cm dish without adding any cells. After 24 h of incubation at 37°C with 5% CO<sub>2</sub>, the CM were collected and filtered through a 0.2 µm syringe filter (Thermo Fisher Scientific) to remove any cell debris. Additionally, cancer-derived CM were concentrated to  $4 \times$  using an Amicon Ultra-15 centrifugal filter tube (MilliporeSigma, Burlington, MA, NMWL10K) performed at  $4,000 \times g$  for 20 min at RT. The CM was stored at 4°C until use.

## 2.8. Neurite outgrowth assay

After 48 h (murine and non-human primate) or 72 h (human) of primary DRG neuronal culture establishment (the time required to achieve 20–30% nerve fiber occupancy on the slide based on Fig. 3A), half (500 µL) of medium was replaced with 500 µL of either control, normal epithelial cell-derived CM, or cancer-derived CM, and then the cells were incubated another 48–72 h (the time required to achieve 70–80% nerve fiber occupancy on the slide based on Fig. 3A). In some cases, the cells were treated with 500 µL of NG medium containing either dimethyl sulfoxide (DMSO) control or paclitaxel (Sigma-Aldrich) for 24 h. At the termination of the experiments, the cells were fixed in 500 µL of 4% paraformaldehyde (PFA) for 10 min at RT, and immediately subjected to immunofluorescence or stored in  $1 \times$  D-PBS at 4°C until use.

## 2.9. Immunofluorescence assay

Fixed cells were blocked with immunofluorescence (IF) buffer [1x D-PBS supplemented with 5% Normal Donkey serum (Jackson ImmunoResearch, West Grove, PA) and 0.03% Triton X-100 (Sigma-Aldrich)] for 1 h at RT and incubated with primary antibodies overnight at 4 °C in IF buffer. Primary antibodies used: mouse anti-β-III tubulin antibody (1:1,000, Biolegend, San Diego, CA, cat #: 801201); chicken anti-200kD neurofilament (NF200) antibody (1:3,000, Neuromics, Cambridge, MA, cat #: ab134459); rabbit anti-protein gene product 9.5 (PGP9.5) antibody (1:1,000; Cederlane, Rosemont, IL, cat #: 14730–1-AP); rabbit anti-calcitonin gene-related peptide (CGRP) antibody (1: 5,000, Sigma-Aldrich, cat #: C8198); biotinylated isolectin B4 (IB4) antibody (1: 2,500, Sigma-Aldrich, cat #: L2140); rabbit anti-S100 antibody (1: 1,000, Abcam, Cambridge, UK, cat #: ab868); or goat anti-glial fibrillary acidic protein (GFAP) antibody (1: 200, Santa Cruz, Dallas, TX, cat #: sc-6170). Thereafter, the cells were incubated with secondary antibodies for 2 h at RT in IF buffer. The specific choices of secondary antibodies were made based on primary antibodies used. Secondary antibodies used: anti-rabbit cyanine 3 (CY3) (1:700, Jackson ImmunoResearch, cat #: 711–165-152); anti-chicken CY2 (1:600, Jackson ImmunoResearch, cat #: 703–225-155); anti-streptavidin CY5 (1:500, Jackson ImmunoResearch, cat #: 016–170-084); anti-goat CY5 (1:500, Jackson ImmunoResearch, cat #: 705–175-147); or anti-mouse CY2 (1:600, Jackson ImmunoResearch, cat #: 715–225-150). After washing 5 times with 1x D-PBS, the cells were mounted with ProLong Gold antifade mountant with DAPI (Thermo Fisher Scientific).

## 2.10. Imaging and quantification of immunofluorescence

For each group, 2–3 coverslips were quantified, and 6–10 images were taken from each coverslip using a Nikon Eclipse Ni fluorescent microscope system (Nikon, Tokyo, Japan). Images were saved in nd2 or tiff files for further analysis using Visiopharm (Hørsholm, Denmark) or Image J (NIH, Bethesda, Maryland) software, respectively.

## 2.11. Image J analysis

Neuron J, a plugin for Image J software was used to manually analyze nerve density, as previously described [43,44]. Briefly, images



were opened in Image J (<https://imagej.net/Fiji/Downloads>) and converted to 8-bit, which were then individually opened in Neuron J plugin. Thereafter, total neurite lengths of neuronal markers NF200 or  $\beta$ -III tubulin positive neurites per each image were traced and normalized with the numbers of neurons, which were counted using a multi-point tool of Image J.

### 2.12. Visiopharm image analysis

An algorithm (called an “APP”) was created in the Visiopharm software, which uses digital masks and associated labels to automatically detect and count the somas of NF200 positive neurons, as well as detect and measure total NF200 positive neurite length. In some cases, PGP9.5,  $\beta$ -III tubulin, or activating transcription factor 3 (ATF3) were used as markers instead of NF200 for neurite length or soma quantification. The APP was designed to exploit the observations that somas are usually brighter in fluorescence intensity than neurites, and neurites are long, thin structures whereas somas are round and larger in diameter. This APP uses thresholds, which were set manually according to the set of images to be analyzed, as sets of images can vary in fluorescence intensity between experiments due to staining and microscope setting differences. The APP includes post-processing for cleaning up the classification (i.e. small object removal, skeletonization, erosion, dilation, etc.) and the calculation of the variable included in our measurements.

### 2.13. Real time qPCR

After murine primary DRG neuron cultures were treated with (i) either control or cancer-derived CM (48 h), or (ii) either DMSO or paclitaxel (10  $\mu$ M) (24 h), cells were lysed in 350  $\mu$ L RLT- $\beta$ -ME buffer. RNA was extracted using the RNeasy plus micro kit (Qiagen, Germantown, MD) and cDNA was generated using Invitrogen SuperScript II Reverse Transcriptase (Invitrogen, Carlsbad, CA). Real time PCR (qPCR) was performed using Taqman gene expression master mix (Applied Biosystems, Foster City, CA) and Taqman gene expression assays on the Bio-Rad CFX Connect instrument (Hercules, CA). Taqman gene expression assays used: growth associated protein 43 (GAP43) (Mm00500404\_m1), NF200 (Mm01191456\_m1), CGRP (Mm00801463\_g1), Substance P (Mm01166996\_m1), Bradykinin (Mm04207315\_s1), tumor necrosis factor- $\alpha$  (TNF- $\alpha$ ) (Mm00443258\_m1), suppressor of cytokine signaling 3 (SOCS3) (Mm00545913\_s1), immunoglobulin superfamily containing leucine rich repeat 2 (ISLR2) (Mm00623260\_s1), and GAPDH (Mm99999915\_g1). For interleukin-6 (IL-6), cDNAs were amplified by qPCR using SsoAdvanced Universal SYBR green supermix (Bio-rad laboratories, Hercules, CA). Primers used: mouse IL-6 Forward: 5'-TTCCTACCCCAATTCCAAT-3' and Reverse: 5'-CCTTCTGTGACTC-CAGCTTATC-3' (Integrated DNA Technologies, Newark, NJ). Data is presented using the delta-delta Ct method, with GAPDH used as the reference gene.

### 2.14. Statistical analysis

Numerical data are expressed as mean  $\pm$  the standard error of the mean (SEM). Statistical analysis was performed by unpaired two-tailed Student's *t* test or one-way ANOVA with Tukey's multiple comparisons, using the GraphPad Prism statistical program (GraphPad Software, San Diego, CA) with significance at  $p \leq 0.05$ . The chi-square goodness-of-fit test was used to test whether the distribution of the three soma size groups (0–599  $\mu$ m<sup>2</sup>, 600–1,199  $\mu$ m<sup>2</sup>, and 1,200–1,300  $\mu$ m<sup>2</sup>) of one species was the same as that of the other species.

## 3. Results

### 3.1. Murine DRGs can survive, and sensory neurons can grow neurites even in serum-free condition

To establish a primary 2D DRG neuron culture, L2-4 DRGs were collected from C57BL/6 mice and dissociated into single cell suspension by enzymatic digestion. The resulting DRGs were plated onto Poly-D-lysine/laminin-coated coverslips and cultured in neuronal growth medium. Unlike other studies [45–48], DRGs were maintained in the condition that serums and nerve-related growth factors (e.g. NGFs, GDNFs) were withdrawn to avoid their effects on the survival of neurons and neurite outgrowth. As shown in Fig. 1A, cells obtained from DRGs, including sensory neurons and satellite cells, could maintain viability for at least 15 days in serum and growth factor-free conditions. Although approximately 90% of sensory neurons extended neurites, it was very difficult to observe under the light microscope since two cell types overlapped with each other. To visualize sensory neurons, DRGs were stained with DAPI and three different neuronal markers: 200kD neurofilament (NF200) (all myelinated A-fibers); calcitonin gene-related peptide (CGRP) (peptidergic myelinated thin A $\delta$ -fibers and unmyelinated C-fibers) and Substance P (peptidergic unmyelinated C-fibers). Sensory neurons expressed these markers, whereas satellite cells failed to do so (Fig. 1B).

### 3.2. Murine DRG sensory neurons were purified using a BSA gradient centrifugation

It has been demonstrated that, in the peripheral nervous system, satellite cells are involved in the regulation of survival and axonal growth of neurons [49,50]. Since one of our main purposes of establishment of primary DRG neuronal culture is to investigate the direct effects of exogenous factors on the neurite outgrowth of sensory neurons or neurite toxicity, our next attempt was to separate sensory neurons from satellite cells. To do so, density gradient centrifugation was performed using 3.5% BSA solution. After purification, sensory neurons were enriched in the pellet fraction, while satellite cells were concentrated in the BSA layer. When cells in the pellet fraction were plated, the numbers of satellite cells (S100 positive) were reduced, compared to those before purification (Fig. 2A). To further confirm the quality of purification, both cells in the pellet fraction and the BSA layer were plated. As expected, cells in the pellet fraction could extend neurites, while cells in the BSA layer failed to do so (Fig. 2B).

Afterwards, the neurite outgrowth of neuronal cells in the pellet fraction were followed over time. The nerve fiber occupancy on the slides increased in a time dependent manner (10% nerve fiber occupancy at 24 h, 20–30% nerve fiber occupancy at 48 h, 50–60% nerve fiber occupancy at 72 h, and 70–80% nerve fiber occupancy at 96 h) (Fig. 3A). Neuronal cells in the pellet fraction were also segregated into three groups based on soma size (Fig. 3B). The size of soma was divided into small ( $\leq 599 \mu$ m<sup>2</sup>), medium (600–1,199  $\mu$ m<sup>2</sup>) and large (1,200–1,300  $\mu$ m<sup>2</sup>), which has been used for *in vivo* characterization of rodent DRGs [51–55]. The majority of murine sensory neuron somas were smaller than 599  $\mu$ m<sup>2</sup> (Fig. 3B). Additionally, cells were stained with NF200, CGRP, and isolectin B4 (IB4) (non-peptidergic unmyelinated C-fibers) to further characterize the subpopulation of the DRG neurons. Interestingly, NF200 positive neurons always co-localized with CGRP positive neurons, but not IB4 positive neurons (Fig. 3C). Additionally, some CGRP positive neurons overlapped with IB4 positive neurons (Fig. 3C). Moreover, small size neurons consisted of NF200 negative/CGRP negative/IB4 positive neurons; medium size neurons consisted of NF200 negative/CGRP positive/IB4 positive, NF200 negative/CGRP positive/IB4 negative, or NF200 positive/CGRP positive/IB4 negative neurons; and large size neurons consisted of NF200 positive/CGRP positive/IB4 negative neurons (Fig. 3C).

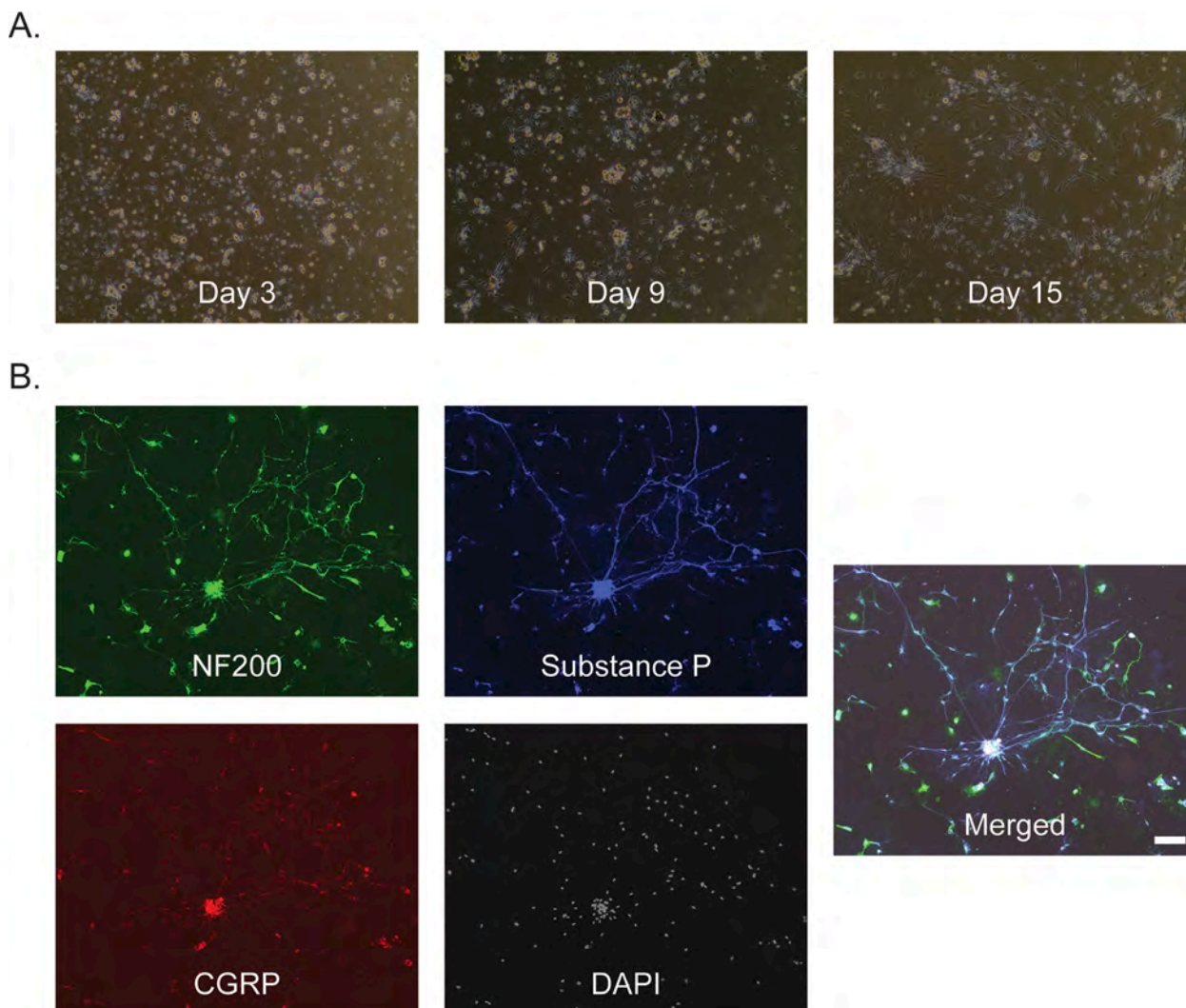


**Fig. 1.** Establishment of a murine primary 2D DRG neuron culture. (A) Representative bright field images of murine primary DRG culture (9–12x lumbar DRGs (L2–L4) from 8 to 12-week-old male C57BL/6 mice) seeded onto Poly-D-lysine/laminin coated coverslips at Day 3, 9, and 15. Magnification 4 $\times$ . (B) Representative immunofluorescence images of (A) at Day 15. Sensory neurons were stained with antibodies against 200 kD neurofilament (NF200) (green) (all myelinated A-fibers), calcitonin gene-related peptide (CGRP) (red) (peptidergic myelinated thin A $\delta$ -fibers and unmyelinated C-fibers), and Substance P (blue) (peptidergic unmyelinated C-fibers). DAPI (gray) is used for nuclear staining. Magnification 10 $\times$ . Bar = 100  $\mu$ m. (For interpretation of the references to colour in this figure legend, the reader is referred to the web version of this article.)

### 3.3. Cancer-derived factors stimulated the neurite outgrowth of murine sensory neurons, whereas a chemotherapeutic agent reduced.

Next, to test whether the growth of sensory neurons can be manipulated *in vitro* by exogenous factors, which again is our main purpose of the establishment of primary sensory neuron cultures, murine primary sensory neurons were treated with either cancer-derived CM or paclitaxel. We chose cancer-derived CM treatments since it is known to (i) enhance neurite sprouting [29,30] and (ii) induce pain behaviors in rodents when delivered with an intraplantar injection [56]. When sensory neurons were exposed to CM derived from human breast cancer cell line MDA-MB-231 cells, human prostate cancer cell line PC3 cells, human lung cancer cell line A549 cells, or murine lung cancer cell line LL/2 cells, the sprouting of sensory neurons significantly increased, compared to those exposed to control CM (Fig. 4A&B). However, CM derived from normal prostate epithelial cells did not affect the growth of sensory nerves (Fig. 4C). Interestingly, we observed more nerve sprouting in sensory neurons treated with CM derived from lung cancer cell lines (A549 and LL/2). This finding might be consistent with orthopedic surgeons' anecdotal evidence that bone metastasis from lung

cancer are more painful than those from other cancer types (e.g. prostate cancer and breast cancer) (personal communications), although further studies to confirm this observation are clearly warranted. On the other hand, when sensory neurons were treated with paclitaxel, the growth of sensory nerve fibers was reduced in a dose dependent manner (Fig. 4D&E). Mouse sensory neurons were treated with 10  $\mu$ M paclitaxel, since this dose is close to a physiological-dose [57].

For quantification of neurite outgrowth, we used a commercially available image analysis software, Visiopharm to automatically measure a total neurite length and Image J to count the numbers of the soma in each coverslip. Then, a total neurite length was normalized with soma count. To validate whether an automated method can accurately be used to measure neurite outgrowth, we first created a novel algorithm (called an "APP") using Visiopharm that enabled us to detect the somas and measure the length of their neurites based on structural differences and fluorescence intensity, respectively (Fig. 5A). Then, values obtained automatically (Visiopharm) were compared to those obtained manually (Image J). As shown in Fig. 5B, total neurite lengths obtained using these two different methods were highly correlated ( $r^2 = 0.8975$ ). However, soma counts were not as highly correlated as total neurite lengths ( $r^2 =$

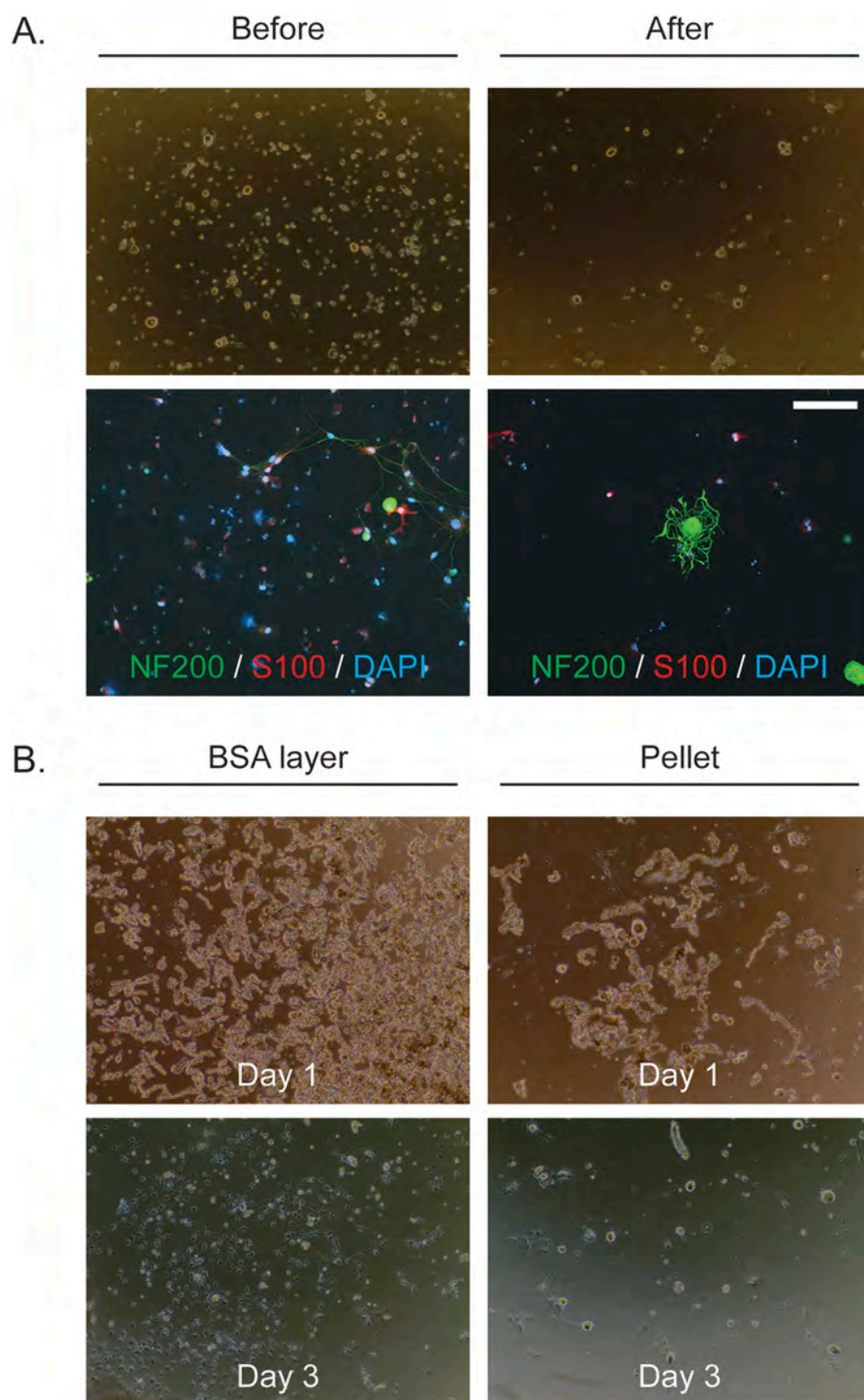


**Fig. 2.** Purification of murine primary DRG sensory neurons using a BSA gradient centrifugation. (A) DRG cells were seeded onto Poly-D-lysine/laminin coated coverslips before or after a BSA gradient centrifugation [3.5% (W/V) BSA solution]. Representative bright field images of murine DRGs before and after a BSA gradient centrifugation (top panels). Magnification 4 $\times$ . Representative immunofluorescence images murine DRGs before and after BSA centrifugation (bottom panels). Sensory neurons were stained with antibodies against 200kD neurofilament (NF200) (green), and satellite cells were stained with antibodies against S100b (red), DAPI (blue) is used for nuclear staining. Magnification 20 $\times$ . Bar = 100  $\mu$ m. (B) After a BSA gradient centrifugation, cells obtained from the pellet fraction (pellet) and BSA layer were seeded onto Poly-D-lysine/laminin coated coverslips. Representative bright field images of cells from the pellet fraction and BSA layer at Day 1 (top panels) and 3 (bottom panels). Magnification 4 $\times$ . (For interpretation of the references to colour in this figure legend, the reader is referred to the web version of this article.)

0.1561) (Fig. 5C). This might in part be due to the difficulty to segregate the cluster of the somas into a single soma. These studies demonstrated the following: (i) the total neurite length obtained using an automated method were similar to that obtained manually; (ii) a manual counting method provided more accurate information regarding the numbers of soma than an automated method; and (iii) counting somas manually was not as time consuming as measuring neurite length. Therefore, we chose the quantification strategy described above.

### 3.4. The impact of cancer-derived factors and a chemotherapeutic agent on the expression of genes, associated with nerve growth and neuro-inflammatory pain, in murine sensory neurons

Next, to determine whether the alterations of sensory neuron length mediated by exogenous factors are associated with pain, gene expression analyses were performed by qPCR on murine primary sensory neurons treated with either cancer-derived CM or paclitaxel. In this case, we chose CM derived from A549 cells (A549 CM), since the greatest enhancement of murine primary sensory neuron sprouting was observed



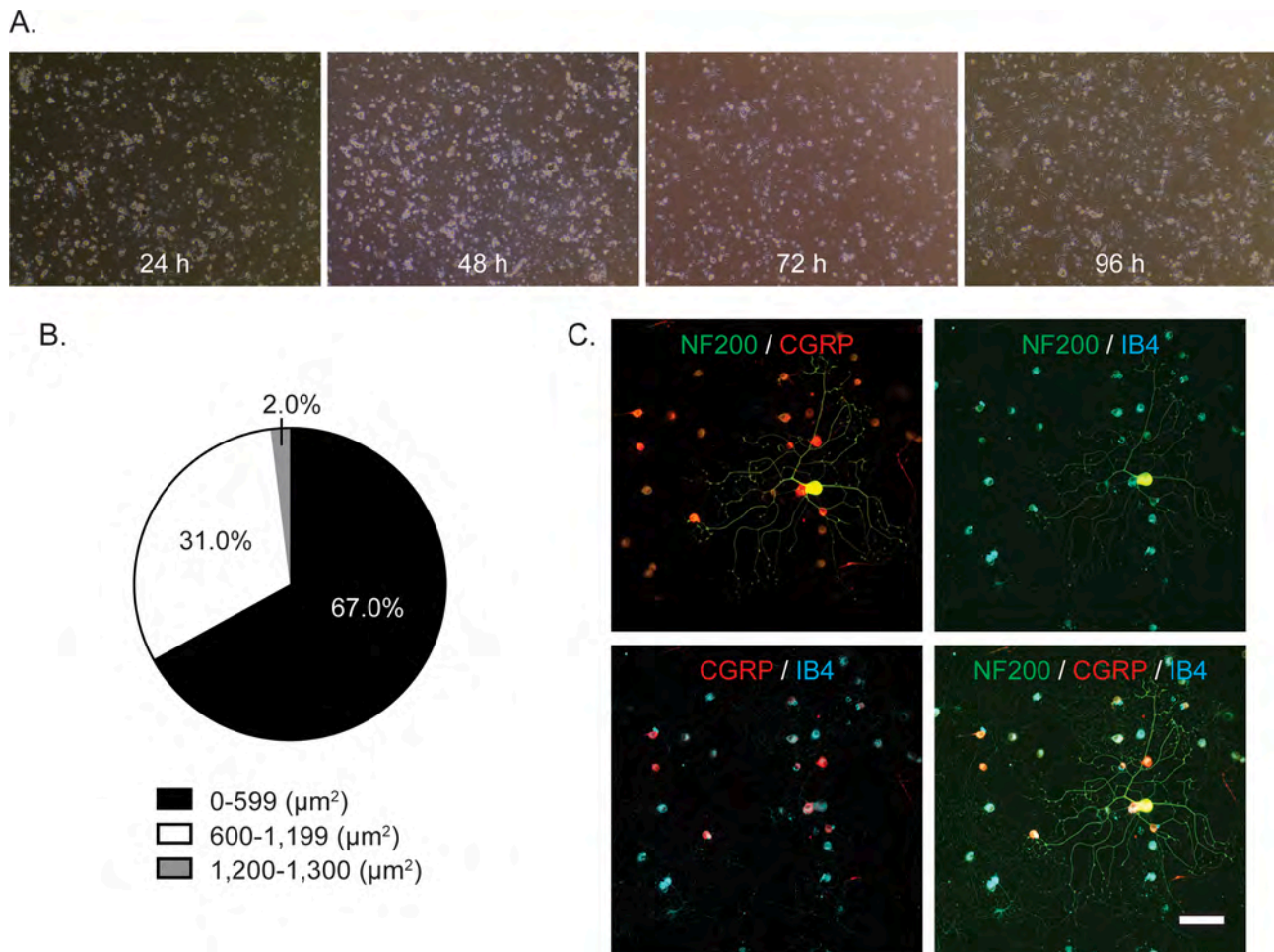


**Fig. 3.** Characterization of murine primary DRG sensory neurons. **(A)** Representative bright field images of murine primary DRG culture (9–12x lumbar DRGs (L2–L4) from 8 to 12-week-old male C57BL/6 mice) after a BSA gradient centrifugation [3.5% (W/V) BSA solution] seeded onto Poly-D-lysine/laminin coated coverslips at 24, 48, 72, and 96 h. Magnification 4x. **(B)** Quantification analysis of the cell size distribution of murine primary DRG sensory neurons ( $n = 467$ ). Areas of soma ( $\mu\text{m}^2$ ) of cells from **(A)** were measured using image J software. **(C)** Representative immunofluorescence images of murine primary DRG sensory neurons after a BSA gradient centrifugation. Sensory neurons were stained with antibodies against 200kD neurofilament (NF200) (Green) (all myelinated A-fibers), calcitonin gene-related peptide (CGRP) (red) (peptidergic myelinated thin A $\delta$ -fibers and unmyelinated C-fibers), and isolectin B4 (IB4) (light blue) (non-peptidergic unmyelinated C-fibers). Magnification 10 $\times$ . Bar = 100  $\mu\text{m}$ . (For interpretation of the references to colour in this figure legend, the reader is referred to the web version of this article.)

when treated with A549 CM (Fig. 4A). To determine whether our observations in the neurite length changes mediated by exogenous factors correlate to gene expression patterns, the levels of growth associated protein 43 (GAP43), a nerve growth marker [58], and NF200 gene expression in A549 CM or paclitaxel-treated murine sensory neurons were measured. Consistent with our findings in the neurite length changes, A549 CM significantly increased GAP43 expression, while paclitaxel exerted opposite effects (Fig. 6A). A similar trend was observed in changes in NF200 gene expression patterns as those of GAP43, although it did not reach statistical significance (Fig. 6B). Then, gene expression levels of pain-related molecules, including neuropeptides (CGRP, Substance P, Bradykinin) and cytokines involved in pathological pain conditions [tumor necrosis factor- $\alpha$  (TNF- $\alpha$ ), interleukin-6 (IL-6)] [59,60] were measured to determine the association between nerve growth and pain. Interestingly, patterns of gene expression changes were different depending on the treatments used. Neither A549 CM nor paclitaxel affected CGRP expression levels (Fig. 6C), while A549 CM significantly decreased Substance P expression levels (Fig. 6D), and both A549 CM and paclitaxel significantly increased Bradykinin expression levels in murine primary sensory neuron (Fig. 6E). Paclitaxel significantly increased TNF- $\alpha$  expression levels (Fig. 6D), whereas A549 CM significantly decreased IL-6 expression levels (Fig. 6G). Additionally, the gene expression levels of suppressor of cytokine signaling 3

(SOCS3) and immunoglobulin superfamily containing leucine rich repeat 2 (ISLR2), which were significantly increased in DRGs derived from patients with neuropathic pain, compared to those derived from patients without pain [36], were measured. SOCS3 and ISLR2 are known to be involved in development of cancer-related pain [61] and nociceptive sensory neuron development [62], respectively. In these cases, A549 CM significantly impacted on the gene expression of SOCS3 (increased, Fig. 6H) and ISLR2 (decreased, Fig. 6I), while paclitaxel failed to do so.

### 3.5. Sensory neurons obtained from non-human primate and human DRGs act similar to those of mice.

To enhance translational potential, non-human primate primary DRG sensory neuron culture was established using similar methods to establish murine primary sensory neuron culture. Consistent with murine culture, the BSA purification method could largely reduce satellite cell population, and about 90% of the viable neurons grew neurite in serum and growth factor-free conditions (Fig. 7A). Additionally, the majority of non-human primate sensory neuron somas were between 600  $\mu\text{m}^2$  to 1,199  $\mu\text{m}^2$  (Fig. 7B). Furthermore, non-human primate sensory neurons responded to cancer-derived CM (Fig. 7C&D) and paclitaxel treatment (Fig. 7E&F), similar to murine sensory neurons.

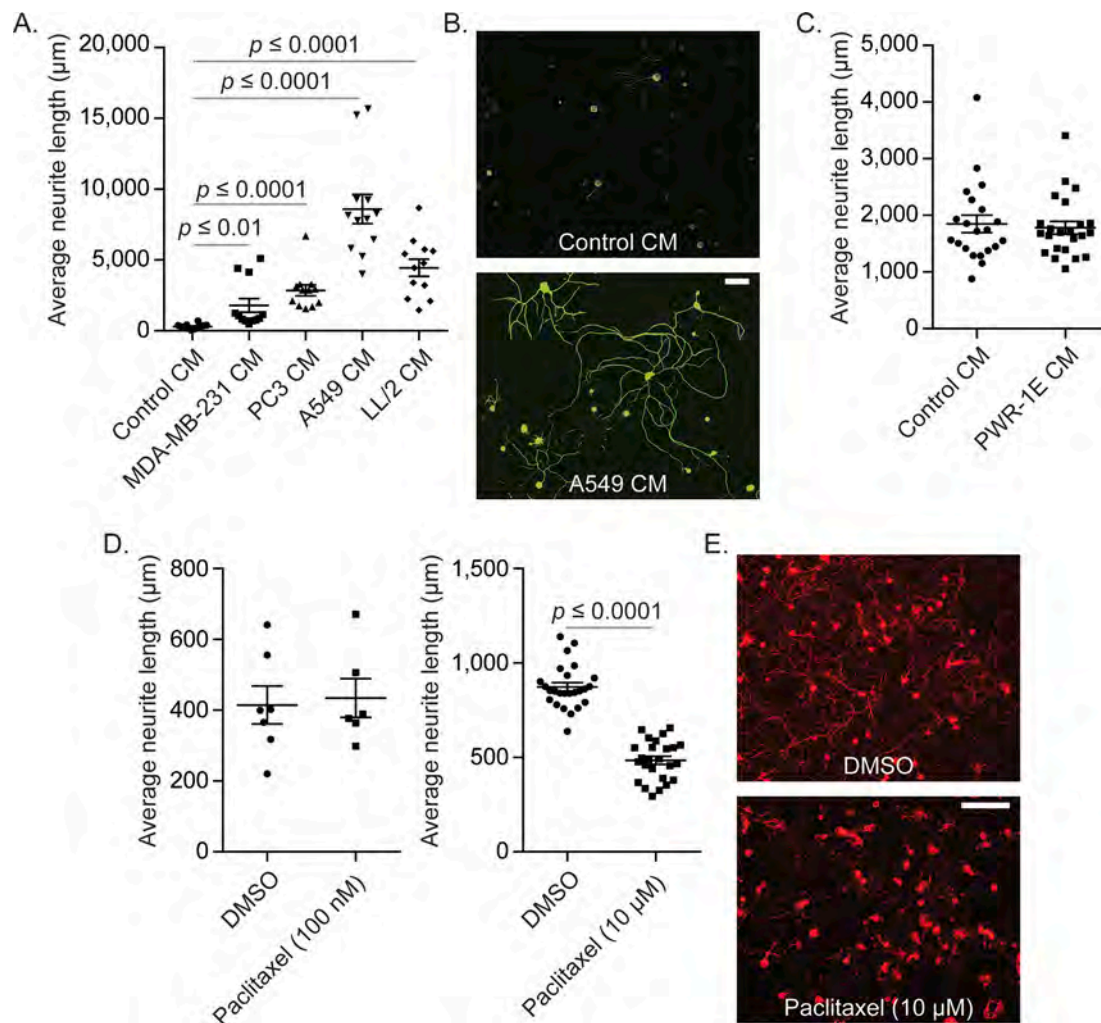


**Fig. 4.** Manipulation of the sprouting of murine primary DRG sensory neurons by exogenous factors. (A) Murine primary DRG sensory neurons were treated with either control medium (Control CM) or conditioned medium (CM, 0% serum) derived from human breast cancer cell line MDA-MB-231 cells (MDA-MB-231 CM), human prostate cancer cell line PC3 cells (PC3 CM), human lung cancer cell line A549 cells (A549 CM), or murine lung cancer cell line LL/2 cells (LL/2 CM) for 48 h. Sensory neurons were stained with antibodies against 200kD neurofilament (NF200). Quantification of the average of the total neurite length. Mean  $\pm$  SEM. Student's *t*-test, significance at  $p \leq 0.05$ . The figure is a representative of two independent experiments, and 6 random images from each coverslip ( $n = 2$ ) were analyzed in a blind manner. (B) Representative immunofluorescence images of murine primary DRG sensory neurons treated with either control or human lung cancer cell line A549 CM. Magnification 10 $\times$ . Bar = 100  $\mu$ m. (C) Murine primary DRG sensory neurons were treated with either control medium (Control CM) or CM derived from human normal prostate epithelial cell line PWR-1E cells (PWR-1E CM) for 48 h. Sensory neurons were stained with antibodies against NF200. Quantification of the average of the total neurite length. Mean  $\pm$  SEM. Student's *t*-test. The figure is a representative of one independent experiment, and 7–8 random images from each coverslip ( $n = 3$ ) were analyzed in a blind manner. (D) Murine primary DRG sensory neurons treated with either DMSO or paclitaxel (100 nM, 10  $\mu$ M) for 24 h. Sensory neurons were stained with antibodies against PGP9.5. Quantification of the average of the total neurite length. Mean  $\pm$  SEM. Student's *t*-test, significance at  $p \leq 0.05$ . Experiment was performed once, and 8–10 random images from each coverslip ( $n = 3$ ) were analyzed in a blind manner. (E) Representative immunofluorescence images of murine primary DRG sensory neurons treated with either DMSO or paclitaxel (10  $\mu$ M) for 24 h. Magnification 10 $\times$ . Bar = 100  $\mu$ m.

Non-human primate and human sensory neurons were treated with 1  $\mu$ M paclitaxel, since a concentration of 10  $\mu$ M used for mouse sensory neurons was too toxic to them (Data not shown).

Primary sensory neuron culture of human DRGs was also established. Consistent with murine and non-human primate culture, the BSA purification method could reduce satellite cell population, and about 93% of the viable neurons grew neurite in serum and growth factor-free conditions (Fig. 8A), and the majority of the soma size was smaller than 599  $\mu$ m<sup>2</sup> (Fig. 8B). Since sensory neurons from three different species showed different size distributions of cell population, we sought to determine whether there are any similarities in the soma size distribution among murine, non-human primate, and human sensory neurons. Interestingly, the chi-square goodness-of-fit test showed that the distributions of the soma size were different among the three species (all *p*-values from pairwise comparisons less than 0.0001). Additionally, when

neurons were treated with cancer-derived CM, the lengths of neurite were significantly longer than those treated with control CM (Fig. 8C&D). On the other hand, when neurons were treated with paclitaxel, the growth of neurite was significantly reduced compare to the neurons treated with vehicle (Fig. 8E&F).

#### 4. Discussion

In this study, we demonstrated four important findings: (1) primary DRG sensory neuron cultures can be derived from mouse, non-human primate, and human tissues and cultured in serum and growth factor-free conditions, (2) a BSA gradient centrifugation method is useful to separate sensory neurons from satellite cells, (3) DRG sensory neurons maintain their heterogeneous subpopulations, and (4) the length of nerve fibers and gene expression pattern, associated with nerve growth,



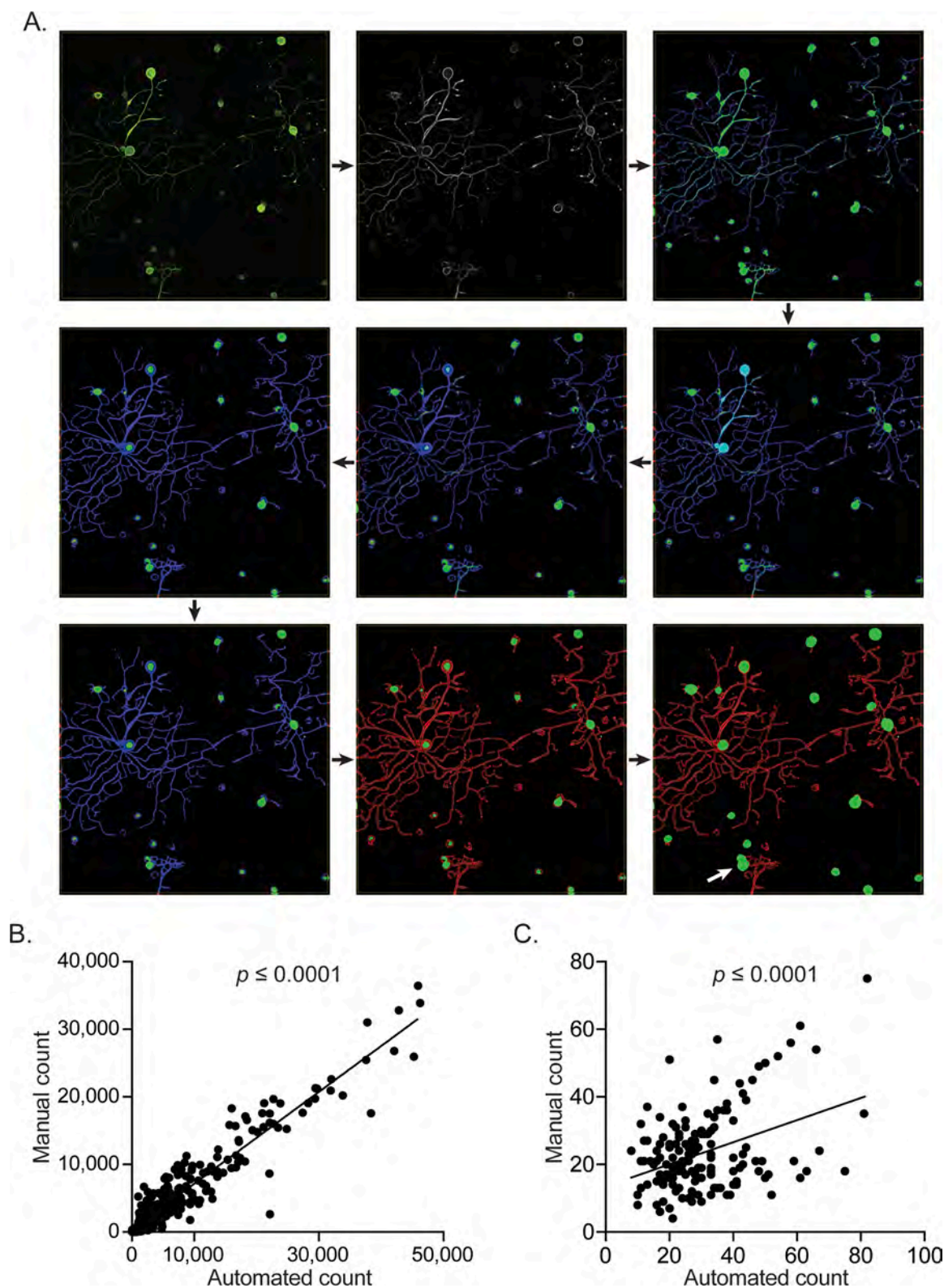


**Fig. 5.** Quantification of total neurite length by automated imaging analysis. (A) Representative images of the image-processing steps performed in the Visiopharm APP used for automated neurite length quantification and soma count, starting from the original fluorescent image of 200kD neurofilament (NF200) stained mouse DRG neurons (top left) to the final quantified image (bottom right) with relevant masks for neurite length (red) and soma count (green). Black arrow: direction of processing steps. White arrow: two neurons inaccurately counted as one. (B) 316 images of murine primary DRG sensory neurons stained with antibodies against NF200 were analyzed using the Visiopharm APP and by manual tracing using ImageJ software and values for total neurite length were plotted ( $\mu\text{m}$ ): Linear regression analyses, significance at  $p \leq 0.05$ . (C) 164 images of murine primary DRG sensory neurons stained with antibodies against NF200 were analyzed using the Visiopharm APP and by manual counting using ImageJ software and values for total soma numbers were plotted (counts): Linear regression analyses, significance at  $p \leq 0.05$ . (For interpretation of the references to colour in this figure legend, the reader is referred to the web version of this article.)



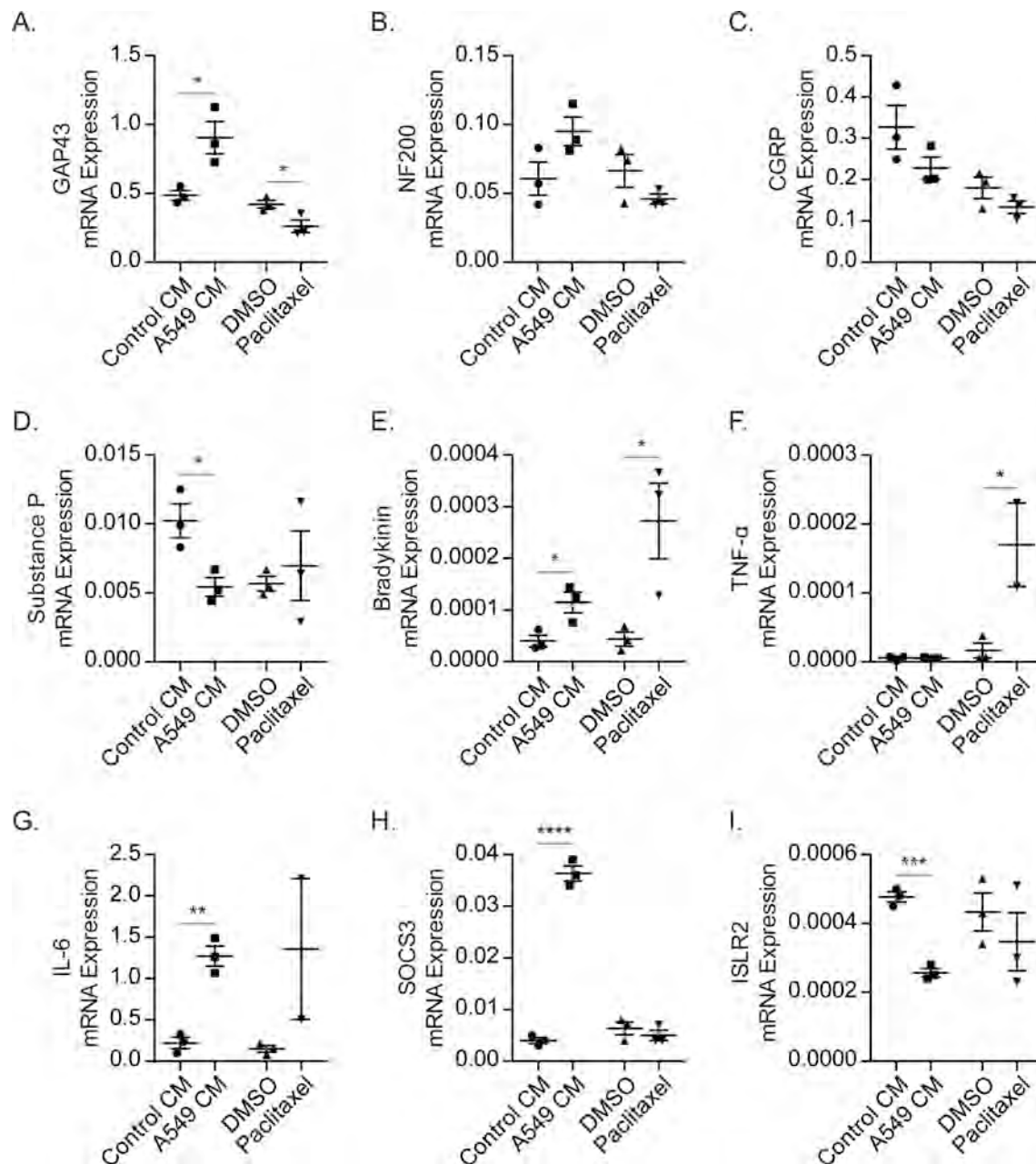


**Fig. 6.** Changes in expression of genes associated with nerve growth and pain in murine primary DRG sensory neurons by exogenous factors. Murine primary DRG sensory neuron cells were treated with control medium (Control CM) or human lung cancer cell line A549 cell-derived conditioned medium (A549 CM) for 48 h, and DMSO or paclitaxel (10  $\mu$ M) for 24 h. Expression of (A) GAP43 and (B) NF200, which are genes associated with nerve growth. Expression of (C) CGRP, (D) Substance P, (E) Bradykinin, (F) TNF- $\alpha$ , (G) IL-6, (H) SOCS3, and (I) ISLR2, which are genes associated with neuro-inflammatory pain and nociceptor development. GAPDH was used reference gene. Delta-delta Ct method. Results were displayed as Mean  $\pm$  SEM. Student's *t*-test. \* $p \leq 0.05$ , \*\* $p \leq 0.01$ , \*\*\* $p \leq 0.001$ , \*\*\*\* $p \leq 0.0001$ . GAP43: growth associated protein 43; NF200: 200kD neurofilament; CGRP: calcitonin gene-related peptide; TNF- $\alpha$ : tumor necrosis factor- $\alpha$ ; IL-6: interleukin-6; SOCS3: suppressor of cytokine signaling 3; ISLR2: immunoglobulin superfamily containing leucine rich repeat 2.

and neuro-inflammatory pain and nociceptor development, of sensory neurons were altered by responding to exogenous factors, such as cancer-derived CM and reduced by responding to a chemotherapeutic agent. We developed a semi-automated quantification method which allowed us to analyze the neurite growth in an accurate and time-efficient manner. Together, these findings suggest that a semi-automated measurement of the neurite growth, along with gene expression analyses, of primary DRG sensory neurons can be a useful *in vitro* tool to study the impact of exogenous factors on the growth of sensory neurons. The schematic workflow of the primary DRG sensory neuron culture preparation and analyses, is described in Fig. 9.

Animal models have been widely used to study pathological

mechanisms underlying human diseases and to test therapeutic strategies. Although *in vivo* studies are useful for addressing large-scale biological questions, *in vitro* methods are better suited for exploring micro-level mechanisms. In this study, using primary neuronal cultures, we demonstrated that (i) cancer-derived CM induced the sprouting of nerve fibers and (ii) the chemotherapeutic agent, paclitaxel inhibited the neurite outgrowth. One of the most important aspects of our studies is that the structural changes observed in our *in vitro* setting recapitulate pathological conditions observed in *in vivo* rodent models. For example, the inoculation of cancer cells into the bone of rodents resulted in increased neurite density around the bone, which is associated with CIBP behaviors [17,18]. Similarly, the systemic administration of

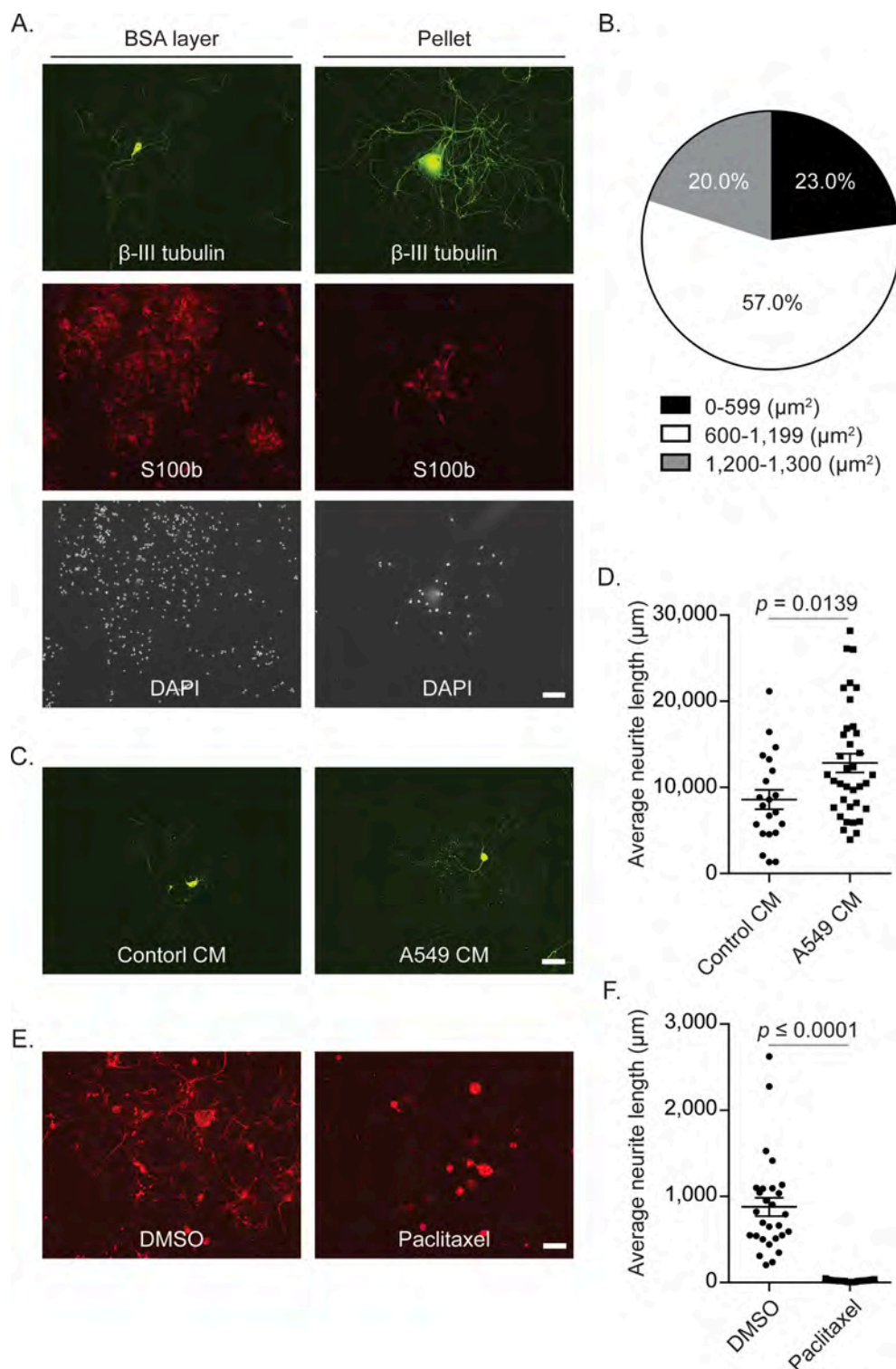
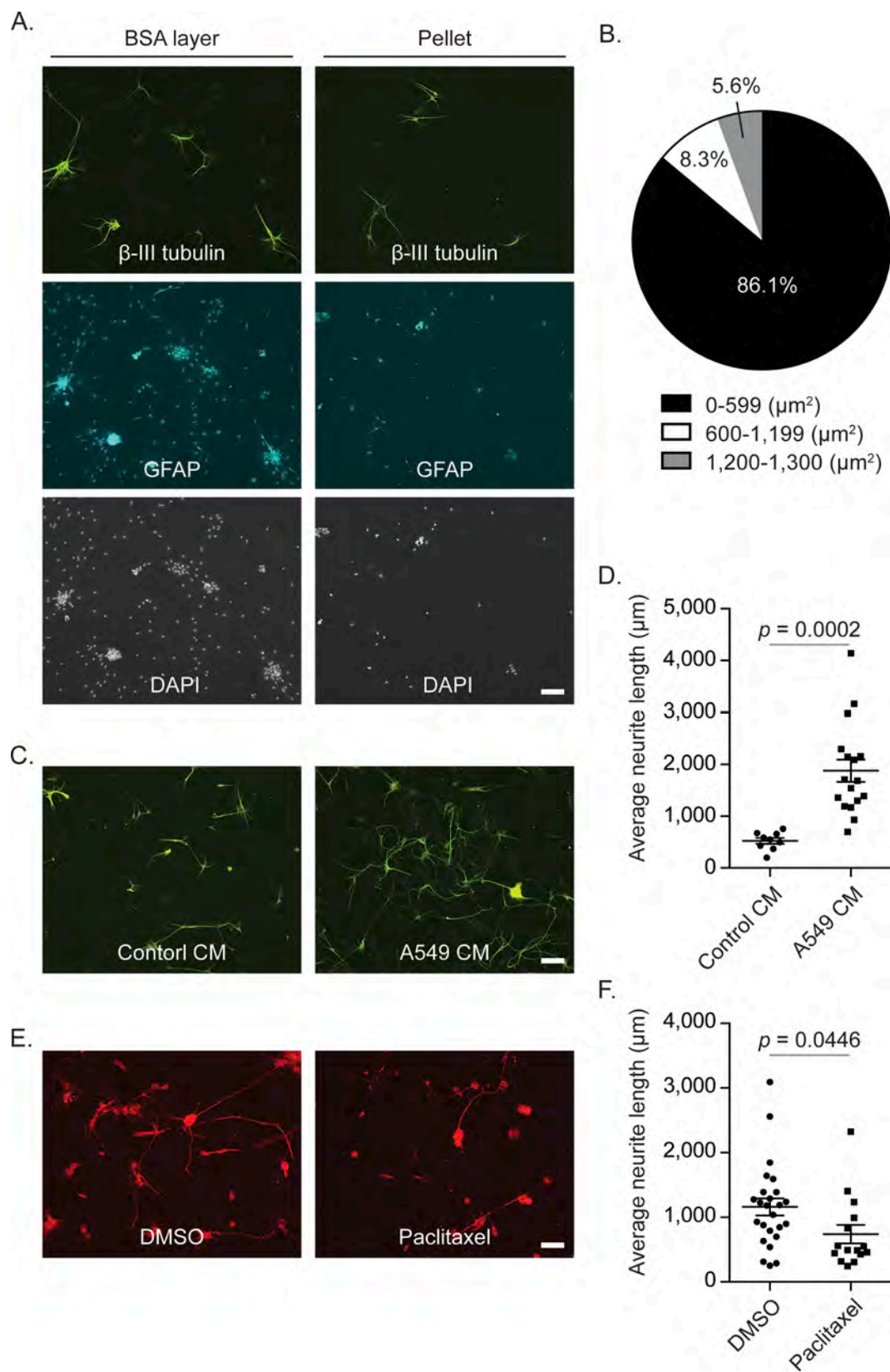


**Fig. 7.** Establishment of a non-human primate primary DRG sensory neuron culture. (A) Representative immunofluorescence images non-human primate DRGs (T12 and L1 of a healthy 8-year old female Rhesus macaque) before and after BSA centrifugation [3.5% (W/V) BSA solution]. Sensory neurons were stained with antibodies against  $\beta$ -III tubulin (green), and satellite cells were stained with antibodies against S100b (red), DAPI (gray) is used for nuclear staining. Magnification 10 $\times$ . Bar = 100  $\mu\text{m}$ . (B) Quantification analysis of the cell size distribution of non-human primate primary DRG sensory neurons ( $n = 309$ ). Areas of soma ( $\mu\text{m}^2$ ) of cells from (A) were measured using image J software. (C) Representative immunofluorescence images of non-human primate primary DRG sensory neurons treated with either control medium (Control CM) or human lung cancer cell line A549 cell-derived conditioned medium (A549 CM) (0% serum) for 72 h. Sensory neurons were stained with antibodies against  $\beta$ -III tubulin. Magnification 10 $\times$ . Bar = 100  $\mu\text{m}$ . (D) Quantification of the average of the total neurite length per image of (C): Mean  $\pm$  SEM. Student's  $t$ -test, significance at  $p \leq 0.05$ . The figure is a representative of two independent experiments, and 8–12 random images from each coverslip ( $n = 3$ ) were analyzed in a blind manner. (E) Representative immunofluorescence images of non-human primate primary DRG sensory neurons treated with either DMSO or paclitaxel (1  $\mu\text{M}$ ) for 24 h. Sensory neurons were stained with antibodies against PGP9.5. Magnification 10 $\times$ . Bar = 100  $\mu\text{m}$ . (F) Quantification of the average of the total neurite length per image of (E): Mean  $\pm$  SEM. Student's  $t$ -test, significance at  $p \leq 0.05$ . Experiment was performed once, and 8–12 random images from each coverslip ( $n = 3$ ) were analyzed in a blind manner. (For interpretation of the references to colour in this figure legend, the reader is referred to the web version of this article.)

paclitaxel to rodents led to a reduction of intraepidermal neuronal fiber density in the skin, which is a hall mark of CIPN [26,27]. Our *in vitro* primary DRG sensory culture manipulations were in line with these *in vivo* structural changes in peripheral sensory neurons. Thus, *in vitro* primary DRG sensory neuron culture system established in this study is an alternative tool to study the impact of soluble factors and/or direct cell–cell interactions on the architectural remodeling of sensory neurons.

Even though the use of rodent *in vivo* and *in vitro* models is essential

for the advancement of science, the results of pre-clinical studies do not always translate to the human condition. In fact, a recent meta-analysis of 2,000 scientific studies using animal models revealed that more than half of these studies (~60%) either could not be replicated or failed to move forward to clinical trials [63]. To overcome this hurdle, studies using human tissues are receiving growing attention. Therefore, an additional salient finding of our studies is the reproducibility of pathologic neurite outgrowth following cancer-derived CM and paclitaxel-induced neurotoxicity in non-human primate and human primary



(caption on next page)



**Fig. 8.** Establishment of a human primary DRG sensory neuron culture. (A) Representative immunofluorescence images human primary DRGs (T10 of a 41-year-old male patient with discitis/osteomyelitis) before and after BSA centrifugation [3.5% (W/V) BSA solution]. Sensory neurons were stained with antibodies against  $\beta$ -III tubulin (green), and satellite cells were stained with antibodies against glial fibrillary acidic protein (GFAP) (blue), DAPI (gray) is used for nuclear staining. Magnification 10x. Bar = 100  $\mu$ m. (B) Quantification analysis of the cell size distribution of human primary DRG sensory neurons ( $n = 72$ ). Areas of soma ( $\mu$ m<sup>2</sup>) of cells from (A) were measured using image J software. (C) Representative immunofluorescence images of human primary DRG sensory neurons treated with either control medium (Control CM) or human lung cancer cell line A549 cell-derived conditioned medium (A549 CM) (0% serum) for 72 h. Sensory neurons were stained with antibodies against  $\beta$ -III tubulin. Magnification 10x. Bar = 100  $\mu$ m. (D) Quantification of the average of the total neurite length per image of (C): Mean  $\pm$  SEM. Student's *t*-test, significance at  $p \leq 0.05$ . The figure is a representative of two independent experiments, and 8–13 random images from each coverslip ( $n = 2$ ) were analyzed in a blind manner. (E) Representative immunofluorescence images of human primary DRG sensory neurons treated with either DMSO or paclitaxel (1  $\mu$ M) for 24 h. Sensory neurons were stained with antibodies against PGP9.5. Magnification 10x. Bar = 100  $\mu$ m. (F) Quantification of the average of the total neurite length per image of (E): Mean  $\pm$  SEM. Student's *t*-test, significance at  $p \leq 0.05$ . Experiment was performed once, and 8–10 random images from each coverslip ( $n = 2$ ) were analyzed in a blind manner. (For interpretation of the references to colour in this figure legend, the reader is referred to the web version of this article.)

## DRG dissection



## DRG dissociation to obtain single cell suspensions

### Enzymatic digestion

Papain (Mouse: 30 min, Non-human primate: 1 h, Human: 1 h @ 37°C)

Collagenase/Dispase (Mouse: 30 min, Non-human primate: 1 h, Human: 1.5 h @ 37°C)

Mechanical dissociation (Gentle trituration 10–15 times using pipette tips)



## BSA centrifugation to separate sensory neurons (pellet) from satellite cells (BSA layer)

3.5% (W/V) BSA solution, 14 x g, 20 min @ room temperature



## Monolayer sensory neuron culture on Poly-D-lysine and laminin-coated coverslips

### Treatment

Cancer-derived CM (48–72 h @ 37°C)

Chemotherapy (48–72 h @ 37°C)



## Analyses

Immunohistochemistry and imaging

Neurite length analyses by Visiopharm app

Gene expression analyses by qPCR

Statistical analyses

**Fig. 9.** The schematic workflow of the primary DRG sensory neuron culture preparation and analyses. Dorsal root ganglia of mice, non-human primate, or human, were dissociated by enzymatic digestion and mechanical dissociation to obtain single cell suspensions. Then, the resulting cells were segregated into sensory neurons and satellite cells using a BSA gradient centrifugation. Thereafter, sensory neurons were plated onto Poly-D-lysine and laminin-coated coverslips to establish monolayer culture. In some cases, sensory neurons were exposed to exogenous factors, such as cancer-derived conditioned medium (CM) or chemotherapeutic agents, and then changes in nerve fiber length and gene expression were analyzed by immunohistochemical analyses and qPCR, respectively.

neuronal cultures, similar to murine neuronal cultures. Our findings also indicate that our approach with rodent sensory neurons provides an alternative to the use of non-human primate or human primary sensory neuron samples so that these precious resources can be used specifically for translational assessments after more thorough characterization with mouse neuron cells. We also recognized that the use of non-human primate or human primary sensory neurons is not trivial and requires a great deal of resources to obtain fresh DRGs. In fact, one of the major challenges that we faced in the course of our studies was the coordination of multiple departments and laboratories. However, these constraints become minor when there is solid coordination and commitment among different departments and laboratories, and a frequent communication and engagement between physicians and basic scientists.

Our study also uncovered that our approach has some limitations. For example, although successful, the numbers of sensory neurons recovered from human DRG were relatively lower than those from mice and non-human primate, which limited the number of conditions

performed in each experiment. This may be in part due to the difficulty in the digestion step of human DRGs. Human DRGs contains more connective tissues, including fibroblasts, blood vessels, and base membrane, than murine and non-human primate DRGs [64]. Consistent with this notion, during preparation of culture, the large number of fibroblasts were observed in human DRG, while few or no fibroblasts were seen in murine and non-human primate DRGs. Since thick connective tissues surrounding neurons may interfere with enzymatic reaction, it is crucial to cut the human DRGs into small pieces prior to the digestion step. Another potential limitation is the fact that the most abundant population of neurons in human DRG was small neurons in contrast to murine and non-human primate DRGs. Although the result is in line with previous findings [65,66], this suggests that our approach might not be ideal for studies targeting medium or large size of human sensory neurons. However, it is important to note that the cell size characterization method used in this study might not translate into non-human primate and/or human sensory neurons. Not only cell size differences, but also

there may be differences in responses to exogenous factors among DRGs derived from these species at a molecular and functional levels, although the effects of cancer-derived CM and paclitaxel treatments on nerve growth were consistent in all species. Indeed, nicotine evoked currents as well as nicotinic receptor expression patterns are significantly different between human and rodent DRGs [34]. Therefore, further subpopulation, molecular, and functional characterizations of murine, non-human primate, and human DRGs are clearly warranted.

Once logistic and technical optimization issues were overcome, we found that the image analysis of neurite length represents a challenge due to the lack of reliable methods to accurately measure the length of nerve fiber, and perhaps this is the reason why very few studies include this outcome. We found that manual measurement is accurate when performed by the same experimenter using a blinded method, but at the same time it is extremely time consuming and experimenter biases might reduce its reproducibility. These challenges prompted us to develop a method of image analysis aimed to reduce potential experimenter biases and increase efficiency in analysis time. In this study, we successfully developed a semi-automated method using the Visiopharm platform for the measurement of neurite length. The highly correlated values between this method and the manual approach using Image J demonstrate that our unbiased approach using the Visiopharm interface is accurate enough to consistently detect neurite length. One of the limitations of our approach however is the lack of tight correlation between automatically and manually generated soma counts. This might be attributed to the use of only one marker for two different cellular structures; i.e. NF200 staining was used to detect both soma count and neurite length. We uncovered that this approach does not allow the algorithm (APP) to differentiate a cluster of multiple neurons from individual neurons, something that the human eye could discern or infer. This limitation could be overcome by using different markers for neuronal soma (or nucleus) from neurites. Thus, the APP in this study was designed to maximize the accuracy of its neurite length measurements at the expense of accurate soma counts, since manually counting somas is significantly easier than manually tracing neurites. We are currently working to develop soma quantification APPs using nuclear stains for future studies capable of generating counts that are highly correlated with manual methods.

Although the importance of nerves for cancer progression has been appreciated [1], there are no treatments yet available which target the nerve-cancer interaction (e.g. cancer-induced nerve sprouting). In addition, chemotherapy is still the gold standard for cancer treatments and results in CIPN in many patients due to drug neurotoxicity. It is, therefore, critical to understand the interactions between cancer and/or chemotherapeutic agents, and sensory nerves, as well as how these interactions affect the progression of these painful complications, so that safer and more effective treatments can be developed. Although further electrophysiological analyses, phenotypical analyses, and chemical neural stimulation (e.g. capsaicin or KCL) on neuronal cell bodies might strengthen our findings, the measurement of neurite length and gene expression changes mediated by exogenous factors (e.g. cancer-derived factors, chemotherapeutic agents) can be a useful tool to elucidate the causes and mechanisms of these painful symptoms. For example, it has been suggested that nerve-related growth factors [29] or exosomes [30,56] derived from cancer cells induce cancer-related pain by stimulating neurite outgrowth [15–19], and that axonal damage mediated by chemotherapeutic agents through mitochondrial dysfunction in nerve cells and oxidative stress on nerve cells are responsible for CIPN symptoms [67]. We believe that our developed approaches could be used to reveal these underlying mechanisms. Moreover, the use of higher species' neuronal tissues in tandem with the development of an accurate and time-efficient methodology to measure neurite length under different pathological conditions will enhance clinical translational of our discovery. For success of this approach, a well-coordinated multi-disciplinary team between physicians and basic scientists, which we began to establish, is clearly essential.

## Author contributions

S.H.P., M.R.E., and Y.S. wrote the manuscript with input from all authors. S.H.P., M.R.E., C.M.P., M.C.K., R.S., W.H., E.A.R-S., and Y.S. designed study and contributed to data interpretation. S.H.P., M.M.F., H. D., and C.M.P. performed animal surgeries. M.C.K. provided monkey DRG. J.A.W. and W.H. provided human DRG. S.H.P. and M.M.F. established DRG culture. S.H.P., M.R.E., M.M.F., K.A.C., and C.M.P. performed immunohistochemistry and quantification analyses. F.H. performed statistical analyses. C.M.P., M.C.K., R.S., W.H., E.A.R-S., and Y.S. supervised the study. All authors reviewed and approved the final manuscript.

## Declaration of Competing Interest

Y.S. has received research funding from TEVA Pharmaceuticals, but not relevant to this study. No conflict of interest exists for remaining authors.

## Acknowledgements

This work is directly supported by the National Cancer Institute (R01-CA238888, Y.S.; R44-CA203184, Y.S.; and R21-CA248106, R.S. and E.A.R-S.), Department of Defense (W81XWH-17-1-0541, Y.S.; W81XWH-19-1-0045, Y.S.; and W81XWH-17-1-0542, C.M.P.), META-vivor (META-vivor Research Award, Y.S.), and the Wake Forest Baptist Comprehensive Cancer Center Internal Pilot Funding (Y.S.). This work is also supported by the National Cancer Institute's Cancer Center Support Grant award number P30-CA012197 issued to the Wake Forest Baptist Comprehensive Cancer Center. The authors wish to acknowledge the support of the Wake Forest Baptist Comprehensive Cancer Center Cell Engineering Shared Resource and Flow Cytometry Shared Resource, supported by the National Cancer Institute's Cancer Center Support Grant award number P30-CA012197. The content is solely the responsibility of the authors and does not necessarily represent the official views of the National Cancer Institute and Department of Defense.

## References

- [1] B. Boilly, S. Faulkner, P. Jobling, H. Hondermarck, Nerve dependence: from regeneration to cancer, *Cancer Cell* 31 (3) (2017) 342–354.
- [2] S. Faulkner, P. Jobling, B. March, C.C. Jiang, H. Hondermarck, Tumor neurobiology and the war of nerves in cancer, *Cancer Discov* 9 (6) (2019) 702–710.
- [3] N. Kuol, L. Stojanovska, V. Apostolopoulos, K. Nurgali, Role of the nervous system in cancer metastasis, *J. Exp. Clin. Cancer Res.* 37 (1) (2018) 5.
- [4] J.J. Fagan, B. Collins, L. Barnes, F. D'Amico, E.N. Myers, J.T. Johnson, Perineural invasion in squamous cell carcinoma of the head and neck, *Arch. Otolaryngol. Head Neck Surg.* 124 (6) (1998) 637–640.
- [5] C. Magnon, S.J. Hall, J. Lin, X. Xue, L. Gerber, S.J. Freedland, P.S. Frenette, Autonomic nerve development contributes to prostate cancer progression, *Science* 341 (6142) (2013) 1236361.
- [6] Y. Hayakawa, K. Sakitani, M. Konishi, S. Asfaha, R. Niikura, H. Tomita, B.W. Renz, Y. Tailor, M. Macchini, M. Middelhoff, Z. Jiang, T. Tanaka, Z.A. Dubeykovskaya, W. Kim, X. Chen, A.M. Urbanska, K. Nagar, C.B. Westphalen, M. Quante, C.S. Lin, M.D. Gershon, A. Hara, C.M. Zhao, D. Chen, D.L. Worthley, K. Koike, T.C. Wang, Nerve growth factor promotes gastric tumorigenesis through aberrant cholinergic signaling, *Cancer Cell* 31 (1) (2017) 21–34.
- [7] C.M. Zhao, Y. Hayakawa, Y. Kodama, S. Muthupalani, C.B. Westphalen, G. T. Andersen, A. Flatberg, H. Johannessen, R.A. Friedman, B.W. Renz, A.K. Sandvik, V. Beisvag, H. Tomita, A. Hara, M. Quante, Z. Li, M.D. Gershon, K. Kaneko, J. G. Fox, T.C. Wang, D. Chen, Denervation suppresses gastric tumorigenesis, *Sci. Transl. Med.* 6 (250) (2014) 250ra115.
- [8] J.L. Saloman, K.M. Albers, D. Li, D.J. Hartman, H.C. Crawford, E.A. Muha, A. D. Rhim, B.M. Davis, Ablation of sensory neurons in a genetic model of pancreatic ductal adenocarcinoma slows initiation and progression of cancer, *Proc Natl Acad Sci U S A* 113 (11) (2016) 3078–3083.
- [9] C. Parker, S. Nilsson, D. Heinrich, S.I. Helle, J.M. O'Sullivan, S.D. Fossa, A. Chodacki, P. Wiechno, J. Logue, M. Seke, A. Widmark, D.C. Johannessen, P. Hoskin, D. Bottomley, N.D. James, A. Solberg, I. Syndikus, J. Kliment, S. Wedel, S. Boehmer, M. Dall'Oglio, L. Franzen, R. Coleman, N.J. Vogelzang, C.G. O'Bryan-Tear, K. Staudacher, J. Garcia-Vargas, M. Shan, O.S. Bruland, O. Sartor, A. Investigators, Alpha emitter radium-223 and survival in metastatic prostate cancer, *N. Engl. J. Med.* 369 (3) (2013) 213–223.





- [10] P.W. Mantyh, The neurobiology of skeletal pain, *Eur. J. Neurosci.* 39 (3) (2014) 508–519.
- [11] P.W. Mantyh, D.R. Clohisy, M. Koltzenburg, S.P. Hunt, Molecular mechanisms of cancer pain, *Nat. Rev. Cancer* 2 (3) (2002) 201–209.
- [12] A.N. Lozano-Ondoua, A.M. Symons-Liguori, T.W. Vanderah, Cancer-induced bone pain: Mechanisms and models, *Neurosci Lett* 557 Pt A (2013) 52–59.
- [13] J.R. Ghilardi, H. Rohrich, T.H. Lindsay, M.A. Sevcik, M.J. Schwei, K. Kubota, K. G. Halvorson, J. Poblete, S.R. Chaplan, A.E. Dubin, N.I. Carruthers, D. Swanson, M. Kuskowski, C.M. Flores, D. Julius, P.W. Mantyh, Selective blockade of the capsaicin receptor TRPV1 attenuates bone cancer pain, *J. Neurosci.* 25 (12) (2005) 3126–3131.
- [14] T. Yoneda, K. Hata, M. Nakanishi, M. Nagae, T. Nagayama, H. Wakabayashi, T. Nishisho, T. Sakurai, T. Hiraga, Involvement of acidic microenvironment in the pathophysiology of cancer-associated bone pain, *Bone* 48 (1) (2011) 100–105.
- [15] K.G. Halvorson, K. Kubota, M.A. Sevcik, T.H. Lindsay, J.E. Sotillo, J.R. Ghilardi, T. J. Rosol, L. Boustany, D.L. Shelton, P.W. Mantyh, A blocking antibody to nerve growth factor attenuates skeletal pain induced by prostate tumor cells growing in bone, *Cancer Res.* 65 (20) (2005) 9426–9435.
- [16] A.P. Bloom, J.M. Jimenez-Andrade, R.N. Taylor, G. Castaneda-Corral, M. J. Kaczmarek, K.T. Freeman, K.A. Coughlin, J.R. Ghilardi, M.A. Kuskowski, P. W. Mantyh, Breast cancer-induced bone remodeling, skeletal pain, and sprouting of sensory nerve fibers, *J. Pain* 12 (6) (2011) 698–711.
- [17] J.R. Ghilardi, K.T. Freeman, J.M. Jimenez-Andrade, W.G. Mantyh, A.P. Bloom, M. A. Kuskowski, P.W. Mantyh, Administration of a tropomyosin receptor kinase inhibitor attenuates sarcoma-induced nerve sprouting, neuroma formation and bone cancer pain, *Mol Pain* 6 (2010) 87.
- [18] J.M. Jimenez-Andrade, A.P. Bloom, J.I. Stake, W.G. Mantyh, R.N. Taylor, K. T. Freeman, J.R. Ghilardi, M.A. Kuskowski, P.W. Mantyh, Pathological sprouting of adult nociceptors in chronic prostate cancer-induced bone pain, *J. Neurosci.* 30 (44) (2010) 14649–14656.
- [19] W.G. Mantyh, J.M. Jimenez-Andrade, J.I. Stake, A.P. Bloom, M.J. Kaczmarek, R. N. Taylor, K.T. Freeman, J.R. Ghilardi, M.A. Kuskowski, P.W. Mantyh, Blockade of nerve sprouting and neuroma formation markedly attenuates the development of late stage cancer pain, *Neuroscience* 171 (2) (2010) 588–598.
- [20] T.J. Price, M.D. Louria, D. Candelario-Soto, G.O. Dussor, N.A. Jeske, A. M. Patwardhan, A. Diogenes, A.A. Trott, K.M. Hargreaves, C.M. Flores, Treatment of trigeminal ganglion neurons in vitro with NGF, GDNF or BDNF: effects on neuronal survival, neurochemical properties and TRPV1-mediated neuropeptide secretion, *BMC Neurosci* 6 (2005) 4.
- [21] D. Hong, M.R. Byers, R.J. Oswald, Dexamethasone treatment reduces sensory neuropeptides and nerve sprouting reactions in injured teeth, *Pain* 55 (2) (1993) 171–181.
- [22] J.R. Ghilardi, K.T. Freeman, J.M. Jimenez-Andrade, K.A. Coughlin, M. J. Kaczmarek, G. Castaneda-Corral, A.P. Bloom, M.A. Kuskowski, P.W. Mantyh, Neuroplasticity of sensory and sympathetic nerve fibers in a mouse model of a painful arthritic joint, *Arthritis Rheum.* 64 (7) (2012) 2223–2232.
- [23] S.R. Chartier, M.L. Thompson, G. Longo, M.N. Fealk, L.A. Majuta, P.W. Mantyh, Exuberant sprouting of sensory and sympathetic nerve fibers in nonhealed bone fractures and the generation and maintenance of chronic skeletal pain, *Pain* 155 (11) (2014) 2323–2336.
- [24] W.H. Xiao, G.J. Bennett, Chemotherapy-evoked neuropathic pain: Abnormal spontaneous discharge in A-fiber and C-fiber primary afferent neurons and its suppression by acetyl-L-carnitine, *Pain* 135 (3) (2008) 262–270.
- [25] J.P. Cata, H.R. Weng, A.W. Burton, E. Villareal, S. Giralt, P.M. Dougherty, Quantitative sensory findings in patients with bortezomib-induced pain, *J. Pain* 8 (4) (2007) 296–306.
- [26] C. Siau, W. Xiao, G.J. Bennett, Paclitaxel- and vincristine-evoked painful peripheral neuropathies: loss of epidermal innervation and activation of Langerhans cells, *Exp. Neurol.* 201 (2) (2006) 507–514.
- [27] G. Lauria, R. Lombardi, M. Borgna, P. Penza, R. Bianchi, C. Savino, A. Canta, G. Nicolini, P. Marmiroli, G. Cavaletti, Intraepidermal nerve fiber density in rat foot pad: neuropathologic-neurophysiologic correlation, *J. Peripher. Nerv. Syst.* 10 (2) (2005) 202–208.
- [28] K.P. Das, T.M. Freudenrich, W.R. Mundy, Assessment of PC12 cell differentiation and neurite growth: a comparison of morphological and neurochemical measures, *Neurotoxicol. Teratol.* 26 (3) (2004) 397–406.
- [29] A.A. Bapat, R.M. Munoz, D.D. Von Hoff, H. Han, Blocking Nerve Growth Factor Signaling Reduces the Neural Invasion Potential of Pancreatic Cancer Cells, *PLoS ONE* 11 (10) (2016), e0165586.
- [30] M. Madeo, P.L. Colbert, D.W. Vermeer, C.T. Lucido, J.T. Cain, E.G. Vichaya, A. J. Grossberg, D. Muirhead, A.P. Rickel, Z. Hong, J. Zhao, J.M. Weimer, W. C. Spanos, J.H. Lee, R. Dantzer, P.D. Vermeer, Cancer exosomes induce tumor innervation, *Nat. Commun.* 9 (1) (2018) 4284.
- [31] W. Chang, T. Berta, Y.H. Kim, S. Lee, S.Y. Lee, R.R. Ji, Expression and role of voltage-gated sodium channels in human dorsal root ganglion neurons with special focus on Nav1.7, species differences, and regulation by paclitaxel, *Neurosci. Bull.* 34 (1) (2018) 4–12.
- [32] S.A. Malin, B.M. Davis, D.C. Molliver, Production of dissociated sensory neuron cultures and considerations for their use in studying neuronal function and plasticity, *Nat. Protoc.* 2 (1) (2007) 152–160.
- [33] R. Liu, G. Lin, H. Xu, An efficient method for dorsal root ganglia neurons purification with a one-time anti-mitotic reagent treatment, *PLoS ONE* 8 (4) (2013), e60558.
- [34] X. Zhang, J.E. Hartung, R.L. Friedman, H.R. Koerber, I. Belfer, M.S. Gold, Nicotine evoked currents in human primary sensory neurons, *J. Pain* 20 (7) (2019) 810–818.
- [35] Y. Li, C.E. Tatsui, L.D. Rhines, R.Y. North, D.S. Harrison, R.M. Cassidy, C. A. Johansson, A.K. Kosturakis, D.D. Edwards, H. Zhang, P.M. Dougherty, Dorsal root ganglion neurons become hyperexcitable and increase expression of voltage-gated T-type calcium channels (Cav3.2) in paclitaxel-induced peripheral neuropathy, *Pain* 158 (3) (2017) 417–429.
- [36] R.Y. North, Y. Li, P. Ray, L.D. Rhines, C.E. Tatsui, G. Rao, C.A. Johansson, H. Zhang, Y.H. Kim, B. Zhang, G. Dussor, T.H. Kim, T.J. Price, P.M. Dougherty, Electrophysiological and transcriptomic correlates of neuropathic pain in human dorsal root ganglion neurons, *Brain* 142 (5) (2019) 1215–1226.
- [37] M.V. Valtcheva, B.A. Copits, S. Davidson, T.D. Sheahan, M.Y. Pullen, J.G. McCall, K. Dikranian, R.W.t. Gereau, Surgical extraction of human dorsal root ganglia from organ donors and preparation of primary sensory neuron cultures, *Nat. Protoc.* 11 (10) (2016) 1877–1888.
- [38] S. Davidson, J.P. Golden, B.A. Copits, P.R. Ray, S.K. Vogt, M.V. Valtcheva, R. E. Schmidt, A. Ghatti, T.J. Price, R.W.T. Gereau, Group II mGluRs suppress hyperexcitability in mouse and human nociceptors, *Pain* 157 (9) (2016) 2081–2088.
- [39] P. Yao, Y. Ding, Z. Han, Y. Mu, T. Hong, Y. Zhu, H. Li, Suppression of asparaginyl endopeptidase attenuates breast cancer-induced bone pain through inhibition of neurotrophin receptors, *Mol. Pain* 13 (2017), 1744806917708127.
- [40] T. Yoneda, P.J. Williams, T. Hiraga, M. Niewolna, R. Nishimura, A bone-seeking clone exhibits different biological properties from the MDA-MB-231 parental human breast cancer cells and a brain-seeking clone in vivo and in vitro, *J. Bone Miner. Res.* 16 (8) (2001) 1486–1495.
- [41] H. Wakabayashi, S. Wakisaka, T. Hiraga, K. Hata, R. Nishimura, M. Tominaga, T. Yoneda, Decreased sensory nerve excitation and bone pain associated with mouse Lewis lung cancer in TRPV1-deficient mice, *J. Bone Miner. Metab.* 36 (3) (2018) 274–285.
- [42] T.T. Wu, R.A. Sikes, Q. Cui, G.N. Thalmann, C. Kao, C.F. Murphy, H. Yang, H. E. Zhou, G. Balian, L.W. Chung, Establishing human prostate cancer cell xenografts in bone: induction of osteoblastic reaction by prostate-specific antigen-producing tumors in athymic and SCID/bg mice using LNCaP and lineage-derived metastatic sublines, *Int. J. Cancer* 77 (6) (1998) 887–894.
- [43] J. Popko, A. Fernandes, D. Brites, L.M. Lanier, Automated analysis of NeuronJ tracing data, *Cytometry A* 75 (4) (2009) 371–376.
- [44] P. Cottrell, S. Ahmed, C. James, J. Hodson, P.J. McDonnell, S. Rauz, G.P. Williams, Neuron J is a rapid and reliable open source tool for evaluating corneal nerve density in herpes simplex keratitis, *Invest. Ophthalmol. Vis. Sci.* 55 (11) (2014) 7312–7320.
- [45] P.B. Tran, R.E. Miller, S. Ishihara, R.J. Miller, A.M. Malfait, Spinal microglial activation in a murine surgical model of knee osteoarthritis, *Osteoarthritis Cartilage* 25 (5) (2017) 718–726.
- [46] S. Katzenell, J.R. Cabrera, B.J. North, D.A. Leib, Isolation, purification, and culture of primary murine sensory neurons, *Methods Mol. Biol.* 1656 (2017) 229–251.
- [47] T. Dong, S. Li, W. Liu, M. Yan, J. Yu, X. Deng, A new method for primary culture of mouse dorsal root ganglion neurons, *bioRxiv* (2018) 466110.
- [48] M. Au Fornaro, H. Au Sharhiya, V. Au Tiwari, Adult mouse DRG explant and dissociated cell models to investigate neuroplasticity and responses to environmental insults including viral infection, *JoVE* 133 (2018) e56757.
- [49] R.R. Jessen, Glial cells, *Int. J. Biochem. Cell Biol.* 36 (10) (2004) 1861–1867.
- [50] R.D. Fields, B. Stevens-Graham, New insights into neuron-glia communication, *Science* 298 (5593) (2002) 556–562.
- [51] X. Zhao, Z. Tang, H. Zhang, F.E. Atianjoh, J.Y. Zhao, L. Liang, W. Wang, X. Guan, S. C. Kao, V. Tiwari, Y.J. Gao, P.N. Hoffman, H. Cui, M. Li, X. Dong, Y.X. Tao, A long noncoding RNA contributes to neuropathic pain by silencing Kcna2 in primary afferent neurons, *Nat. Neurosci.* 16 (8) (2013) 1024–1031.
- [52] J.E. Roa-Coria, J.B. Pineda-Farias, P. Barragan-Iglesias, G.N. Quinonez-Bastidas, A. Zuniga-Romero, J.C. Huerta-Cruz, J.G. Reyes-Garcia, F.J. Flores-Murrieta, V. Granados-Soto, H.I. Rocha-Gonzalez, Possible involvement of peripheral TRP channels in the hydrogen sulfide-induced hyperalgesia in diabetic rats, *BMC Neurosci* 20 (1) (2019) 1.
- [53] Q. Mao, J. Yuan, X. Ming, S. Wu, L. Chen, A. Bekker, T. Yang, Y.X. Tao, Role of dorsal root ganglion K2p1.1 in peripheral nerve injury-induced neuropathic pain, *Mol. Pain* 13 (2017), 1744806917701135.
- [54] C. Lyu, G.W. Lyu, A. Martinez, T.S. Shi, Effect of nerve injury on the number of dorsal root ganglion neurons and autotomy behavior in adult Bax-deficient mice, *J. Pain Res* 10 (2017) 2079–2087.
- [55] M. Malet, P.R. Brumovsky, VGLUTs and Glutamate Synthesis-Focus on DRG Neurons and Pain, *Biomolecules* 5 (4) (2015) 3416–3437.
- [56] A. Bhattacharya, M.N. Janal, R. Veeramachaneni, I. Dolgalev, Z. Dubeykovskaya, N.H. Tu, H. Kim, S. Zhang, A.K. Wu, M. Hagiwara, A.R. Kerr, M.D. DeLacure, B. L. Schmidt, D.G. Albertson, Oncogenes overexpressed in metastatic oral cancers from patients with pain: potential pain mediators released in exosomes, *Sci. Rep.* 10 (1) (2020) 14724.
- [57] F.A. Fitzpatrick, R. Wheeler, The immunopharmacology of paclitaxel (Taxol), docetaxel (Taxotere), and related agents, *Int. Immunopharmacol.* 3 (13–14) (2003) 1699–1714.
- [58] A.B. Oestreich, P.N. De Graan, W.H. Gispen, J. Verhaagen, L.H. Schrama, B-50, the growth associated protein-43: modulation of cell morphology and communication in the nervous system, *Prog. Neurobiol.* 53 (6) (1997) 627–686.
- [59] L. Leung, C.M. Cahill, TNF-alpha and neuropathic pain—a review, *J. Neuroinflammation* 7 (2010) 27.
- [60] J. Gonzalez-Lopez, F. Macias-Garcia, J. Larino-Noia, J.E. Dominguez-Munoz, Theoretical approach to local infusion of antibiotics for infected pancreatic necrosis, *Pancreatology* 16 (5) (2016) 719–725.



- [61] J. Wei, M. Li, D. Wang, H. Zhu, X. Kong, S. Wang, Y.L. Zhou, Z. Ju, G.Y. Xu, G. Q. Jiang, Overexpression of suppressor of cytokine signaling 3 in dorsal root ganglion attenuates cancer-induced pain in rats, *Mol. Pain* 13 (2017), 1744806916688901.
- [62] K. Mandai, T. Guo, C. St Hillaire, J.S. Meabon, K.C. Kanning, M. Bothwell, D. D. Ginty, LIG family receptor tyrosine kinase-associated proteins modulate growth factor signals during neural development, *Neuron* 63 (5) (2009) 614–627.
- [63] N. Tageja, Bridging the translation gap - new hopes, new challenges, *Fundam. Clin. Pharmacol.* 25 (2) (2011) 163–171.
- [64] R.V. Haberberger, C. Barry, N. Dominguez, D. Matusica, Human dorsal root ganglia, *Front. Cell. Neurosci.* 13 (271) (2019).
- [65] S. Davidson, B.A. Copits, J. Zhang, G. Page, A. Ghetti, R.W. Gereau, Human sensory neurons: Membrane properties and sensitization by inflammatory mediators, *Pain* 155 (9) (2014) 1861–1870.
- [66] U. Anand, M. Sinisi, M. Fox, A. MacQuillan, T. Quick, Y. Korchev, C. Bountra, T. McCarthy, P. Anand, Mycolactone-mediated neurite degeneration and functional effects in cultured human and rat DRG neurons: Mechanisms underlying hypoalgesia in Buruli ulcer, *Mol. Pain* 12 (2016).
- [67] Y. Han, M.T. Smith, Pathobiology of cancer chemotherapy-induced peripheral neuropathy (CIPN), *Front. Pharmacol.* 4 (2013) 156.

**ARTICLE**

# Nicotine promotes brain metastasis by polarizing microglia and suppressing innate immune function

Shih-Ying Wu<sup>1</sup>, Fei Xing<sup>1</sup>, Sambad Sharma<sup>1</sup>, Kerui Wu<sup>1</sup>, Abhishek Tyagi<sup>1</sup>, Yin Liu<sup>1</sup>, Dan Zhao<sup>1</sup>, Ravindra Pramod Deshpande<sup>1</sup>, Yusuke Shiozawa<sup>1</sup>, Tamjeed Ahmed<sup>2</sup>, Wei Zhang<sup>1</sup>, Michael Chan<sup>4</sup>, Jimmy Ruiz<sup>2,3</sup>, Thomas W. Lycan<sup>2</sup>, Andrew Dothard<sup>2</sup>, and Kounosuke Watabe<sup>1</sup>

**Up to 40% of lung cancer patients develop brain metastasis, and the median survival of these patients remains less than 6 months. Smoking is associated with lung cancer. However, how smoking impacts the development of brain metastasis remains elusive. We examined 281 lung cancer patients with distant metastasis and found that smokers exhibited a significantly high incidence of brain metastasis. We found that nicotine enhanced brain metastasis, while a depletion of microglia suppressed this effect in vivo. Nicotine skewed the polarity of microglia to the M2 phenotype, thereby increasing the secretion of IGF-1 and CCL20, which promoted tumor progression and stemness. Importantly, nicotine enhanced the expression of SIRPα in microglia and restricted their phagocytic ability. We also identified a compound, parthenolide, that suppressed brain metastasis by blocking M2 polarization. Our results indicate that nicotine promotes brain metastasis by skewing the polarity of M2 microglia, which enhances metastatic tumor growth. Our results also highlight a potential risk of using nicotine for tobacco cessation.**

## Introduction

Approximately 170,000 patients in the United States are diagnosed with brain metastasis every year (Ellis et al., 2012). Lung, breast, and skin cancers are the most common tumor types that metastasize to the brain (Bacha et al., 2018; Huang et al., 2018; Redmer, 2018; Xing et al., 2018). Patients with metastatic lung cancer have a very poor prognosis (Mujoomdar et al., 2007), and those with brain metastasis have a 1-yr survival rate of 4–20% (Gaspar et al., 1997; Sperduto et al., 2008; Verger et al., 2005). Despite significant improvements in the treatment of metastatic cancer, the therapeutic options for brain metastasis are still limited mainly due to inefficient drug delivery to brain as well as limited surgical approaches to multiple metastases. Radiation therapies, such as stereotactic radio surgery and fractionated whole brain radiation, are standard therapeutic techniques employed for brain metastasis; however, they provide only limited local tumor control and, more often than not, intracranial failure leading to neurological death. The development of lung cancer brain metastasis is a complex process, requiring the invasion of primary tumor cells into surrounding tissue and vessels, trafficking through the circulatory system, and colonizing into the brain parenchyma (Fidler, 2015). Therefore, understanding the underlying mechanisms that drive brain

metastasis and developing more effective therapies are urgently needed.

Cigarette smoking is one of the major risk factors for lung cancer (Lee et al., 2012). Our previous study have shown that smoking is correlated to rapid progression of lung cancer brain metastasis (Shenker et al., 2017). Tobacco smoke contains a toxic mix of >7,000 chemicals. Among them, nicotine is a major cigarette component associated with human tobacco consumption and addiction (Braverman, 1999; Heishman, 1999). Nicotine is not a carcinogen; however, several studies have reported the tumor-promoting effects of nicotine via activation of nicotinic acetylcholine (nACh) receptor in the tumor cells. The nACh receptor is comprised of combination of multiple subunits, and they are expressed in a variety of brain cells including neuron, astrocytes, endothelial cells, and microglia (Mazzaferro et al., 2017). The α4β2 is the most abundant class of nACh receptor in the brain and is the principal mediator of nicotine dependence (Hawkins et al., 2004; Mazzaferro et al., 2017). This suggests that nicotine may be capable of reprogramming the brain tumor microenvironment (TME) via activation of its receptor to promote tumor progression.

Several studies have shown that the interaction of neoplastic cells with microglial cells, brain-residing macrophages, profoundly

<sup>1</sup>Department of Cancer Biology, Wake Forest Baptist Medical Center, Winston-Salem, NC; <sup>2</sup>Department of Medicine, Section of Oncology and Hematology, Wake Forest Baptist Medical Center, Winston-Salem, NC; <sup>3</sup>Section of Hematology and Oncology, W.G. (Bill) Hefner VA Medical Center, Salisbury, NC; <sup>4</sup>Department of Radiation Oncology, Wake Forest Baptist Medical Center, Winston-Salem, NC.

Correspondence to Kounosuke Watabe: [kwatabe@wakehealth.edu](mailto:kwatabe@wakehealth.edu).

© 2020 Wu et al. This article is distributed under the terms of an Attribution–Noncommercial–Share Alike–No Mirror Sites license for the first six months after the publication date (see <http://www.rupress.org/terms/>). After six months it is available under a Creative Commons License (Attribution–Noncommercial–Share Alike 4.0 International license, as described at <https://creativecommons.org/licenses/by-nc-sa/4.0/>).

affects tumor progression in glioblastoma (da Fonseca and Badie, 2013; Roesch et al., 2018; Wei et al., 2013). In brain metastatic lesions of lung cancer patients, abundant activated microglia were found to be infiltrated (He et al., 2006). Importantly, nACh receptor has been shown to be expressed on microglia (Morioka et al., 2015; Sadigh-Eteghad et al., 2016), raising the possibility that nicotine may stimulate microglia's immunomodulatory pathways, which affects their immune function. Microglia are known to polarize into classical (M1) or alternative (M2) phenotypes by various microenvironment stimuli (Wei et al., 2013; Wu and Watabe, 2017). M1 cells suppress tumors by releasing cytotoxic factors and also by phagocytosis. In contrast, M2 cells have a pro-tumor response by activating immunosuppressive factors. It is virtually unknown how metastatic cells escape immune attack of microglia and then colonize in the brain. In this study, we showed that nicotine promoted lung cancer brain metastasis by enhancing both tumor progression and stemness by skewing microglial polarization and inhibiting its anti-tumor phagocytic ability. We also found that a natural compound, parthenolide (PTL), effectively suppressed tumor progression and stemness by blocking nicotine-induced polarization of the microglia in the brain.

## Results

### Smoking increases brain metastasis of lung cancer

To examine the effect of tobacco smoking on brain metastasis, we analyzed the incidence and mortality rate of 281 patients with lung cancer brain metastasis (Fig. S1) with or without a history of smoking. All patients were diagnosed with stage IV disease. Among them, 79 patients were diagnosed with brain metastasis. 59 patients were current smokers at the time of diagnosis and treatment, while 222 of them had either a previous or no smoking history. We found that the incidence of brain metastasis was significantly higher in current smokers compared with the never or the former smokers group (Fig. 1 A). The results of Kaplan–Meier analyses indicate that the current smokers were associated with worse brain metastasis progression free (Fig. 1 B) and overall survival (Fig. 1 C) compared with those who were not currently smoking. Since activation of microglia was previously reported to be associated with brain tumor progression (da Fonseca and Badie, 2013; He et al., 2006; Roesch et al., 2018; Wei et al., 2013), we examined the status of microglia activation in brain metastatic lesions and found that current smokers exhibited a significantly increased number of Iba1<sup>+</sup> (pan-microglial marker) cells in the brain metastatic lesions (Fig. 1 D) compared with noncurrent smokers. Importantly, the majority of infiltrated microglia in current smokers was identified to be pro-tumor M2 microglia (CD206<sup>+</sup> cells; Fig. 1 D). These results suggest a role of smoking-mediated M2 microglial polarization in brain metastatic tumor growth.

### Nicotine promotes brain metastasis through activation of microglia

Because M2 microglia are abundantly infiltrated in brain metastatic lesions of current smokers, we examined the possibility that nicotine promotes brain metastasis by polarizing microglia to M2 microglia. We first examined the expression of nicotine receptors in microglia cells and in tumor cells and found that

microglia expressed high levels of  $\alpha 4\beta 2$ , which is the most sensitive receptor of nicotine in the brain (Fig. 2 A). We also found that microglia expressed a significantly higher level of  $\alpha 4\beta 2$  receptor than macrophage (Fig. S2 A). Moreover, the expression of  $\alpha 4\beta 2$  receptor in microglia dramatically increased upon nicotine treatment (Fig. S2 A). We then examined the effect of nicotine on microglia polarization and tumor progression using the LL/2 mouse Lewis lung carcinoma model. The LL/2 cell is originated from the C57BL/6 mouse; however, this cell line can grow tumors in both C57BL/6 and BALB/c mice as reported previously (Janker et al., 2018; Kamei et al., 2009; Scholar et al., 1989). Therefore, we tested the effect of nicotine in both models. We intracardially inoculated luciferase-labeled LL/2 cells into both wild-type mice (C57BL/6 or BALB/c) followed by injecting nicotine (1 mg/kg) every 3 d until the end point. We found that nicotine significantly increased the incidence and growth of brain metastasis in both models (Fig. S2, B–D, for C57BL/6 model; Fig. 2 B and Fig. S2, E and F, for BALB/c model). On the other hand, nicotine did not promote bone metastasis (Fig. 2 B). The result of our immunohistochemical analysis for brain metastatic lesions revealed that high levels of activated microglial cells accumulated in the tumor mass in the nicotine-treated group (Fig. 2 C). Importantly, the majority of these microglia in the nicotine-treated mice were found to be M2 microglia (CD206<sup>+</sup>/Iba1<sup>+</sup>), and fewer M1 microglia (Iba1<sup>+</sup>/F4/80<sup>+</sup>) were identified in the brain lesions (Fig. 2 D and Fig. S2, G and H), suggesting that nicotine promoted microglia polarization to the M2 phenotype in the brain metastatic lesions. Infiltrated peripheral macrophages/microglia are known to modulate brain tumor progression (Bacha et al., 2018; Ellis et al., 2012). To define the exact role of macrophage and microglia on brain metastasis, we stained brain metastatic tumors with antibody against the macrophage marker CD45. We also examined the ratio of the number of microglia (CD45<sup>+</sup>/Iba1<sup>+</sup>) and peripheral macrophages (CD45<sup>+</sup>/Iba1<sup>+</sup>) in the brain metastatic lesions and found that macrophages comprised only 12–14% of CD45<sup>+</sup>/Iba1<sup>+</sup> cells, and the number of macrophages was not altered between nicotine-treated and -untreated groups (Fig. S2 I). These results strongly suggest that nicotine promotes brain metastasis by skewing microglia to the M2 phenotype. To further validate this hypothesis, we examined the effect of depletion of “original” microglia by treating animals with the inhibitor for CSF1 receptor (CSF1R), PLX3397. CSF1 signaling is necessary for microglia viability, and treating mice with PLX3397 has been previously shown to eliminate ~99% of all microglia in the brain (Elmore et al., 2014). We therefore treated immune-competent wild-type mice with PLX3397 and transplanted them with LL/2 mouse lung cancer cells followed by nicotine treatment. To avoid a whole-body effect of PLX3397, the PLX3397 was locally injected into brain through intracranial injection 1 wk after the transplantation of LL/2 cells followed by nicotine treatment (Fig. S2 J). Strikingly, blocking microglia by PLX3397 significantly suppressed nicotine-related brain metastasis of lung cancer (Fig. 2, E–G), prolonged brain metastasis-free survival (Fig. 2 H), and repressed the nicotine-related M2 microglial polarization (Fig. 2, I and J) in the BALB/c mouse model. Similarly, PLX3397 suppressed nicotine-related brain metastasis and inhibited M2

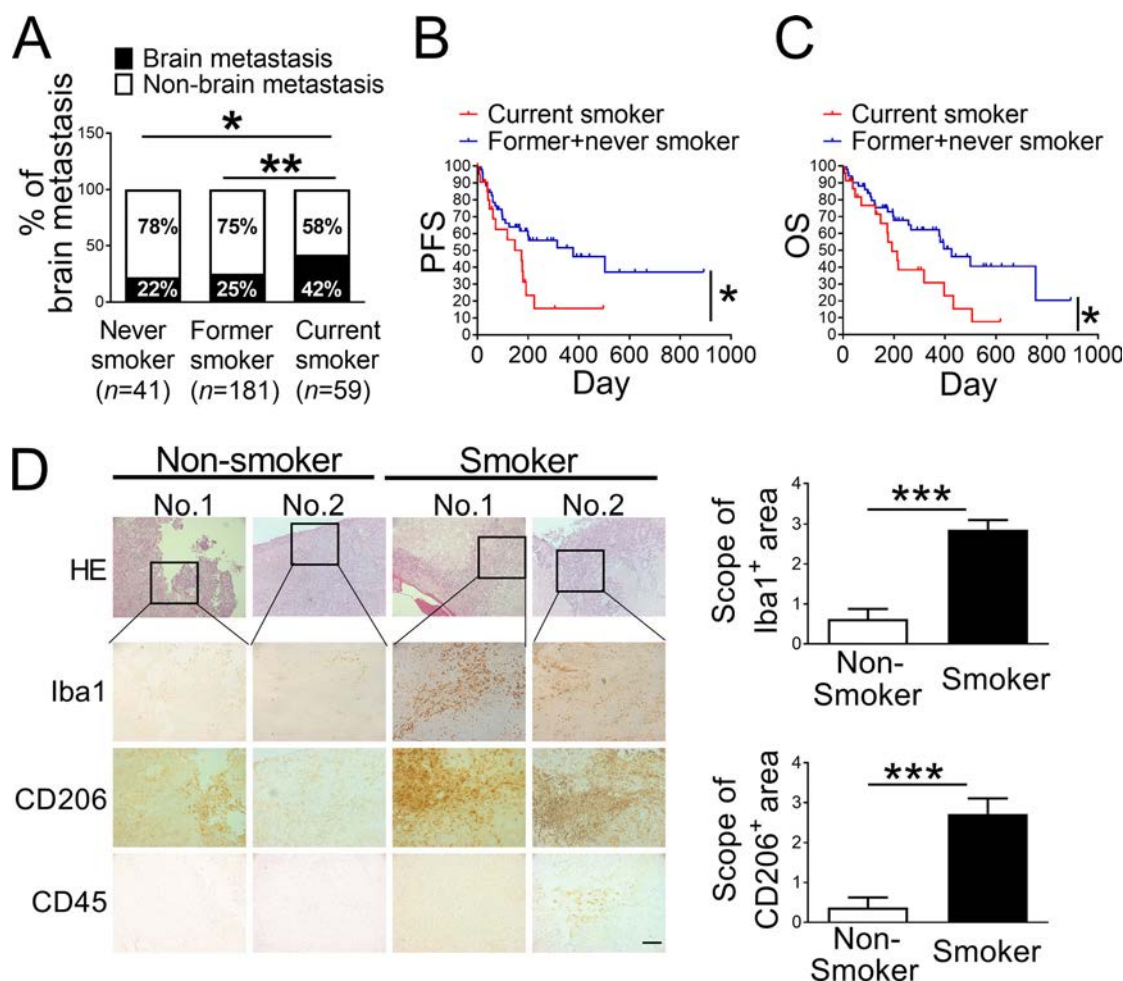


**Figure 1. Cigarette smoking increases incidence and mortality rate of lung cancer brain metastasis.** (A) Incidence of brain metastasis among 281 stage IV lung cancer patients composed of both current and noncurrent smokers at the time of diagnosis. All patients were admitted to Wake Forest Baptist Hospital. (B and C) Progression-free survival (PFS; B) and overall survival (OS; C) of patients with brain metastasis (n = 79) and with or without smoking history were examined by Kaplan–Meier analysis. (D) Representative images of immunohistochemical analysis for Iba1<sup>+</sup>, CD206<sup>+</sup>, and CD45<sup>+</sup> cells in the H&E-stained brain metastatic lesions of lung cancer patients who were current smokers (n = 7) and noncurrent smokers (n = 4). Scale bar, 100  $\mu$ m. \*, P < 0.05; \*\*, P < 0.01; and \*\*\*, P < 0.001.

microglial polarization in the C57BL/6 mouse model (Fig. S2, K–N). We also treated nude mice with PLX3397 and transplanted them with H2030BrM cells via an intracardiac injection followed by nicotine treatment (Fig. S2, O–R). Nicotine-induced brain metastasis was significantly suppressed after PLX3397 treatment (Fig. S2, O–Q). The brain metastasis-free survival was also significantly prolonged by PLX3397 treatment (Fig. S2 R). PLX3397 treatment showed no detectable liver toxicity (Fig. S2 S). These results suggest that the nicotine-induced brain metastasis is indeed mediated by the effect of nicotine on microglia.

#### Nicotine skewed M2 microglial polarization

As shown in Fig. 2 D, the number of M2 microglia was increased after nicotine treatment, suggesting that nicotine promotes microglial polarization. To further investigate the effect of nicotine on microglia polarization, the microglial cells were treated with nicotine followed by measurement of expression of M1 and M2 markers. Our results showed that nicotine did not affect tumor cell proliferation (Fig. S2 T) at 1  $\mu$ M concentration, but the

same dose of nicotine significantly increased the mRNA expression of M2-related genes, *arginase-1* (*Arg1*), *arginase-2* (*Arg2*), and *CD204*, in both human and mouse microglial cells lines (Fig. 3, A and B) and mouse primary microglial cells (Fig. 3 C). Since STAT3 pathway is involved in M2 microglia (Qin et al., 2017), we examined the status of phospho-STAT3 and JAK expression in microglia with or without nicotine treatment, and found that nicotine treatment indeed enhanced the expressions of JAK/STAT3 (Fig. 3 D). We then treated the microglia with nicotine in the presence of STAT3 inhibitor (STAT3i) and found that inhibiting the STAT3 by STAT3i significantly suppressed the nicotine-induced STAT3 activation (Fig. 3 E). The *Arg1* gene is an M2 marker and is known to be regulated by STAT3 (Yi and Kim, 2017). We found that nicotine-induced up-regulation of the *Arg1* gene promoter was significantly suppressed by STAT3i treatment (Fig. 3 F). Moreover, inhibition of STAT3 reversed the nicotine-mediated suppression of Iba1<sup>+</sup>/F4/80<sup>+</sup> (M1) and promotion of Iba1<sup>+</sup>/CD206<sup>+</sup> cells (M2; Fig. 3, G and H). These results suggest that the nicotine promotes M2 microglial polarization via activation of the STAT3 pathway.



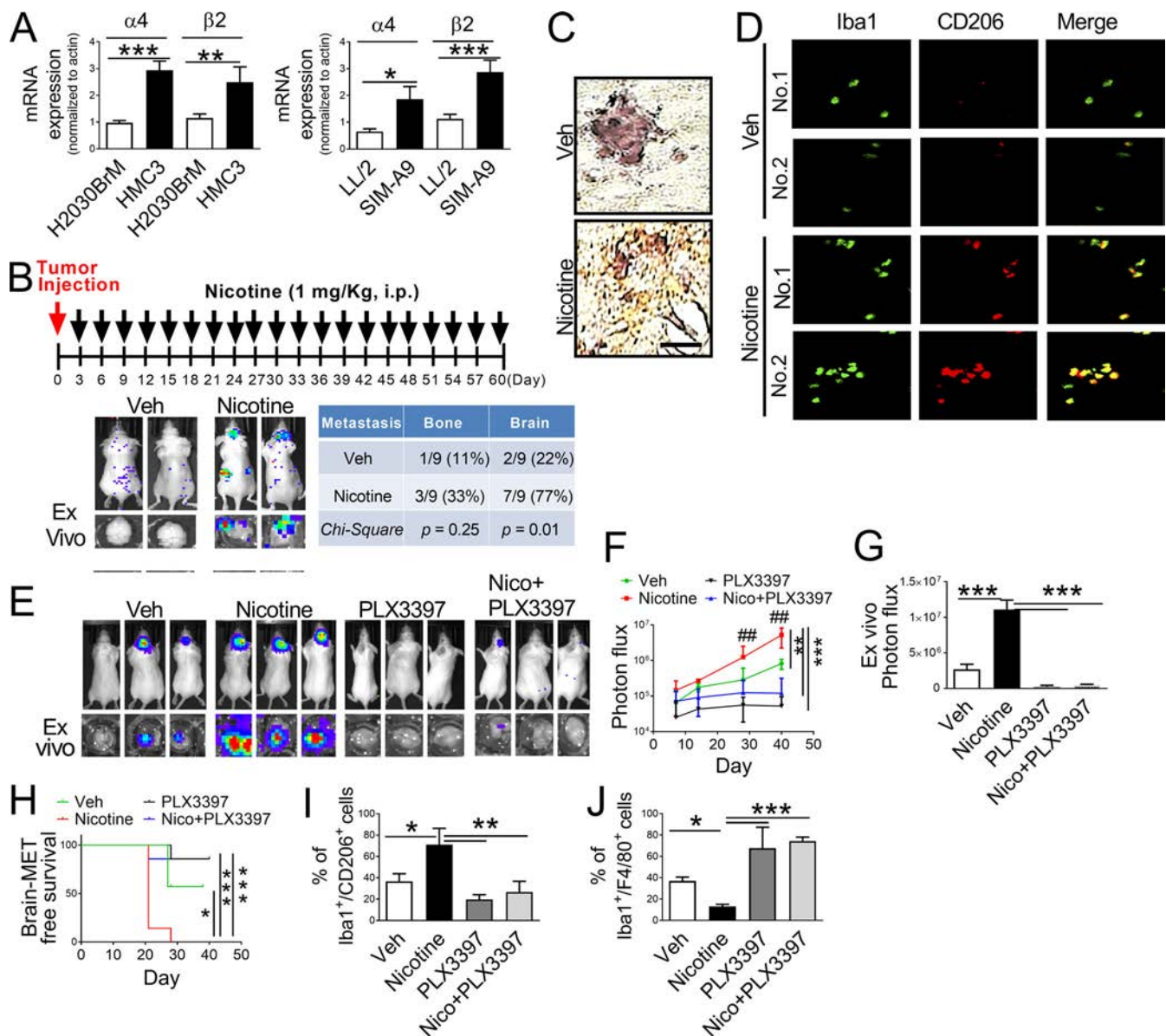


**Figure 2. Nicotine promotes brain metastasis by activating microglia in vivo.** (A) Expression of  $\alpha 4\beta 2$  nicotine receptor on human microglia (HMC3), mouse microglia (SIM-A9), human lung cancer cells (H2030BrM), and mouse lung cancer cells (LL/2) were evaluated by qRT-PCR ( $n = 3$ /group). (B) LL/2 ( $5 \times 10^4$  cells) were intracardially injected into immune-competent BALB/c mice ( $n = 9$ ). After 3 d of intracardiac transplantation of LL/2 cells, mice received nicotine treatment (1 mg/kg) by intraperitoneal injection every 3 d for 60 d. Upper panel: BLI images of brain metastatic lesions of representative mice from each experimental group (vehicle alone or nicotine treatment). Lower panel: total photon flux of ex vivo image of brain metastatic lesions was measured by BLI at the end point (day 60). Quantitative data of bone and brain metastasis of lung cancer are shown in the right panel. (C) At the end point, the brain sections from mice with or without treatment with nicotine were examined for Iba1<sup>+</sup> signal (brown) on microglia. Scale bar, 20  $\mu$ m. (D) Representative images of immunohistochemical analysis for CD206<sup>+</sup> and Iba1<sup>+</sup> microglia in the metastatic brain lesions of mice that were treated with or without nicotine ( $n = 9$ /group). Scale bar, 100  $\mu$ m. (E) Mouse lung cancer LL/2 cells were intracranially injected into wild-type BALB/c mice ( $n = 9$ /group) followed by administering PLX3397 by intracranial injection. Upper panels are BLI images of brain metastatic lesions of representative mice from each experimental group at day 40. Lower panels represent the total photon flux of ex vivo brain metastatic lesions as measured by BLI at the end point (day 40). (F) Quantitative data of in vivo brain metastasis of lung cancer ( $n = 9$ /group). (G) Ex vivo BLI signals in the brain at the end point ( $n = 9$ /group). (H) Kaplan-Meier analysis of brain metastasis-free survival was performed ( $n = 9$ /group). (I and J) Metastatic brain tumors in E were isolated from the brain and were examined by FACS for M2 (I) and M1 (J) microglial polarization ( $n = 4$  or 5/group). The data are presented as the mean  $\pm$  SD. \*,  $P < 0.05$ ; \*\*,  $P < 0.01$ ; and \*\*\*,  $P < 0.001$  versus respective nicotine group. ##,  $P < 0.01$  versus respective PLX3397 or Nico+PLX3397 group.

### Nicotine-treated microglial cells promote tumor growth and stemness

To examine the effect of nicotine-induced M2 microglia on tumor progression, we treated lung cancer brain metastatic cells, H2030BrM and PC9BrM, with conditioned medium (CM) generated from human microglia that were treated with or without

nicotine. We found that CM derived from nicotine-treated microglia significantly increased sphere formation (Fig. 4 A) and population of ESA<sup>+</sup>/CD44<sup>+</sup> or aldehyde dehydrogenase (ALDH<sup>+</sup>) cancer stem cells (CSCs; Fig. 4 B). The expression of stemness-inducing genes, SOX2 and NANOG, was also significantly up-regulated when the brain metastatic cells were treated with



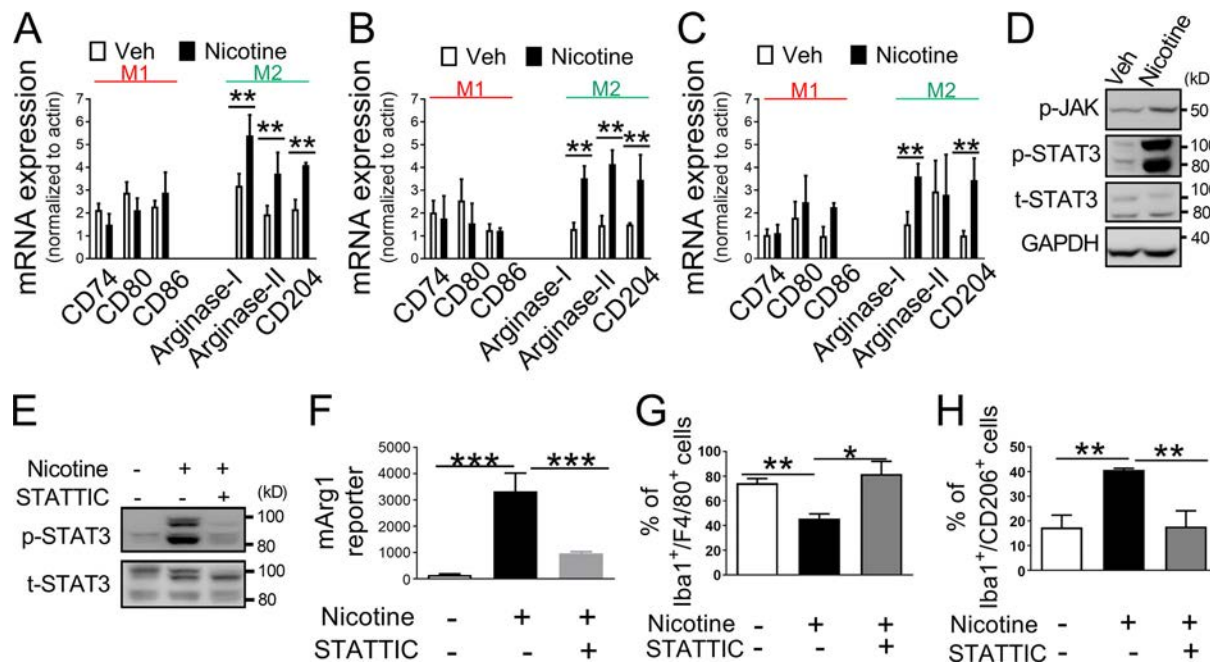


**Figure 3. Nicotine promotes M2 microglial polarization via STAT3 activation.** (A–C) Expressions of M1/M2 microglia markers were examined after the treatment of human microglia (HMC3) (A), mouse microglia (SIM-A9; B), and primary mouse microglia (C) with either vehicle or nicotine (1  $\mu$ M). The value of qRT-PCR in each figure was normalized using actin as a control. The y axis indicates arbitrary unit ( $n = 3$ /group). (D) Human microglia (HMC3) were treated with or without nicotine (1  $\mu$ M), and the expressions of JNK and STAT3 were examined by Western blot. (E) Human microglia (HMC3) were treated with or without nicotine and/or STAT3 (0.5  $\mu$ M) for 24 h, and the expression of STAT3 was examined by Western blot. (F) Mouse microglia cells (SIM-A9) were treated with or without nicotine and/or STAT3 (0.5  $\mu$ M) for 24 h followed by examining the luciferase-promoter activity of *Arg1* (M2;  $n = 4$ /group). (G and H) Mouse microglia (SIM-A9) were treated with or without nicotine (1  $\mu$ M) and/or the STAT3 inhibitor (0.5  $\mu$ M) for 24 h. Cells were then subjected to FACS analysis for analysis of Iba1<sup>+</sup>/F4/80<sup>+</sup> (M1 cell; G) and Iba1<sup>+</sup>/CD206<sup>+</sup> (M2 cell; H;  $n = 9$ /group). The data are presented as the mean  $\pm$  SD. \*,  $P < 0.05$ ; \*\*,  $P < 0.01$ ; and \*\*\*,  $P < 0.001$ .

the CM of nicotine-treated microglia (Fig. 4, C and D). Furthermore, nicotine-treated microglial CM also promoted the colony-forming ability of both H2030BrM and PC9BrM cells (Fig. 4 E). We then sought to identify the factor(s) in CM that are responsible for the increase in stemness. We performed the cytokine array analysis (consisting of 99 factors) and found that nicotine significantly augmented the secretion of CCL20 and IGF-1 in the microglial CM (Fig. S3 A). The results of screening were verified using human microglial cells (Fig. S3 B). Furthermore, blocking STAT3 by STAT3 inhibitor significantly suppressed nicotine-mediated up-regulation of CCL20 and IGF-1 (Fig. S3 B). We observed that microglia produced higher levels of IGF-1 and CCL20 than macrophage (Fig. S3 C). The expression of receptors of IGF-1 and CCL20 were significantly increased in H2030BrM cells after the treatment with CM of microglia that were exposed to nicotine (Fig. 4 F). We then treated lung cancer cells with recombinant CCL20 and IGF-1 and examined their effect on CSC properties. We found that both cytokines significantly enhanced the sphere formation (Fig. 4 G), ESA<sup>+</sup>/CD44<sup>+</sup> CSC population (Fig. 4 H), and mRNA expression of CSC markers SOX2 and NANOG (Fig. 4, I and J). In addition, IGF-1 and CCL20 significantly increased the colony-forming ability of brain metastatic lung cancer cells (Fig. 4 K). To understand the clinical relevance of these results, we used The Cancer Genome Atlas (TCGA) dataset and found that high expression of CCL20 was associated with poor overall survival in lung cancer patients (Fig. S3 D);

however, no such correlation was observed for the IGF-1 gene (Fig. S3 E). Furthermore, expressions of both CCL20 and its receptor, CCR6, were up-regulated in the primary tumor site of lung cancer patients compared with normal lung tissue in the same dataset (Fig. S3, F and G). Moreover, microglia expressed a higher level of CCL20 mRNA than lung cancer cells, indicating that microglia are potentially major sources of CCL20 in brain TME (Fig. S3, H and I). To examine whether CCL20 is involved in the growth-promoting effect of CM derived from nicotine-treated microglia, CCL20 was depleted in the CM using CCL20 neutralizing antibody. Our result indicates that depletion of CCL20 significantly suppressed the generation of CSC by nicotine-treated CM (Fig. 4 L). To further validate our results, we examined the levels of CCL20 in brain and serum of the nicotine-treated mice represented in Fig. 2 E and found that CCL20 indeed increased in the brain and serum of nicotine-treated animals (Fig. 4, M and N). In contrast, depletion of microglia by PLX3397 significantly suppressed the levels of nicotine-induced CCL20 in brain and serum of nicotine-treated animals (Fig. 4, M and N). Furthermore, consistent with our in vivo results, we found that the serum level of CCL20 was significantly higher in lung cancer patients who were current smokers compared with noncurrent smokers (Fig. 4 O).

We also examined the direct effect of nicotine on cell growth by treating the human lung cancer brain metastatic cells, H2030BrM, with nicotine alone or with nicotine-treated

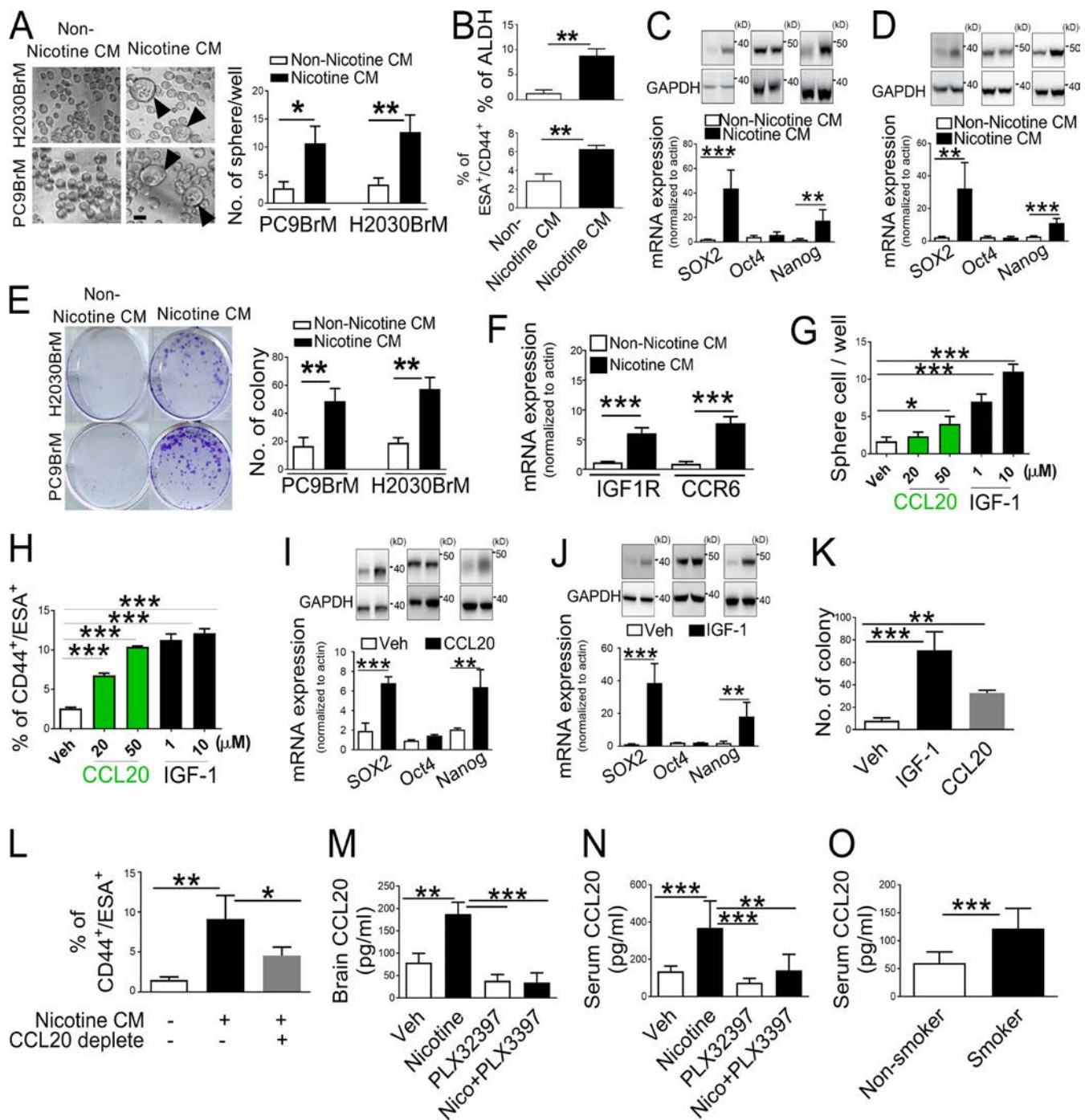


**Figure 4. Nicotine-mediated microglial polarization promotes tumor stemness.** (A) Effect of human microglial cells (HMC3) treated with or without nicotine (1 μM), and collection of CM. Brain metastatic lung cancer cells (H2030BrM and PC9BrM) were treated with the non-nicotine and nicotine CM for 24 h, and their sphere-forming ability was measured. Left panel: representative images. Arrowheads indicate sphere formation. Right panel: quantification of number of spheres. Non-nicotine or nicotine CM: microglia cells were treated with PBS or nicotine (1 μM) for 24 h, and they were washed with PBS and incubated in the fresh DMEM/F12 medium supplemented with 2% FBS for 24 h (*n* = 4/group). Scale bar, 10 μm. (B) Effect of the human microglial CM on CSC markers, ESA<sup>+</sup>/CD44<sup>+</sup>, and ALDH activity were examined using FACS (*n* = 4/group). (C and D) Expressions of stemness genes in H2030BrM (C) and in PC9BrM cells (D) were examined after the treatment with or without nicotine-derived human microglial CM by qRT-PCR (*n* = 6/group). (E) Colony-forming abilities of H2030BrM and PC9BrM cells were measured in the presence or absence of the CM derived from nicotine-treated human microglia. Left panel: representative images. Right panel: quantification of number of colonies (*n* = 4/group). (F) Expressions of IGF-1 and CCL20 receptors in H2030BrM cells were examined after the treatment of cells with or without nicotine-derived human microglial CM by qRT-PCR (*n* = 4/group). (G) Effect of recombinant proteins, CCL20 and IGF-1, on sphere formation ability of H2030BrM was measured (*n* = 3/group). (H) H2030BrM cells were treated with CCL20 or IGF-1 for 24 h followed by measuring the ESA<sup>+</sup>/CD44<sup>+</sup> stem cell population by FACS (*n* = 4/group). (I and J) H2030BrM cells were treated with or without 20 μM of CCL20 (I) or 1 μM of IGF-1 (J) for 24 h, and the expressions of stemness genes were examined by qRT-PCR and Western blot (*n* = 4/group). (K) Colony-forming assay was performed for the same set of samples as in G and H (*n* = 4/group). (L) Human microglia were treated with or without nicotine (1 μM) for 24 h, and their CM was prepared. The CM was then

added with anti-CCL20 antibody to deplete CCL20. H2030BrM cells were then treated with the CCL20-depleted CM followed by assaying the ESA<sup>+</sup>/CD44<sup>+</sup> stem cell population by FACS ( $n = 4/\text{group}$ ). **(M and N)** Metastatic lesions in the brain and serum were prepared from the mice used in Fig. 2 E. The protein expression of CCL20 in the brain (M) and in the serum (N) in each group was measured by ELISA ( $n = 6/\text{group}$ ). **(O)** The protein expression of CCL20 in the serum of lung cancer patients with or without smoking history were measured by ELISA ( $n = 10/\text{group}$ ). The data are presented as the mean  $\pm$  SD. \*,  $P < 0.05$ ; \*\*,  $P < 0.01$ ; and \*\*\*,  $P < 0.001$ .

microglial CM. Although colony-forming ability increased in both groups (Fig. S3 J), the CSC population and expression of stem cell markers were significantly elevated only in cells treated with the nicotine-treated microglial CM (Fig. S3, K and L). Consistent with these results, treating the mouse lung cancer cell, LL/2, with CM derived from nicotine-treated mouse microglia significantly increased the levels of CSCs (Fig. S3 M) and promoted the colony-forming ability (Fig. S3 N) and tumor cell viability (Fig. S3 O). We also examined whether nicotine-induced brain metastasis is mediated via M2 microglial polarization by STAT3 activation. We blocked the M2 polarization of microglia by STAT3IC and examined the expression of *IGF-1* and *CCL20* by quantitative real-time PCR (qRT-PCR). We found that the nicotine treatment significantly up-regulated the *IGF-1* and *CCL20*, while STAT3IC reversed the effect (Fig. S3, P and Q). The CM was then added to the culture of LL/2 cells. We found that CM derived from microglia that were treated with both nicotine and STAT3IC significantly suppressed CSC population (Fig. S3 R) and tumor cell viability (Fig. S3 S).

#### Nicotine suppresses innate immune function of microglia

Microglia are known to exhibit phagocytic activity against brain tumor cells, like macrophages (Hutter et al., 2019). However, to escape from microglia-mediated phagocytosis, tumor cells express CD47 on their cell surface, which activates so-called “do not eat me” signaling. To investigate if nicotine affects this immune function of microglia, we measured the expression of signal-regulatory protein  $\alpha$  (SIRP $\alpha$ ) on microglia and CD47 on tumor cells. We found that the mRNA and protein expression of SIRP $\alpha$  were up-regulated in human microglia after nicotine treatment (Fig. 5 A). We also found that nicotine significantly increased the mRNA and protein expression of CD47 in both H2030BrM and PC9BrM cells (Fig. 5 B). Importantly, the expression of CD47 is up-regulated in brain metastasis of lung cancer patients with smoking history (Fig. 5 C). We then examined the effect of nicotine on phagocytic ability of microglia. We prelabeled H2030BrM cells with the fluorochrome-PKH26, a red-fluorescent vital dye that binds tightly to cell membranes (Munn and Cheung, 1990). The labeled cells were incubated with microglia that were treated with or without nicotine. We found that the size of PKH26<sup>+</sup> tumor cells and microglia cells was similar at 0 h in the co-culture (Fig. 5 D). However, after 24 h of incubation, the small and irregular shape of PKH26<sup>+</sup> cells was accumulated in the microglia. This result suggests that tumor cells were rapidly degraded by nicotine-treated microglia through phagocytosis. As shown in Fig. 5, D and F, both human and mouse microglial cells showed strong phagocytic activities toward the H2030BrM and LL/2 cells. Importantly, this phagocytic ability was greatly compromised in the presence of nicotine (Fig. 5, E and G). Blocking STAT3 signaling by STAT3IC

treatment suppressed nicotine-mediated down-regulation of phagocytic ability of microglia (Fig. 5 E). We also examined the expression of SIRP $\alpha$  in microglia of the nicotine-treated mouse brain represented in Fig. 2 E and found that the CD47 and SIRP $\alpha$  expression were strongly elevated in the brain of mice treated with nicotine (Fig. 5, H–J). These results suggest that nicotine promotes M1/M2 conversion and suppresses the innate immune function of microglia, which promotes brain metastasis progression.

#### PTL suppresses nicotine-induced M2 microglia polarization and enhances their phagocytic ability

Our results strongly suggest that blocking M2 polarization of microglia may be an effective therapeutic approach for brain metastasis. Therefore, we screened a natural compound library to identify compounds that block M2 macrophage polarization using an Arg1 promoter reporter system. We screened a total of 103 compounds that are known to be blood–brain barrier (BBB) permeable. As shown in Fig. S4 and Fig. 6 A, we identified three compounds (>15-fold change,  $P < 0.001$ ) that effectively suppressed the nicotine-induced activation of Arg1 promoter at a concentration of 1  $\mu\text{M}$ . We selected the top compound, PTL, which suppressed the Arg1 promoter activity by >20-fold, for further study (Fig. 6 A). PTL is an abundant sesquiterpene lactone found in the medicinal herb Feverfew (*Tanacetum parthenium*). It has been used to treat inflammation and headache for centuries in Europe (Liu et al., 2018). To confirm the suppressive effect of PTL on nicotine-induced M2 microglial polarization, microglia were treated with nicotine in the presence or absence of PTL (Fig. S5 A), and expressions of M1 and M2 markers were examined. We found that PTL significantly decreased the nicotine-mediated M2 polarization of microglia (Fig. 6 B). Furthermore, the nicotine-mediated reduction of Iba1<sup>+</sup>/CD11b<sup>+</sup> cells (M1) and elevation of Iba1<sup>+</sup>/CD206<sup>+</sup> cells (M2) were significantly reversed by PTL (Fig. 6 C). Previous studies have shown that PTL modulated the JAK2/STAT3 signaling in response to cytokine stimulations (Liu et al., 2018; Sobota et al., 2000). We indeed found that PTL suppressed the nicotine-induced JAK2/STAT3 activation (Fig. 6 D), suggesting that PTL blocks the nicotine-induced M2 microglial polarization by targeting STAT3. Furthermore, the nicotine-induced suppression of phagocytic ability of microglia was restored when cells were treated with PTL (Fig. 6 E). The H2030BrM cells were treated with CM of microglia that were exposed to nicotine only or nicotine plus PTL. We found that the ESA<sup>+</sup>/CD44<sup>+</sup> CSCs (Fig. 6 F) and colony-forming ability (Fig. 6 G) were significantly suppressed by CM of microglia treated with nicotine plus PTL. We also examined the mRNA expression of *CCL20* and found that the nicotine-mediated secretion of *CCL20* was down-regulated by the PTL treatment (Fig. 6 H). Next, to investigate the effect of PTL on



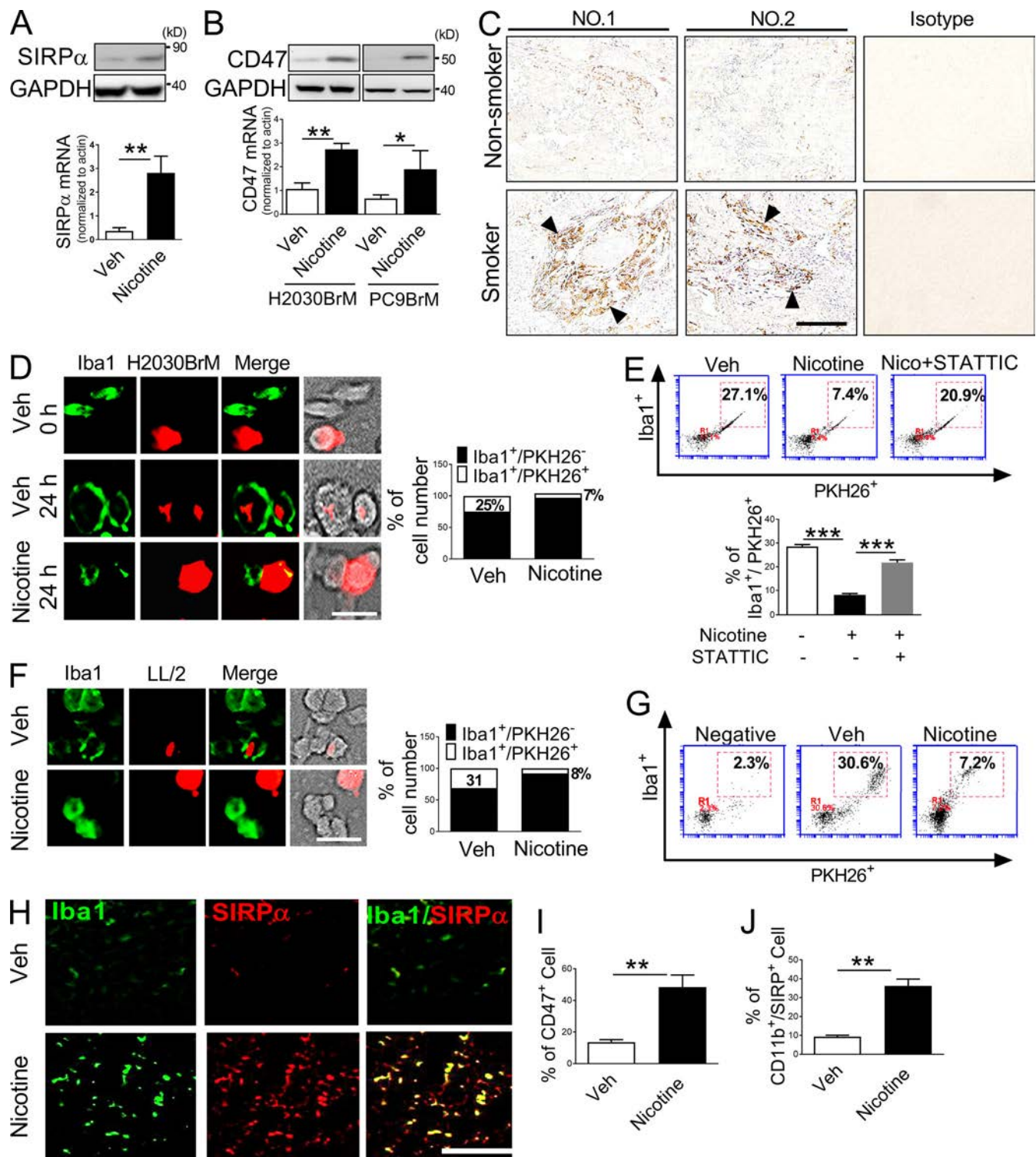


**Figure 5. Nicotine suppresses innate anti-tumor immune function of microglia.** (A) Human microglia cells (HMC3) were treated with or without nicotine (1  $\mu$ M) for 24 h, and the expression of SIRP $\alpha$  was examined by qRT-PCR and Western blot ( $n = 4$ /group). (B) H2030BrM and PC9BrM cells were treated with or without nicotine (1  $\mu$ M) for 24 h, and the expression of CD47 was examined by qRT-PCR and Western blot ( $n = 4$ /group). (C) Representative images of immunohistochemical analysis for CD47 $^{+}$  cells in the metastatic brain lesions of lung cancer patients with or without smoking history. Arrows indicate CD47 $^{+}$  cells. Non-smoker ( $n = 4$ ) and smoker ( $n = 7$ ). Scale bar, 50  $\mu$ m. (D) Phagocytic activities of HMC3 human microglial cells (green) with or without nicotine treatment were examined using PKH26-labeled H2030BrM cells (red). Both cells were incubated together for 0 or 24 h and photographed (left panels), and the number of microglia that phagocytosed tumor cells was counted to quantify microglial phagocytic activity as shown in the right panel ( $n = 4$ /group). Scale bar, 10  $\mu$ m. (E) A parallel set of cells in D was analyzed by FACS to quantify phagocytic abilities of microglia after nicotine or STATTC treatment. Upper panels: representative FACS data. Lower panel: statistical analysis of the FACS data ( $n = 4$ /group). (F) Mouse microglia (SIM-A9; green) were incubated with PKH26-labeled LL/2 mouse lung cancer cells (red) for 24 h. They were then photographed under a fluorescent microscope ( $n = 4$ /group). Scale bar, 100  $\mu$ m.

(G) Phagocytic abilities of microglia with or without nicotine treatment were examined by incubating mouse microglia with PKH26-labeled LL/2 mouse lung cancer cells for 24 h, followed by analysis of the cells by FACS ( $n = 4$ ). (H) The metastatic lesions in the brain of mice in Fig. 2 E were sectioned, and they were subjected to immunohistochemical analysis for SIRPα and Iba1. Representative immunohistochemistry images of the microglia are shown ( $n = 9/\text{group}$ ). Scale bar, 100  $\mu\text{m}$ . (I and J) The metastatic lesions in the brain of mice in Fig. 2 E were subjected to FACS analysis for CD47<sup>+</sup> tumor cell (I) and SIRPα/CD11b<sup>+</sup> (J) microglia cells ( $n = 9/\text{group}$ ). The data are presented as the mean  $\pm$  SD. \*,  $P < 0.05$ ; \*\*,  $P < 0.01$ ; and \*\*\*,  $P < 0.001$ .

nicotine-related brain metastasis in vivo, wild-type mice (C57BL/6 and BALB/c) were transplanted with LL/2 mouse lung cancer cells followed by administering nicotine (1 mg/kg) only or nicotine plus PTL (1 mg/kg) via an intraperitoneal injection. As shown in Fig. 6, I–K (BALB/c) and Fig. S5, B and C (C57BL/6), PTL treatment significantly suppressed nicotine-mediated brain metastasis and prolonged the brain metastasis-free survival (Fig. 6 L). To examine whether the PTL treatment also reverses microglia polarization in the brains of these mice, we performed flow cytometry (FACS) analysis of mouse brain and stained brain sections for M1 and M2 markers. A significant increase in Iba1<sup>+</sup>/F4/80<sup>+</sup> (M1 marker) and decrease in Iba1<sup>+</sup>/CD206<sup>+</sup> (M2 marker) were observed in brain microglia of PTL-treated mice (Fig. 6, M and N; and Fig. S5, D and E). To validate our results in human cell line, we used the xenograft model of H2030BrM cell and tested the efficacy of PTL. As shown in Fig. S5, F–K, PTL significantly suppressed the nicotine-induced brain metastasis and M2 microglia polarization. PTL treatment did not affect body weight of mice and showed no detectable liver toxicity (Fig. S5 L). We also examined the direct effect of PTL on cell viability and CSC population in vitro (Fig. S5 M). Our results showed that PTL suppressed the abundance of CD44<sup>+</sup>/ESA<sup>+</sup> CSC and cell viability at the concentration of 10–20  $\mu\text{M}$ , but not at 1  $\mu\text{M}$ , which is the dose used throughout our in vitro experiments (Fig. S5, N and O), indicating that the anti-tumor effect of PTL is not mediated by direct cytotoxic effect, and it is rather mediated by the effect on microglia. Furthermore, PTL significantly suppressed stemness promoting effect of nicotine on microglia (Fig. S5 P) and the expression of stemness-related genes (Fig. S5, Q and R). These results suggest that PTL suppresses nicotine-related brain metastasis of lung cancer by skewing polarity of M1 microglia and up-regulating their phagocytic ability.

## Discussion

The incidence of brain metastasis among lung cancer patients is 10–36% (Bacha et al., 2018; Barnholtz-Sloan et al., 2004; Schouten et al., 2002), although these data are considered to be underestimated (Bacha et al., 2018; Schouten et al., 2002). The majority of the lung cancer patients are diagnosed with advanced stage disease, most with stage IV cancer. More than 90% of lung cancer deaths are attributed directly to the metastatic disease and include those brain metastases (Ali et al., 2013; Kakusa et al., 2018). Cigarette smoking is a major risk factor for lung cancer (Lee et al., 2012), and our previous study showed a negative impact of smoking on lung cancer brain metastasis (Shenker et al., 2017). In the present study, we have found a significantly higher incidence of brain metastasis among current smokers with stage IV lung cancer.

Nicotine is not a carcinogen, but it causes addiction by activating nACh receptor, which is abundantly expressed by various

brain cells including microglia. Direct tumor promoting effects of nicotine have been previously reported (Schaal and Chellappan, 2014; Sun et al., 2017; Wang et al., 2017; Yoneyama et al., 2016); however, how nicotine promotes tumor by activating TME is still poorly understood. The current report is the first to show the critical impact of nicotine on brain TME to promote brain metastasis by skewing microglia to M2 phenotype and suppressing their role in innate immunity. Our results indicate that the phenotypic conversion of microglia by nicotine is mediated through the nACh receptor–STAT3 pathway, and that inhibition of STAT3 blocked the M2 conversion, suppressed the secretion of pro-tumor M2 cytokines, and reactivated their phagocytic activity toward tumor cells (Fig. 6 O).

Previous studies showed that microglial cells and macrophages in the brain are derived from two different sources, parenchymal resident microglia and monocytes/macrophages that enter the brain from the bone marrow (Wu and Watabe, 2017). Although microglia and macrophage cells show similarity in their surface markers and physiological functions, recent studies have demonstrated that microglia and macrophages are two distinct myeloid populations with different developmental origins (Gomez Perdiguero et al., 2015; Prinz and Priller, 2014; Schulz et al., 2012). Microglial cells originate from erythromyeloid progenitors that begin on embryonic day (E) 7.5–E8.0 in the blood islands of the yolk sac. Until E9.5, erythromyeloid progenitors migrate to the developing central nervous system and mature into microglia (Gomez Perdiguero et al., 2015; Prinz and Priller, 2014; Schulz et al., 2012). These early microglial cells reside in the brain throughout life and are thought to sustain the local microglial population. In contrast, macrophages originate from the hematopoietic stem cells that start in the aorta–gonad–mesonephros region at E10.5, and then in the fetal liver at E12.5. After the postnatal stage, macrophages are produced from monocytes in the bone marrow (Gomez Perdiguero et al., 2015; Prinz and Priller, 2014; Schulz et al., 2012). Furthermore, recent studies demonstrated that microglial cells and macrophage have distinct and specific surface antigens (Feng et al., 2015). Studies on CX3CR1<sup>+</sup>/GFP/CCR2<sup>+</sup>/RFP knock-in fluorescent protein reporter mice revealed that microglial cells are CX3CR1<sup>+</sup>/CCR2<sup>−</sup>/CD45<sup>−</sup>, while the macrophages are CX3CR1<sup>−</sup>/CCR2<sup>+</sup>/CD45<sup>+</sup> (Feng et al., 2015), strongly supporting the notion that microglial cells and macrophages are from different populations and they can be distinguished. Badie and Scharfner performed flow cytometric analysis and characterized the distribution of microglial cells and macrophages in experimental gliomas and found that microglial cells (CD11b/c<sup>high</sup>, CD45<sup>low</sup>), mainly present at the site of tumor or tumor periphery, accounted for 13–34% of the tumor mass. In contrast, macrophages (CD11b/c<sup>high</sup>, CD45<sup>high</sup>) were less prominent within the tumors or the tumor periphery and accounted for just



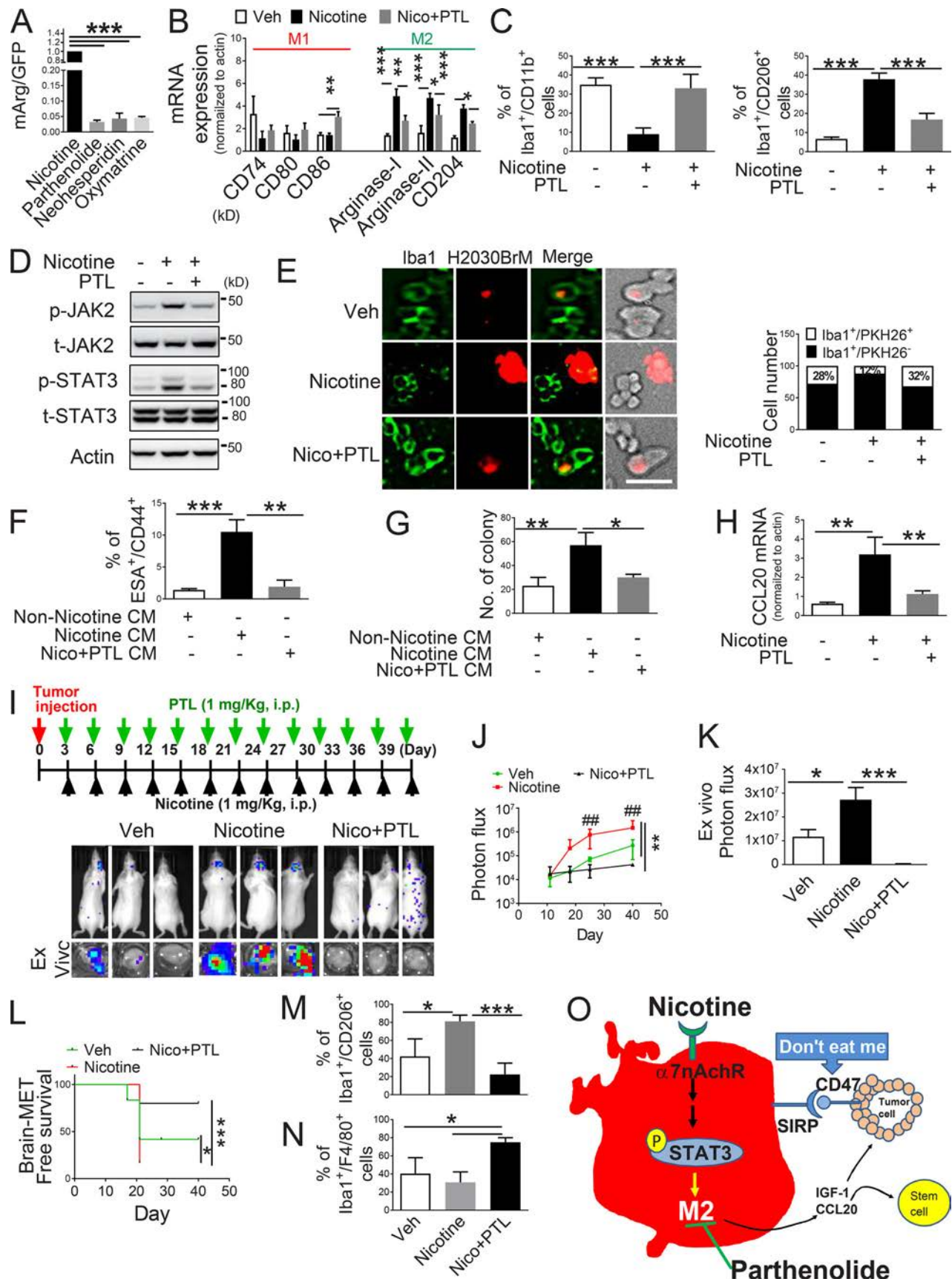


Figure 6. **PTL suppresses brain tumor progression by blocking nicotine-induced M2 microglia polarization.** (A) Human microglia cells (HMC3) with the Arg1 reporter plasmid were cultured in the presence or absence of compounds that were identified as the top three most effective inhibitors for Arg1 during our

initial screening (see Materials and methods). After 48 h of incubation, luciferase reporter activity was measured ( $n = 4/\text{group}$ ). **(B)** Expression of surface markers of M1/M2 microglia was examined by qRT-PCR after microglial cells were treated with or without nicotine plus PTL ( $n = 4/\text{group}$ ). **(C)** The same set of samples in B was evaluated for quantification of Iba1<sup>+</sup>/CD11b<sup>+</sup> (M1) cells and Iba1<sup>+</sup>/CD206<sup>+</sup> (M2) cells by FACS ( $n = 4/\text{group}$ ). **(D)** The same set of samples in C was examined for quantification of the protein expression of JAK2 and STAT3 by Western blot. **(E)** Human microglial (HMC3) cells (green) with or without nicotine treatment (1  $\mu\text{M}$ ) in the presence or absence of PTL (1  $\mu\text{M}$ ) were incubated with PKH26-labeled H2030BrM cells (red) for 24 h and photographed (left panels), followed by measurement of the microglial phagocytic activity (right panel;  $n = 4/\text{group}$ ). Scale bar, 10  $\mu\text{m}$ . **(F)** CM was prepared from human microglia (HMC3) treated with or without nicotine and PTL. The CM was added to the culture of H2030BrM, and cells were incubated for 48 h followed by evaluation of CSC population by FACS. Non-nicotine, nicotine, or Nico+PTL CM: microglia were treated with PBS, nicotine, or nicotine plus PTL for 24 h. They were then washed twice with PBS and incubated in the fresh DMEM/F12 medium supplemented with 2% FBS for a further 24 h ( $n = 4/\text{group}$ ). **(G)** For the same set of samples as F, colony-forming ability was also measured ( $n = 4/\text{group}$ ). **(H)** Human microglia were treated with or without nicotine (1  $\mu\text{M}$ ) in the presence or absence of PTL for 24 h, followed by assessment of the expression of CCL20 by qRT-PCR ( $n = 4/\text{group}$ ). **(I)** The mouse lung cancer cells, LL/2, were intracardially injected into wild-type BALB/c mice. After 3 d of intracranial transplantation of LL/2 cells, mice received nicotine (1 mg/kg) plus PTL (1 mg/kg) by an intraperitoneal injection every 3 d for 40 d. Upper panel: BLI images of representative mice from each experimental group at day 40. Lower panel: total photon flux of ex vivo brain metastatic lesions was measured by BLI at the endpoint (day 40;  $n = 9/\text{group}$ ). **(J)** Quantitative data of BLI in the brain regions are shown ( $n = 9/\text{group}$ ). **(K)** Ex vivo signals in the whole brains at the end point were quantified. **(L)** The Kaplan–Meier analysis of brain metastasis-free survival was performed ( $n = 9/\text{group}$ ). **(M and N)** Metastatic brain tumors in I were isolated from the brain and were examined by FACS for M2 (M) and M1 (N) microglial polarization ( $n = 9/\text{group}$ ). **(O)** A proposed model illustrating a nicotine-induced brain metastasis ( $n = 9/\text{group}$ ). The data are presented as the mean  $\pm$  SD. \*,  $P < 0.05$ ; \*\*,  $P < 0.01$ ; and \*\*\*,  $P < 0.001$ .

4.2–12% of the tumor mass (Badie and Schartner, 2000). These results also suggest that microglial cells play a key role in mediating brain tumor progression.

We have also found that nicotine dramatically increased the mRNA expression of  $\alpha 4\beta 2$  receptor on microglia cell compared with macrophage. These results suggest that microglia is more responsive to nicotine compared with macrophage, resulting in increase in the incidence of brain metastasis. Furthermore, it was reported that the numbers of macrophage/microglia were significantly higher in the central nervous system than in the peripheral system after injury (Leskovar et al., 2000). In addition, the peak concentrations of three cytokines, TNF $\alpha$ , IL-1, and IL-6, appeared earlier and were significantly higher in the injured central nervous system than peripheral system (Leskovar et al., 2000), suggesting differences in the reparative responses of macrophage/microglia in the PNS and central nervous system to injury.

In this study, we showed that blocking microglia CSF1R by PLX3397 significantly suppressed nicotine-mediated brain metastasis, suggesting that cancer cells lose growth support function from M2 microglia. Previous studies showed that PLX3397 reprogrammed tumor-infiltrating macrophages, enhanced antigen presentation (Zhu et al., 2014), and suppressed TAM infiltration in the tumor (Butowski et al., 2016; Cannarile et al., 2017; Cuccarese et al., 2017). We also found that PLX3397 skewed the population of microglia/macrophage to M1 phenotype. Therefore, while blocking the proliferation of microglia/macrophage, PLX3397 also promotes the residual microglia's innate immune function to tumor cells. Our results indicate that nicotine increased the secretion of IGF-1 and CCL20 in the CM of microglial cells. IGF-1 is known to enhance tumor cell survival and proliferation via activation of the PI3K-Akt signaling (Park et al., 2016; Zhu et al., 2011). However, the role of CCL20 on tumor progression has not yet been well defined. CCL20 is a critical chemoattractant responsible for the recruitment of inflammatory immune cells (Nandi et al., 2014). The expression of CCL20 has been shown to be overexpressed in a variety of tumors including lung cancer (Liu et al., 2016; Wang et al., 2015, 2016). In pancreatic cancer, CCL20 has been found to be

overexpressed in metastatic tumor tissues (Liu et al., 2016). It was reported to promote epithelial-mesenchymal transition and invasive ability of tumor cells by activating the MAPK and PI3K pathways and matrix metalloproteinase signaling (Marsigliante et al., 2016; Wang et al., 2016). Previous studies showed that CCL20 promotes cell proliferation through activation of MAPK pathway (Lu et al., 2017) and up-regulating transcription of c-Fos and c-Myc. Others have shown that CCL20 enhanced the chemotherapy resistance of triple-negative breast cancer by promoting ALDH<sup>+</sup> population of breast cancer cells through PKC $\zeta$ - and p38 MAPK-mediated NF- $\kappa$ B activation (Chen et al., 2018). We found that stem cell genes NANOG and SOX2 were up-regulated in CCL20-treated cells, suggesting that CCL20 promoted the stemness of lung cancer brain metastatic cells via NANOG/SOX2. One of the major sources of CCL20 is a tumor-associated macrophage, especially M2 macrophage (Liu et al., 2016). In this study, we found that nicotine strongly promoted phenotypic conversion of microglia to M2 and enhanced secretion of CCL20 to stimulate tumor cell growth and cancer cell stemness. The depletion of microglia in our animal model significantly reversed the effect of nicotine on brain metastasis. Furthermore, we showed that the effect of CCL20 on tumor stem cell was mediated by up-regulation of SOX2 and NANOG genes. These results suggest that CCL20 may serve as a novel therapeutic target and biomarker for brain metastasis of lung cancer.

SIRP $\alpha$  is expressed predominantly in myeloid and neuronal cells (Adams et al., 1998; Kharitononkov et al., 1997). Normal cells express CD47 that interacts with SIRP $\alpha$  on macrophage/microglia to suppress their phagocytic activity. Several studies have shown that the expression of SIRP $\alpha$  is also associated with polarization of microglia/macrophage (Pan et al., 2013). Furthermore, knockdown of SIRP $\alpha$  in macrophages increased the production of M1 cytokines in the tumor environment (Pan et al., 2013). Blocking SIRP $\alpha$  also triggered the Akt survival signal in macrophages and enhanced macrophage migratory activities toward tumors (Pan et al., 2013), suggesting that SIRP $\alpha$  also affects microglia's function. In this study, we found that the nicotine increased the expression of SIRP $\alpha$  on microglia, while nicotine also promoted the expression of CD47 on the tumor

cells, resulting in suppression of phagocytic ability of microglia. There are two possible mechanisms that are involved in the anti-tumor effect of microglia. One is direct internalization of tumor cells into the lysosome of microglia by phagocytosis. The other possibility is that tumor cells are first killed by cytotoxic factors released by microglia followed by phagocytosis of the apoptotic debris by microglia. In addition, it is noteworthy that the CD47-SIRP $\alpha$  signal was previously found to modulate T cell differentiation and regulate T cell priming to the tumor site (Liu et al., 2015b; Zhang and Petro, 1996). Therefore, the CD47-SIRP $\alpha$  signal that was activated by nicotine plays a pivotal role in modulating anti-tumor innate as well as adaptive immune responses in TME.

By screening a BBB permeable natural compound library, we identified PTL as a potent inhibitor for nicotine-induced M2 conversion of microglia. PTL is an abundant sesquiterpene lactone found in the medicinal herb Feverfew (*T. parthenium*). It has been used for centuries as a traditional medicine to treat arthritis, fever, and headache (Liu et al., 2015a; Rummel et al., 2011). PTL was also previously shown to exhibit direct tumor suppressive activity (Talib and Al Kury, 2018) by modulating multiple pathways, including p53, vascular endothelial growth factor (Talib and Al Kury, 2018), B-Raf/MAPK/Erk (Lin et al., 2017), and STAT3 pathways (Carlisi et al., 2011; Skoumal et al., 2011; Song et al., 2014). However, these direct tumor cytotoxic effects mediated by PTL require a relatively high dose, typically >10  $\mu$ M. In this study, we found that sub-micromolar dose (<1  $\mu$ M) of PTL effectively suppressed nicotine-induced polarization of microglia to M2 phenotype and enhanced its M1 phenotype. On the other hand, the low concentration (1  $\mu$ M) of PTL did not affect the population of CSC or tumor cell growth, which strongly suggests that the anti-tumor effect of PTL on nicotine-promoted brain metastasis shown in our study is mediated via modulation of microglial function and not by direct effect of PTL on tumor cells. Importantly, PTL was shown to be able to cross the BBB due to high membrane permeability (Könczöl et al., 2013). Considering the inhibitory effect of PTL on nicotine-induced microglial activation and their minimum toxicity at the effective dose, PTL could be used for the prevention and treatment of brain metastasis, particularly for patients with past and current smoking history.

Nicotine is highly addictive and considered as the major obstacle for smoking cessation (Henningfield et al., 1991). Unfortunately, many cancer patients have difficulty in quitting smoking even after their diagnosis due to nicotine addiction. E-cigarette, nicotine patch, and nicotine gum are nicotine replacement therapies for smoking cessation used by these patients (Hartmann-Boyce et al., 2018; Stead et al., 2012). Although nicotine, per se, is not a carcinogen, many reports document its tumor-promoting effects (Li et al., 2017; Schaal and Chellappan, 2014; Schaal et al., 2018) as well as its pro-inflammatory effect, which suppresses the phagocytosis ability of the alveolar macrophages (Scott et al., 2018). Considering our results that clearly demonstrated profound and long-term effects of nicotine on brain metastasis progression, extra caution should be paid in the use of nicotine for smoking cessation.

## Materials and methods

### Human subjects

We used a cohort of patients with a diagnosis of nonsmall cell lung cancer with or without brain metastases treated at Wake Forest Baptist Comprehensive Cancer Center between May 2015 and April 2018. We collected a total of 281 stage IV nonsmall cell lung cancer patients with or without a history of smoking. Among them, 79 patients were diagnosed with brain metastasis. 59 patients were current smokers at the time of diagnosis and treatment. We defined the “never smokers” ( $n = 44$ ) as those who have no smoking history and those who had smoked <10 pack/year but stopped smoking. The “former smokers” ( $n = 181$ ) are defined as those who smoked >10 pack/year but quit smoking in the past. Patient characteristics included histology status, smoking history, pack/years, progression status, and date of death. Patient information about age, gender, cancer type, and smoking status are described in Fig. S1. All samples used in this study were obtained under the approval of the institutional review boards of Wake Forest School of Medicine Institutional and Wake Forest Baptist Comprehensive Cancer Center. Written informed consent was obtained from all participants.

### Cell culture and reagents

Human lung cancer cell lines, H2030BrM and PC9BrM, were kind gifts from J. Massagué (Memorial Sloan-Kettering Cancer Center, New York, NY). H2030BrM and PC9BrM cell lines were authenticated by using GenePrint 10 STR System (Promega, B9510). SIM-A9 was obtained from Kumi Nagamoto-Combs, through Kerafast.com. HMC3 and LL/2 cells were purchased from American Type Culture Collection (ATCC) and were authenticated by ATCC. The H2030BrM and PC9BrM were cultured in RPMI supplemented with 10% FBS, streptomycin (100 mg/ml), and penicillin (100 U/ml). LL/2 cells were cultured in DMEM medium supplemented with 10% FBS. SIM-A9 and HMC3 were cultured in DMEM/F12 medium supplemented with 5% FBS. All cells were grown at 37°C under 5% CO<sub>2</sub>. All cell lines were obtained between 2010 and 2016, and they were ensured to be negative of mycoplasma. The HMC3 and SIM-A9 cells were seeded in a 10-cm dish. After reaching 70% confluence, cells were incubated with or without 1  $\mu$ M nicotine in DMEM/F12 medium supplemented with 2% FBS or in medium containing nicotine plus the STAT3 inhibitor STAT3i (0.5  $\mu$ M). After 24 h, cells were washed twice with PBS and then incubated in the fresh DMEM/F12 medium supplemented with 2% FBS for 24 h. The CM harvested from the cell culture were centrifuged at 300  $g$  for 10 min to remove the cells and stored at -80°C. To investigate the effect of nicotine-derived CM on tumor progression, we harvested CM from microglial cells that were treated with or without nicotine, followed by treatment of tumor cells with the CM. All cell lines were tested by using universal mycoplasma detection kit (ATCC, 30-1012k, lot 70008746).

### Animal models

Animals were treated in accordance with the U.S. National Institutes of Health Animal Protection Guidelines, and the protocol was approved by the Wake Forest Baptist Health Institutional



Animal Care and Use Committee. Female nude, BALB/c, and C57BL/6 mice of 5–6 wk of age were used. The mice were housed (four to five per cage) at a stable temperature ( $24 \pm 1^\circ\text{C}$ ), in a 12-h light/dark cycle, and with unrestricted access to food and water. Several studies showed that human lung adenocarcinoma cell H2030BrM and mouse Lewis lung carcinoma cell LL/2 exhibited their highly metastatic abilities in the nude, C57BL/6, and BALB/c mice, respectively (Chen et al., 2016; Janker et al., 2018; Kamei et al., 2009; Malladi et al., 2016; Nguyen et al., 2009; Scholar et al., 1989). Actively growing luciferase-labeled H2030BrM and LL/2 cells were intracardially injected at a concentration of  $2 \times 10^5$  H2030BrM cells or  $5 \times 10^4$  LL/2 cells in 100  $\mu\text{l}$  PBS into the left cardiac ventricle. To confirm a successful injection, the photon flux from whole body of the mice was immediately measured using IVIS Xenogen bioimager (Caliper). To examine the effect of nicotine, the mice received nicotine (1 mg/kg) by intraperitoneal injection every 3 d. To examine the role of microglia on nicotine-related brain metastasis, the mice were administered PLX3397 (20 mg in 7  $\mu\text{l}$ , Selleck Chemicals USA), a selective inhibitor of CSF1R (also known as macrophage colony-stimulating factor receptor), which reduces viability of microglial cells. To avoid whole-body effect, the PLX3397 was directly injected into the right mouse brain after 1 wk of transplantation of mouse lung cancer cell LL/2. Mice were divided into four groups: (1) tumor transplant only, (2) tumor transplant plus nicotine, (3) tumor transplant plus PLX3397, and (4) tumor transplant plus PLX3397 and nicotine. To examine the effect of natural compound (PTL) on modulation of microglial cell polarization, the mice were administered PTL (1 mg/kg) plus nicotine by intraperitoneal injection. Mice were divided into three groups: (1) tumor transplant only, (2) tumor transplant plus nicotine, and (3) tumor transplant plus PTL and nicotine. Tumor growth was monitored by bioluminescence until day 60. For bioluminescent imaging, the mice were injected with D-luciferin intraperitoneally (100 mg/kg), followed by capturing images every week using IVIS Xenogen bioimager. The brain metastasis was monitored, and the luminescence was quantified once per week. Finally, whole brain was removed and incubated in PBS with 0.6 mg/ml luciferin for 5 min, and photon flux was measured by an in vivo image system (IVIS).

### Intracranial implantation

Mice were anesthetized with a ketamine/xylazine (90–120/7–10 mg/kg) mixture and fixed into a stereotactic head frame (Kopf stereotactic frame). A 1.5-mm bur hole was drilled 1 mm anterior to the coronal suture on the right hemisphere and 2 mm lateral from the midline. A Hamilton syringe fixed onto the head frame was used to inject LL/2 ( $2 \times 10^5$  cells/5  $\mu\text{l}$ ) into the right frontal lobe of the brain. The skin incision was then closed with 4–0 silk thread. The ketoprofen (2 mg/kg) was given to the mice to reduce pain. After 1 wk of tumor transplantation, 36 mice were randomly divided into four groups: (1) tumor transplant only (control group), (2) tumor transplant plus nicotine, (3) tumor transplant plus PLX3397, and (4) tumor transplant plus PLX3397 and nicotine. The PLX3397 and PLX3397 plus nicotine groups received PLX3397 (20 mg in 7  $\mu\text{l}$ ) treatment by intracranial injection every 2 wk at the same area of tumor transplantation. The control group received the same volume of PBS.

### Arg1 gene promoter reporter assay and natural compound screening

To examine the nicotine-induced M2 microglial polarization and examine the effect of natural compounds on microglial polarization, SIM-A9 cells were first infected with lentivirus containing GFP gene, and GFP<sup>+</sup> cells were sorted by flow cytometry (FACS). The GFP<sup>+</sup> SIM-A9 cells were seeded in 96-well plates for 1 d and were transfected with the Arg1 promoter reporter plasmid (Addgene) using Lipofectamine 2000 (Invitrogen). After 24 h, the cells were treated with only nicotine or nicotine plus natural compound in presence of 2% FBS and cultured for another 24 h. Cells were washed twice and were treated with D-luciferin for 5 min. The expression of luciferase was detected by using an IVIS Xenogen bioimager. For Arg1 promoter luciferase normalization, the photon flux was divided by GFP signal, which was measured by a Multi-Mode Reader (Biocompare). Each experiment was conducted a minimum of three times.

### qRT-PCR

For qRT-PCR, the treated cells were washed with PBS and lysed using the TRIzol reagent. The isolated total RNA was quantified by a NanoDrop 2000 (Thermo Fisher Scientific). Then, RNA was reverse transcribed to cDNA using a Reverse Transcription Superscript kit (Bio-Rad). The cDNA was then amplified with a pair of forward and reverse primers for the following genes: hCD74-F 5'-GCGACCTTATCTCCAACAATG-3', hCD74-R 5'-GTCCTCCAGTTCCAGTGACT-3', hCD80-F 5'-CTCTTGCTGGCTGGCTGGTCTT-3', hCD80-R 5'-GCCAGTAGATGCGAGTTTGTGC-3', hCD86-F 5'-CCATCAGCTTGTCTGTTTCATTCC-3', hCD86-R 5'-GCTGTAATCCAAGGAATGTGGTC-3', hArginase-1-F 5'-GCGGGCGGACGC TGGCG-3', hArginase-1-R 5'-GCAGCGGGACCATGTCCACTC-3', hArginase-2-F 5'-AGACGCGAGTGCATTCCATC-3', hArginase-2-R 5'-CACTAATGGTACCGATTGCCA-3', hCD204-F 5'-GGTTTC AATTGTAAGAGAGAGAAG-3', hCD204-R 5'-CTGAGCAATTCT TCGTTTCCC-3', mCD74-F 5'-AGAGCCAGAAAGGTGCAGC-3', mCD74-R 5'-GATGCATCACATGGTCTCTGG-3', mCD80-F 5'-ACG TATTGGAAGGAGATTACAGCT-3', mCD80-R 5'-TCTGTCAGC GTTACTATCCCGC-3', mCD86-F 5'-TTACGGAAGCACCCACGA TG-3', mCD86-R 5'-CCTGTTACATTCTGAGCCAGT-3', hCHR NA7-F 5'-CGTGGATGAGAAGAACCAAG-3', hCHRNA7-R 5'-CCATTGGGGATATAGCCACT-3', hSOX2-F 5'-GGGAAATGGGAG GGGTGCAAAAGAGG-3', hSOX2-R 5'-TTGCGTGAGTGTGGATGG GATTGGTG-3', hOCT4-F 5'-GCTGGAGAAGGAGAAGCTGGAGC-3', hOCT4-R 5'-GCTAAGCTGCAGAGCCTCAAAGC-3', hNanog-F 5'-CTTGGAAGCTGCTGGGGAAG-3', hNanog-R 5'-GATGGGAGG AGGGGAGAGGA-3', hCD47-F 5'-GCTAAAATATCGTGTGTTTC ATGGTTTTC-3', hCD47-R 5'-GCTGTACTAAACACATAGTAGTG AAGT-3', hSIRP-F 5'-GCCTTAGTCGTTCCGCCGCG-3', hSIRP-R 5'-GCCGCTTGCCCTACTCCT-3', hIGF-1-F 5'-GCTGTGCCTGC TCACCTTCACCAG-3', hIGF-1-R 5'-GCCTCCTTAGATCACAGCTC CGGAAG-3', hCCL20-F 5'-TCTCGCTCCAGCATGAAAG-3', and hCCL20-R 5'-CAGATCTCCTTGCCACAATG-3'.

PCR reactions were performed using iTaq Universal SYBR Green Supermix (Bio-Rad) and CFX Connect (Bio-Rad). The thermal cycling conditions composed of an initial denaturation step at  $95^\circ\text{C}$  for 5 min, followed by 35 cycles of PCR using the following profile:  $94^\circ\text{C}$ , 30 s;  $60^\circ\text{C}$ , 30 s; and  $72^\circ\text{C}$ , 30 s.



### Immunocytochemistry and immunofluorescence

The human brain metastasis tissues of lung cancer were obtained from Wake Forest Baptist Comprehensive Cancer Center Tumor Tissue and Pathology Shared Resource. Tissue sections were stained using anti-CD206 (1:200, R&D Systems) for M2 microglia and anti-ionized calcium-binding adapter molecule-1 (Iba1; 1:1,000, Abcam) for microglia and CD45 (1:500, Abcam) for macrophage. Brain sections were then incubated with appropriate biotin-conjugated secondary antibodies and diaminobenzidine as the substrate. As a control, isotype antibodies were used. To examine the expression of SIRP $\alpha$  on microglia, 10- $\mu$ m-thick frozen mouse brain sections were stained using rabbit anti-Iba1 (1:1,000; Abcam) for microglia and anti-SIRP $\alpha$  (1:200) (Cell Signaling). Brain sections were incubated for 1 h in a PBS solution containing 0.1% Triton X-100 and 3% bovine serum albumin at room temperature, and then transferred to a solution containing anti-SIRP $\alpha$  antibody overnight at 4°C. The secondary antibody conjugated with fluorescent dye Alexa Fluor 594 (1:1,000, Invitrogen) was used to detect the expression of SIRP $\alpha$ . Sections were then incubated overnight at 4°C in a solution containing anti-Iba1 antibodies. Antibodies against rabbit IgG conjugated with fluorescent dye Alexa Fluor 488 (1:1,000, Invitrogen) were used to detect the microglial cells. Fluorescence images were acquired using a microscope (BZ-X710, Keyence) connected to a computer equipped with imaging software (BZ-X Viewer). Appropriate isotype antibodies were used as controls. To determine the area of Iba1<sup>+</sup> and CD206<sup>+</sup> cells in brain metastasis, we chose three randomly selected fields in each tumor and measured staining intensity after taking images followed by using the Image-Pro software. We also chose three nontumor areas in the corresponding slide and measured intensity as background, and this background was subtracted from the intensity in the tumor area. The average intensity of three fields was used as the score of that patient. Therefore, each patient has a single score. We then divided the score range by setting the lowest score as 0 and the highest to be +3.

### Western blot

Cells were homogenized in the radioimmunoprecipitation assay buffer and then centrifuged at 17,000 *g* for 30 min at 4°C. The protein concentrations of the supernatants were determined by NanoDrop 2000. Supernatants (30  $\mu$ g of total protein) were mixed with sample buffer containing 0.5 M dithiothreitol, heated to 80°C for 10 min, loaded into each well of 10% polyacrylamide gel, and resolved at 120 V for 2 h. The separated proteins bands were transferred to a polyvinylidene fluoride membrane, blocked with 5% milk, and probed with respective primary antibodies: total-STAT3 (1:1,000, Cell Signaling), phospho-STAT3 (1:1,000, Cell Signaling), GAPDH (1:10,000, Cell Signaling), SOX2 (1:500, Cell Signaling), OCT4 (1:1,000, Cell Signaling), NANOG (1:500, Cell Signaling), and SIRP $\alpha$  (1:1,000, Cell Signaling). The bound antibodies were detected using an enhanced chemiluminescence detection kit (GE Healthcare Lifescience). The band intensities were measured using an imaging system (Amersham Imager 600; UVP) and analyzed using ImageJ (1.43u; <http://rsb.info.nih.gov/ij/>). For gel loading control, membranes were incubated with monoclonal GAPDH antibody.

### CCL20 ELISA

Mouse brain specimens were homogenized in radioimmuno-precipitation assay lysis buffer and centrifuged at 13,000 *g* for 30 min at 4°C. The protein concentrations of the supernatant were measured and adjusted to 1 mg/ml. The human serum of lung cancer patients was obtained from FOX CHASE Cancer Center. The serum was further diluted fourfold in assay buffer. The levels of CCL20 in the mouse brain supernatants and mouse and human serum were determined using mouse and human CCL20 ELISA kits (Sigma-Aldrich). Briefly, 96-well plates were first coated with anti-CCL20 monoclonal antibodies followed by addition of 100  $\mu$ l of the supernatants and serum under investigation or the same volume of the CCL20 standards. The plate was incubated at 4°C overnight on a rocking platform. After washing the plates, the detection antibody and streptavidin solution were added to each well. After incubation, the 3,3',5,5'-tetramethylbenzidine (TMB) and stop solution were added to each well. Finally, the plates were examined at an absorbance wavelength of 450 nm. Standard curves were obtained from values generated from known concentrations of mouse and human CCL20 provided by the kits.

### IGF-1 ELISA

Microglial cells (HMC3) were treated with or without nicotine (1  $\mu$ M) plus STATTIC (0.5  $\mu$ M) for 24 h. Cells were washed with PBS twice and incubated in the fresh DMEM/F12 medium supplemented with 2% FBS for an additional 24 h. The human monocyte/macrophage cells were treated with or without nicotine for 24 h. CM was collected and analyzed by the human IGF-1 ELISA kit (Sigma-Aldrich). Briefly, 96-well plates were first coated with anti-IGF-1 monoclonal antibodies followed by addition of 100  $\mu$ l of the microglia conditional medium or the same volume of the IGF-1 standards. The plate was incubated at 4°C overnight on a rocking platform. After washing the plates, the detection antibody and streptavidin solution were added to each well. After incubation, the TMB and stop solution were added to each well. Finally, the plates were examined at an absorbance wavelength of 450 nm. Standard curves were obtained from values generated from known concentrations of mouse and human IGF-1 provided by the kit.

### Phagocytosis assay

H2030BrM and LL/2 cells were labeled with PKH26 dye (Sigma-Aldrich). The labeled cells were then washed three times and cultured overnight to reduce nonspecific leaking of dye during the assay. Tumor cells were 95% viable after the incubation. Labeled tumor cells were mixed with microglia that were pretreated with or without nicotine. Co-cultured tumor and microglia cells in the culture slides were harvested after 24 h and fixed with 4% paraformaldehyde. Microglial cells were counterstained with anti-Iba1 antibody overnight. Secondary antibody conjugated with the fluorescent dye Alexa Fluor 488 (1:1,000, Invitrogen) was used to detect the microglia. The phagocytic activities were measured by immunofluorescence microscope and FACS. For quantification of phagocytosis, the phagocytic percentage was calculated as  $100 \times (\text{percent Iba1}^+ /$

PKH26<sup>+</sup> cells/[percent Iba1<sup>+</sup>/PKH26<sup>+</sup> cells + percent Iba1<sup>+</sup>/PKH26<sup>+</sup> cells]).

### Statistical analysis

Data are represented as mean  $\pm$  SD. Significance was set at  $P < 0.05$ . The nicotine effect on M1/M2 gene expression, effect of nicotine-derived microglial CM on tumor growth, and effect of nicotine on microglia phagocytosis ability were analyzed using the unpaired Student's *t* test. One-way ANOVA was used to analyze the effect of nicotine, PTL3397, or STATTIC treatment on M1/M2 gene polarization and tumor progression, the effect of different concentrations of IGF-1 or CCL20 on cancer progression, the effect of different natural compounds on M2 gene polarization, and the effect of nicotine or PTL treatment on M1/M2 gene polarization and cancer cell progression and nicotine effect in animal studies. Significance between groups was represented as \*,  $P < 0.05$ ; \*\*,  $P < 0.01$ ; and \*\*\*,  $P < 0.001$ .

### Online supplemental material

Fig. S1 shows the effect of smoking and nicotine on brain metastasis. Fig. S2 demonstrates that the nicotine promotes brain metastasis in a mouse model. Fig. S3 shows that nicotine treatment of microglia increases secretion of CCL20 and IGF-1 followed by promotion of tumor cell stemness. Fig. S4 shows the effect of natural compounds on nicotine-mediated activity of Arg1 reporter. Fig. S5 shows PTL suppressed nicotine-promoted brain metastasis in syngeneic mouse model.

### Acknowledgments

We thank Dr. Joan Massagué for providing the H2030-BrM cell line.

This work was supported by National Institutes of Health grants RO1CA173499, RO1CA185650, and RO1CA205067 (to K. Watabe). This research used Cancer Center Shared Resources, The Tumor Tissue and Pathology, Cell Engineering, Flow Cytometry, Biostatistics and Bioinformatics that are supported by the Comprehensive Cancer Center of the Wake Forest University National Cancer Institute, National Institutes of Health grant P30CA012197. The content is solely the responsibility of the authors and does not necessarily represent the official views of the National Cancer Institute.

Author contributions: S. Wu and K. Watabe designed the study and wrote the manuscript. S. Wu, F. Xing, and K. Wu conducted experiments and acquired, analyzed, and interpreted the data. S. Sharma, A. Tyagi, and K. Wu performed animal experiments. F. Xing and Y. Liu performed intracardiac injections. T. Lycan and A. Dothard performed clinical sample analysis. S. Wu, F. Xing, S. Sharma, A. Tyagi, K. Wu, Y. Liu, D. Zhao, R.P. Deshpande, Y. Shiozawa, T. Ahmed, W. Zhang, M. Chan, J. Ruiz, and K. Watabe reviewed and edited the manuscript and interpreted the data. K. Watabe supervised the study.

Disclosures: Dr. Shiozawa reported grants from Teva Pharmaceutical Industries outside the submitted work. Dr. Chan reported other from Elekta and other from Monteris outside the submitted work. No other disclosures were reported.

Submitted: 20 June 2019

Revised: 9 September 2019

Accepted: 2 March 2020

### References

- Adams, S., L.J. van der Laan, E. Vernon-Wilson, C. Renardel de Lavalette, E.A. Döpp, C.D. Dijkstra, D.L. Simmons, and T.K. van den Berg. 1998. Signal-regulatory protein is selectively expressed by myeloid and neuronal cells. *J. Immunol.* 161:1853–1859.
- Ali, A., J.R. Goffin, A. Arnold, and P.M. Ellis. 2013. Survival of patients with non-small-cell lung cancer after a diagnosis of brain metastases. *Curr. Oncol.* 20:e300–e306. <https://doi.org/10.3747/co.20.1481>
- Bacha, S., H. Cherif, D. Rabaa, S. Habibech, S. Cheikhrouhou, H. Racil, N. Chaouch, M.L. Megdiche, and A. Chabbou. 2018. Brain metastases of non-small cell lung cancer: prognostic factors and management. *Tunis. Med.* 96:165–171.
- Badie, B., and J.M. Scharfner. 2000. Flow cytometric characterization of tumor-associated macrophages in experimental gliomas. *Neurosurgery*. 46: 957–961. <https://doi.org/10.1097/00006123-200004000-00035>
- Barnholtz-Sloan, J.S., A.E. Sloan, F.G. Davis, F.D. Vigneau, P. Lai, and R.E. Sawaya. 2004. Incidence proportions of brain metastases in patients diagnosed (1973 to 2001) in the Metropolitan Detroit Cancer Surveillance System. *J. Clin. Oncol.* 22:2865–2872. <https://doi.org/10.1200/JCO.2004.12.149>
- Braverman, M.T.. 1999. Research on resilience and its implications for tobacco prevention. *Nicotine Tob. Res.* 1(Suppl 1):S67–S72. <https://doi.org/10.1080/14622299050011621>
- Butowski, N., H. Colman, J.F. De Groot, A.M. Omuro, L. Nayak, P.Y. Wen, T.F. Cloughesy, A. Marimuthu, S. Haidar, A. Perry, et al. 2016. Orally administered colony stimulating factor 1 receptor inhibitor PLX3397 in recurrent glioblastoma: an Ivy Foundation Early Phase Clinical Trials Consortium phase II study. *Neuro-oncol.* 18:557–564. <https://doi.org/10.1093/neuonc/nov245>
- Cannarile, M.A., M. Weisser, W. Jacob, A.M. Jegg, C.H. Ries, and D. Rüttinger. 2017. Colony-stimulating factor 1 receptor (CSF1R) inhibitors in cancer therapy. *J. Immunother. Cancer.* 5:53. <https://doi.org/10.1186/s40425-017-0257-y>
- Carlisi, D., A. D'Anneo, L. Angileri, M. Lauricella, S. Emanuele, A. Santulli, R. Vento, and G. Tesoriere. 2011. Parthenolide sensitizes hepatocellular carcinoma cells to TRAIL by inducing the expression of death receptors through inhibition of STAT3 activation. *J. Cell. Physiol.* 226:1632–1641. <https://doi.org/10.1002/jcp.22494>
- Chen, Q., A. Boire, X. Jin, M. Valiente, E.E. Er, A. Lopez-Soto, L. Jacob, R. Patwa, H. Shah, K. Xu, et al. 2016. Carcinoma-astrocyte gap junctions promote brain metastasis by cGAMP transfer. *Nature.* 533:493–498. <https://doi.org/10.1038/nature18268>
- Chen, W., Y. Qin, D. Wang, L. Zhou, Y. Liu, S. Chen, L. Yin, Y. Xiao, X.H. Yao, X. Yang, et al. 2018. CCL20 triggered by chemotherapy hinders the therapeutic efficacy of breast cancer. *PLoS Biol.* 16. e2005869. <https://doi.org/10.1371/journal.pbio.2005869>
- Cuccarese, M.F., J.M. Dubach, C. Pfirsichke, C. Engblom, C. Garriss, M.A. Miller, M.J. Pittet, and R. Weissleder. 2017. Heterogeneity of macrophage infiltration and therapeutic response in lung carcinoma revealed by 3D organ imaging. *Nat. Commun.* 8:14293. <https://doi.org/10.1038/ncomms14293>
- da Fonseca, A.C., and B. Badie. 2013. Microglia and macrophages in malignant gliomas: recent discoveries and implications for promising therapies. *Clin. Dev. Immunol.* 2013. 264124. <https://doi.org/10.1155/2013/264124>
- Ellis, T.L., M.T. Neal, and M.D. Chan. 2012. The role of surgery, radiosurgery and whole brain radiation therapy in the management of patients with metastatic brain tumors. *Int. J. Surg. Oncol.* 2012. 952345. <https://doi.org/10.1155/2012/952345>
- Elmore, M.R., A.R. Najafi, M.A. Koike, N.N. Dagher, E.E. Spangenberg, R.A. Rice, M. Kitazawa, B. Matusow, H. Nguyen, B.L. West, et al. 2014. Colony-stimulating factor 1 receptor signaling is necessary for microglia viability, unmasking a microglia progenitor cell in the adult brain. *Neuron.* 82:380–397. <https://doi.org/10.1016/j.neuron.2014.02.040>
- Feng, X., F. Szulzewsky, A. Yerevanian, Z. Chen, D. Heinzmann, R.D. Rasmussen, V. Alvarez-Garcia, Y. Kim, B. Wang, I. Tamagno, et al. 2015. Loss of CX3CR1 increases accumulation of inflammatory monocytes and promotes gliomagenesis. *Oncotarget.* 6:15077–15094. <https://doi.org/10.18632/oncotarget.3730>

- Fidler, I.J.. 2015. The Biology of Brain Metastasis: Challenges for Therapy. *Cancer J.* 21:284–293. <https://doi.org/10.1097/PPO.0000000000000126>
- Gaspar, L., C. Scott, M. Rotman, S. Asbell, T. Phillips, T. Wasserman, W.G. McKenna, and R. Byhardt. 1997. Recursive partitioning analysis (RPA) of prognostic factors in three Radiation Therapy Oncology Group (RTOG) brain metastases trials. *Int. J. Radiat. Oncol. Biol. Phys.* 37: 745–751. [https://doi.org/10.1016/S0360-3016\(96\)00619-0](https://doi.org/10.1016/S0360-3016(96)00619-0)
- Gomez Perdiguero, E., K. Klapproth, C. Schulz, K. Busch, E. Azzoni, L. Crozet, H. Garner, C. Trouillet, M.F. de Bruijn, F. Geissmann, et al. 2015. Tissue-resident macrophages originate from yolk-sac-derived erythro-myeloid progenitors. *Nature.* 518:547–551. <https://doi.org/10.1038/nature13989>
- Hartmann-Boyce, J., S.C. Chepkin, W. Ye, C. Bullen, and T. Lancaster. 2018. Nicotine replacement therapy versus control for smoking cessation. *Cochrane Database Syst. Rev.* 5. CD000146. <https://doi.org/10.1002/14651858.CD000146.pub5>
- Hawkins, B.T., T.J. Abbruscato, R.D. Egleton, R.C. Brown, J.D. Huber, C.R. Campos, and T.P. Davis. 2004. Nicotine increases in vivo blood-brain barrier permeability and alters cerebral microvascular tight junction protein distribution. *Brain Res.* 1027:48–58. <https://doi.org/10.1016/j.brainres.2004.08.043>
- He, B.P., J.J. Wang, X. Zhang, Y. Wu, M. Wang, B.H. Bay, and A.Y. Chang. 2006. Differential reactions of microglia to brain metastasis of lung cancer. *Mol. Med.* 12:161–170. <https://doi.org/10.2119/2006-00033.He>
- Heishman, S.J.. 1999. Behavioral and cognitive effects of smoking: relationship to nicotine addiction. *Nicotine Tob. Res.* 1:S143–S147, NaN–S166. <https://doi.org/10.1080/14622299050011971>
- Henningfield, J.E., C. Cohen, and J.D. Slade. 1991. Is nicotine more addictive than cocaine? *Br. J. Addict.* 86:565–569. <https://doi.org/10.1111/j.1360-0443.1991.tb01809.x>
- Huang, Z., B. Sun, S. Wu, X. Meng, Y. Cong, G. Shen, and S. Song. 2018. A nomogram for predicting survival in patients with breast cancer brain metastasis. *Oncol. Lett.* 15:7090–7096. <https://doi.org/10.3892/ol.2018.8259>
- Hutter, G., J. Theruvath, C.M. Graef, M. Zhang, M.K. Schoen, E.M. Manz, M.L. Bennett, A. Olson, T.D. Azad, R. Sinha, et al. 2019. Microglia are effector cells of CD47-SIRPα antiphagocytic axis disruption against glioblastoma. *Proc. Natl. Acad. Sci. USA.* 116:997–1006. <https://doi.org/10.1073/pnas.1721434116>
- Janker, F., W. Weder, J.H. Jang, and W. Jungraithmayr. 2018. Preclinical, non-genetic models of lung adenocarcinoma: a comparative survey. *Oncotarget.* 9:30527–30538. <https://doi.org/10.18632/oncotarget.25668>
- Kakusa, B., S. Han, S. Aggarwal, B. Liu, G. Li, S. Soltys, and M. Hayden Gephart. 2018. Clinical factors associated with mortality within three months after radiosurgery of asymptomatic brain metastases from non-small cell lung cancer. *J. Neurooncol.* 140:705–715. <https://doi.org/10.1007/s11060-018-03002-0>
- Kamei, D., M. Murakami, Y. Sasaki, Y. Nakatani, M. Majima, Y. Ishikawa, T. Ishii, S. Uematsu, S. Akira, S. Hara, et al. 2009. Microsomal prostaglandin E synthase-1 in both cancer cells and hosts contributes to tumour growth, invasion and metastasis. *Biochem. J.* 425:361–371. <https://doi.org/10.1042/BJ20090045>
- Kharitonov, A., Z. Chen, I. Sures, H. Wang, J. Schilling, and A. Ullrich. 1997. A family of proteins that inhibit signalling through tyrosine kinase receptors. *Nature.* 386:181–186. <https://doi.org/10.1038/386181a0>
- Könczöl, A., J. Müller, E. Földes, Z. Béni, K. Végh, A. Kéry, and G.T. Balogh. 2013. Applicability of a blood-brain barrier specific artificial membrane permeability assay at the early stage of natural product-based CNS drug discovery. *J. Nat. Prod.* 76:655–663. <https://doi.org/10.1021/np300882f>
- Lee, P.N., B.A. Forey, and K.J. Coombs. 2012. Systematic review with meta-analysis of the epidemiological evidence in the 1900s relating smoking to lung cancer. *BMC Cancer.* 12:385. <https://doi.org/10.1186/1471-2407-12-385>
- Leskovaar, A., L.J. Moriarty, J.J. Turek, I.A. Schoenlein, and R.B. Borgens. 2000. The macrophage in acute neural injury: changes in cell numbers over time and levels of cytokine production in mammalian central and peripheral nervous systems. *J. Exp. Biol.* 203(Pt 12):1783–1795.
- Li, T., J. Zhang, J. Zhang, N. Zhang, Y. Zeng, S. Tang, Z. Tao, X. Qu, J. Jia, W. Zhu, et al. 2017. Nicotine-enhanced stemness and epithelial-mesenchymal transition of human umbilical cord mesenchymal stem cells promote tumor formation and growth in nude mice. *Oncotarget.* 9: 591–606. <https://doi.org/10.18632/oncotarget.22712>
- Lin, M., H. Bi, Y. Yan, W. Huang, G. Zhang, G. Zhang, S. Tang, Y. Liu, L. Zhang, J. Ma, et al. 2017. Parthenolide suppresses non-small cell lung cancer GLC-82 cells growth via B-Raf/MAPK/Erk pathway. *Oncotarget.* 8:23436–23447. <https://doi.org/10.18632/oncotarget.15584>
- Liu, Q., J. Zhao, R. Tan, H. Zhou, Z. Lin, M. Zheng, E. Romas, J. Xu, and N.A. Sims. 2015a. Parthenolide inhibits pro-inflammatory cytokine production and exhibits protective effects on progression of collagen-induced arthritis in a rat model. *Scand. J. Rheumatol.* 44:182–191. <https://doi.org/10.3109/03009742.2014.938113>
- Liu, X., Y. Pu, K. Cron, L. Deng, J. Kline, W.A. Frazier, H. Xu, H. Peng, Y.X. Fu, and M.M. Xu. 2015b. CD47 blockade triggers T cell-mediated destruction of immunogenic tumors. *Nat. Med.* 21:1209–1215. <https://doi.org/10.1038/nm.3931>
- Liu, B., Y. Jia, J. Ma, S. Wu, H. Jiang, Y. Cao, X. Sun, X. Yin, S. Yan, M. Shang, et al. 2016. Tumor-associated macrophage-derived CCL20 enhances the growth and metastasis of pancreatic cancer. *Acta Biochim. Biophys. Sin. (Shanghai).* 48:1067–1074. <https://doi.org/10.1093/abbs/gmw101>
- Liu, M., C. Xiao, M. Sun, M. Tan, L. Hu, and Q. Yu. 2018. Parthenolide Inhibits STAT3 Signaling by Covalently Targeting Janus Kinases. *Molecules.* 23. E1478. <https://doi.org/10.3390/molecules23061478>
- Lu, E., J. Su, Y. Zhou, C. Zhang, and Y. Wang. 2017. CCL20/CCR6 promotes cell proliferation and metastasis in laryngeal cancer by activating p38 pathway. *Biomed. Pharmacother.* 85:486–492. <https://doi.org/10.1016/j.biopha.2016.11.055>
- Malladi, S., D.G. Macalinao, X. Jin, L. He, H. Basnet, Y. Zou, E. de Stanchina, and J. Massagué. 2016. Metastatic Latency and Immune Evasion through Autocrine Inhibition of WNT. *Cell.* 165:45–60. <https://doi.org/10.1016/j.cell.2016.02.025>
- Marsigliante, S., C. Vetrugno, and A. Muscella. 2016. Paracrine CCL20 loop induces epithelial-mesenchymal transition in breast epithelial cells. *Mol. Carcinog.* 55:1175–1186. <https://doi.org/10.1002/mc.22360>
- Mazzaferro, S., I. Bermudez, and S.M. Sine. 2017. α4β2 Nicotinic Acetylcholine Receptors: Relationships Between Subunit Stoichiometry and Function at the Single Channel Level. *J. Biol. Chem.* 292:2729–2740. <https://doi.org/10.1074/jbc.M116.764183>
- Morioka, N., S. Harano, M. Tokuhara, Y. Idenoshita, F.F. Zhang, K. Hisaoka-Nakashima, and Y. Nakata. 2015. Stimulation of α7 nicotinic acetylcholine receptor regulates glutamate transporter GLAST via basic fibroblast growth factor production in cultured cortical microglia. *Brain Res.* 1625:111–120. <https://doi.org/10.1016/j.brainres.2015.08.029>
- Mujoomdar, A., J.H. Austin, R. Malhotra, C.A. Powell, G.D. Pearson, M.C. Shiau, and H. Raftopoulos. 2007. Clinical predictors of metastatic disease to the brain from non-small cell lung carcinoma: primary tumor size, cell type, and lymph node metastases. *Radiology.* 242:882–888. <https://doi.org/10.1148/radiol.2423051707>
- Munn, D.H., and N.K. Cheung. 1990. Phagocytosis of tumor cells by human monocytes cultured in recombinant macrophage colony-stimulating factor. *J. Exp. Med.* 172:231–237. <https://doi.org/10.1084/jem.172.1.231>
- Nandi, B., C. Pai, Q. Huang, R.H. Prabhala, N.C. Munshi, and J.S. Gold. 2014. CCR6, the sole receptor for the chemokine CCL20, promotes spontaneous intestinal tumorigenesis. *PLoS One.* 9. e97566. <https://doi.org/10.1371/journal.pone.0097566>
- Nguyen, D.X., A.C. Chiang, X.H. Zhang, J.Y. Kim, M.G. Kris, M. Ladanyi, W.L. Gerald, and J. Massagué. 2009. WNT/TCF signaling through LEF1 and HOXB9 mediates lung adenocarcinoma metastasis. *Cell.* 138:51–62. <https://doi.org/10.1016/j.cell.2009.04.030>
- Pan, Y.F., Y.X. Tan, M. Wang, J. Zhang, B. Zhang, C. Yang, Z.W. Ding, L.W. Dong, and H.Y. Wang. 2013. Signal regulatory protein α is associated with tumor-polarized macrophages phenotype switch and plays a pivotal role in tumor progression. *Hepatology.* 58:680–691. <https://doi.org/10.1002/hep.26391>
- Park, Y.S., D.J. Kim, H. Koo, S.H. Jang, Y.M. You, J.H. Cho, S.J. Yang, E.S. Yu, Y. Jung, D.C. Lee, et al. 2016. AKT-induced PKM2 phosphorylation signals for IGF-1-stimulated cancer cell growth. *Oncotarget.* 7: 48155–48167. <https://doi.org/10.18632/oncotarget.10179>
- Prinz, M., and J. Priller. 2014. Microglia and brain macrophages in the molecular age: from origin to neuropsychiatric disease. *Nat. Rev. Neurosci.* 15:300–312. <https://doi.org/10.1038/nrn3722>
- Qin, C., W.H. Fan, Q. Liu, K. Shang, M. Murugan, L.J. Wu, W. Wang, and D.S. Tian. 2017. Fingolimod Protects Against Ischemic White Matter Damage by Modulating Microglia Toward M2 Polarization via STAT3 Pathway. *Stroke.* 48:3336–3346. <https://doi.org/10.1161/STROKEAHA.117.018505>
- Redmer, T. 2018. Deciphering mechanisms of brain metastasis in melanoma - the gist of the matter. *Mol. Cancer.* 17:106. <https://doi.org/10.1186/s12943-018-0854-5>
- Roesch, S., C. Rapp, S. Dettling, and C. Herold-Mende. 2018. When Immune Cells Turn Bad-Tumor-Associated Microglia/Macrophages in Glioma. *Int. J. Mol. Sci.* 19. E436. <https://doi.org/10.3390/ijms19020436>



- Rummel, C., R. Gerstberger, J. Roth, and T. Hübschle. 2011. Parthenolide attenuates LPS-induced fever, circulating cytokines and markers of brain inflammation in rats. *Cytokine*. 56:739–748. <https://doi.org/10.1016/j.cyto.2011.09.022>
- Sadigh-Eteghad, S., A. Majidi, J. Mahmoudi, S.E.J. Goltari, and M. Talebi. 2016. Astrocytic and microglial nicotinic acetylcholine receptors: an overlooked issue in Alzheimer's disease. *J. Neural Transm. (Vienna)*. 123: 1359–1367. <https://doi.org/10.1007/s00702-016-1580-z>
- Schaal, C., and S.P. Chellappan. 2014. Nicotine-mediated cell proliferation and tumor progression in smoking-related cancers. *Mol. Cancer Res.* 12: 14–23. <https://doi.org/10.1158/1541-7786.MCR-13-0541>
- Schaal, C.M., N. Bora-Singhal, D.M. Kumar, and S.P. Chellappan. 2018. Regulation of Sox2 and stemness by nicotine and electronic-cigarettes in non-small cell lung cancer. *Mol. Cancer*. 17:149. <https://doi.org/10.1186/s12943-018-0901-2>
- Scholar, E.M., L.A. Violi, J. Newland, E. Bresnick, and D.F. Birt. 1989. The effect of dietary fat on metastasis of the Lewis lung carcinoma and the BALB/c mammary carcinoma. *Nutr. Cancer*. 12:109–119. <https://doi.org/10.1080/01635588909514009>
- Schouten, L.J., J. Rutten, H.A. Huveneers, and A. Twijnstra. 2002. Incidence of brain metastases in a cohort of patients with carcinoma of the breast, colon, kidney, and lung and melanoma. *Cancer*. 94:2698–2705. <https://doi.org/10.1002/cncr.10541>
- Schulz, C., E. Gomez Perdiguerro, L. Chorro, H. Szabo-Rogers, N. Cagnard, K. Kierdorf, M. Prinz, B. Wu, S.E. Jacobsen, J.W. Pollard, et al. 2012. A lineage of myeloid cells independent of Myb and hematopoietic stem cells. *Science*. 336:86–90. <https://doi.org/10.1126/science.1219179>
- Scott, A., S.T. Lugg, K. Aldridge, K.E. Lewis, A. Bowden, R.Y. Mahida, F.S. Grudzinska, D. Dosanjh, D. Parekh, R. Foronjy, et al. 2018. Pro-inflammatory effects of e-cigarette vapour condensate on human alveolar macrophages. *Thorax*. 73(12):1161–1169. <https://doi.org/10.1136/thoraxjnl-2018-211663>
- Shenker, R.F., E.R. McTyre, J. Ruiz, K.E. Weaver, C. Cramer, N.K. Alphonse-Sullivan, M. Farris, W.J. Petty, M.R. Bonomi, K. Watabe, et al. 2017. The Effects of smoking status and smoking history on patients with brain metastases from lung cancer. *Cancer Med.* 6:944–952. <https://doi.org/10.1002/cam4.1058>
- Skoumal, R., M. Tóth, R. Serpi, J. Rysä, H. Leskinen, J. Ulvila, T. Saiho, J. Aro, H. Ruskoaho, I. Szokodi, et al. 2011. Parthenolide inhibits STAT3 signaling and attenuates angiotensin II-induced left ventricular hypertrophy via modulation of fibroblast activity. *J. Mol. Cell. Cardiol.* 50: 634–641. <https://doi.org/10.1016/j.yjmcc.2011.01.001>
- Sobota, R., M. Szwed, A. Kasza, M. Bugno, and T. Kordula. 2000. Parthenolide inhibits activation of signal transducers and activators of transcription (STATs) induced by cytokines of the IL-6 family. *Biochem. Biophys. Res. Commun.* 267:329–333. <https://doi.org/10.1006/bbrc.1999.1948>
- Song, J.M., X. Qian, P. Upadhyaya, K.H. Hong, and F. Kassie. 2014. Dimethylaminoparthenolide, a water soluble parthenolide, suppresses lung tumorigenesis through down-regulating the STAT3 signaling pathway. *Curr. Cancer Drug Targets*. 14:59–69. <https://doi.org/10.2174/15680096113136660108>
- Sperduto, P.W., B. Berkey, L.E. Gaspar, M. Mehta, and W. Curran. 2008. A new prognostic index and comparison to three other indices for patients with brain metastases: an analysis of 1,960 patients in the RTOG database. *Int. J. Radiat. Oncol. Biol. Phys.* 70:510–514. <https://doi.org/10.1016/j.ijrobp.2007.06.074>
- Stead, L.F., R. Perera, C. Bullen, D. Mant, J. Hartmann-Boyce, K. Cahill, and T. Lancaster. 2012. Nicotine replacement therapy for smoking cessation. *Cochrane Database Syst. Rev.* 11. CD000146. <https://doi.org/10.1002/14651858.CD000146.pub4>
- Sun, H.J., Y.F. Jia, and X.L. Ma. 2017. Alpha5 Nicotinic Acetylcholine Receptor Contributes to Nicotine-Induced Lung Cancer Development and Progression. *Front. Pharmacol.* 8:573. <https://doi.org/10.3389/fphar.2017.00573>
- Talib, W.H., and L.T. Al Kury. 2018. Parthenolide inhibits tumor-promoting effects of nicotine in lung cancer by inducing P53 - dependent apoptosis and inhibiting VEGF expression. *Biomed. Pharmacother.* 107:1488–1495. <https://doi.org/10.1016/j.biopha.2018.08.139>
- Vergier, E., M. Gil, R. Yaya, N. Viñolas, S. Villà, T. Pujol, L. Quintó, and F. Graus. 2005. Temozolomide and concomitant whole brain radiotherapy in patients with brain metastases: a phase II randomized trial. *Int. J. Radiat. Oncol. Biol. Phys.* 61:185–191. <https://doi.org/10.1016/j.ijrobp.2004.04.061>
- Wang, G.Z., X. Cheng, X.C. Li, Y.Q. Liu, X.Q. Wang, X. Shi, Z.Y. Wang, Y.Q. Guo, Z.S. Wen, Y.C. Huang, et al. 2015. Tobacco smoke induces production of chemokine CCL20 to promote lung cancer. *Cancer Lett.* 363: 60–70. <https://doi.org/10.1016/j.canlet.2015.04.005>
- Wang, B., L. Shi, X. Sun, L. Wang, X. Wang, and C. Chen. 2016. Production of CCL20 from lung cancer cells induces the cell migration and proliferation through PI3K pathway. *J. Cell. Mol. Med.* 20:920–929. <https://doi.org/10.1111/jcmm.12781>
- Wang, C., W. Gu, Y. Zhang, Y. Ji, Y. Wen, and X. Xu. 2017. Nicotine promotes cervical carcinoma cell line HeLa migration and invasion by activating PI3k/Akt/NF-κB pathway in vitro. *Exp. Toxicol. Pathol.* 69:402–407. <https://doi.org/10.1016/j.etp.2017.03.006>
- Wei, J., K. Gabrusiewicz, and A. Heimberger. 2013. The controversial role of microglia in malignant gliomas. *Clin. Dev. Immunol.* 2013. 285246. <https://doi.org/10.1155/2013/285246>
- Wu, S.Y., and K. Watabe. 2017. The roles of microglia/macrophages in tumor progression of brain cancer and metastatic disease. *Front. Biosci.* 22: 1805–1829. <https://doi.org/10.2741/4573>
- Xing, F., Y. Liu, S.Y. Wu, K. Wu, S. Sharma, Y.Y. Mo, J. Feng, S. Sanders, G. Jin, R. Singh, et al. 2018. Loss of XIST in Breast Cancer Activates MSN-c-Met and Reprograms Microglia via Exosomal miRNA to Promote Brain Metastasis. *Cancer Res.* 78:4316–4330. <https://doi.org/10.1158/0008-5472.CAN-18-1102>
- Yi, W.J., and T.S. Kim. 2017. Melatonin protects mice against stress-induced inflammation through enhancement of M2 macrophage polarization. *Int. Immunopharmacol.* 48:146–158. <https://doi.org/10.1016/j.intimp.2017.05.006>
- Yoneyama, R., K. Aoshiba, K. Furukawa, M. Saito, H. Kataba, H. Nakamura, and N. Ikeda. 2016. Nicotine enhances hepatocyte growth factor-mediated lung cancer cell migration by activating the α7 nicotine acetylcholine receptor and phosphoinositide kinase-3-dependent pathway. *Oncol. Lett.* 11:673–677. <https://doi.org/10.3892/ol.2015.3930>
- Zhang, S., and T.M. Petro. 1996. The effect of nicotine on murine CD4 T cell responses. *Int. J. Immunopharmacol.* 18:467–478. [https://doi.org/10.1016/S0192-0561\(96\)00054-9](https://doi.org/10.1016/S0192-0561(96)00054-9)
- Zhu, C., X. Qi, Y. Chen, B. Sun, Y. Dai, and Y. Gu. 2011. PI3K/Akt and MAPK/ERK1/2 signaling pathways are involved in IGF-1-induced VEGF-C up-regulation in breast cancer. *J. Cancer Res. Clin. Oncol.* 137:1587–1594. <https://doi.org/10.1007/s00432-011-1049-2>
- Zhu, Y., B.L. Knolhoff, M.A. Meyer, T.M. Nywening, B.L. West, J. Luo, A. Wang-Gillam, S.P. Goedegebuure, D.C. Linehan, and D.G. DeNardo. 2014. CSF1/CSF1R blockade reprograms tumor-infiltrating macrophages and improves response to T-cell checkpoint immunotherapy in pancreatic cancer models. *Cancer Res.* 74:5057–5069. <https://doi.org/10.1158/0008-5472.CAN-13-3723>



## Supplemental material

	Adenocarcinoma	Non-adenocarcinoma
Age	62.78	65.21
Male gender (%)	94 (33%)	60 (21%)
<b>Smoking status</b>		
-Never/Former	149	73
-Current	43	16
<b>Pack years</b>		
<20	81	23
20-60	88	38
>60	23	28

Figure S1. **Effect of smoking and nicotine on brain metastasis.** Patient profile and their smoking history.

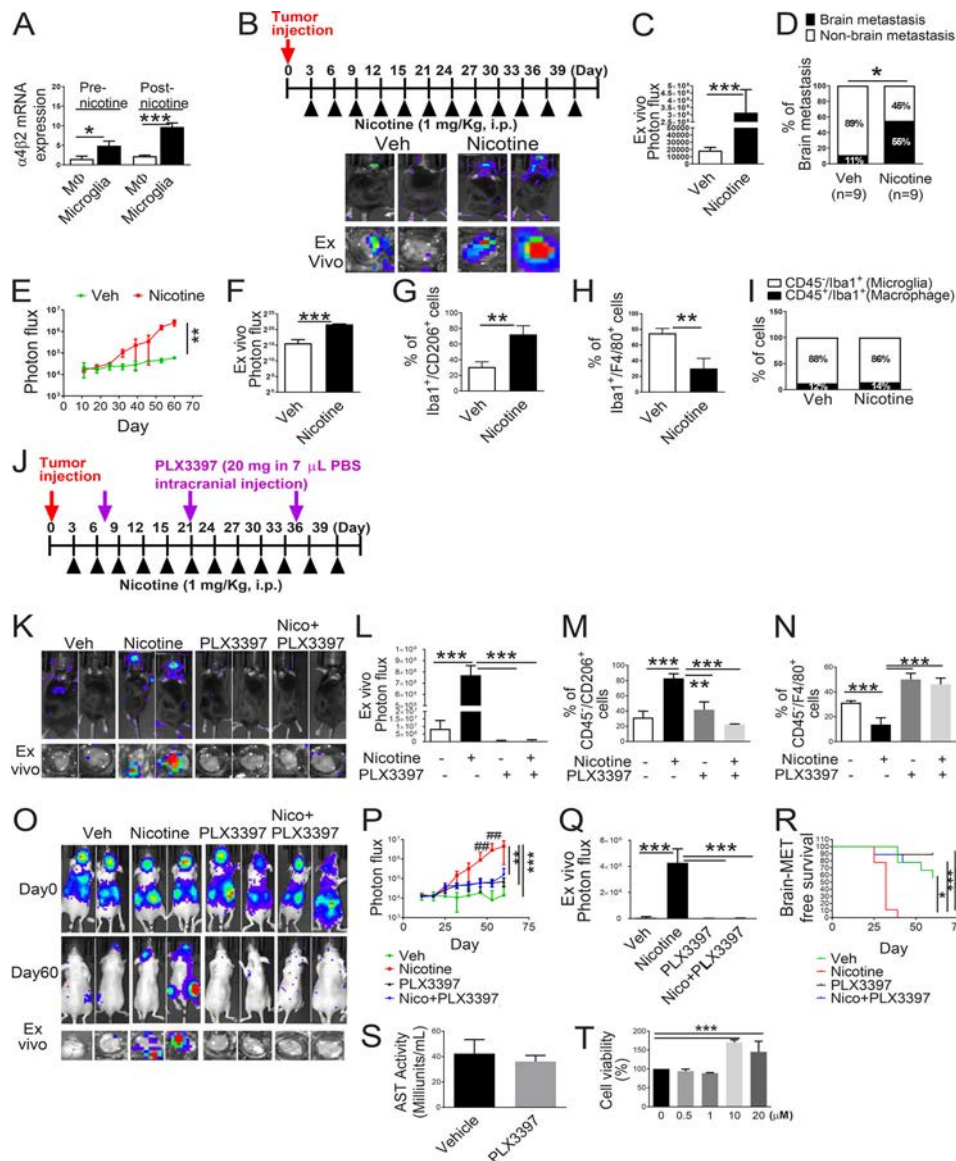


**Figure S2. Nicotine promotes brain metastasis in mouse model.** (A) Expression of the  $\alpha 4 \beta 2$  nicotine receptor on human microglia (HMC3) and human monocyte/macrophage (THP-1) were evaluated before and after nicotine treatment by qRT-PCR ( $n = 4$ /group). (B) Mouse lung cancer LL/2 cells were intracardially injected into wild-type C57BL/6 mice ( $n = 9$ /group). After 3 d of intracardiac transplantation of LL/2 cells, mice received nicotine (1 mg/kg) treatment by intraperitoneal injection every 3 d. Upper panels are BLI images of brain metastatic lesions of representative mice from each experimental group at day 40. The lower panels represent the total photon flux of ex vivo brain metastatic lesions as measured by BLI at the endpoint (day 40). (C) Quantitative data of in vivo brain metastasis of lung cancer ( $n = 9$ /group). (D) Percentage of brain metastasis of lung cancer in C57BL/6 mice with or without nicotine treatment ( $n = 9$ /group). (E and F) Quantitative data of in vivo brain metastasis of lung cancer (left panel) and ex vivo signals in the brain at the end point (right panel) of the experiment conducted in Fig. 2 B ( $n = 9$ /group). (G and H) Metastatic brain tumor tissues in Fig. 2 B were dissociated, and the effect of nicotine was examined on Iba1<sup>+</sup>/CD206<sup>+</sup> (G) or Iba1<sup>+</sup>/F4/80<sup>+</sup> cells (H) by FACS ( $n = 9$ /group). (I) Metastatic brain tumor tissues in Fig. 2 B were dissociated, and the Iba1<sup>+</sup>/CD45<sup>+</sup> (microglia) and Iba1<sup>+</sup>/CD45<sup>+</sup> (macrophage) were measured and plotted in relation to the nicotine treatment ( $n = 9$ /group). (J) Scheme of the experimental design. After 3 d of intracranial transplantation of LL/2 cells, the mice received nicotine (1 mg/kg) by intraperitoneal injection every 3 d. After 1 wk of tumor transplantation, PLX3397 (20 mg/kg in 7  $\mu$ L PBS) was directly injected into the right brain of the mice every 2 wk. (K) Upper panels are BLI images of brain metastatic lesions of representative mice from each experimental group at day 40. The lower panels represent the total photon flux of ex vivo brain metastatic lesions as measured by BLI at the endpoint (day 40;  $n = 9$ /group). (L) Quantitative data of ex vivo brain metastasis of lung cancer at the end point. (M and N) Metastatic brain tumors in K were isolated from the brain and examined by FACS for M2 (M) and M1 (N) microglial polarization ( $n = 9$ /group). (O) H2030BrM ( $2 \times 10^5$  cells) were intracardially injected into nude mice ( $n = 9$ /group) followed by administering them with nicotine plus PLX3397 (1 mg/kg) by intraperitoneal injection every 3 d. Upper and middle panels are BLI images of brain metastatic lesions of representative mice from each experimental group at day 0 and day 60, respectively. Lower panels represent the total photon flux of ex vivo brain metastatic lesions as measured by BLI at the endpoint (day 60;  $n = 9$ /group). (P and Q) Quantitative data of in vivo brain metastasis of lung cancer and (Q) ex vivo signals in the brain at the end point (day 60;  $n = 9$ /group). (R) Kaplan-Meier analysis of brain metastasis-free survival was performed. (S) Serum of mice in Fig. 2 E was collected, and an aspartate aminotransferase test (AST) was measured using the AST activity assay kit (Sigma-Aldrich) ( $n = 9$ /group). (T) H2030BrM cells were incubated with the indicated concentration of nicotine for 24 h. They were then examined for cell viability ( $n = 9$ /group). The data are presented as the mean  $\pm$  SD. \*,  $P < 0.05$ ; \*\*,  $P < 0.01$ ; and \*\*\*,  $P < 0.001$  versus respective nicotine group. ##,  $P < 0.01$  versus respective PLX3397 and Nico+PLX3397 groups.

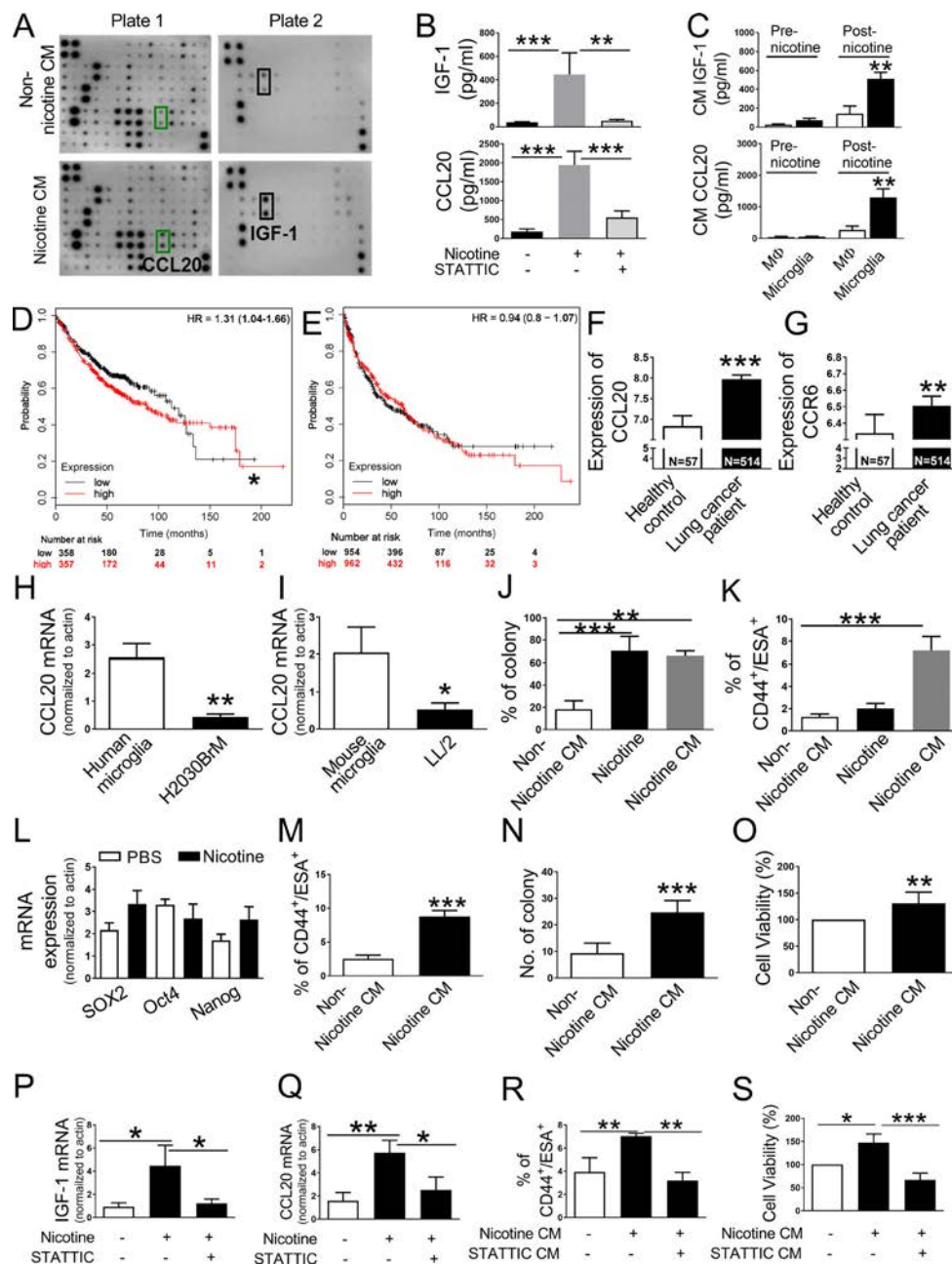


**Figure S3. Nicotine treatment of microglia increases secretion of CCL20 and IGF-1 followed by promotion of tumor cell stemness.** (A) Human microglial (HMC3) cells were treated with PBS or nicotine (1  $\mu$ M) for 24 h. CM was collected and analyzed by using the cytokine/growth factor array (Raybio). (B) Human microglial (HMC3) cells were treated with or without nicotine (1  $\mu$ M) plus STAT3C (0.5  $\mu$ M) for 24 h. Cells were washed with PBS twice and incubated in the fresh DMEM/F12 medium supplemented with 2% FBS for additional 24 h. CM was collected and analyzed by IGF-1 and CCL20 ELISA ( $n = 4$ /group). (C) Human microglial (HMC3) cells and macrophage (THP-1) were treated with or without nicotine (1  $\mu$ M) for 24 h. Cells were washed with PBS twice and incubated in the fresh DMEM/F12 medium supplemented with 2% FBS for an additional 24 h. CM was collected and analyzed by IGF-1 and CCL20 ELISA ( $n = 4$ /group). (D and E) Kaplan–Meier analysis was performed for examining relapse-free survival of lung cancer patients in relation to CCL20 ( $P = 0.02$ ; D) and IGF-1 ( $P = 0.36$ ; E) expression using the TCGA dataset. (F and G) Expressions of CCL20 (F) and CCR6 (G) were examined in lung tumor tissues from healthy individual and lung cancer patients using the GEO dataset (GSE22220). (H and I) Expression of CCL20 in human microglia and tumor cells (H) or mouse microglia and mouse tumor cells (I) were examined by qRT-PCR ( $n = 4$ /group). (J–L) H2030BrM cells were treated with or without nicotine or CM extracted from human microglia that were treated with nicotine for 24 h. These cells were examined for their colony-forming ability (J), CD44<sup>+</sup>/ESA<sup>+</sup> CSC population (K), and mRNA expression of stemness-related genes (L;  $n = 4$ /group). (M) Effect of CM extracted from nicotine-treated mouse microglial cells on LL/2 mouse lung CSC population was examined by FACS. (N) Colony-forming ability of LL/2 was measured in the presence or absence of the CM derived from nicotine-treated microglia by qRT-PCR ( $n = 4$ /group). (O) LL/2 cells were incubated with the CM derived from nicotine-treated microglia for 24 h. They were then examined for cell viability ( $n = 4$ /group). (P and Q) Mouse microglia cells were treated with or without nicotine in the presence or absence of STAT3 inhibitor for 24 h. Cells were then examined for the expression of IGF-1 (P) or CCL20 (Q) by qRT-PCR. LL/2 cells were treated with CM derived from microglia that were treated with or without nicotine and/or STAT3C for 24 h ( $n = 4$ /group). (R and S) The cells were then examined for CD44<sup>+</sup>/ESA<sup>+</sup> CSC population (R) and for cell viability (S;  $n = 4$ /group). The data are presented as the mean  $\pm$  SD. \*,  $P < 0.05$ ; \*\*,  $P < 0.01$ ; and \*\*\*,  $P < 0.001$ .

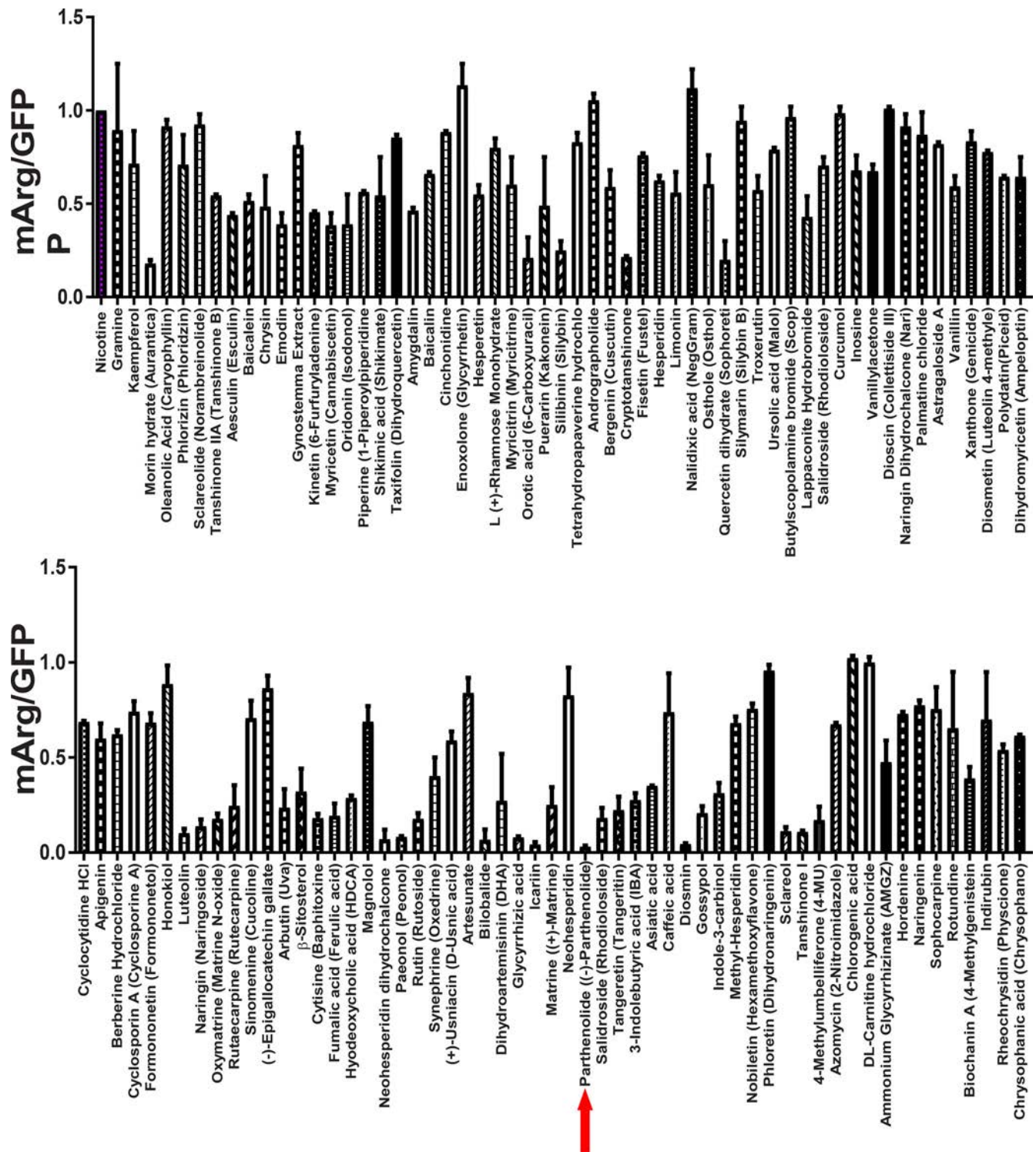
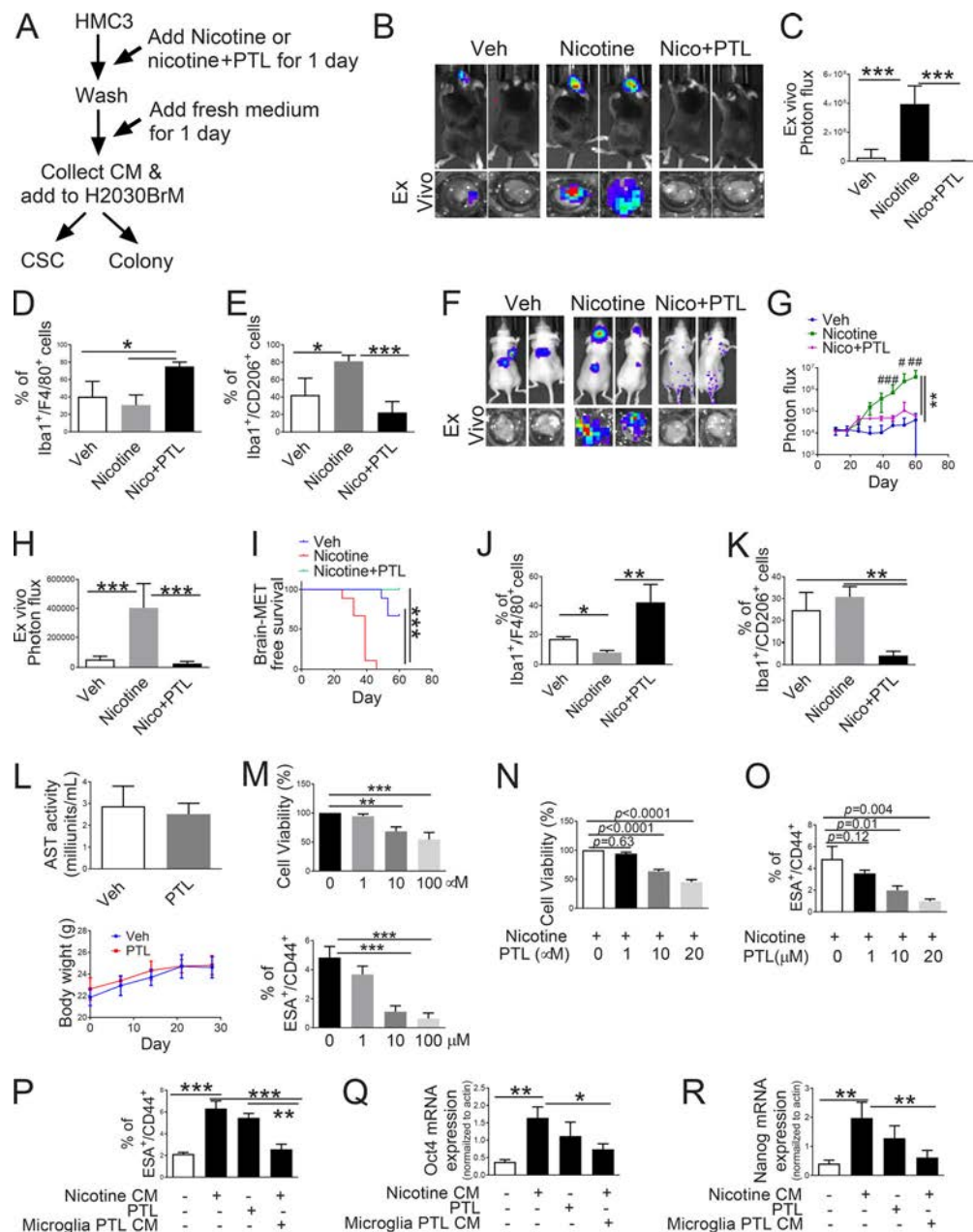


Figure S4. **Effect of natural compounds on nicotine-mediated activity of Arg1.** HMC3 cells containing Arg1 reporter plasmid were cultured in the presence or absence of nicotine (1  $\mu$ M) and/or each natural compound for 24 h. These cells were then examined for direct effect of compound on nicotine-mediated activity of Arg1 reporter ( $n = 4$ /group).





**Figure S5. PTL suppressed nicotine-promoted brain metastasis in syngeneic mouse model.** (A) Scheme of the experimental design. (B) Mouse lung cancer LL/2 cells were intracardially injected into wild-type C57BL/6 mice ( $n = 9/\text{group}$ ) followed by administering nicotine (1 mg/kg) or PTL (1 mg/kg) by intraperitoneal injection every 3 d after tumor injection. Upper panels are BLI images of brain metastatic lesions of representative mice from each experimental group at day 40. Lower panels represent the total photon flux of ex vivo brain metastatic lesions as measured by BLI at the end point (day 40). (C) Quantitative data of ex vivo brain metastasis of lung cancer in the brain at the end point of the experiment conducted in B ( $n = 9/\text{group}$ ). (D and E) Metastatic brain tumor tissues in B were dissociated and the effect of nicotine was examined for Iba1<sup>+</sup>/F4/80<sup>+</sup> (D) and Iba1<sup>+</sup>/CD206<sup>+</sup> (E) by FACS ( $n = 9/\text{group}$ ). (F) H2030BrM ( $2 \times 10^5$  cells) were intracardially injected into nude mice followed by administering them with nicotine (1 mg/kg) plus PTL (1 mg/kg) by an intraperitoneal injection every 3 d for 60 d. Upper panel: BLI images of brain metastatic lesions of representative mice from each experimental group at day 60. Lower panel: total photon flux of ex vivo brain metastatic lesions was measured by BLI at the endpoint (day 60;  $n = 9/\text{group}$ ). (G) Quantitative data of brain metastasis of lung cancer in vivo are shown ( $n = 9/\text{group}$ ). (H) Ex vivo signals in the brain at the end point were examined ( $n = 9/\text{group}$ ). (I) The Kaplan–Meier analysis of brain metastasis-free survival was performed. ( $n = 9/\text{group}$ ). (J and K) Metastatic brain tumors were isolated from the brain and were examined by FACS for M1 (J) and M2 (K) microglial polarization using FACS ( $n = 5/\text{group}$ ). (L) Serum of mice in Fig. 6 I was collected, and AST was measured by AST activity assay kit (Sigma-Aldrich). Body weight of the mice was also measured at the indicated time points ( $n = 9/\text{group}$ ). (M) Direct effect of PTL on tumor cell viability by MTS assay and ESA<sup>+</sup>/CD44<sup>+</sup> CSC population by FACS ( $n = 4/\text{group}$ ). (N and O) H2030 cells were cultured in the presence or absence of nicotine (1  $\mu$ M) and PTL at various concentrations for 24 h. These cells were then examined for direct effect of PTL on cell viability by MTS assay (N) and on ESA<sup>+</sup>/CD44<sup>+</sup> CSC population by FACS (O;  $n = 4/\text{group}$ ). (P) H2030BrM cells were incubated with CM derived from microglia that were treated with or without nicotine and/or PTL (1  $\mu$ M) for 24 h, followed by examination of ESA<sup>+</sup>/CD44<sup>+</sup> CSC population by FACS ( $n = 4/\text{group}$ ). (Q and R) The same set of samples in P was examined for the expression of stemness-related genes, OCT4 (Q) and NANOG (R), by qRT-PCR ( $n = 4/\text{group}$ ). The data are presented as the mean  $\pm$  SD. \*,  $P < 0.05$ ; \*\*,  $P < 0.01$ ; and \*\*\*,  $P < 0.001$ . #,  $P < 0.05$ ; ##,  $P < 0.01$ ; and ###,  $P < 0.001$  versus respective Nico+PTL group.